HRVATSKO DRUŠTVO
ZA STROJARSKE TEHNOLOGIJE

CROATIAN SOCIETY
FOR MECHANICAL TECHNOLOGIES

ISSN 1847-7917

11ᵗʰ International Conference

Mechanical Technologies and Structural Materials 2022

General sponsors:
University of Split - FESB,
The Split - Dalmatia County,
The City of Split,
EVN Croatia Plin d.o.o.

http://www.strojarska-tehnologija.hr

September, 22ⁿᵈ - 23ʳᵈ , 2022.
FESB, Ruđera Boškovića 32, Split

CONFERENCE PROCEEDINGS

MECHANICAL TECHNOLOGIES AND STRUCTURAL MATERIALS

Split

Croatia

22 - 23 September 2022

ORGANIZED BY:

CROATIAN SOCIETY FOR MECHANICAL TECHNOLOGIES, Croatia

CO-ORGANIZERS:

UNIVERSITY OF SPLIT
FACULTY OF ELECTRICAL ENGINEERING, MECHANICAL ENGINEERING AND NAVAL ARCHITECTURE

CROATIAN SOCIETY FOR MATERIALS AND TRIBOLOGY

DUBLIN INSTITUTE OF TECHNOLOGY

SLOVAK ACADEMY OF SCIENCE INSTITUTE OF MATERIALS AND MACHINE MECHANICS

ROGANTE ENGINEERING OFFICE

UNIVERSITY OF SPLIT
UNIVERSITY DEPARTMENT OF PROFESSIONAL STUDIES

ORGANIZING COMMITTEE:

- Nikša Čatipović (Croatia) - Chairman
- Zvonimir Dadić (Croatia) – Vice Chairman

- Ante ALUJEVIĆ (Croatia)
- Amanda ALJINOVIĆ (Croatia)
- Andrej BAŠIĆ (Croatia)
- Marina CRNJAC ŽIŽIĆ (Croatia)
- Ivana DUMANIĆ (Croatia)
- Igor Ćulum (Croatia)
- Igor GABRIĆ (Croatia)
- Nikola GJELDUM (Croatia)
- Karla GRGIĆ (Croatia)
- Jure KROLO (Croatia)
- Petar LJUMOVIĆ (Croatia)
- Zvonimir MRDULJAŠ (Croatia)
- Stipe PERIŠIĆ (Croatia)
- Slaven ŠITIĆ (Croatia)

PROGRAMME AND REVIEW COMMITTEE:

- Dražen ŽIVKOVIĆ (Croatia) – President
- Dražen BAJIĆ (Croatia) – Vice President

- Boris ANZULOVIĆ (Croatia)
- Frane BARBIR (Croatia)
- Franjo CAJNER (Croatia)
- Goran CUKOR (Croatia)
- Krešimir GRILEC (Croatia)
- Dario ILJKIĆ (Croatia)
- Vinko IVUŠIĆ (Croatia)
- Zlatko JANKOSKI (Croatia)
- Jaroslav JERZ (Slovakia)
- Sonja JOZIĆ (Croatia)
- David KENNEDY (Ireland)
- Marko MLADINEO (Croatia)
- Branimir LELA (Croatia)
- Zoran PANDILOV (Macedonia)
- Mladen PERINIĆ (Croatia)
- Massimo ROGANTE (Italy)
- Zdravko SCHAUPERL (Croatia)
- František SIMANČIK (Slovakia)
- Božo SMOLJAN (Croatia)

- Goran ŠIMUNOVIĆ (Croatia)
- Katica ŠIMUNOVIĆ (Croatia)
- Matej VESENJAK (Slovenia)
- Ivica VEŽA (Croatia)

Mechanical Technologies
and Structural Materials
MTSM2022

CONTENT

Application of 3D technologies in footwear trace evidence collection and identification

Andrej BAŠIĆ[1], *Toni PERKOVIĆ*[1], *Slobodan MARENDIĆ*[2]

1) University of Split, Faculty of Electrical Engineering, Mechanical Engineering and Naval Architecture, R. Boškovića 32, 21000 Split, **Croatia**

2) Split – Dalmatia County Police Headquarters, Trg Hrvatske bratske zajednice 8, 21000 Split, **Croatia**

Andrej.Basic@fesb.hr
Toni.Perkovic@fesb.hr
marendic.ms@gmail.com

Keywords

Sole impression
Sole imprint casting
Photogrammetry
3D scanning
3D printing
Fused deposition modeling

Professional paper

Abstract: Footprints are one of the most common traces found at the crime scene. They can be extremely important in discovering the perpetrators, and their proper collection, documentation and analysis is crucial for the case solving. Footprints can be found on different surfaces; smooth (e.g., floor) or more specific (e.g., mud, snow etc.). The collection of footwear trace evidence depends on the surface, and weather conditions. Sometimes it is necessary to act quickly (for example, collecting an impression in mud in rainy weather) and find the proper collection method. The most widespread technique of collecting impressions is casting but depending on the conditions, it is possible to apply other techniques. Considering the progress of technology, in this case of 3D scanning and printing, it is necessary to introduce new methods that will enable faster, safer, and more precise collection of traces, with maximum preservation of the integrity of the evidence. In this study, methods of extracting two-dimensional and three-dimensional traces are explained as well as the analysis of sole traces using conventional (casting) and non-conventional (3D scanning, photogrammetry and 3D printing by fused deposition modeling) methods with a detailed elaboration of the mentioned methods. To better understand the advantages and disadvantages of conventional and modern methods, the experiment on one footprint trace evidence was performed using casting, 3D scanning, photogrammetry, model preparation and 3D printing. The special emphasis on the duration and simplicity of each individual procedure was given.

1. Introduction

One of the basic principles of forensic science is individualization. To individualize means to prove the common origin (connection) of material evidence with reference samples. The individualization is based on matching of morphological, biochemical, physical and genetical features when comparing material evidence with reference samples. In case of investigation of a committed crime, to individualize means to prove from which person or object the trace originated. Based on the traces found at the scene it is necessary to establish the accuracy of the match between the evidence and the reference sample, that is, to present evidence of their common origin based on the results of the investigation as well as the knowledge and experience of the court expert (1).

Material or physical traces can be divided into four basic forms: transient evidence, traces of special appearance, conditional and transfer traces (2).

A transient or short-lived trace is a temporary trace that can easily change or disappear. For this reason, it is necessary that the person who first arrives to the scene properly documents and describes this type of trace. The category of transient traces includes odors, temperature, prints, impressions, and stains (2).

Apart from dactyloscopy traces (traces of papillary lines), traces of prints and impressions are examined in the framework of mechanoscopic expertise. They are created by the contact of one object with the surface of another, whereby a recognizable pattern is transferred. Analysis of these traces can be performed to determine group characteristics and individual characteristics (3).

It is necessary to distinguish footprints from impression traces. Footprints are planar (two-dimensional) traces that are created by the transfer of a medium like soil, mud, blood, fat, etc. onto a solid, smooth surface. These traces are mostly found indoors, and rarely outdoors (Figure 1). Such traces can be visible or invisible and can be made visible by using certain techniques (3).

Unlike footprint, an impression is a relief-like three-dimensional trace that is created by pressing an object using force into the soft surface such as snow, mud, soil, and sand (3). Such trace, for example, can be created by pressing car tires, shoes, tools, body parts etc. into the above-mentioned media, after which a three-dimensional image remains in the form of a negative (Figure 2).

Figure 1. Example of transfer imprint on hard surface.

Figure 2. Example of sole impression into the soft surface, soil.

Based on the previous research, footprints and sole impressions at the crime scene comprise a total of 35% of all traces found (4). Sole traces can indicate whether a person was walking or running, whether a person was carrying a heavy object, as well as information about the knowledge of the terrain on which the person was operating. Recovered traces can also provide physical information about the person, such as their height, weight, walking problems, as well as gait characteristics that can serve as comparative samples with the suspect's footwear (5). The location of footprints or sole impressions at the scene can also help in reconstruction of crime scene (4).

Methods of recording of the sole impression traces from the scene have remained unchanged for decades and they are mainly based on photography (2D) or exclusion by plaster casting (3D). Both techniques are characterized by disadvantages where, for example, it is not possible to obtain data on the depth of the impression with photography, and the plaster casting process can be lengthy with the risk of failure. Additionally, casting permanently destroys the trace, and it is not possible to capture all the details of the trace itself (6). Because of that, the use of 3D scanners and additive technology is increasingly enlarging its application in forensic science as part of one of the scientific methods under the name forensic engineering.

Application of additive technology and 3D scanning provides several potential advantages over standard methods: greater efficiency in multiple overlays of footwear impressions after processing data collected by scanning, the ability to segment the image to highlight individual characteristics, the creation of a high-resolution physical 3D model in detail, as well as other potential advantages due to its non-destructive nature (7). Regardless of the complexity of the model, the technology of additive manufacturing enables the rapid creation of the basic model in a short time. Additive manufacturing or rapid prototyping is defined as an automated process of creating a physical 3D model constructed with a computer (CAD - Computer Aided Design) modeling program or by converting the three-dimensional form of an existing object into a digital form using a 3D scanner (8).

The aim of this paper is to provide an overview of classic and modern methods of removing sole print marks and, based on the experiments carried out, draw conclusions about the advantages and disadvantages of these methods.

2. Experimental procedures

Experimental methods of extracting traces of footwear sole impressions were carried at the Laboratory for the crime scene investigation at the University Department of Forensic Sciences after training in the Split-Dalmatia County Police Headquarters (criminalistics police sector).

For the purposes of performing the experiments, two plastic containers were used, dimensions 400x280x80 mm, volume 9 liters, which were filled with sifted soil. One container contained a sample of completely dry soil while the other contained moist soil. The process of collecting traces was first carried out by the process of molding, where using classical plaster as a basic material, an attempt was made to obtain a sole impression model identical to the original with all its characteristics (Figure 3).

The second method included the photogrammetry process where, using a mobile phone as a basic tool, a minimum of 48 photos of the sole impression were taken in a full 360º range to capture all the trace details (Figure 4). For this purpose, a mobile phone from the Chinese manufacturer OnePlus, model OnePlus 8, was used as an appropriate tool (OnePlus, PR China, 2020).
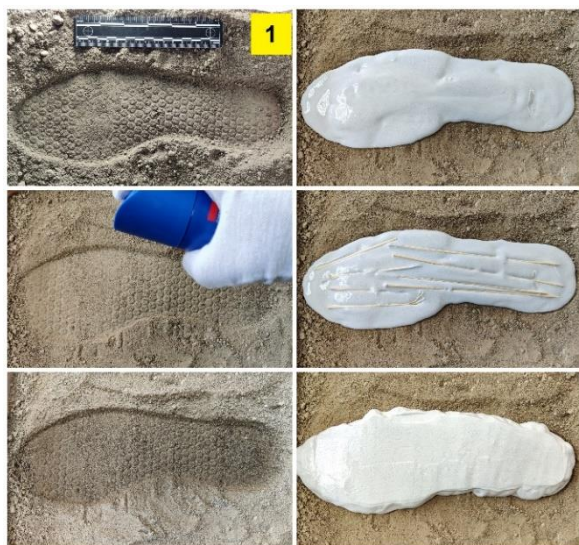
Figure 3. Steps in process of molding footwear sole impression left into the soft soil

Figure 4. Photographing sole impression in a 360º

Photographs were processed using the Agisoft Metashape software (Agisoft LLC, Russia, 2021, version 1.7.2) and a virtual impression model was obtained by merging them. The resulting virtual model was exported in OBJ format, and processed using Microsoft's 3D Builder (Microsoft, USA, 2017, version 18.01931.0). After processing virtual model in 3D Builder, the model was saved in STL format for printing on a 3D printer (Figure 5).

The third method of collecting sole impression trace was performed using the REVOPOINT POP 3D scanner (REVOPOINT, USA, 2021). A minimum of 1500 trace positions were scanned to capture all trace details. Obtained scans were first processed using 3D scanner original software, and then in the trial version of the Zbrush software (Pixologic, USA, 2020, version 1709). The obtained virtual 3D model was subsequently processed using Microsoft's 3D Builder and saved in STL format, which is suitable for processing with the 3D printer original software (Figure 6).
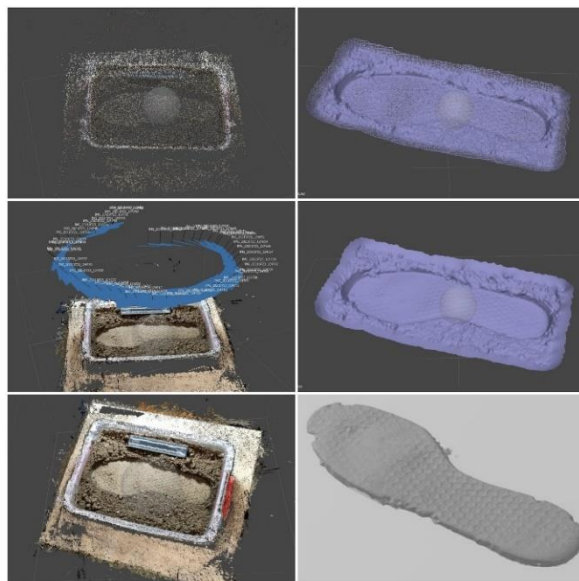
Figure 5. Steps in making virtual sole imprint model using photogrammetry process
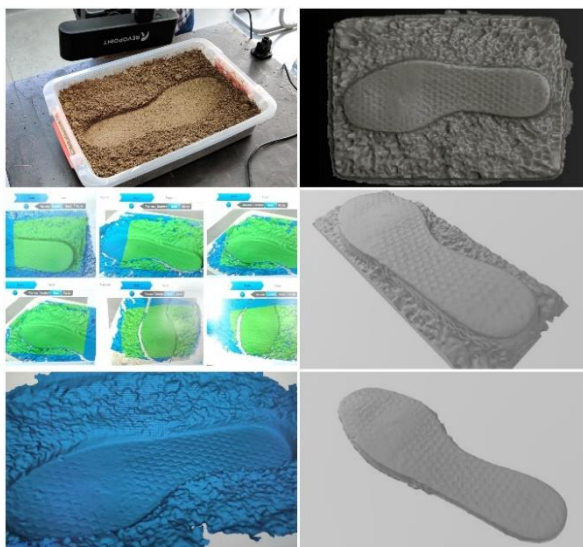
Figure 6. Steps in making virtual sole imprint model using 3D scanning process

Model of sole impression collected by a 3D scanner was printed on a 3D printer, PRUSA i3 Mk3 (PRUSA, R. Czech Republic, 2018). Preparation for printing was performed with PrusaSlicer software. Material used to make the model was Flexfill TPU 92A from the Czech manufacturer Fillamentum (Fillamentum, R. Czechia, 2018), which is characterized by flexibility and elasticity, as well as impact resistance and durability. Due to its elasticity, this material ensures that the final model is soft to touch, as is the case with real footwear soles.

Model was printed following the manufacturer's recommended settings for the specified material:

- printing temperature: 220 – 240 °C
- printing speed: 25 – 50 mm/s
- temperature of the heated work surface: 50 – 60 °C

Considering the size of the working surface of the 3D printer, 250x210x210 mm, it was not possible to print the model in full size, so the print was made in two parts (Figure 7.).

Figure 7. Model of the complete footwear sole printed on a 3D printer

3. Results

The following figures compare the results of the methods used to reproduce footwear sole imprints, showing its individual characteristics (Figure 8 - Figure 10).
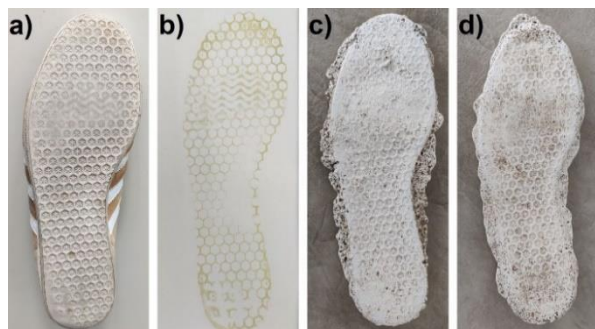
Figure 8. a) Footwear sole, b) reference sample, c) sole model from wet soil obtained by the molding process, d) sole model from dry soil obtained by the molding process
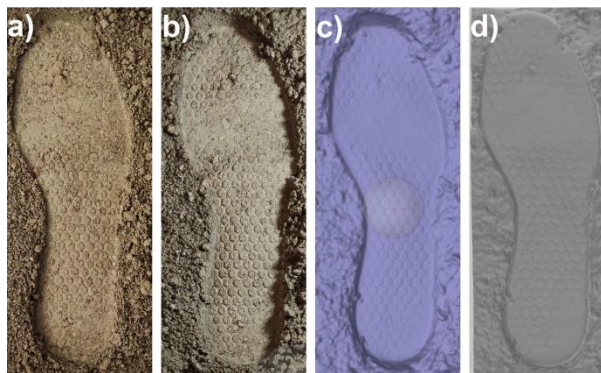
Figure 9. Model obtained using photogrammetry process: a) sole impression in wet soil, b) virtual model – density cloud c) virtual 3D model, d) model made with 3D Builder
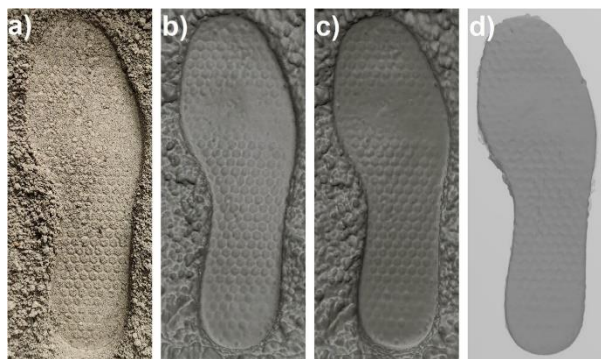
Figure 10. Model obtained using 3D scanning process: a) sole impression in wet soil, b) virtual model of the sole impression - gray filter c) virtual model of the sole impression - green filter, d) model made with 3D Builder

Table 1. shows a comparison of the time spent for extracting footwear sole impression using different methods.

Table 1.   Comparison of the sole impression extraction time using different methods.

Experimental procedure	Type of action	Spent time (h/min/sec)
Moulding - wet soil	Making a plaster cast	9' 38"
	Sample extraction and packaging	15' 22"
	Drying sample	24h
	Cleaning sample	5' 20"
	Total time	**24h 30' 20"**
Moulding - dry soil	Making a plaster cast	10' 44"
	Sample extraction and packaging	17' 28"
	Drying sample	24h
	Cleaning sample	5' 45"
	Total time	**24h 33' 57"**
Photogrammetry - wet soil	Photographing	5'
	Photo processing - AgiSoft	6h 5 '
	3D model processing – 3D Builder	25'
	Total time	**6h 30'**
3D scanning - wet soil	3D Scanning	15'
	Scans processing	1h 45'
	3D model processing – 3D Builder	20'
	Total time	**2h 20'**
3D printing - model created with 3D scanner	3D printing - heel	12h 43'
	3D printing - toes	17h 22'
	Total time	**30h 5'**

4. Discussion

With the completion of the practical part of collecting the footwear sole impressions, it was evident that each of three procedures had its advantages and disadvantages. The conventional process of excluding by molding was suitable due to the cheap and easily available material. The process itself did not require too much time, on average it took 20 minutes, which included the preparation, but the drying of the obtained sample required a period of 24 to 48 hours before it could be used and archived. The density of the prepared mixture depended on the type of soil (dry, moist, wet), and for the right component ratio, a certain amount of experience was necessary. The procedure was destructive, it was not repeatable, which could lead to the loss of the trace if proper exclusion was not carried out, and to the loss of part of the samples that could help in the reconstruction of the committed crime, such as certain biological, chemical, and other micro traces. Mulching unnecessarily samples, could lead to their deterioration and loss of forensic evidence, what was not the case for photogrammetry and 3D scanning procedures.

Unlike molding, the photogrammetry process was repeatable because the trace was not destroyed, and thus there was no loss of micro traces. The procedure itself was not complex and no expensive equipment was required as today almost all mobile phones have a high-quality camera that meets the conditions for obtaining quality photos. There was also a wide range of free photogrammetry software's, which offered a handful of additional functions for better processing, creation, and analysis of the virtual model. Collecting traces with this procedure also enabled the creation of a virtual database, and thus there was no accumulation of samples, which was the case with molding, but, if necessary, the impression model could be printed on a 3D printer. Also, photogrammetry allowed better visibility of the collected trace, because photography captured its essential segments, and the individual characteristics of the impression could be observed and analyzed in more detail. As a disadvantage of this procedure, an additional investment in more professional equipment could be accentuated if we wanted to obtain higher quality photos and the final product, i.e., 3D virtual model. An additional investment in a computer that requires a faster processor and more working memory for processing photos in some of the more functional software could also be needed; and if necessary, in a 3D printer with better performance so that the final model could be more accurate with a more realistic representation of the significant characteristics. In addition to all of the above, certain IT knowledge was also required to work with the devices and photo processing programs. The disadvantage of this procedure was that the final model

was not made on a real scale, so it was necessary to scale it up to its real dimensions. As it was the case with 3D scanning process, it is recommended that the photographing process does not take place directly under sunlight, as this could lead to the reduction in the quality of the photo, and thus to reduction in the virtual impression model quality and its essential features. This feature mainly applies to low-budget 3D scanners.

Collecting impressions using 3D scanning process had its similarities with the photogrammetry process; repeatability without loss of micro traces, the possibility of creating a virtual database, the possibility of additional processing of virtual impression model within the software (zooming of details, better visibility of the sample, the possibility of overlapping with the existing one, etc.) and no unnecessary accumulation of the sample; which can also be printed on a 3D printer if necessary. The advantage of this procedure compared to photogrammetry was the fact that the virtual model did not need to be subsequently scaled to the dimensions of the real sample because the 3D scanner captured and stored its real values. When scanning sole impression with an IR 3D scanner, there was no need to cover all 360° to create the model as was the case with photogrammetry. The 3D scanning process was characterized by a better resolution in contrast to the photogrammetry process and there would be no influence of weather conditions on the work if a professional forensic 3D scanner is used.

The shortcoming was manifested in the necessary investment in more professional and sophisticated equipment (3D scanner, 3D printer, computer, etc.) that did not have its limitations, as was the case with the low-budget 3D scanner used in this work. According to its characteristics and the need for forensic scanning, 3D-FORENSICS/FTI (GEXCEL, 2019, Italy) can be singled out as an example (9). The advantage of this 3D scanner is that weather conditions do not limit its use, nor does the type of terrain, and it is also distinguished by the dimensional accuracy of the recorded model and the amount of captured impression trace details essential for its individualization.

As is the case with photogrammetry, it is necessary to know the basic principles of working with the equipment and some IT knowledge to use the full potential of this method of excluding impression traces.

5.   Conclusion

Classical excluding methods are cheaper, faster, and simpler than the modern ones. Modern collection methods are less destructive than classical methods and allow the possibility to re-examine the evidence and to apply additional analyses of trace evidence. A more sophisticated and professional camera, 3D scanner and 3D printer, will give better results than the low-budget ones used in this research, although progress was already visible in contrast to the standard method. We recommended that, in addition to the classic impression collection, one of the modern methods should be used to enable additional trace analyses.

REFERENCES

[1]   Modly, D., Mršić, G. 2014. *Uvod u kriminalistiku*, Hrvatska sveučilišna naklada, Zagreb

[2]   Marendić, S., Anđelinović, Š., Kružić, I., Bašić, Ž., et al., 2021. *Forenzička analiza tragova krvi*, Sveučilište u Splitu, Sveučilišni odjel za forenzične znanosti, Split

[3]   Lee, C., Henry, et al., 1998. *Materijalni tragovi*, Birotisak, Zagreb

[4]   Andaló F.A., Goldenstein S., 2012. *Computer vision methods applicable to forensic science*, University of Campinas, Brazil

[5]   BCA - Bureau of Criminal Apprehension, SICAR® (Shoeprint Image Capture and Retrieval Database), USA, 2021. https://dps.mn.gov/divisions/bca/bca-divisions/forensic-science/Pages/trace-shoeprints-tiretracks.aspx (accessed 30 August 2022).

[6]   Crabbe, S., Kühmstedt, P., Ramm, R., Hendrix, A., Smolders, P, van Spanje, W., et al., 2015. *Results from 3D-forensics–mobile high-resolution 3D-scanner and 3D data analysis for forensic, evidence*. 10th Future Security, Security Research Conference 2015, Berlin, Germany

[7]   Thompson, T., Norris, P.J.S., 2018. A new method for the recovery and evidential comparison of footwear impressions using 3D structured light scanning. Justice. 58(3):237-43.

[8]   Peko, I., Bašić, A., Aljinović, A., 2018. *Računalom podržani dizajn, aditivna proizvodnja i 3D skeniranje proizvoda. Inovativno pametno poduzeće.* FESB, Split

[9]   Treccani, S., Italy, 2021. 3D-Forensics - Gexcel. https://gexcel.it/en/solutions/3d-forensics (accessed 30 August 2022)

Multi-criteria decision-making for mobile cobot stand

Marina CRNJAC ŽIŽIĆ[1]**, Nikola GJELDUM**[1]**, Karlo PETROVIĆ**[1]**, Marko MLADINEO**[1]**, Amanda ALJINOVIĆ**[1]

1) Faculty of Electrical Engineering, Mechanical Engineering and Naval Architecture, Ruđera Boškovića 32, 21000, Split, **Croatia**

mcrnjac@fesb.hr
ngjeldum@fesb.hr
kpetro00@fesb.hr
mmladine@fesb.hr
amaljino@fesb.hr

Keywords

Mobile cobot stand
Multi-criteria decision making
Learning factory
SMART method
AHP method

Original scientific paper

Abstract: Today's production trends are directed towards the production of personalized products. On the one hand, customers are often faced with dilemmas regarding product characteristics and sometimes find it difficult to make decisions, on the other hand, manufacturers are faced with difficulties in understanding the wishes and needs of customers and translating them into product characteristics. This paper presents the selection of appropriate mobile cobot stand for Learning factory purposes at the University of Split. Mobile cobots play a significant role in the Learning factory environment, especially for assembly tasks where collaborate with humans. A mobile stand is necessary for the cobot, so it can move between stations and come closer to the station for performing tasks. Two different multi-criteria decision-making methods were used for the selection of the stand. The comparison of results obtained from two different methods has been made and the appropriate mobile cobot stand has been selected.

1. Introduction

In the context of transformation towards new industrial paradigms, cobots are important participants in many industrial processes [1]. Cobots represent a new generation of robots which allow human-robot collaboration (HRC). Human-Robot Collaboration (HRC) is a form of direct interaction between humans and robots, principally aimed at achieving a common goal [2]. Humans have intelligence, flexibility and abilities to solve problems and robots can support them with precision, repeatability and power. Cobot's sensors make them highly reliable colleagues because if there is any detection of unexpected force, they have the ability to stop immediately [3].

With the introduction of the Learning factory concept, the real factory environment is brought to the University of Split, to face students with real industrial problems during their study. For safety reasons, the assembly process is the most common process in the Learning Factory concept [4]. The Learning factory is equipped with Franka Emika cobot which satisfies educational and research needs, Figure 1. It is currently set on a fixed element in the Learning factory environment. It was inevitable to find an appropriate mobile cobot stand to achieve higher flexibility in the application of cobot for assembly. Moreover, the mobility of the cobot will

enable the creation of a dynamic and flexible environment in which assembly lines can be changed and quickly adapted to new products.

Although there are different designs of robots, the most commonly used version is a robot arm.
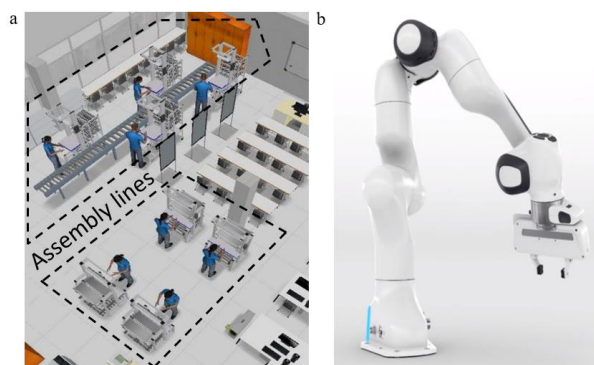
Figure 1. A digital twin of Learning factory and assembly lines (a) and Franka Emika cobot arm (b)

A robot arm should stay at the stable and mobile stand to cover the required work area. There is no standardized stand, usually, it is made according to the user's preferences. There are many possible designs for the mobile cobot stand, but for mentioned purposes, it should

satisfy several criteria. The process of multi-criteria decision making (MCDM) includes the selection, sorting and ranking of the best alternative from several suitable options, which are exposed to two or more competing criteria with the help of mathematical modelling.

2.   Problem description

In a Learning factory environment, the cobot usually does simple repetitive tasks cooperating with worker in the assembly process. There are several cobot characteristics important when making the mobile cobot stand.

Franka Emika includes the sensitive robotic arm with 7 axes and a grip. There is also the control unit which comes with the application. The application includes robot programs representing a partial step of a robot task. It is easy for worker to program robot, to perform some joint motions which usually include picking the object, then moving and placing it. There is enabling button as a part of the arm which allows worker the activation of the arm's motion. Franka Emika's arm has its reachable space, Figure 2.
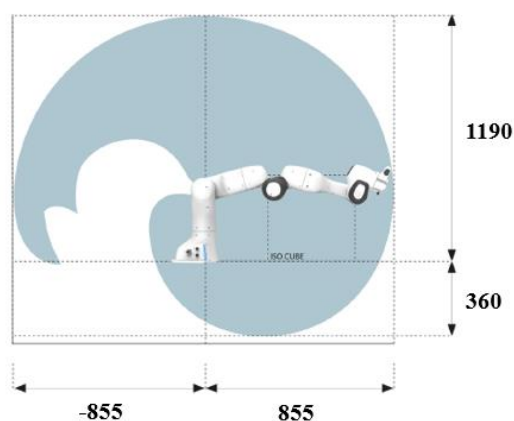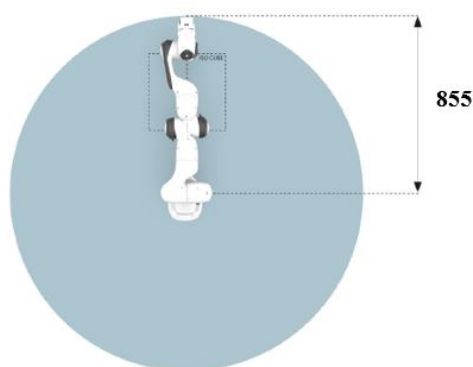
Figure 2.   Reachable space for Franka Emika: Side view (a) and Top-view (b), dimensions in mm [5]

Besides the reachable space, there are other impotrant characteristics summarized in Table 1.

Table 1.   Franka Emika robot arm's characteristics

Characteristics with units	
Degrees of freedom	7
Payload	3 kg
Maximum reach	855 mm
Force [N]	
Fx	-150-115 N
Fy	-275-275 N
Fz	-115-155 N
Torque sensing [Nm]	
Mx	-70-70 Nm
My	-16-12 Nm
Mz	-12-12 Nm
Weight	~17.8 kg
Controller size	355 x 483 x 89 mm (DxWxH)
Controller weight	~7 kg
Monitored signals	joint position, velocity, torque cartesian position, force

The arm is equipped with highly sensitive sensor technology and fine-tuned control algorithms, which requires installation on a stable, non-moving and non-vibrating platform. The following maximum forces must be supported during static and dynamic operation [5]:

- vertical force: 410 N
- horizontally force: 300 N
- tilting torque: 280 Nm
- torque around axis1: 90 Nm
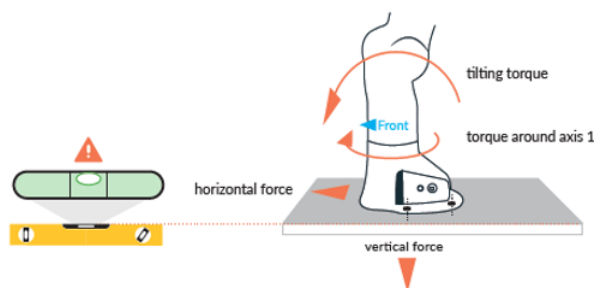
Figure 3.   Robot arm with torques and forces [5]

The criteria to design different variants of mobile cobot stands are generated from the characteristics mentioned above. Figure 4. is given to summarize all the equipment that a mobile cobot stand should carry.
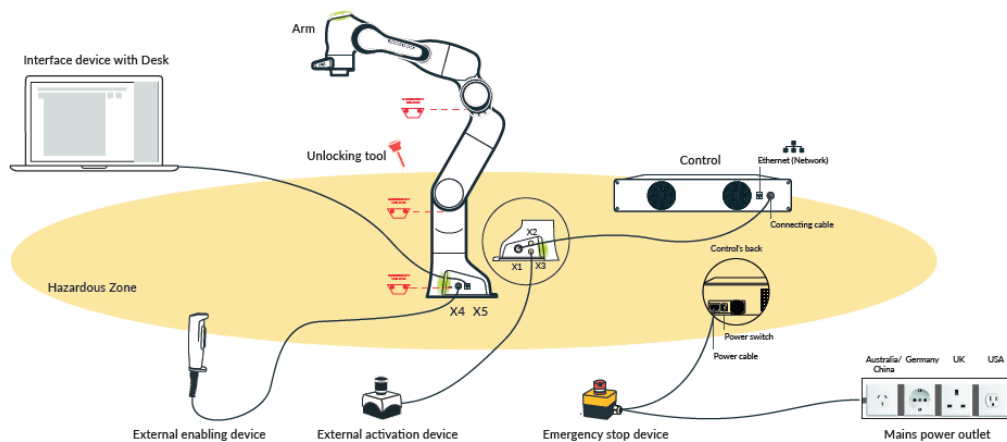
Figure 4. Robot arm with equipment overview [5]

3. Multi-criteria decision making: methods selection

The general workflow of the multi-criteria decision-making process can be described through 7 steps [6]:

1. Explore the "Big picture" (widely)
2. Identify the problem
3. Identify possible solutions
4. Define Criteria
5. Get the data
6. Compare the alternatives
7. Recommend a solution

There are many multi-criteria decision methods used in different areas. Table 2 shows several methods with their area of application. Since there is no single method that is equally successful for all areas, the decision maker chooses the method based on experience and the areas of application.

Simple Multi-Attribute Rating Technique (SMART) is a compensatory decision-making method with multiple criteria. It was developed by Edwards in 1971 [7]. This approach is actually a simplification of the Multi-Attribute Utility Theory (MAUT). Several studies highlighted the main advantages of SMART, which are simplicity of use, its ease of translating values to a requirement of low resource amounts and its allowance for both relative and absolute weight assignment techniques [8]. The simplicity of asking a question and getting an adequate answer directly affects the decision maker's understanding of the process how to find a solution to a problem.

Analytic Hierarchy Process (AHP), developed by Saaty [9], describes decision problems in a hierarchical, multilevel structure, with the goal of making the decision on the highest level.

Table 2. MCDM methods with their area of application [10]

No.	Method	Area of application
1	Multi-Attribute Utility Theory (MAUT)	Economics, finance, actuarial, water management, agriculture
2	Simple Multi-Attribute Rating Technique (SMART)	Transportation, logistics, planning, environmental, construction, military, manufacturing, assembly problems
3	Analytic Hierarchy Process (AHP)	Performance-type problems, resource management, corporate policy and strategy, public policy, political strategy, planning
4	Fuzzy Set Theory	Engineering, economics, environmental, social, medical, management
5	Goal Programming (GP)	Production and energy planning, scheduling, healthcare, portfolio selection, water and wildlife management, scheduling
6	ELECTRE	Energy, environmental management, water management, transportation
7	PROMETHEE	Environmental, water management, business and finance, chemistry, logistics and transportation, manufacturing and assembly, energy, agriculture
8	Simple Additive Weighting(SAW)	Water management, business, and financial management
9	TOPSIS	Supply chain management and logistics, engineering, manufacturing systems, business and marketing, environmental, human resources, management

The advantage of AHP is its simple use, adaptation in size to satisfy decision-making problems due to its hierarchical structure and it is straightforward in its approach.

Due to the applicability of the SMART method to the type of problem in this research and its stated advantages, the SMART method is primarily used for the selection of the proper stand variant, which best meets all the given criteria. AHP is used for comparative purposes.

3.1. SMART method - steps

The SMART method is based on 10 steps [10]:

1. Identify the person or agency whose utilities are to maximize
2. Identify the issue
3. Identify the alternatives for evaluated
4. Identify the relevant dimensions of value for evaluation of the alternatives
5. Rank the dimensions in the order of importance
6. Rate dimensions in importance, preserving ratios
7. Sum the importance weights, and divide each by the sum
8. Measure the location of each alternative evaluated on each dimension
9. Calculate Utilities for alternatives
10. Decide - For the last step, it is necessary to choose the alternative with the maximum utility if there is a single alternative to be selected. Otherwise, if budget constraint exists, then alternatives are selected by the highest ratio of utility and the costs of the alternative.

3.2. AHP method - steps

The AHP method is based on four main steps [11]:

1. Generate a paired comparison matrix
2. Compute the relative importance of various attributes by using the normalization of the geometric mean (NGM) technique
3. Calculate the consistency of the obtained degree of importance for the attributes.
4. Define the relative overall importance degrees of different attributes

4. Results and discussion

The reason for constructing the stand is that the existing models offered on the market do not fully meet the requirements that must be met when using the Franka Emika arm in the Learning factory. As can be seen from Figure 5, the proposed stand designs have a place for mounting the wheels and therefore the mobility requirements are met. They are modular, and the vertical support of the robot can be moved horizontally and vertically along the lower frame of the structure. The entire stand is connected via a screw connection, which allows it to be completely disassembled, thus facilitating transport.

The criteria used for the selection of the mobile cobot stand are the thickness of the base plate for the robot, the way of tying the vertical support to the lower frame of the structure (in tables: way of tying), the type of material and the cost of the material. The combination of all criteria results in eight different alternatives (performances) for the stand. All alternatives are included to select the most appropriate variant using the SMART and AHP method.
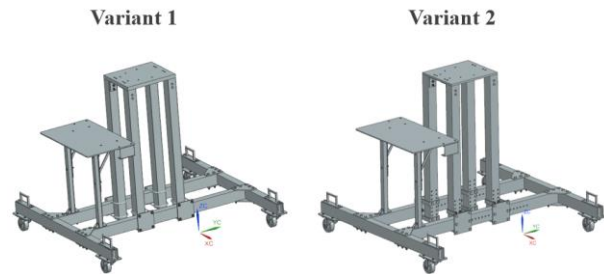
Figure 5. Two variants of mobile cobot stand

Different values for criteria used for each variant are given in Table 3.

Table 3. Different values for criteria used for each variant

Criteria Alternative	Thickness of base plate [mm]	Way of tying	Material	Costs
Variant 1	10	medium (clips)	cheap (steel)	400
Variant 2	10	great (screws)	cheap (steel)	450
Variant 3	20	medium (clips)	cheap (steel)	500
Variant 4	20	great (screws)	cheap (steel)	550
Variant 5	10	medium (clips)	expensive (aluminium)	600
Variant 6	10	great (screws)	expensive (aluminium)	650
Variant 7	20	medium (clips)	expensive (aluminium)	800
Variant 8	20	great (screws)	expensive (aluminium)	850

4.1. SMART method – application and results

To reflect the difference between preferences, the values from 0 to 100 (where 0 represents low importance and 100 represents high importance) are assigned to criteria, Table 4.

Table 4. Evaluation of criteria by importance

Criteria	Importance	Weight
Thickness of base plate	20	0.75
Way of tying	100	0.377
Material	65	0.245
Costs	80	0.302
Sum	265	1

The value is added to the alternatives for each criterion in Table 5. Values to evaluate criteria "thickness" is 100 for the best option and 0 for the worst option. Values to evaluate criteria "tying" is 0 for insufficient, 25 for sufficient, 50 for good, 75 for very good and 100 for excellent. Material costs depend on the type of material, the thickness of the panel and the method of fixing the vertical support. A cheaper variant is preferred. The costs are normalized.

Table 5.   Evaluation of variants

Criteria / Alternative	Thickness of base plate [mm]	Way of tying	Material	Costs	Value
Var.1	100	50	25	100	62.7
Var.2	100	100	25	88.89	78.2
Var.3	0	50	25	77.78	48.5
Var.4	0	100	25	66.67	64
Var.5	100	50	75	55.56	61.6
Var.6	100	100	75	44.44	77.1
Var.7	0	50	75	11.11	40.6
Var.8	0	100	75	0	56.1

According to the SMART method, there is a rank of alternatives, where the best is variant 2., Table 6.

Table 6.   Results according to the SMART method

Variant	Rank
Variant 2	76.6
Variant 6	75.4
Variant 4	68.8
Variant 1	59.9
Variant 5	58.7
Variant 8	60.4
Variant 3	52.1
Variant 7	43.7

4.2. AHP method – application and results

The value of one criterion in relation to other criteria is presented in paired comparison matrix or Table 7.

Table 7.   Paired comparison matrix with normalized values

	Thickness	Way of tying	Material	Costs
Thickness	0.048	0.069	0.02	0.033
Way of tying	0.429	0.621	0.49	0.691
Material	0.19	0.104	0.082	0.046
Costs	0.333	0.207	0.408	0.23

After the importance of all criteria for all variants is calculated, their values are entered in a table together with previously calculated weightings of the importance of individual criteria. Then, for each criterion, the value of each variant is calculated by multiplying the weight of the importance of each criterion with the importance of each variant in relation to that criterion. In the end, all the values of each variant are added up according to all criteria, which gives the total value of each variant, Table 8.

Table 8.   Results according to the AHP method

Variant	Rank
Variant 2	0.607
Variant 4	0.586
Variant 8	0.509
Variant 6	0.502
Variant 1	0.302
Variant 3	0.266
Variant 7	0.177
Variant 5	0.174

4.3. Comparison of results

After using two MCDM methods, it is evident that the best variant for mobile cobot stand is variant 2. Although the methods have different approaches to solve problems in this research, they gave the same variant as the result. The selected mobile cobot stand has a lower frame made of rectangular tubes with dimensions of 1000 x 40 x 60 [mm], and the vertical support of the robot consists of square tubes with dimensions of 800 x 50 x 50 [mm] with a plate for the robot with dimensions of 300 x 250 x 10 mm. The dimensions of the laptop board are 500 x 300 x 5 mm, and it is mounted on vertical square tubes 450 x 25 x 25 mm. The stand is made of steel.

5.   Conclusion

Today, the industry is mostly based on automation processes and strives for Industry 4.0, which implies the cooperation of humans and robots with the aim of

achieving optimal results. The wide application of robots has simultaneously encouraged the development of supporting equipment that contributes to their maximum efficiency. This development of supporting equipment appeared as a task in the Learning factory environment, where the mobile robot stand will be produced. In order to minimize costs and facilitate assembly, it is necessary to design the stand as simply as possible. Also, it is preferable to check all criteria and variants before the production process starts. The way of choosing the appropriate design presented in this paper was useful. Two different MCDM methods showed the same variant as an appropriate one. However, there are differences when comparing these two methods by observing the rank of other variants. This suggests further research on the methods that would be appropriate for this specific type of problem when searching for an adequate product design.

REFERENCES

[1] Zizic, M.C., Mladineo, M, Gjeldum, N, Celent L, 2022. From Industry 4.0 towards Industry 5.0: A Review and Analysis of Paradigm Shift for the People, Organization and Technology. Energies (Basel) 15, 5221.

[2] Gervasi, R., Mastrogiacomo, L., Franceschini, F., 2020. A conceptual framework to evaluate human-robot collaboration. International Journal of Advanced Manufacturing Technology 108, 841–865. https://doi.org/10.1007/s00170-020-05363-1.

[3] ISO/TS 15066:2016: Robots and robotic devices – collaborative robots. Standard ISO/TS 15066:2016, International Organization for Standardization, Geneva, CH, 2016. https://www.iso.org/standard/62996.html (accessed 7 Jul 2022).

[4] Veza, I., Mladineo, M., Kutlesa, M., et al., 2022. *Selection of the Cobot Workstation for the Learning Factory by using the Multi-Criteria Analysis*, CLF 2022, Singapore

[5] Franka Emika, 2020. PANDA'S INSTRUCTION HANDBOOK. https://wwwpub.zih.tu-dresden.de/~s5990957/Franka-Panda-UserGuide-eng.pdf (accessed 7 Jul 2022).

[6] De Brouwer, P.J.S., 2016. Quantitative Methods PART 4: Multi Criteria Decision Analysis, University of Warsaw, Poland

[7] Edwards, W., Barron, F.H., 1994. SMARTS and SMARTER: Improved simple methods for multiattribute utility measurement. Organ Behav Hum Decis Process. 60, 306–325.

[8] Velasquez, M., Hester, P. T., 2013. An analysis of multi-criteria decision making methods. International journal of operations research 10, 56-66.

[9] Saaty, R.W., 1987. The analytic hierarchy process—what it is and how it is used. Mathematical Modelling 9, 161–176. https://doi.org/10.1016/0270-0255(87)90473-8.

[10] Patel, M.R., Vashi, M.P., Bhatt, B.V., 2017. *SMART-Multi-criteria decision-making technique for use in planning activities*. Proceedings of New Horizons in Civil Engineering (NHCE-2017), Surat India.

[11] Ghaleb. A.M., Kaid, H., Alsamhan, A., et al., 2020. Assessment and Comparison of Various MCDM Approaches in the Selection of Manufacturing Process. Advances in Materials Science and Engineering 2020. https://doi.org/10.1155/2020/4039253.

Modelling of process parameters in cross-wire welding of S235 steel wires using Design of Experiments

Ivana ČABRIJAN[1], Maja VLATKOVIĆ[1], Elvis KRULČIĆ[1], Duško PAVLETIĆ[1]

1) University of Rijeka, Faculty of Engineering, Vukovarska 58, 51000 Rijeka, **Croatia**

icabrijan@riteh.hr

Keywords

Cross-wire welding
Welding current
Setdown
Weld breaking force
Electrode position
Design of experience
Regression model

Original scientific paper

Abstract: Finished products such as stands, wire containers, shopping carts, grids, baskets, gratings, fencing systems, etc. are widely used in daily life. These products are manufactured by joining wires using a special welding process. In this paper, the process of making high quality welded joints using one of the most commonly used resistant welding processes, cross wire welding, is described. Before conducting experiments, it is necessary to determine the process parameters to be observed and analysed. For this purpose, Design of Experiments is used. Design of Experiments is one of the quality tools that can be used for various investigations, e.g. modelling of the process, determination of influencing factors and process parameters, process variations, etc. The aim of introducing this tool is to gain new and better knowledge and at the same time to increase the competitiveness of the company by improving the quality and reliability of the products. The welding current, time and electrode position are input parameters. The setdown and weld breaking force is an output parameter and was measured for each sample after welding. The aim of this paper is to show the influencing parameters, their correlation and the regression model to create a reversible prediction of the observed process parameters, which was verified by analysis of variance. The statistical analysis was performed using the Minitab programme, and the results show that the welding current in relation to the welding time and the position of the electrode has the greatest influence on the welding process.

1. Introduction

This research was conducted as part of a European Regional Development Fund project. The aim of the research is to determine cause-and-effect relationships and empirical modelling of the resistance welding process.

The production of metal products is increasing every day, and competition between manufacturers is becoming fiercer. Metal joints play a very important role in modern production technology. Welding is used as a production process in both small and large industries. Welding increases the productivity of better-quality materials. The welding process is carried out on a large scale, which can affect the quality of the weld, productivity and production costs [1].

Resistance welding is a highly efficient production method which is particularly suitable for automated production lines and mass production. Resistance welding can also be used for small batch production because the process is flexible, the equipment is simple and the welding process can be easily controlled [2].

Projection welding is a type of resistance welding, in which projection welds are made by localizing the welding current, welding pressure and heating during welding at one or more predefined points [3].

In this study, cross wire welding is used, which is actually a form of projection welding. The general factors affecting projection welding also apply to cross-wire welding [3]. Generally a series of parallel wires is welded at a 90° angle to one or more other rods or wires.

Depending on the production requirements, there are several specific methods for performing the welding process, but the end product is the same regardless of the method used [4]. Bushell [5] and Jordan [6] in their works described the process of producing meshes by welding several points simultaneously. For this research, this welding procedure is used in which the electrode is modified so that three welds are welded simultaneously. In each process there are certain parameters that affect its stability, reliability and quality. The main goal of scientific research is to prove the statistical significance of the effects of each parameter [7]. Therefore, various experimental methods are used in research.

This paper presents the application of Design of Experiments to cross-wire processes to determine important process parameters. DOE is a scientific method for determining critical parameters of a process. It enables the realization of optimal settings for these process parameters to improve the performance and capability of the process [8].

Various studies of process parameters in different types of welding have been carried out. Fukumoto and Zhou [9] performed input parameter test with detailed mechanical and metallurgical tests based on the mechanism for joining fine nickel wires [9].

Kim et al. [10] investigated the infuene of process parameters (welding current, welding force and welding time) during resistance cross-wire welding on the metal strength of the weld, represented by the breaking force of the joint [10].

In addition to the Design of Experiment, a model of the parameters of the cross-wire welding process is defined. This is achieved through experiments and statistical analysis of the obtained data. The correlation between the input-output process parameters and the regression model verified by analysis of variance is presented. A well-constructed regression model can recommend which parameters should be used to make the weld as optimal as possible. This often leads to an increase in engineering efficiency and product quality [11]. The applications of such models and analyses vary depending on the area in which they can be used.

For example, in the field of TIG welding process, Dutta and Pratihar [11] performed a conventional regression analysis on 36 randomly generated test cases using full factorial design of experiments (DOE) and two neural network based approaches. Chandel [12] showed the correlation between welding process parameters and grain-to-grain geometry when welding plates with CO_2 gas. He confirmed that arc current is the most important parameter for determining grain geometry. Park and Kim [13] in their paper present an interval regression analysis to build models that can help in analysing uncertain data and support decision making based on the model. Eshraghi et al. [14] quantified the effects of welding parameters on various welding properties of DP600 steel using a finite element model and found that current in the range of 6-10 kA was the most influential factor among all welding parameters.

Therefore, the main parameters of the cross-wire welding process are presented and analysed in this and future research.

2. Experimental procedure

2.1. Material

In this paper, steel wire S235 with a diameter of Ø4h9 mm is taken for the welding process. "S" is a steel symbol, which means that it is structural steel, which is most often used in construction and the field of general mechanics, i.e. welded structures, load-bearing and dynamically loaded structures. The mechanical properties are shown in Table 1 [15].

Before welding, the wire material must be clean, free of rust, paint, dirt, heavy grease or high-resistance coatings. Wires are supplied in large spools, Figure 1, which are cut, Figure 2, on a cutting machine to a certain length before the welding begins.

Table 1. The mechanical properties of grade S235 [15]

Steel grade	Minimum yield strength [MPa]						Tensile strength Rm [MPa]		Minimum elongation – A $Lo = 5.65 * \sqrt{So}$ (%)				Notch impact test	
	Nominal thickness [mm]						Nominal thickness [mm]		Nominal thickness [mm]				Temperature	Min. absorbs energy
	≤16	>16 ≤40	>40 ≤63	>63 ≤80	>80 ≤100	>100 ≤125	>3 ≤100	>100 ≤125	>3 ≤40	>40 ≤63	>63 ≤100	>100 ≤125	[°C]	[J]
S235J0	235	225	215			195	360-510	350-500	26	25	24	22	0	27
S235J2	235	225	215			195	360-510	350-500	26	25	24	22	-20	27
S235JR	235	225	215			195	360-510	350-500	26	25	24	22	+20	27

Figure 1. Spools of wires
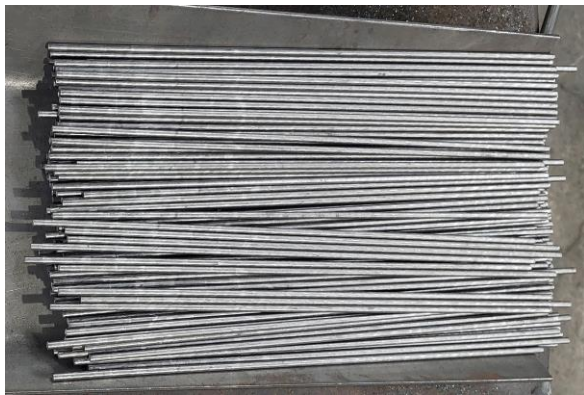
Figure 2. Cutted wires to required dimension

2.2. Process parameters

Before starting the welding process, it is necessary to define which parameters will be observed.

According to [16], before adjusting the machine, it is necessary to pay attention to:

1. Weld breaking force, weld appearance and setdown
2. Welding electrodes
3. Welding force (pressure)
4. Welding time
5. Welding current (heat)
6. Weld testing

Therefore, it was defined that the input parameters that will be observed for this work will be welding current, welding time and electrode position, Table 2, while the pressure will be kept constant.

The position of the electrode will be observed because in previous research, [17] it was found to affect the stability of the process. This paper will show its influence on the observed output parameters. Also, the influence of welding current and welding time will be shown.

The output parameters that will be observed and can be measured are setdown and weld breaking force, while weld appearance will be analysed in future research.

Table 2.   Input parameters of cross-wire welding process

Process parameter	Factor	Units	Levels	Level Values		
Welding current	A	kA	3	1	2	3
				8	12	16
Welding time	B	ms	3	1	2	3
				20	50	100
Electrode position	C	-	3	1	2	3
				1	2	3

2.3. Cross-wire welding process

After cutting the wires and defining the parameters, the welding process follows. The operator places the cut wires in a certain device, adjusts the input parameters on the control panel and starts the program to start the welding process. Welding begins by pressing the wire between two electrodes. The force on the electrodes is transmitted to the wires, and the welding current flows through the electrodes, which leads to the generation of heat in localized spots. There is a melting of the material, mixing and after cooling to a solid joint. The electrode is specially designed to be able to weld three welds at the same time, Figure 3. Therefore, the output parameters will be observed according to the position of the electrode.

Figure 3. Cross-wire welding process

2.4. Sample preparation and measurement

After the welding process is completed, the mesh is cut to obtain samples of smaller dimensions, Figure 4, which would enable simpler, faster and more functional measurement.

The samples are placed in a specific order in a box specially designed for this type of experiment. One mesh consists of 9 vertical and horizontal wires, which means a total of 81 samples from each mesh. After cutting and placing in a box, each sample is individually placed in a micrometer screw gauge which measures the diameter of the wire after welding, which is the starting point for

obtaining the value of the setdown, which is measured according to the following formula [17]:

$$"PERCENT\ SETDOWN" = \frac{A-B}{C} \cdot 100[\%] \qquad (1)$$

where:

A - sum of diameters of two wires before welding, mm
B - sum of diameters of two wires after welding, mm
C- wire diameter (diameter of one wire before and after welding is the same or approximately the same), mm

After the setdown measurement, the breaking force measurement follows, [18].

This is followed by an analysis of the obtained results in the Minitab software, which is presented in the next chapter.

Figure 4.   Sample

3.   Results

3.1. Design of experiments

Design of Experiments (DOE) tool is commonly used to investigate hidden causes of process variation and study the possible effects of variables during process design and development. Experiments range from uncontrolled factors introduced at random to carefully controlled factors [19].

The full factorial design as part of DOE is useful during experimental work when it is necessary to investigate the influence of parameters. In order to properly understand DOE, it is necessary to have a good understanding of the process. The process is the transformation of inputs into outputs [20].

According to [7], if one wants to study 7 factors, the required number of runs in the experiment would be $2^7 = 128$. To study 10 factors, you will need $2^{10} = 1024$ runs in the experiment, and for 15 factors, you will need $2^{15} = 32,768$ runs. Because each run can require time-consuming and expensive set-up and re-setup of machines, it is often not feasible to require many different productions runs for an experiment.

Therefore, due to a large number of samples for analysis, the mean value was taken according to the position of the electrode within one mesh. So, there are a total of 9

meshes with 81 samples each. The electrode welds three welds simultaneously, which means that there are three positions of the electrode within the mesh. Knowing the path of the electrode, the measured values can be selected according to the position of the electrode.

The results of the conducted experiment are shown in Table 3.

In the first three runs, the values of setdown and weld breaking force is equal to 0, because when the welding current is 8kA and the time is 20ms, the welding of the mesh does not occur.

To determine whether two process parameters are interacting or not, an interaction plot can be used. If the lines in the interaction plot are parallel, there is no interaction between the process parameters. This implies that the change in mean response from low to high levels of a factor does not depend on the level of another factor. On the other hand, if the lines are non-parallel, there is an interaction between the parameters (factors) [7].

Figure 5 and Figure 6 show that there is an interaction of welding current and time on setdown and breaking force. Also, parallel lines can be seen on the diagrams at the electrode position, which establishes that it has no interaction.
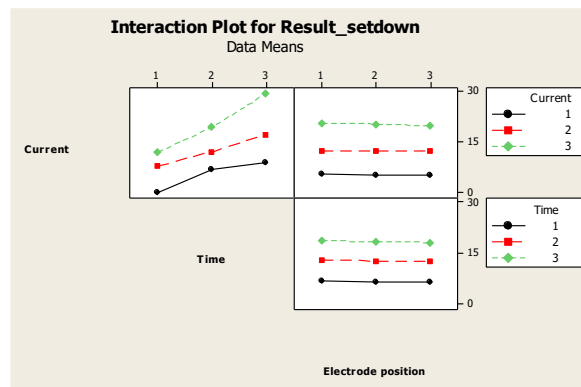
Figure 5.   Interaction plot for setdown
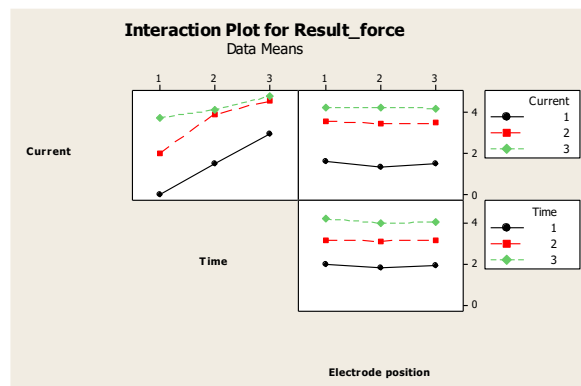
Figure 6.   Interaction plot for weld breaking force

Table 3. Results of the experiment

Run	A	B	C	Setdown (%)	Weld breaking force (kN)
1	1	1	1	0.000	0.000
2	1	1	2	0.000	0.000
3	1	1	3	0.000	0.000
4	1	2	1	7.060	1.511
5	1	2	2	6.730	1.375
6	1	2	3	6.830	1.595
7	1	3	1	9.280	3.308
8	1	3	2	9.000	2.672
9	1	3	3	8.620	2.892
10	2	1	1	7.900	2.233
11	2	1	2	7.760	1.740
12	2	1	3	7.530	2.128
13	2	2	1	12.090	3.975
14	2	2	2	12.040	3.984
15	2	2	3	12.020	3.811
16	2	3	1	17.060	4.599
17	2	3	2	17.000	4.603
18	2	3	3	17.130	4.551
19	3	1	1	12.200	3.799
20	3	1	2	12.060	3.816
21	3	1	3	11.510	3.681
22	3	2	1	19.600	4.122
23	3	2	2	19.400	4.079
24	3	2	3	18.860	4.214
25	3	3	1	29.720	4.812
26	3	3	2	29.350	4.845
27	3	3	3	28.820	4.754

3.2. Correlation

Corelations are shown in Table 4 and Table 5.

Table 4. Correlation between setdown and parameters

	Setdown	Electrode position	Time
Current	0.762		
	0.000		
Time	0.608	0.000	
	0.001	1.000	
Electrode position	-0.020	0.000	0.000
	0.920	1.000	1.000

Table 5. Correlation between weld breaking force and parameters

	Breaking force	Electrode position	Time
Current	0.739		
	0.000		
Time	0.586	0.000	
	0.001	1.000	
Electrode position	-0.022	0.000	0.000
	0.914	1.000	1.000

The highest Pearson correlation coefficient between setdown and welding current is 0.762 with p-values of

0.000, and between weld breaking force and welding current is 0.739 with p-values of 0.000. P-values are less than the 0.05 significance level, indicating that the correlation is significant.

Then comes the welding time with a coefficient of 0.608 for the setdown and 0.586 for the breaking force. The p-values are also 0.000.

The Pearson correlation coefficient between setdown and electrode position is -0.020 with a p-value of 0.920, and between breaking force and electrode position is -0.022 with a p-value of 0.914, indicating no correlations.

3.3. Regression model

Regression analysis generates an equation to describe the statistical relationship between one or more predictors and a response variable and to predict new observations. Regression generally uses the ordinary least squares method which derives the equation by minimizing the sum of the squares of the residuals [21].

Correlation analysis and interaction plots showed that the position of the electrode has no effect on the output parameters. Therefore, the welding current and time are used for the regression model in order to be able to predict, given various combinations of input parameters, the output parameters. Therefore, the welding current and time are used for the regression model in order to be able to predict various combinations of input parameters on the output parameters.

The experimental results were interpolated by the following regression model for percentage setdown and weld breaking force:

Percent setdown
$$= -18.0 + 1.86 * Current + 0.145 * Time \quad (2)$$

Breaking force
$$= -2.55 + 0.344 * Current + 0.0264 * Time \quad (3)$$

The R^2 value for setdown is 94%, which means that the predictors explain 94% of the variance of setdown. The R^2(adj) is 93.5%. Both values show that the model fits the data well. The R^2 value for weld breaking force is 87.5%, which means that the predictors explain 87.5% of the variance of weld breaking force. The R^2(adj) is 86.5%. As with setdown, the values show that the model fits the data well.

3.4. Analysis of variance (ANOVA)

Analysis of variance (ANOVA) tests the hypothesis that the means of two or more populations are equal. ANOVA assesses the importance of one or more factors by comparing the mean values of the response variable at different levels of the factor. The null hypothesis states that all population means (factor level means) are equal, while the alternative hypothesis states that at least one is different [21].

The model validation was given by analysis of variance whose results are shown in Table 6 and Table 7.

The p-values in the analysis of variance tables (0.000) indicate that the model estimated by the regression procedure is significant at the a-level of 0.05.

P-values of current and time with 0.000 indicate a significant association with setdown and weld breaking force.

Table 6.   ANOVA for setdown

Predictor	Coef	SE Coef	T	P
Constant	-17.980	1.662	-10.82	0.000
Current	1.8611	0.1218	15.28	0.000
Time	0.14512	0.01206	12.04	0.000

Source	DF	SS	MS	F	P
Regression	2	1616.68	808.34	189.14	0.000
Residual Error	24	102.57	4.27		
Total	26	1719.25			

Source	DF	Seq SS
Current	1	997.56
Time	1	619.12

Table 7. ANOVA for weld breaking force

Predictor	Coef	SE Coef	T	P	
Constant	-2.5459	0.4582	-5.56	0.000	
Current	0.34401	0.03358	10.24	0.000	
Time	0.026391	0.003324	7.94	0.000	
Source	DF	SS	MS	F	P
Regression	2	54.560	27.280	83.98	0.000
Residual Error	24	7.796	0.325		
Total	26	62.356			
Source	DF	Seq SS			
Current	1	34.084			
Time	1	20.477			

4. Conclusion

The meshes were tested to statistically analyse the input and output parameters of the cross-wire welding process. The statistical analysis included the Design of Experiment, which determine how the experiment should be conducted. In addition, a graphical representation of the interactions was created, showing that the positions of the electrodes do not affect the setdown and breaking force, either individually or in combination with other parameters. Unlike the electrode, the welding current and the welding time have an interaction, and how large this value is shown in the correlation tables. The welding current has the largest effect on the output parameters. For setdown, the Pearson correlation coefficient is 0.762, and for breaking force, 0.739. Welding current has a slightly lower coefficient, 0.608 for setdown and 0.586 for breaking force. The P-values are less than 5%, which means that the correlation is significant. Since position was found to have no influence, two input and output parameters were used in the construction of the regression model. The objective was to define a regression model for the setdown and breaking force, to allow a reversible prediction of the observed process parameters. The validation of the model is done by analysis of variance, the results of which show that the model fits the data well. This means that if a previously unexamined combination of input parameters is used, this model can be used to predict how much setdown and breaking force can be obtained. The research carried out can certainly serve as a basis for further research, e.g. for a comparison of these parameters and the weld appearance or for a comparison of the same input and output parameters but with different wire diameters.

Acknowledgements

REFERENCES

[1] Naik, A.B., Reddy, A.C., 2018. Optimization of Tensile Strength in TIG Welding Using Taguchi Method and Analysis of Variance (ANOVA). Thermal Science and Engineering Progress. 8, 327-339.

[2] Ruukki, R., 2009. Resistance Welding Manual. United States Documents.

[3] Phillips, A.L., 1969. *Welding Handbook,* American Welding Society, USA

[4] O'Brien, R.L., 1991. Welding handbook. American Welding Society, Miami

[5] Bushell, R., 1951. Resistance welding of cross-wire joints. Weld. Metal Fabr. 19(5), 175-178.

[6] Jordan, R.H., 1964. Productivity in multiple cross-wire welding. Weld. Metal Fabr. 32(1), 19-26.

[7] Hron, J., Macák, T., 2013. Application of design of experiments to welding process of food packaging. Acta Universitatis Agriculturae et Silviculturae Mendelianae Brunensis. 61(4), 909-915.

[8] Rowlands, H., Antony, J., 2003. Application of design of experiments to a spot welding process. Assembly Automation. 23(3), 273-279.

[9] Fukumoto, S. and Zhou, Y., 2004. Mechanism of resistance microwelding of crossed fine nickel wires. Metallurgical and Materials Transactions A. 35(10), 3165–3176.

[10] Kim, J., Seo, J., Batish, A., Bhattacharya, A., 2011. Effect of parameters in resistance micro-welding of

stainless steel cross wire using fractional factorial experimental design. Int. J. Manufacturing Research. 6, 290–303.

[11] Dutta, P., Pratihar, D.P., 2007. Modeling of TIG welding process using conventional regression analysis and neural network-based approaches. Journal of Materials Processing Technology. 184, 56–68.

[12] Chandel, R.S., 1988. *Mathematical modeling of as metal arc weld features*. Proceedings of the Fourth International Conference on Modeling of Casting and Welding Processes, 109-120.

[13] Park, J., Kim, K., 2918. Evaluation of interval regression analysis for uncertain resistance spot welding quality data. International Journal of Computer Integrated Manufacturing. 760-768.

[14] Eshraghi, M., Tschopp, M.A., Zaeem, M.A., Felicelli, S.D., 2014. Effect of resistance spot welding parameters on weld pool properties in a DP600 dual-phase steel: a parametric study using thermomechanically-coupled finite element analysis. Materials & Design. 56, 387-397.

[15] Major, M., Nawrot, J., Major, I., 2019. *Structural S235 and S355 Steels – Numerical Analysis of Selected Rods Connection*. 5th Annual International Workshop on Materials Science and Engineering, Poland

[16] Deffenbaugh, J. F., 2003. Resistance Welding Manual. Resistance Welder Manufacturers Association.

[17] Čabrijan, I., Vrtovšnik, D., Vlatković, M., Pavletić, D. 2021. Analysis of the cross-wire welding process stability. Technical Journal. 16(2), 240-245.

[18] Vrtovšnik, D., Čabrijan, I., Brčić, M., Doboviček, S. 2021. Influence of the Process input parameters on the cross-wire weld breaking force. Technical Journal. 16(2), 227-230.

[19] Konda, R., Rajurkar, K.P., Bishu, R.P., Guha, A., Parson, M., 1999. Design of experiments to study and optimize process performance. International Journal of Quality & Reliability Management. 16, 56-71.

[20] Antony, J., 2003. Design of Experiments for Engineers and Scientists. Elsevier Science & Technology Books

[21] https://support.minitab.com/en-us/minitab/19/ (accessed 20 July 2022)

Influence of cutting parameters on cutting forces and surface roughness in milling of aluminum foam

Igor ĆULUM[1], **Ivana DUMANIĆ**[1], **Sonja JOZIĆ**[1], **Dražen BAJIĆ**[1], **Branimir LELA**[1]

1) Faculty of Electrical Engineering, Mechanical Engineering and Naval Architecture, University of Split Ruđera Boškovića 32, 21 000 Split, **Croatia**

Igor.Culum.00@fesb.hr
Ivana.Dumanic.00@fesb.hr
Sonja.Jozic@fesb.hr
Drazen.Bajic@fesb.hr
Branimir.Lela@fesb.hr

Keywords

Closed cell aluminum foam
Profilometer
Milling
Surface roughness
Cutting forces

Original scientific paper

Abstract: Metal foams present a new form of porous materials with a unique combination of light weight and good mechanical properties. Such materials have already been implemented in a myriad of high-tech industries such as aerospace, automotive and biomedicine. The main focus of this paper is to determine the influence of cutting speed, v_c and feed per tooth, f_t on cutting forces and surface roughness of closed cell aluminum alloy, A380 foam. Cutting force measurements were conducted using a multi-component dynamometer. Both cutting force components, Fx and Fy increased as feed per tooth increased. Increasing cutting speed led to a lower value of Fx cutting force component. The value of Fy cutting force component initially decreased with an increase in cutting speed. An increase in Fy cutting force component was observed at high cutting speeds and low feed per tooth. An optical profilometer which is used for quantifying the surface roughness provides non-contact 3D texture measurements. Test results show that increasing feed per tooth leads to a drastic increase in surface roughness of the cell walls while increasing cutting speed produces a lower surface roughness. Using the test results, regression models were generated that allow for accurate prediction of Sa, Fx and Fy variables based on input cutting parameters.

1. Introduction

Metal foams are a form of light, porous material inspired by natural materials such as sponge, bones, corals, cork, etc. They are produced using discarded metal chips and a foaming agent, such as titanum hydrate, TiH_2. A myriad of different materials can be used to produce metal foams such as: copper, steel, nickel, magnesium, titanium and aluminum. The latter is the most common metal for foam production due to its low weight and melting point, high corrosion resistance and non-toxicity [1], [2], [3]. Although their properties significantly depend on cell structure, wall thickness, homogeneity, anisotropy and relative density, metal foams provide a unique blend of low weight while retaining good mechanical and thermal properties of the base metal [2], [4]. This unique combination of properties has led to the implementation of metal foams in automotive, aerospace, naval, biomedical and many other high-tech industries. Metal foams are typically classified into two categories: open cell and closed cell foams. Walls of closed cell foams are interconnected by means of a thin membrane while the space in between the walls of open celled foams is hollow. Owing to great impact absorption, closed cell foams are most commonly used as structural and passive safety elements. They are also used as sound and vibration dampening, thermal insulation and floatation [1], [3], [5]. Due to their biocompatibility and non-toxicity, titanium open cell foams are famously used in biomedicine as bone implants. The porous open cell structure allows for increased blood flow and ease of bone growth around the implant [6].

To increase applicability of metal foams, a certain amount of machining is required. Conventional machining of metal foams has not been extensively researched. Most common method of machining porous metals is conducted using a wire EDM machine. The main reason this technology is preferred is due to very low cutting forces produced by the process [7]. Higher cutting forces, exhibited by conventional machining processes such as turning or milling, often lead to deformation rather than cutting of the cell walls. This phenomenon is commonly known as smearing. A novel way to reduce smearing of the cell walls during milling of porous metals involves using an infiltrant material which supports the cell walls during machining and prevents smearing from occurring. A suggested infiltrant material is machinable wax which can infiltrate and exfiltrate pores of a foam in a molten state at temperatures far below melting point of the alloy [6]. Machinability of metal foams can be improved using additives blended into the base foam material. Additives increase machinability while not altering the mechanical properties of the workpiece.

Symbols

f_t	- feed per tooth, mm/tooth		Ra	- arithmetic deviation of the profile, μm
$f_{t.max}$	- maximum feed per tooth, mm/tooth		RSM	- response surface methodology
$f_{t.min}$	- minimum feed per tooth, mm/tooth		Sa	- arithmetic mean of the absolute height, μm
F_x	- x-axis cutting force, N		v_c	- cutting speed, m/min
Fy	- y-axis cutting force, N		$v_{c,max}$	- maximum cutting speed, m/min
R^2	- standard deviation		$v_{c,min}$	minimal cutting speed, m/min

Machining additives promote chip fracture ahead of the tool tip which reduces the chance of built-up-edge forming on the rake face of the tool and leads to a finer surface finish [8]. Karabulut et al. [9] investigated the influence of feed per tooth and cutting speed on arithmetic deviation of the profile, *Ra* on SiC foam-reinforced composite. Their findings showed that feed per tooth had a significant impact on roughness. Cutting speed, however, had a minimal influence on *Ra* surface roughness parameter. Using the test results, regression models were generated that enabled a precise prediction of surface roughness. Schoop et al. [10] experimented on porous tungsten material using varying tool geometries and cutting parameters. Their findings showed that increasing cutting speeds from 20 m/min to 400 m/min led to a drastic decrease in *Ra* surface roughness parameter. They concluded that the main reasons for this trend were increased cutting temperatures exhibited at high cutting speeds which made cutting of the material easier. Negative influence of high surface roughness on corrosion resistance was reported in multiple papers such as those written by Danaila et al. [11] and Alshasmi et al. [12]. The former paper focused on corrosion testing biocompatible titanium alloy with varying surface roughness in a saliva solution. Their research found that surface roughness had a critical role in corrosion behavior of the implant. Workpieces with a higher surface roughness were far more susceptible to corrosion than specimen with a low surface roughness. The latter paper tested the influence of surface roughness of iron in hydrochloric and sulfuric acids. Both acids are prominent in sea environments such as docks and shipyards. Their research found that higher roughness had a profound influence on corrosion with the rougher specimen having far lower corrosion resistance. Determining the influence of cutting parameters on surface roughness can help in producing a durable, high-quality product which, in the long run, reduces production and maintenance costs.

In a paper written by Liu Y. [13] copper foam was tested to determine the influence of spindle speed and feed rate on cutting forces and cutting temperature. Their findings showed that increasing the feed rate increased cutting forces. Increasing cutting speed, however, led to a decrease in cutting forces. Liu Z. [14] assessed the influence of micro-milling cutting parameters of stainless steel on surface quality and cutting forces. Their experiments concluded that there are no strict rules that dictate the quality of the machined surface. Evaluation of the cutting parameters should be conducted on a per-specimen basis. Their research found that cutting forces decreased with increased cutting speed. Gradually increasing of cutting speed, however, led to an increase in cutting forces. Increasing feed rates caused an increase in cutting forces as well. Tutunea et al. [15] compared cutting forces exhibited during milling of solid and porous titanium. Their measurements showed that forces generated while machining porous metal exhibit a large amount of variation based on the porosity of the metal. At places where the tool encountered a porosity in the material, a drastic drop in the cutting forces was observed indicating a correlation between surface porosity and cutting force measurements.

From this brief literature overview, it is evident that there is a lack of understanding on how machining influences metal foams, primarily the influence of milling parameters on both cutting forces and surface roughness. In this paper, a series of thirteen milling experiments will be conducted on closed cell aluminium foam. Base metal used for foam production was aluminum alloy A380 (EN AC-46500). Cutting forces and surface roughness will be observed. Using the measured test results, regression models will be generated allowing for accurate surface roughness and cutting force predictions based on input cutting parameters.

2. Experimental work

The main goal of this paper is to determine the influence of cutting parameters on surface roughness and cutting forces on aluminum alloy A380 closed cell metal foam. Aluminum alloy A380, whose chemical composition is shown in Table 1, is a widely used die casting aluminum alloy that allows for production of high-quality, durable casts often used in automotive industry. The main

advantages of aluminum alloy A380 is its high corrosion resistance and excellent machinability [16], [17], [18]. The workpiece, shown in Figure 1, was produced using discarded milled chips and TiH_2 foaming agent. Experimental research consisted of face milling of the metal foam using varying cutting parameters while measuring the cutting force and surface roughness. Experiments were carried out on a Spinner VC560 vertical machining centre.
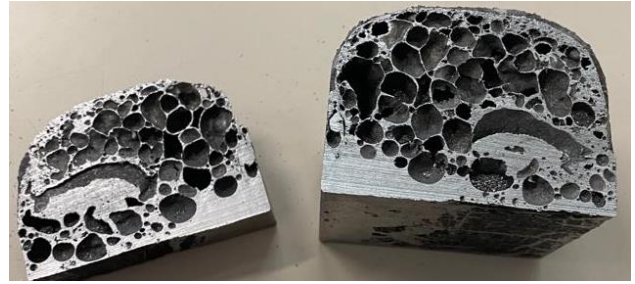
Figure 1   Metal foam specimen

Table 1   Chemical composition of the alloy A380 according to the ASTM B179 standard [19]

Alloy	Si	Fe	Cu	Mn	Mg	Ni	Zn	Ti	Other	Al
EN A380	7.5 – 9.5	max 1.3	3.0 – 4.0	max 0.5	max 0.1	max 0.5	max 3	max 0.35	max 0.5	rest

Face milling operations were performed without any cooling, using a two flute end mill, M4132-032-W32-02-09 manufactured by Walter AG. The end mill was equipped with interchangeable carbide inserts SDHT09T304-G88. Cutting speed, v_c and feed per tooth, f_t were selected according to tool manufacturer specifications. Specified cutting parameters, shown in Table 2, were input into Design Expert software. Using

response surface methodology, RSM implemented into the software, a central composite plan of thirteen cutting speed and feed per tooth combinations was generated. Axial and radial depths of cut were kept at a constant 1 mm and 32 mm, respectively. Experiments were carried out in a randomized order. Cutting forces were measured using a Kistler 9257 A multi-component dynamometer, shown in Figure 2.
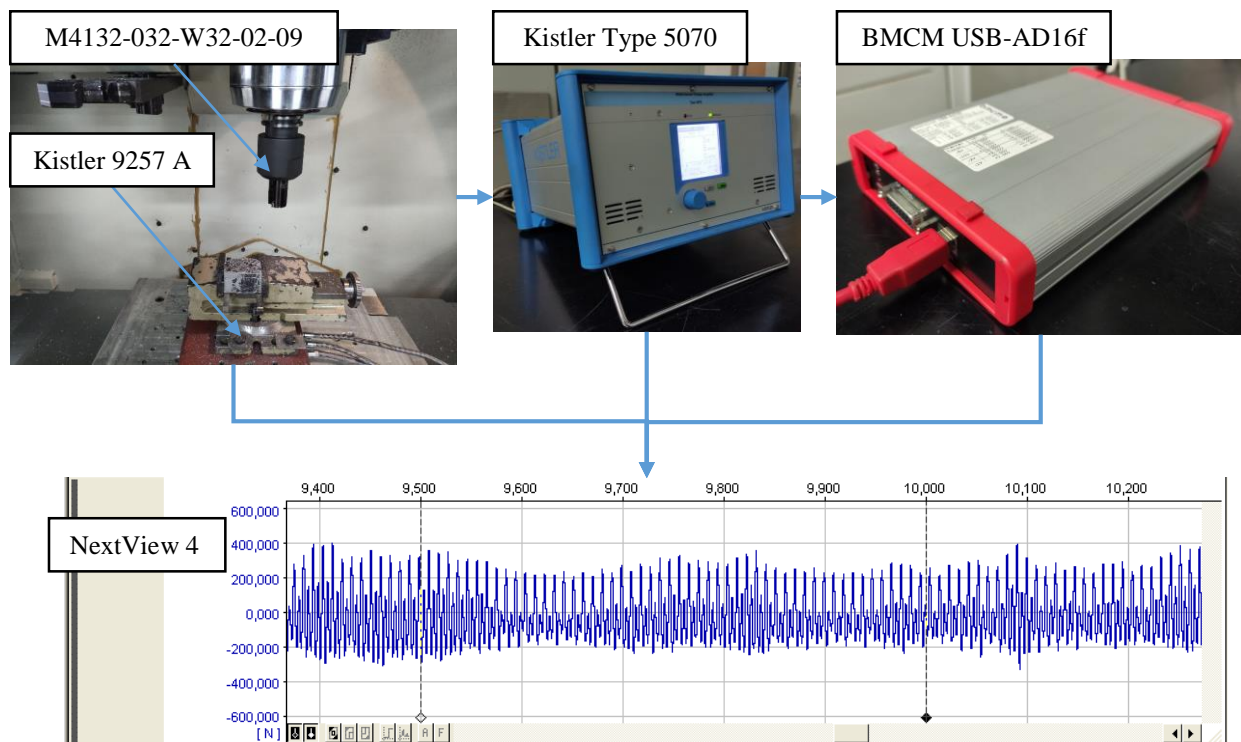
Figure 2   Force measuring setup

Area Roughness			
General			
Average	3.536	µm	Mean height
Minimum	0	µm	Minimum height
Maximum	6.223	µm	Maximum height
Range	6.223	µm	Maximum - Minimum
ASME B46.1 3D			
Sp	2.686	µm	Peak height
Sv	3.536	µm	Valley depth
St	6.223	µm	Maximum peak to valley height
Sa	0.6334	µm	Arithmetic mean height
Sq	0.791	µm	Root mean square height
Ssk	-0.2936		Skewness
Sku	3		Kurtosis
EUR 15178N Amplitude			
Sp	2.686	µm	Maximum peak height
Sv	3.536	µm	Maximum pit height
St	6.223	µm	Maximum height
Sa	0.6334	µm	Arithmetic mean height
Sq	0.791	µm	Root mean square height
Ssk	-0.2936		Skewness
Sku	3		Kurtosis
ISO 25178 Height			
Sp	2.686	µm	Maximum peak height
Sv	3.536	µm	Maximum pit height
Sz	6.223	µm	Maximum height
Sa	0.6334	µm	Arithmetic mean height
Sq	0.791	µm	Root mean square height
Ssk	-0.2936		Skewness
Sku	3		Kurtosis

Figure 3 Surface roughness measurement setup

The output of the dynamometer was amplified by a Kistler Type 5070 multichannel charge amplifier. The amplified signal was processed using a BMCM USB-AD16f data acquisitioning system. NextView 4 software was used to analyze the cutting forces. Surface roughness of the porous specimen was measured using a Profilm 3D optical profilometer.

Table 2   Selected cutting parameters

Minimum feed per tooth, $f_{t,min}$	0.05 mm/tooth
Maximum feed per tooth, $f_{t,min}$	0.25 mm/tooth
Minimum cutting speed, $v_{c,min}$	50 m/min
Maximum cutting speed, $v_{c,max}$	600 m/min

The setup for roughness measurements is shown in Figure 3. Arithmetic mean of the absolute height parameter, *Sa*

was measured for each milling run and mean values were given. Measurements were carried out in accordance with the international standard ISO 25178. Scanning properties were kept constant throughout the testing.

3.   Results and discussion

3.1. Influence of cutting parameters on cutting forces
Measured cutting forces are presented in Table 3. Using the test results, regression models were generated with an R^2 value of 0.8971 and 0.88 for F_x and F_y respectively. The modells, shown in equation (1) for *Fx* cutting force component and equation (2) for *Fy* cutting force component, can reliably predict both components based on input feed per tooth and cutting speed.

$$Fx = 16.78444 + 524.8268 f_t - 0.00644 v_c + 0.008375 f_t v_c - 681.06 f_t^2 - 6.8 * 10^{-6} v_c^2 \quad (1)$$

$$Fy = 16.65374 + 361.8358 f_t - 0.14461 v_c - 0.0.28928 f_t v_c - 473.569 f_t^2 - 0.00022 v_c^2 \quad (2)$$

Analysis of the equations showed that the main contributing factor to increased cutting force is feed per

tooth. Surface plots, shown in Figure 4 and Figure 5, were generated using RSM methodology and show the

influence of cutting parameters on the cutting forces. Observing tests conducted at a constant cutting speed of 350 m/min and feeds per tooth of 0.05 mm/tooth, 0.15 mm/tooth and 0.25 mm/tooth, Fx cutting force component increased from 39.0578 N at a feed per tooth of 0.05 mm/tooth to 109.53 N at a feed per tooth of 0.25 mm/tooth. Fy cutting force component increased from 9.09 N at a feed per tooth of 0.05 mm/tooth to 24.11 N at a feed per tooth of 0.25 mm/tooth. Tests results conducted at a constant feed per tooth of 0.15 mm/tooth and cutting speeds of 67.16 m/min, 350 m/min and 632.84 m/min showed that increasing the cutting speed lowers Fx cutting force component. Similarly, comparing experiments conducted with a constant feed per tooth of 0.08 mm/tooth and 0.22 mm/tooth and cutting speeds of 150 m/min and 550 m/min, a very small decrease of 1.5 % in Fx cutting force component was noted. Fy cutting force component initially lowered with increased cutting speed but showed a slight increase at higher cutting speeds. Similar trend was reported by Liu Z. et al. [14].
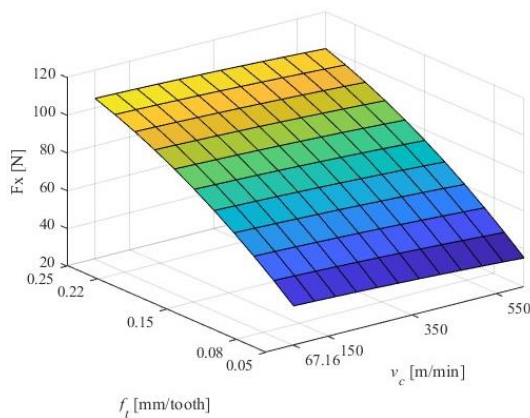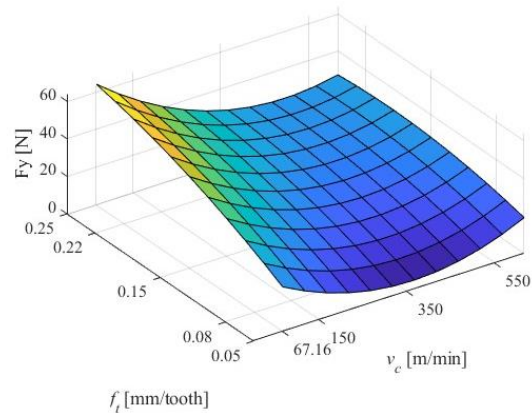

Figure 4　Influence of feed per tooth and cutting speed on Fx cutting force component

3.2. Influence of cutting parameters on surface roughness

Using an optical profilometer Profilm 3D, surface roughness was measured for each run. Measuring results are shown in **Table 4**.

Using the measured data and central composite plan, a regression model, shown as equation (3), was generated that allows for precise surface roughness estimation based on input cutting parameters. The generated model has an R^2 value of 0.8705 meaning that 87.05 % of all the measured data fits the generated model, making the model a reliable tool for predicting the surface roughness parameter based on input cutting parameters.

Figure 5　Influence of feed per tooth and cutting speed on Fy component cutting force

Table 3　Cutting force measurements

Test no.	f_t [mm/tooth]	v_c [m/min]	F_x [N]	F_y [N]
1	0.05	350	39.0578	9.0857
2	0.08	150	50.4847	16.5850
3	0.08	550	49.7481	17.1849
4	0.15	350	84.6379	20.5475
5	0.15	350	63.5334	17.2468
6	0.15	67.16	62.5500	23.0990
7	0.15	350	79.6270	16.8386
8	0.15	632.84	75.1310	24,2880
9	0.15	350	85.4108	24.5103
10	0.15	350	74.4451	25.6198
11	0.22	550	90.7144	20.2270
12	0.22	150	90.9820	32.1672
13	0.25	350	109.530	24.1118

Table 4　Results of surface roughness measurements

Test no.	f_t [mm/tooth]	v_c [m/min]	Sa [µm]
1	0.05	350	0.6336
2	0.08	150	0.8423
3	0.08	550	0.5302
4	0.15	350	0.8774
5	0.15	350	1.0090
6	0.15	67.16	1.3080
7	0.15	350	0.8774
8	0.15	632.84	0.8029
9	0.15	350	0.8709
10	0.15	350	0.8890
11	0.22	550	0.8152
12	0.22	150	2.0235
13	0.25	350	1.1980

$$Sa = 0.153124 + 10.21064f_t - 5.7*10^{-5}v_c - 0.016f_t - 1.88648f_t^2 + 1.51*10^{-6}v_c^2 \qquad (3)$$

Analysis of the generated model showed that feed per tooth was the more influential parameter in terms of surface roughness. Figure 6 depicts a surface plot showing the influence of cutting speed and feed per tooth on surface roughness. Generally, an increase in feed per tooth leads to a drastic increase in surface roughness. By observing tests conducted at 0.05 mm/tooth, 0.15 mm/tooth and 0.25 mm/tooth at a constant cutting speed of 350 m/min, an increase in surface roughness can be observed from 0.6336 µm at 0.05 mm/tooth to 1.198 µm at 0.25 mm/tooth. Comparing the roughness of surfaces cut at a cutting speed of 67.16 m/min, 350 m/min and 632.84 m/min and a constant feed per tooth of 0.15 mm/tooth, a decrease in *Sa* parameter surface roughness parameter was observed.
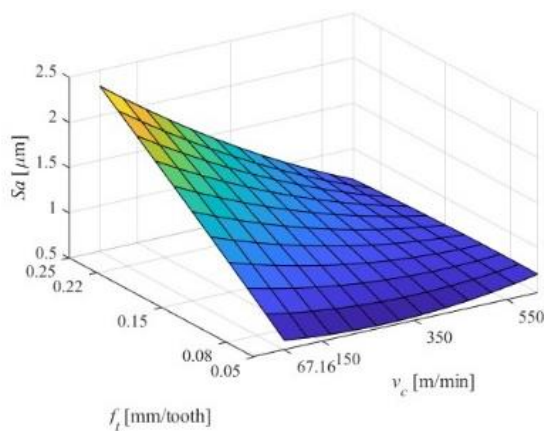

Figure 6   Influence of feed per tooth and cutting speed on surface roughness parameter Sa

A similar trend was observed at other test points conducted with a feed per tooth of 0.08 mm/tooth and 0.22 mm/tooth and cutting speeds of 150 m/min and 550 m/min. This effect was explained by Zurita et al. [20]. Increasing the cutting speed leads to increased cutting temperatures which softens the workpiece and makes material removal easier. Additionally, higher cutting temperatures also lead to lower cutting forces. Test results coincide with the findings reported by Karabulut et al. [9]. Further literature research would lead to indicate that porosity does not affect the cut surface integrity as similar findings were reported by Rahman et al. [21] and Iqbal et al. [22] while testing non-porous materials.

3.3. Workpiece surface scanning

Using a Filmetrics Profilm 3D optical profilometer, it was not only possible to measure surface roughness values but to generate a 3D model of the analyzed surfaces. Scanning, as well as roughness measurements, were conducted on the walls of the foamed material. All thirteen experiments were scanned using the same scanning properties. Figure 7 shows surface scans of the aluminum foam conducted at a constant cutting speed of 150 m/min and varied feed per tooth of 0.08 mm/tooth and 0.22 mm/tooth. From the figures below, it was observed that an increase in feed per tooth led to an increased distance between the toolpaths. Other than influencing the tool path distances, the scans show a clear increase in the height of the profile which directly correlates to increased surface roughness measurements. Figure 8 shows surface scans of the workpiece produced at a constant feed per tooth of 0.22 mm/tooth and a varied cutting speed of 150 m/min and 550 m/min. From the figure below, no changes in the distance between tool paths was noted, however, a drastic decrease in the height of the profile was observed.

a)

b)
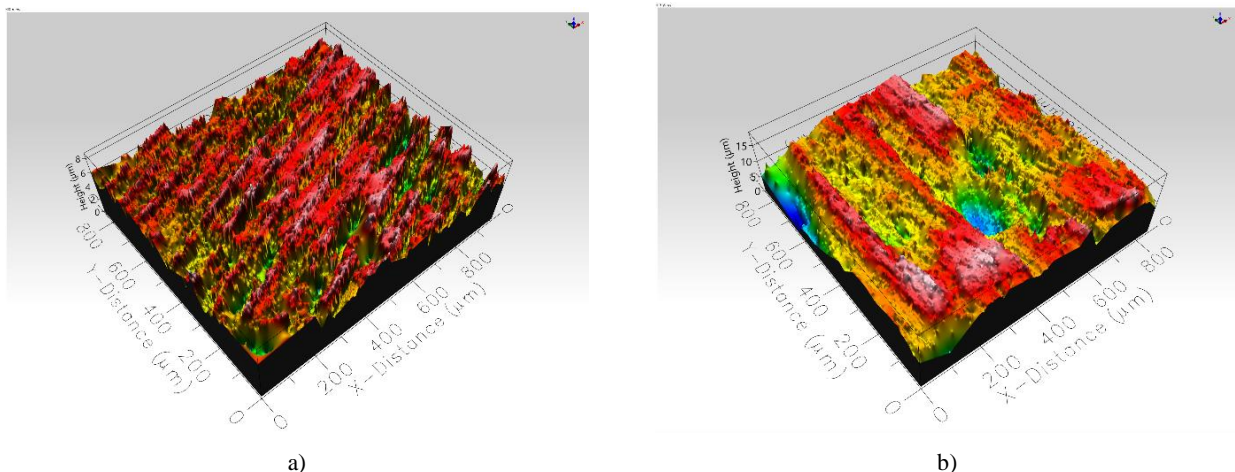
Figure 7   Surface scans produced at a constant cutting speed of 150 m/min and varying feed per tooth: a) 0.08 mm/tooth, b) 0.22 mm/tooth

| a) | b) |
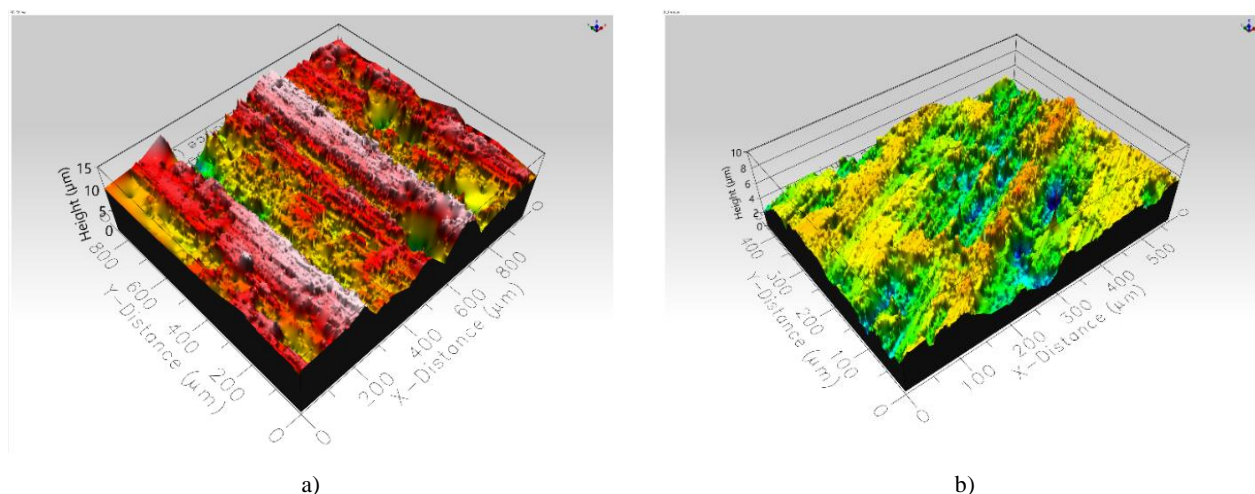
Figure 8   Surface scans produced at a constant feed per tooth of 0.22 mm/tooth and varying cutting speed: a) 150 m/min, b) 550 m/min

4. Conclusion

The influence of cutting parameters on surface roughness and cutting force of closed cell aluminum foam was examined in this paper. Cutting forces were measured using a multi-component dynamometer where both *Fx* and *Fy* cutting force components were analyzed. Surface roughness measurements and surface scans were acquired using an optical profilometer. From the conducted experiments the following can be concluded:

- – Increasing feed per tooth leads to a substantial increase in cutting forces. Increasing cutting speed, however, leads to a lower cutting force. This could be contributed to the increased cutting temperatures produced by higher cutting speeds. Higher cutting temperatures lead to softening of the workpiece and ease the cutting process.
- – Feed per tooth greatly increases surface roughness of the cell walls of the foam. The main cause for this is an increase in the removed material as was shown with surface scans using an optical profilometer.

Acknowledgement

REFERENCES

[1] Banhart, J., 2001. Manufacture, characterization and application of cellular metals and metal foams. Progress in Materials Science. 46, 559–632.

[2] Papantoniou, I. G., Pantelis, D. I., Manolakos, D. E, 2018. *Powder metallurgy route aluminium foams: A study of the effect of powder morphology, compaction pressure and foaming temperature on the porous structure*. GSEMM 2018, Athens, Greece.

[3] Kumar Rajak, D., Gupta, M., 2020. Advanced Structured Materials An Insight Into Metal Based Foams Processing, Properties and Applications. Advanced Structured Materials. 145

[4] Razboršek B., Gotlih J., Karner T., Ficko M., 2019. The influence of machining parameters on the surface porosity of a closed-cell aluminium foam. Strojniški vestnik - Journal of Mechanical Engineerin. 66, 29–37.

[5] Lei, Q., Ren, J., Ren, H., Chao, H., Du W., 2019. Study on dynamic characteristic of closed-cell aluminum foam. Vibroengineering Procedia. 28, 142–147.

[6] Vaira Hunt, C., 2009. *A method to reduce smearing in the milling of metal foams*. Iowa State University, Ames, Iowa

[7] Miller, S. F., Shih A. J., Qu J., 2004. Investigation of the spark cycle on material removal rate in wire electrical discharge machining of advanced materials. International Journal of Machine Tools and Manufacture. 44, 391–400.

[8] Alizadeh, E., 2008. Factors influencing the machinability of sintered steels. Powder Metallurgy and Metal Ceramics. 47, 51-65.

[9] Karabulut, Ş., Karakoç H., 2017. Investigation of surface roughness in the milling of Al7075 and open-cell SiC foam composite and optimization of machining parameters. Neural Computing and Applications. 28, 313–327.

[10] Schoop, J., Ambrosy F., Zanger F., Schulze V., Balk T. J., Jawahir I. S., 2016. Cryogenic machining of porous tungsten for enhanced surface integrity. Journal of Materials Processing Technology. 229, 614–621.

[11] Danaila, E., 2015. *The Effect of Surface Roughness on Corrosion Behavior of Ti-6Al-4V Alloy in Saliva Solution*. EHB 2015, Iasi, Romania.

[12] Alshamsi, A. S., AlBlooshi, A., 2019. Effect of surface roughness on the corrosion behavior of pure iron in acidic solutions. International Journal of Electrochemical Science. 14, 5794–5812.

[13] Liu, Y., Zhou, W., Li, X., Chu X., Cai S., 2020. Experimental investigations on cutting force and temperature in milling process of copper foam with high porosity. International Journal of Advanced Manufacturing Technology. 108, 759–767.

[14] Liu, Z., Han, J., Su,, Y., An Q. L., 2018. Experimental investigation of porous metal materials in high-speed micro-milling process. Proceedings of the Institution of Mechanical Engineers, Part B: Journal of Engineering Manufacture. 232, 2488–2498.

[15] Tutunea-Fatan, O. R., Fakhri, M. A., Bordatchev, E. V., 2011. Porosity and cutting forces: From macroscale to microscale machining correlations. Proceedings of the Institution of Mechanical Engineers, Part B: Journal of Engineering Manufacture. 225,619–630.

[16] Aluminum and Die Casting Aluminum and Cast aluminum *https://www.investmentcastingpci.com/a380-aluminum-alloy/* (accessed 14 July 2022)

[17] Aluminum Alloy A380 Properties https://www.sunrise-metal.com/aluminum-alloy-a380-properties/ (accessed 14 July 2022)

[18] Lela, B., Grgić, K., 2021. *Production of closed cell foams from the aluminium chip waste. MTSM 2021,* Split, Croatia.

[19] Zurita, O., Di-Graci, V., Capace, M., 2018. Effect of cutting parameters on surface roughness in turning of annealed AISI-1020 steel. Revista Facultad de Ingeniería. 27, 111–118.

[20] Rahman, M., Senthil Kumar A., 2001. Evaluation of Minimal Quantities of Lubricant in End Milling. Springer-Verlag London Limited. 18, 234-241.

[21] Iqbal, A., Suhaimi, H., Zhao, W., Jamil, M., Nauman M, He N., Zaini J., 2020. Sustainable milling of Ti-6Al-4V: Investigating the effects of milling orientation, cutter′s helix angle, and type of cryogenic coolant. Metals. 10, 258.

Effect of pulse arc welding parameters with low-alloy welding materials on weld formation and its geometric parameters

Alexandr GAIVORONSKIY[1], Anatoliy ZAVDOVEEV[1], Andrey MAKSIMENKO[1], Valeriy POZNIAKOV[1], Massimo ROGANTE[2], Sergej JDANOV[1], Anatoliy DENISENKO[1]

1) Paton Electric Welding Institute of NAS of Ukraine, 03150 Kyiv, **Ukraine**
2) Rogante Engineering Office, Contrada San Michele n. 61, I-62012 Civitanova Marche, **Italy**

avzavdoveev@gmail.com
main@roganteengineering.it

Keywords

PA-GMAW welding
Penetration depth
Heat affected zone
Seam width
Optimization

Original scientific paper

Abstract: Pulse arc welding (PA-GMAW) provides controlling the process of melting and transfer of electrode metal, improves the formation of seams and reduces the mixing of electrode and base metals and the size of the heat affected zone (HAZ).

The criterion for an optimal welding mode is to obtain the required values of the geometric parameters of the seam, namely the depth of penetration, the width of the HAZ and the width of the seam. The optimal modes of PA-GMAW welding is developed, which provide the set values of the penetration depth, namely the minimum and maximum. The verification experiment has shown that, within small deviations, the predicted values of the penetration depth correlate with the experimental ones.

1. Introduction

It is known that for modern building and machine-building of metal structures high-strength low-alloy steels of strength class C460 and above are used, which acquire high static strength and toughness due to thermoregulated rolling [1–5]. To provide welded joints of these steels, currently, the necessary set of mechanical properties of their welding is performed in limited modes, which, firstly, make the welding process unproductive, and secondly, increase the risk of inadmissible defects in the joints [6–8]. In modern structural steels, with increasing welding modes in the HAZ of welded joints, there is a decrease of the hardness, strength, and toughness of the metal to a level lower than the established standards [9, 10]. This also increases the HAZ size, which negatively affects the performances of these steels. To solve these problems, in our opinion, is possible due to the portion of heat introduction into the welded joint, which can be implemented in PA-GMAW [11–14].

PA-GMAW, in comparison with the Gas Metal Arc Welding (GMAW), expands the possibilities of controlling the process of melting and transfer of electrode metal, improves the formation of seams and reduces the mixing of electrode and base metals as well

as the HAZ size [15, 16]. Such PA-GMAW influence parameters affects structure and mechanical properties of the metal seams and the HAZ of welded joints [1, 12, 15, 17–19].

The main difficulties in welding new low-carbon high-strength alloy steels are related to the need to prevent in the HAZ and weld metal the formation of cold cracks as well as of structures that reduce the resistance of welds to brittle fracture [7, 8, 20]. The solution of these problems is complicated by the condition according to which the necessary indicators of service and technological properties of welded joints must be in a state after welding without additional heat treatment (HT). Structure, mechanical properties and viscosity of the HAZ metal of welded joints of thermally hardened steels are significantly affected by the heating and cooling parameters of the specified area in the thermal welding cycle. Given this, the study of the PA-GMAW influence on the formation of the seam and its geometric parameters [21] and as a consequence of the structure and mechanical properties of welded joints of thermally hardened steels is of some interest.

In PA-GMAW there are four variable mode parameters: pause current, pulse current, frequency and duty cycle. A large number of experiments are required to select the

optimal mode. The criterion for the optimal welding mode is to obtain the required values of the geometric parameters of the seam, namely the penetration depth, the HAZ width and the seam width (SW). Taguchi experimental calculation method [22–24] allows estimating the influence of each parameter of the mode on the formation of the welded joint, with a minimum number of experiments.

2.   Experimental work

For PA-GMAW in the environment of shielding gases a device type ewm Phoenix Pulse 501 has been adopted with semiautomatic built-in. As a power source, it uses an inverter rectifier that provides different frequencies of pulses. To ensure a constant welding speed, a specialized cart has been adopted with a drive that provides a stable speed of the burner in the characteristic range of welding speeds (from 10 m/h to 25 m/h).

The adopted parameters of the PA-GMAW pulsating arc are reported in Table 1. The choice of such ranges for each of the PA-GMAW parameters is based on empirical data. For pulse current, e.g., the most commonly used values are from 160 to 240 A, for pause current the minimum values are 80 A, which ensure arc continuity, and 140 A, which is less than the minimum pulse current.

The change range of pulse repetition frequency has been chosen to ensure the criterion of pulsating arc, i.e. less than 25 Hz. In our case, the minimum frequency of 0,5 Hz has been selected, which provides a high-quality weld formation. The maximum frequency of 5 Hz has been selected, for effective control of the crystallization processes in the welding bath.

In this experiment there are four independently controlled process parameters and three experimental levels. A $3^4 = 81$ experiment would have to be performed for four factors and three levels. The method proposed by Taguchi uses orthogonal arrays (OAs) to determine in real time the minimum number of experiments to estimate all design factors. In such an experimental scheme, each factor is evaluated individually and one does not affect the other. The conditions that emerged in this study, ie the four parameters together with their three levels, are suitable for the selection of the L9 matrix as an experimental project. Table 2 presents nine real-time experimental tests, which were compiled according to the scheme L9 (3^4) following the Taguchi method [22–24]. In this case, the experiments must be carried out in random order to bypass noise sources.

Table 1.   Selected parameter for PA-GMAW.

Parameter	Note	Level					
		Value			Coding		
		Min.	Ser.	Max.	Min.	Ser.	Max.
Pulse current, A	A	160	200	240	1	2	3
Current pauses, A	B	80	120	140	1	2	3
Frequency, Hz	C	0.5	1	5	1	2	3
Smoothness,%	D	40	60	80	1	2	3

Table 2.   Execution of tests on the basis of the project plan [25].

№	Pulse current, A		Current pauses, A		Frequency, Hz		Smoothness, %	
	Size	Code	Size	Code	Size	Code	Size	Code
1	160	1	80	1	0,5	1	40	1
2	160	1	120	2	1	2	60	2
3	160	1	140	3	5	3	80	3
4	200	2	80	1	1	2	80	3
5	200	2	120	2	5	3	40	1
6	200	2	140	3	0,5	1	60	2
7	240	3	80	1	5	3	60	2
8	240	3	120	2	0,5	1	80	3
9	240	3	140	3	1	2	40	1

Calculation of signal-to-noise ratio. When conducting experiments, different process parameters are used, which give different "response" values. The penetration

depth (PD, seam width (SW) and heat affected zone (HAZ) width is selected as the "response" parameters. In the course of experimental trials, it was necessary to

assess the impact of each selected factor using the received "feedback", which may not be unique and has both desirable and undesirable characteristics. According to the method, tensile signal-to-noise ratio (S/N) is a deviation of the qualitative characteristic from the desired value. When calculating the S/N ratio higher or lower should be chosen.

The calculation of the S/N ratio was performed according to equation 1. Generalized calculated S/N ratios for all experiments are presented in Table 3.

$$\frac{S}{N} = -10 \cdot \log\left(\frac{\sum_1^n \frac{1}{Y^2}}{n}\right) \qquad (1)$$

The next step in the analysis is to divide the impact of each individual parameter on all three considered levels and rank them in the order of their impact on the response parameter. This is possible since the chosen experimental scheme is embedded in the orthogonal matrix L9.

The average efficiency of the factor is calculated by dividing the sum of the results of tests involving the factor by the number of tests performed at the same level e.g., $<S/N>_{A1} = (S/N_1 + S/N_2 + S/N_3)/3$.

Contribution of individual factors to the penetration depth. Nominal control of the final answer requires knowledge of the contribution degree of individual process parameters, and they can be estimated using a statistical method, namely ANOVA [24, 26, 27]. In the ANOVA methodology, SS, SS', D, V and P are typical symbols of the parameters used in the above mentioned analysis to represent factors, sum and adjusted sum of squares, degree of freedom, variance and percentage contribution of each factor, respectively. A brief explanation of these factors is provided elsewhere [24].

3. Results and discussion

The general view of the welded rollers and macro sections of the cross section of the surfacing is shown in Figure 1, where the number corresponds to the mode of surfacing performed in accordance with the program (Table 2). From the given data it is visible that, at use of various welding modes by pulsating arc, the general look of the weld metal differs essentially, first of all. This effect is due to the influence of different pulse repetition frequencies during PA-GMAW. For a detailed analysis of the geometric parameters formation of seams, measurements were performed, which are shown in Table 3. Results of measurements of geometric parameters of the weld performed on the same welding modes but using low- and high-alloy welding material showed a significant difference between these parameters. As already mentioned, this is due to the characteristics of welding materials, namely melting temperature and viscosity of the molten material. It should be expected, therefore, that the contribution of

each parameter of pulsating arc welding modes will also have significant differences.
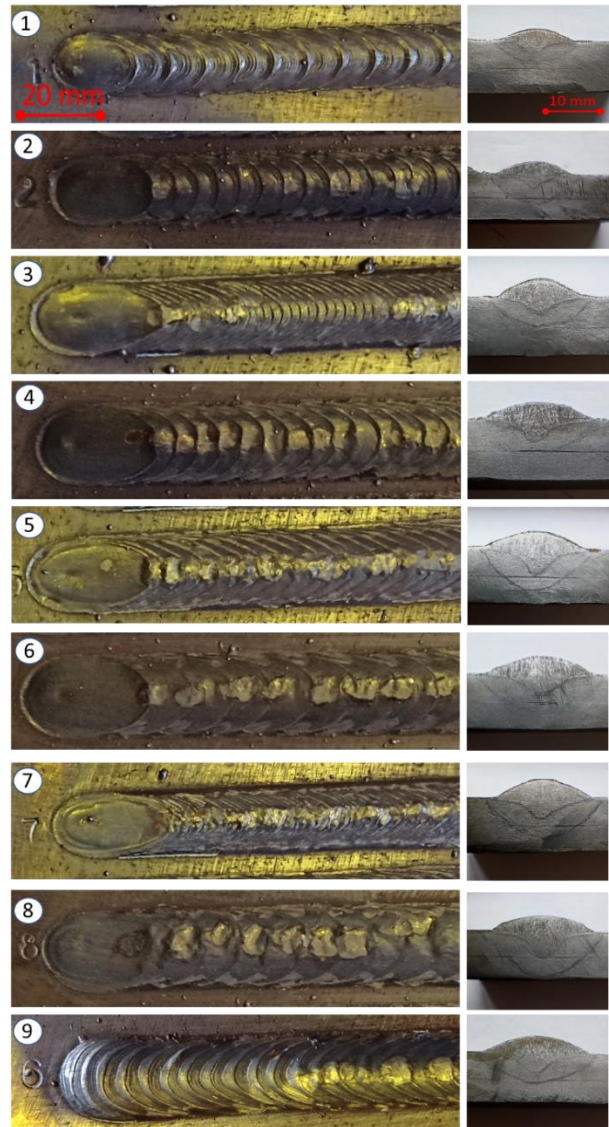
Figure 1. Photos of macro sections of experimental surfacing in accordance with the modes shown in table 2. a - general view of surfacing, b - cross section.

The next stage of the study was the calculation of the average value of the signal-to-noise ratio for each of the levels and parameters of welding and for each investigated geometric parameter of the seam. Summarized results are shown in Table 4. As it can be seen from the calculations, the pulse current for the penetration depth parameter is ranked by the number "1", which indicates its greater impact on the penetration depth than the pause current, frequency and duty cycle.

Table 3. The results of measuring the parameters of the seam and the signal-to-noise ratio for surfacing made of low-alloy welding material

№	Parameter of the seam and S/N ratio						Heat Input kJ/mm
	PD, mm	S/N	SW, mm	S/N	HAZ, mm	S/N	
1	2.251	7.042	10.98	20.8073	1.3	2.28	0,42
2	2.941	9.363	13.51	22.612	2.94	9.349	0.55
3	2.093	6.406	12.04	21.6082	2.3	7.236	0.61
4	3.345	10.49	15.09	23.5701	1.81	5.139	0.68
5	4.611	13.27	14.94	23.4834	2.18	6.763	0.62
6	3.633	11.2	15.42	23.7609	3.12	9.871	0.72
7	3.359	10.52	13.69	22.7208	3.01	9.555	0.67
8	4.939	13.87	16.92	24.5682	3.32	10.42	0.93
9	3.442	10.73	16.01	24.0898	2	5.988	0.75

Table 4. Calculation of average values of S/N according to the Taguchi algorithm.

| Parameter	Level 1			Level 2			Level 3			Delta(Δ)=Max-Min			Rank		
	PD	HAZ	SW	PD	HAZ	SW	PD	HAZ	SW	PD	HAZ	SW	PD	HAZ	SW
Pulse current, A	7.604	6.29	21.68	11.65	7.26	23.6	11.71	8.66	23.79	4.1	2.37	2.12	1	3	1
Current pauses, A	9.35	5.66	22.37	12.17	8.84	23.55	9.447	7.7	23.15	2.82	3.19	1.19	2	2	2
Frequency, Hz	10.71	7.52	23.05	10.19	6.83	23.42	10.07	7.85	22.6	0.64	1.03	0.82	3	4	3
Duty Cycle, %	10.35	5.01	22.79	10.36	9.59	23.03	10.25	7.6	23.25	0.11	4.58	0.46	4	1	4

The ANOVA results provide information on the quantitative contribution of each parameter (Figure 2). *Compliance test to verify repeatability.* After selecting the optimal level of design process parameters, this is a mandatory step to determine and test the improvement of quality characteristics using the optimal level of design parameters. According to the reference [23, 24, 26, 28], the predicted signal-to-noise ratio for the optimal level of parameters of the design process can be calculated as:

$$\eta = \eta_m + \sum_{i=1}^{n} (\overline{\eta_i} - \eta_m) \qquad (2)$$

In the above equation η_m, η_i and n represent the average S/N ratio (Table 4) and the total number of important projects of experimental parameters that affect quality. The predicted S/N ratio can be found using the optimal parameters of the pulsating arc welding process (Table 5)

[24]. The results of testing the predicted welding modes in order to obtain the maximum and minimum penetration depth during PA-GMAW are shown in Table 5. As it can be seen, Taguchi 's experimental calculation algorithm allows predicting with high accuracy the response of the studied parameter, namely the penetration depth.

It should be noted that the Taguchi method can be used also when selecting the modes of PA-GMAW of multilayer joints in order to obtain optimal dimensions of HAZ. This is a very important factor that significantly affects the technological and operational properties of welded joints of critical metal structures made of high-strength alloy thermally strengthened steels. Research in this area is underway, the results of which will be presented in future publications.
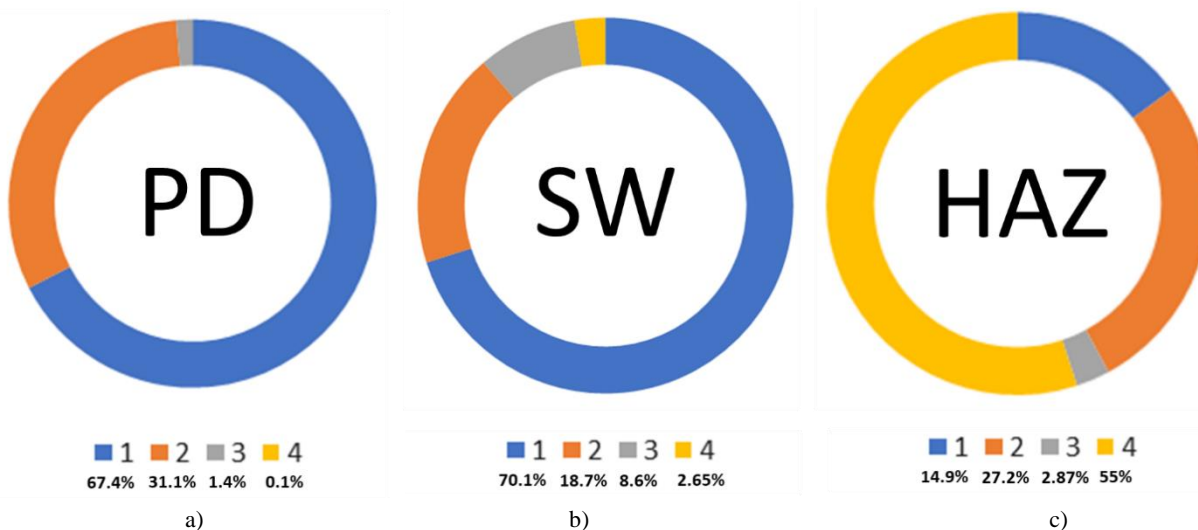
Figure 2. The results of calculations of the quantitative contribution of the parameters of pulsed arc welding (1 - Pulse current, 2 - Pause current, 3 - Frequency, 4 - Roughness) in the formation of geometric parameters of the seam (a - penetration depth; b - seam width; c - HAZ width)

Table 5. Results of estimating the predicted number and confirming the results for the optimal state of the PA-GMAW process

Parameters	A	B	C	D	S / N	
					prediction	experiment
PD maximum						
Optimal coding value	3	2	1	2	13,98	14
Optimal value	240	120	0,5	4 0		
PD minimal						
Optimal coding value	1	1	3	3	6,3	6,2
Optimal value	16 0	8 0	5	8 0		
HAZ minimal						
Optimal coding value	1	1	2	1	-2,56	-2,4
Optimal value	16 0	80	1	40		
SW maximum						
Optimal coding value	3	2	3	3	23,7	25,5
Optimal value	2 4 0	12 0	5	8 0		

4. Conclusions

The influence of PA-GMAW modes (welding current, pause current, frequency, duty cycle) on the weld geometry when using low-alloy welding wire using the experimental calculation method Taguchi is investigated. The possibility of controlling the parameters of pulsating arc welding in order to obtain the required penetration depth in a wide range has been shown.

It is established that the predominant influence on the penetration depth (PD) and the SW has a pulse current. The next valuable impact is the pause current, then frequency, and duty cycle. Quantitative analysis revealed that the influence of these parameters is distributed as follows: Pulse current 68% and 70%, Pause current 31% and 19%, Frequency 1% and 8%, Pattern 0% and 3%, respectively, for PD and SW. The HAZ width is most affected by porosity and the contribution of all welding parameters is distributed as follows: Pulse current 15%, Pause current 27%, Frequency 3%, Porosity 55%.

The conducted researches allowed offering the optimal modes of PA-GMAW welding, which provide the set values of the penetration depth, namely the minimum and the maximum. The verification experiment showed that within small deviations, the predicted values of the penetration depth correlate with the experimental ones.

The experimental-calculation Taguchi method is a powerful and promising tool that can be used in the selection of optimal modes and the development of PA-GMAW welding technologies.

REFERENCES

[1] Lopes, J.G., Machado, C.M., Duarte, V.R., Rodrigues, T.A., Santos, T.G., Oliveira, J.P., 2020. Effect of milling parameters on HSLA steel parts produced by Wire and Arc Additive Manufacturing (WAAM). J. Manuf. Process. 59, 739–749.

[2] Mayo, U., Isasti, N., Rodriguez-Ibabe, J.M., Uranga, P., 2020. On the characterization procedure to quantify the contribution of microstructure on mechanical properties in intercritically deformed low carbon HSLA steels. Mater. Sci. Eng. A. 792, 139800.

[3] Shome, M., Gupta, O.P., Mohanty, O.N., 2004. Effect of simulated thermal cycles on the microstructure of the heat-affected zone in HSLA-80 and HSLA-100 steel plates. Metall. Mater. Trans. A. 35, 985–996.

[4] Lee, S., Kim, B.C., Kwon, D., 1992. Correlation of microstructure and fracture properties in weld heat-affected zones of thermomechanically controlled processed steels. Metall. Trans. A. 23, 2803–2816.

[5] Porter, D., Laukkanen, A., Nevasmaa, P., Rahka, K., Wallin, K., 2004. Performance of TMCP steel with respect to mechanical properties after cold forming and post-forming heat treatment, Int. J. Press. Vessel. Pip. 81(10-11), 867-877.

[6] Lobanov, L., Poznyakov, V., Pivtorak, V., Mikhodui, O., Orlovs'Kyi, V., 2009. Residual stresses in welded joints of high-strength steels. Mater. Sci. 45, 768–778.

[7] Park, G., Jeong, S., Lee, C., 2021. Fusion Weldabilies of Advanced High Manganese Steels: A Review. Met. Mater. Int. 27, 2046–2058.

[8] Brozda, J., Zeman, M., Lomozik, M., 2000. The weldability of thermomechanically rolled S460ML steel, Weld. Int. 14(8), 593-605.

[9] Lee, C.H., Shin, H.S., Park, K.T., 2012. Evaluation of high strength TMCP steel weld for use in cold regions. J. Constr. Steel Res. 74, 134-139.

[10] Janardhan, G., Kishore, K., Mukhopadhyay, G., Dutta, K., 2021. Fatigue Properties of Resistance Spot Welded Dissimilar Interstitial-Free and High Strength Micro-Alloyed Steel Sheets. Met. Mater. Int. 27, 3432–3448.

[11] Wu, K., Ding, N., Yin, T., Zeng, M., Liang, Z., 2018. Effects of single and double pulses on microstructure and mechanical properties of weld joints during high-power double-wire GMAW. J. Manuf. Process. 35, 728–734.

[12] Zavdoveev, A., Rogante, M., Poznyakov, V., Heaton, M., Acquier, P., Kim, H.S., Baudin, T., Kostin, V., 2020. Development of the PC-GMAW welding technology for TMCP steel in accordance with welding thermal cycle, welding technique, structure, and properties of welded joints. Reports Mech. Eng. 1, 26–33.

[13] Wang, L., Xue, J., 2017. Perspective on Double Pulsed Gas Metal Arc Welding. Appl. Sci. 7(9), 894.

[14] Palani, P.K., Murugan, N., 2006. Selection of parameters of pulsed current gas metal arc welding, J. Mater. Process. Technol. 172, 1–10.

[15] Dorn, L., Devakumaran, K., Hofmann, F., 2009. Pulsed current gas metal arc welding under different shielding and pulse parameters; Part 2: Behaviour of metal transfer. ISIJ Int. 49(2), 261–269.

[16] Sen, M., Mukherjee, M., Singh, S.K., Pal, T.K., 2018. Effect of double-pulsed gas metal arc welding (DP-GMAW) process variables on microstructural constituents and hardness of low carbon steel weld deposits. J. Manuf. Process. 31, 424–439.

[17] Zavdoveev, A., Pozniakov, V., Rogante, M., Skoryk, M., Alekseenko, I., 2019. *Study of the welding thermal cycle for hsla steel grade alform plate 620m: Structure and mechanical properties*, MTSM 2019, Split, Croatia

[18] Zavdoveev, A., Pozniakov, V., Rogante, M., Jdanov, S., Maksimenko, A., 2017. *Weldability of S460M high strength low-alloyed steel*, MTSM 2017, Split, Croatia

[19] Rodrigues, T.A., Duarte, V.R., Tomás, D., Avila, J.A., Escobar, J.D., Rossinyol, E., Schell, N., Santos, T.G., Oliveira, J.P., 2020. In-situ strengthening of a high strength low alloy steel during Wire and Arc Additive Manufacturing (WAAM). Addit. Manuf. 34, 101200.

[20] Nam, H., Park, C., Kim, C., Kim, H., Kang, N., 2018. Effect of post weld heat treatment on weldability of high entropy alloy welds. Sci. Technol. Weld. Join. 23, 420–427.

[21] Benakis, M., Costanzo, D., Patran, A., 2020. Current mode effects on weld bead geometry and heat affected zone in pulsed wire arc additive manufacturing of Ti-6-4 and Inconel 718. J. Manuf. Process. 60, 61–74.

[22] Peng, D.X., 2014. Optimization of chemical mechanical polishing parameters on surface roughness of steel substrate with aluminum nanoparticles via Taguchi approach. Ind. Lubr. Tribol. 66, 685–690.

[23] Ma, Y., Hu, H., Northwood, D., Nie, X., 2007. Optimization of the electrolytic plasma oxidation processes for corrosion protection of magnesium alloy AM50 using the Taguchi method. J. Mater. Process. Tech. 182, 58–64.

[24] Zavdoveev, A., Pozniakov, V., Baudin, T., Kim, H.S., Klochkov, I., Motrunich, S., Heaton, M., Aquier, P., Rogante, M., Denisenko, A., Gajvoronskiy, A., Skoryk, M., 2022. Optimization of the pulsed arc welding parameters for wire arc additive manufacturing in austenitic steel applications. Int. J. Adv. Manuf. Technol. 119, 5175–5193.

[25] Poznyakov, V.D., Markashova, L.I., Zhdanov, S.L., Berdnikova, E.N., Zavdoveev, A.V., Maksimenko, A.A., 2016. Comparison of procedures for evaluation of effect of welding thermal cycle on impact toughness of HAZ metal of welded joints from low-alloy steels. Pat. Weld. J. 10, 26-32.

[26] Wang, Y., DO, N., (2008). Optimization of the polypyrrole-coating parameters for proton exchange membrane fuel cell bipolar plates using the Taguchi method. J. Power Sources 185, 226–232.

[27] Javid, Y., 2020. Multi-response optimization in laser cladding process of WC powder on Inconel 718, CIRP J. Manuf. Sci. Technol. 31, 406–417.

[28] Yousefieh, M., Shamanian, M., Saatchi, A., 2011. Optimization of the pulsed current gas tungsten arc welding (PCGTAW) parameters for corrosion resistance of super duplex stainless steel (UNS S32760) welds using the Taguchi method. J. Alloys Compd 509, 782–788.

Aluminium foams made of various aluminium alloys scrap and various foaming agents

Karla GRGIĆ[1]**, Branimir LELA**[1]**, Sonja JOZIĆ**[1]**, Jure KROLO**[1]

1) Faculty of Electrical Engineering, Mechanical Engineering, and Naval Architecture, University of Split Ruđera Boškovića 32, 21 000 Split, **Croatia**

kgrgic00@fesb.hr
blela@fesb.hr
sonja.jozic@fesb.hr
jkrolo@fesb.hr

Keywords

Aluminium foam
Chip waste
Recycling
Closed cell foam
Microhardness

Original scientific paper

Abstract: Metal foams are lightweight materials with wide applications. Their production from chip waste promotes recycling and reduces the costs of the process. The main aim of this article was to analyze the differences between metal foams produced from different aluminium alloys and foaming agents. Base material used in experimental work were chips from aluminum alloys such as A360 (EN AC 43400), A380 (EN AC 46000), AA 6082 (EN AW 6082), and AA 7075 (EN AW 7075), whereas foaming agents were TiH_2 and $CaCO_3$. Relative densities, microhardness and homogeneity of obtained samples were investigated. It has been concluded that aluminium alloy foams obtained by using the foaming agent TiH_2 regardless of the base material have more homogenous pores, higher expansion at lower temperatures, and also lower relative density, despite the lower percentage of the foaming agent. Aluminium foam produced out of aluminium alloy (A360) chips as base material, had the highest growth rate when the TiH_2 agent was used, and the most homogeneous structure was obtained with AA 7075 alloy. On the other hand, foam made of alloy AA 7075, when foaming with $CaCO_3$, had the most homogenous structure, and also the lowest relative density.

1. Introduction

Metal foams are materials that are consisted of gas pores, separated by thin walls [1]. They are often used because of their capability for high energy absorption, high stiffness, and acoustic insulation followed by low density [2, 3]. Metal foams also have low thermal conductivity and high vibration damping [2, 4]. They still do not have a wide range of applications because of their high production costs and problems with the repeatability of the process [2, 5]. Closed cell foams are mainly used in the transport industry and open cell foams as heat exchangers, purificators, filters, and electrodes [4, 6]. One of the materials for metal foam production is aluminium alloy. Chip waste made of that metal is highly resistant to corrosion, and its recycling process uses only 5 % of the energy needed for primary aluminium production [5]. Another advantage of aluminium foams is their harmless influence on the environment [7]. There are several ways to produce metal foams from liquid or solid states of base material [8]. In a liquid state, there is an injection of gas in molten alloy or foaming agent which decomposes and creates pores [5]. In the solid state, in order to first produce the precursor, the process starts with the consolidation of the foaming agent and matrix by cold and hot compressing or extrusion [3]. After that, the precursors are heated in a semi-solid or liquid state to decompose foaming agents and make gases that expand and create pores. The most commonly used blowing agent is TiH_2. The reason for its frequent use is

its fast and early decomposition that matches the melting temperature of the often-used aluminium alloys.
The main disadvantage is its high cost as well as a premature gas release when the melting process is used [1, 6, 9]. Foams made with this agent have a smooth surface and larger pores compared to the pores obtained with the same amount of $CaCO_3$ [9]. The alternative agents are ZrH_2, or carbonate group with $CaCO_3$ and dolomite [6, 8]. $CaCO_3$ decomposes to CaO and CO_2 which makes pores in foams [8]. As some authors experimented, it is an acceptable alternative to TiH_2, because of the reduction of premature release of gas, also there is no need for pre-treatment of agents and the cost of material is low [10]. However, much higher temperatures are needed and expansion lasts longer [11]. When using chip waste instead of powder, it is difficult to merge matrix material and blowing agent. There are a few reasons. Firstly, chip waste has a much bigger geometrical shape than the foaming agent [3]. That can result in the accumulation of agents in some parts of the precursor and consequently lead to anisotropy because of the larger pores in some regions of the foam. Secondly, their surface can be contaminated with oxides because of previous machining processes [3]. The benefit of using the chip waste in the foam production process is that there is less need for stabilizers and the cost of a metal matrix is much lower. There is no need for stabilizers due to oxides on the chip surface which promotes viscosity and stabilization [12, 13]. There are only a few articles with production metal foams out of chips.

2. Literature review

Haesche et al. [14] made foams using AlSi9Cu3 and AlMg4.5Mn alloy chips with the addition of $CaCO_3$ and dolomite as well as CaO stabilizer. Higher porosity was made with dolomite addition and higher temperature. The former alloy more than 100 % expansion, whereas the latter did not reach that expansion at any of the used temperatures. In another study [15] foams were produced using A360 powder, SiC stabilizer, and $CaCO_3$. It is concluded that with the addition of a stabilizer, foam viscosity and density increase. The optimum value of $CaCO_3$ is 3 wt% because it has a lower density than the foam with 1 wt% of $CaCO_3$ and is more uniform than the foam with 5 wt% of $CaCO_3$. That percentage is also proved in another article [16], in which a conclusion has been made that the porosity and compressive properties drop has been visible with the addition of $CaCO_3$ above 3,6 wt%. Osman et al. [5] proved that the percentage of $CaCO_3$ higher than 5 wt%, leads to a decrease in porosity because of the higher viscosity and shrinkage. It is the same with the addition of stabilizer Al_2O_3 over 3 wt%. Up to that value, the breakage of bubbles is prevented and the viscosity is increased. The best mechanical properties are made by foaming when the temperature is lower than 800 °C. To continue, in another two articles, A356 powder was mixed with 2.5, 3, and 3.5 wt% of $CaCO_3$ and foamed with the melting process. Foam height is higher with the increment of foaming time and also with the rise of the $CaCO_3$ percentage. Cell size rises within 5 minutes and later is almost constant. Compressive properties increase with higher density, and also energy absorption while cell size decreases [1, 17]. Osman et al. [6] made a foam from aluminum scrap with Al_2O_3 and $CaCO_3$. The measured electrical resistivity of foam is higher than in dense aluminum and thermal conductivity is much lower because of the cellular structure. Energy absorption is very high. Therefore it is widely used in the automotive industry.

Tsuda et. al [3] made metal foams using aluminium AA 6063 machining chips with the addition of 0.5 to 3 % TiH_2. Al_2O_3 was also added in the range from 3 to 5 wt%. For comparison, a sample with powder alloy AA 6061 was made and 0.5 % TiH_2 was added to it. Porosity was higher for the foam made of powder alloy AA6061, than one made of AA6063 chip waste. The shape of pores is irregular with aluminium chips. Consequently, pore coalescence occurs easily. Porosity increases with the increase of TiH_2 percentage up to 2 wt%. Al_2O_3 promotes expansion and leads to higher viscosity which prohibits drainage and coarsening. Another article [2] was made of machining chips 6063 and 4032 using TiH_2 as a foaming agent and Al_2O_3 as a stabilizer. It is confirmed that porosity depends on the material i.e. the foam made of 4032 alloy has smaller pores than the one made of 6063 alloy. The expansion started near the solidus line, and by reaching the liquidus line, maximum expansion can be seen. It is higher with 4032 alloy because of the lower solidus line and earlier expansion. A foam with a mixture of those two alloys followed that statement. Kumar et al. [12] made foams with LM26 machining chips for automotive industry. They were primarily heated to expand oxygen content. Mg was added as a stabilizer and TiH_2 as a foaming agent. With the heat treatment, there is an increase in oxygen content. The addition of Mg increased foam expansion and homogeneity of pores. Oxides slow down the expansion process. They also increase foam viscosity, and adding Mg makes expansion slower but homogenous with smaller pores [13].

The objective of this study is to find out the differences between the foaming time, temperature, and density when foaming machining chip waste made of alloys A360, A380, AA 6082, and AA 7075 with TiH_2 and $CaCO_3$ as foaming agents.

3. Experimental procedure

Chips were produced by face milling operations, on vertical machining center Spinner VC 560, Figure 1. Foaming agents, used for the process were TiH_2 and $CaCO_3$.
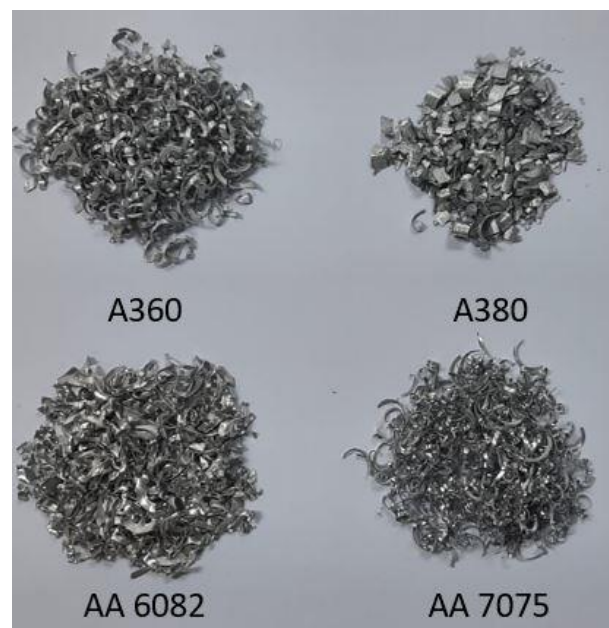
Figure 1. Machining chips of alloys A360, A380, AA 6082, and AA 7075

The experiment began with the mixing of alloy chips and the foaming agent with a small amount of distilled water to promote consolidation. The amount of TiH_2 was 1 wt% and of $CaCO_3$ was 5 wt% of the total sample mass. Furthermore, the mixture was cold pressed on a hydraulic press with the force of 700 kN in a mold with a 38 mm diameter and height of 150 mm. Force was measured with the HBM load cell C6A 1MN sensor. Cold pressed

samples were heated at 420 °C for 20 minutes in the furnace Demiterm Easy 9. To continue, after heating of samples, hot pressing was made at 400 °C with the same force as there was in cold compaction with the hydraulic press and tool shown in Figure 2. a). The temperature was controlled with Omron temperature regulator E5CC and relay G3PE-225B DC12-24. The samples of 40 mm in diameter and height in a range of 17 to 22 mm were made.

a)

b)

Figure 2.   a) Hot compaction tool; b) Foaming mold

In the end, the foaming process took place in the furnace Demiterm Easy 9 in the mold, which can be seen in Figure 2. b). The foaming temperature and time of processes have been chosen in accordance with obtained results in the preliminary experiments, Table 1. For purpose of this research, the temperature of the foaming process with the TiH_2 agent was also chosen according to the liquidus points of the alloys. The main reason is its low decomposition range starting above 400 °C to 600 °C. To start the foaming reaction, alloys must reach semisolid or melting conditions [8, 9]. Since the decomposition of $CaCO_3$ starts above 680 °C, which is higher than the melting point of chosen alloys, foaming temperatures for samples with $CaCO_3$ foaming agents are selected regarding its decomposition [18]. DTA analysis was carried out on TG/DTG-DTA Pyris Diamond, Perkin Elmer measurement device to determine liquidus lines for the alloys. The liquidus temperature of alloy A380 is 600 °C, for A360 is 610 °C, for AA 7075 640 °C, and for the last one AA 6082 is 660 °C.

Table 1.   Foaming parameters of the samples

Sample number	Alloy	Foaming agent	Foaming temperature	Foaming time (min)
1	A380	TiH_2	610 °C	20
2	A360	TiH_2	630 °C	15
3	AA 7075	TiH_2	650 °C	23
4	AA 6082	TiH_2	690 °C	15
5	A380	$CaCO_3$	800 °C	30
6	A360	$CaCO_3$	780 °C	15
7	AA 7075	$CaCO_3$	850 °C	30
8	AA 6082	$CaCO_3$	800 °C	30

Hardness represents one of the main properties in the mechanical industry. This work analyzes how the most important foam parameter, relative density influences hardness. Four different materials have been used in the experiments. Because of the pore structure, the applied force should have been smaller than in the usual process with solid material. Microhardness was measured using Shimadzu tester HMV 2T with a value of HV1 on sanded cross-section foam cell walls. The average of five measurements was calculated for each sample.

The relative density is calculated as a ratio of foam (ρ_f) and aluminium alloy (ρ_i) density, and can be written as [4]:

$$\rho_{rel} = \frac{\rho_f}{\rho_i} \tag{1}$$

4.   Results and discussion

According to Figure 3, samples 5 to 8 made with $CaCO_3$ do not have a spheroidal shape of pores. It is rather directed in the opposite direction of hot and cold compaction. One of the reasons is the difference between

the size of chips and the foaming agent which resulted in the accumulation of $CaCO_3$ in a few places of precursor. According to Ramirez et al. [19], the compaction of samples is not enough to succeed in a uniform structure. There is a need for double axial compaction or extrusion because of breaking up the oxide layer around the particles and better bonding between alloy and agent. Another reason is the greater percentage of $CaCO_3$ powder. Its particles bond together and create a barrier that enables connection with the base alloy. That samples

also have a higher relative density than samples 1 to 4, even though the foaming temperatures were much higher, Table 2. This is due to the slower decomposition of $CaCO_3$ than TiH_2, regardless of base alloy [10]. In accordance with the results, relative density is not following the statement of the proportional increase with the percentage of foaming agent. That is in relation to the statement that 10 wt% of $CaCO_3$ is needed to expand the foam as 1.5 wt% of TiH_2 [10].
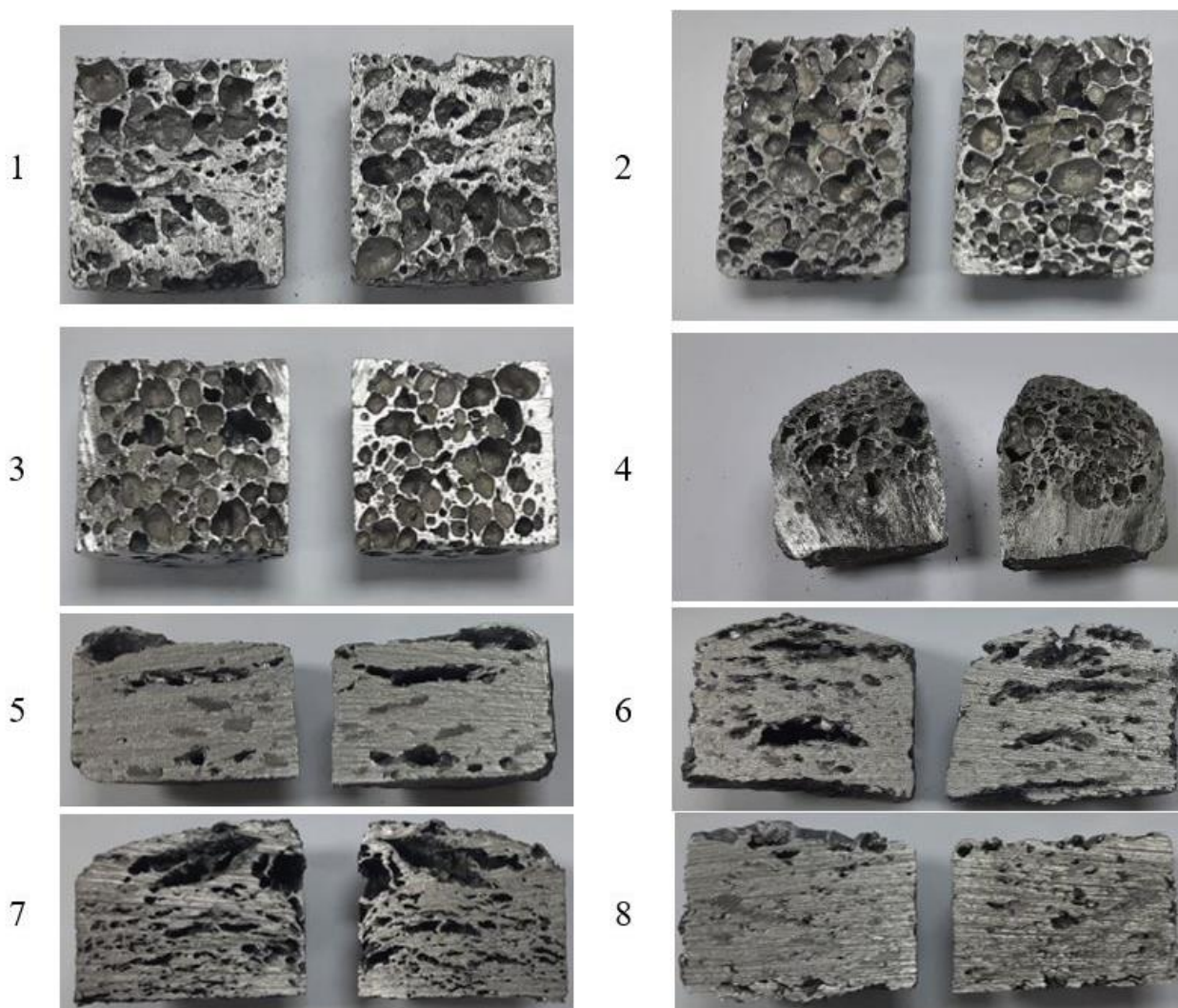
Figure 3. Samples after foaming

As it can be seen from Figure 3, sample 3, AA 7075 has the best homogeneity of pores. Despite the fact that every sample was held at the temperature above the liquidus line, not all samples have a homogenous porous structure over the entire section. In other samples with TiH_2, there are several larger pores due to higher temperature or

longer holding time than necessary, which may cause coalescence. The secton surface of sample 4 is divided into two regions. The upper layer is a porous structure, and the second, lower layer, does not have pores. This can be a result of a lower mixing time or higher gas tendency to reach the upper layer while foaming [10].

When comparing samples foamed with $CaCO_3$, alloy AA 7075 has the greatest porous structure which can be a result of higher temperature, while samples 5 and 6 have only large horizontal pores. Sample 8 made of AA 6082 did not have larger pores, but less number of smaller pores which lead to the highest relative density.

This research is in opposition to the statement that porosity increases with a higher foaming temperature by foaming with TiH_2 [20]. According to Table 2, even though sample 3, made of alloy AA 7075, had a higher foaming temperature, its relative density is similar to sample 1 made of alloy A380. It can also be visible that sample 2 made of A360 alloy has the lowest density, despite the fact that is foamed at a lower temperature than samples 3 and 4.

Table 2.   Relative density of samples

Sample number	Relative density
1	0.4
2	0.23
3	0.41
4	0.5
5	0.69
6	0.56
7	0.56
8	0.69

When different materials are used, there is also an influencing factor in their solidus and liquidus line. Kanetake et. al [2] proved that a sample with a higher liquidus line has slower expansion and higher relative density. In their study, it can be seen that the foams made of alloy AA 6082 with the highest liquidus line have the highest relative density, while the porosity is the smallest, despite its higher foaming temperature compared to all samples made of TiH_2.

The lowest density of A360 foam with TIH_2 proves that, not only foaming temperature influences foams properties but also its chemical composition. This is especially important for foams with $CaCO_3$ because of the tendency of some chemical elements to react with oxygen from this agent. Oxides usually provide higher viscosity and prevent shrinkage and coalescence of pores. However, they also delay the expansion of foam [10].

From Table 3., it can be concluded that the foams made of AA 7075 have the highest microhardness. The results show that the used foaming agent does not influence the microhardness. The only influential factor is the chemical composition of the used base alloy.

Table 3.   Microhardness of foamed alloys

Material	Sample number	Microhardness (HV1)
A380	1, 5	75
A360	2, 6	58
AA 7075	3, 7	113
AA 6082	4, 8	60

In the previous experiments, changing foaming temperature did not significantly change microhardness. That is proven in this research, where microhardness was similar with samples made with TiH_2 and $CaCO_3$, using the same alloys.

5. Conclusion

Foams were made with alloys A360, A380, AA 6082, and AA 7075 using TiH_2 and $CaCO_3$ as foaming agents. The conclusions are as follows:

- Samples foamed with TiH_2 have a lower relative density and more homogenous structure with more pores in cross-section than the samples made with $CaCO_3$ agent. Foams made with $CaCO_3$ foaming agent have larger pores in the opposite direction of compaction. The exception is foam made of AA 6082 alloy.
- Alloy AA 7075 had the most homogenous structure when foaming with TiH_2 and $CaCO_3$, while the sample height when foaming with the TiH_2 agent was highest in the A360 alloy.
- Foams made of AA 6082 had the greatest relative densities with both foaming agents. That is due to the fact that chemical composition influences foaming possibility. Sample 4 did not have pores in a lower layer, while sample 8 contains less pores than other samples.
- Foam growth is dependent on the foaming agent as well as chemical composition and it is not equal regardless of the same foaming conditions.
- Foaming temperature and agent do not influence microhardness. The most influential factor is the chemical composition of alloys.
- It is required to carry out further investigation to succeed in production of more homogenous foams with lower relative density when using $CaCO_3$ as foaming agent.

Acknowledgment

REFERENCES

[1] Ghaleh, M. H., Ehsani, N., Baharvandi, H.R., 2021. High-Porosity Closed-Cell Aluminum Foams Produced by Melting Method Without Stabilizer Particles. International Journal of Metalcasting. 15 (3), 899–905.

[2] Kanetake, N., Kobashi, M., Tsuda, S., 2008. Foaming behavior of aluminum precursor produced from machined chip waste. Advanced Engineering Materials. 10 (9), 840–844.

[3] Tsuda, S., Kobashi, M., Kanetake, N., 2006. Producing technology of aluminum foam from machined chip waste. Materials Transactions. 47 (9) 2125–2130.

[4] Ashby, M.F. et al., 2002. Metal foams: a design guide, Materials & design. 23 (1), ISBN 0-7506-7219-6

[5] Osman, H.O.A., 2015. Fabrication of aluminum foam from aluminum scrap. International Journal of Engineering Research and Applications. 5 (2), 109–115.

[6] Osman, H.A., Omran, A.M., Atlam, A.A., Moatasem M Kh., 2017. Characterization of aluminium foam produced from aluminium scrap by using CaCO$_3$ as foaming agent. JES. Journal of Engineering Sciences. 45 (4), 448–459.

[7] Kevorkijan, V., 2010. *Low cost aluminium foams made by CaCO$_3$ particulates*, Association of Metallurgical Engineers of Serbia AMES

[8] Soloki, A. and Esmailian, M., 2015. Carbonate-Foaming Agents in Aluminum Foams: Advantages and Perspectives. Metallurgical and Materials Transactions B: Process Metallurgy and Materials Processing Science. 46 (2), 1052–1057.

[9] Papadopoulos, D. P. et al., 2011. The use of dolomite as foaming agent and its effect on the microstructure of aluminium metal foams-Comparison to titanium hydride. Colloids and Surfaces A: Physicochemical and Engineering Aspects. 382 (1–3),118–123.

[10] Lázaro, J., Solórzano, E., Rodríguez-Pérez, M.A., 2014. *Alternative Carbonates to Produce Aluminium Foams via Melt Route*. Procedia Materials Science. 4, 275–280.

[11] Kevorkijan, V. et al., 2010. Synthesis and Characterisation of Closed Cells Aluminium Foams Containing Dolomite Powder As Foaming Agent," Materiali in Tehnologije. 44 (6), 363–371.

[12] Kumar, G..SV., et al., 2013. Foaming of aluminum alloys derived from scrap," Advanced Engineering Materials. 15 (3), 129–133.

[13] Kumar, G.S.V., García-Moreno, F., Banhart, J., Kennedy, A.R., 2015. The stabilising effect of oxides in foamed aluminium alloy scrap. International Journal of Materials Research. 106 (9), 978–987.

[14] Haesche, M. et al., 2010. Carbonates as foaming agent in chip-based aluminium foam precursor. Journal of Materials Science and Technology. 26 (9), 845–850.

[15] Rajak, D.K., Nikhil, N.M., Das, S., 2019. Fabrication and investigation of influence of CaCO3 as foaming agent on Al-SiCp foam. Materials and Manufacturing Processes. 34 (4), 379–384.

[16] Jaafar, A.H., Al-Ethari, H., Farhan, K., 2019. Modelling and optimization of manufacturing calcium carbonate-based aluminum foam. Materials Research Express. 6 (8).

[17] Ghaleh, M.H., Ehsani, N., Baharvandi, H.R., 2021. Compressive Properties of A356 Closed-Cell Aluminum Foamed with a CaCO3 Foaming Agent Without Stabilizer Particles. Metals and Materials International. 27 (10) 3856–3861.

[18] Sutarno, S., Nugraha, B., Kusharjanto, S., 2017. Optimization of calcium carbonate content on synthesis of aluminum foam and its compressive strength characteristic. AIP Conference Proceedings. 1805, 1–10.

[19] Ramirez, A.M.M., Vintila, R.R., Drew, R.A.L. 2019. Morphology of aluminum alloy foams produced with dolomite via partial sintering of precursors. Materials. 12 (10), 1691.

[20] Ali, H., et al. 2021. Effect of the manufacturing parameters on the pore size and porosity of closed-cell hybrid aluminum foams. International Review of Applied Sciences and Engineering. 12 (3), 230.

Experimental analysis of distribution of bending stresses in layers of wood with numerical verification

Nedim HUEM[1], Amra TALIĆ-ČIKMIŠ[1], Aida IMAMOVIĆ[2]

1) Faculty of Mechanical Engineering, Fakultetska 1, 72000 Zenica, **Bosnia and Herzegovina**
2) Faculty of Metallurgy and Technology of Zenica, Travnička 1, 72000 Zenica, **Bosnia and Herzegovina**

nedim_hurem@gmail.com
amra.talic.cikmis@unze.ba
aida.imamovic@unze.ba

Keywords
Bending stresses,
Mathematical model
Numerical analysis

Original scientific paper

Abstract: The paper presents the determination of the mathematical model of the breaking force of a solid wood panel. For this purpose, an experiment with thirteen repetitions was planned and carried out. The force was measured in such a way that the fibers of the plate are parallel to the bending direction of the plate. Numerical simulation defined the model of the beam on which the defined breaking force and stress distribution were applied. The model can readily accommodate different geometries and material properties, and is therefore a useful tool to optimize the design of the beams.

1. Introduction

The advantages of solid wood panels are: low weight, high strength, easy processing, attractive colours and different textures. It is pleasant to the touch, warmly acting, a good insulator of heat and electricity, has good acoustic properties, and great design possibilities and lengths of elements. Significant advantages of wood are based on the fact that it is an easily accessible, environmentally friendly and renewable material. In addition to these advantages, wood also has its disadvantages that need to be addressed in order to successfully eliminate them. These are: wood defects, rot, the influence of insects and fungi, anisotropy, hygroscope, the dependence of mechanical properties on the water content in wood, shrinkage, swelling and flammability here necessary).

The aim of the experimental research is to examine the significance of the influenced parameters of solid wood board, specifically its density (ρ) and thickness (d) on its bending strength in parallel with the stretching of wood fibers and the analysis of experimental data from the aspect of possible higher bending strength, while not compromising the quality of the plate material and reducing the total cost of production. Based on the experimental results, i.e. the maximum bending force at four points, in accordance with the standard BAS EN 789, modelling of the influencing parameters to the maximum fracture force (Fmax) has to be done, [1,2].

| **Symbols**			
b	Width, mm	ρ	Density, kgm^{-3}
l	Length, mm	Kh	Cochran coefficient, -
v	Bending speed, mm/min	R	Regression cofficient
u	Wood humidity, %	E	Elastic modulus E, MPa
d	Thicknesses, mm	v	Poisson coefficients, -
F	Force, kN	G	Slip modulus. MPa
Fmax	Maximum fracture force, kN		Yield stress, MPa
	Greek letters		
α	Significance level,-		

2. Design of experiment

Experimental research related to this work is based on measuring the maximum bending stress forced up to the moment of fracture of a solid board, made in five different thicknesses and five types of wood: spruce, poplar, beech, ash and oak, previously processed into clean workpieces and thereafter cut into sample dimensions according to BAS EN 789, [3]. Solid boards are produced on the basis of longitudinal joining of clean workpieces by means of a wedge joint in the required dimension of the board length, and then they are width wise joined to a flat joint in the required width of solid board format. Production of clean workpieces, wedge milling operation, and length and width joining in the format of the board was done in "Rosewood" d.o.o. Visoko, as well as cutting the necessary tests in the direction of stretching wood fibers, or perpendicular to the stretching of wood fibers from the plate format 1800 (mm) x 1200 (mm) x d (mm). Measurement of moisture content, determination of wood density and testing of tests for bending strength up to the maximum fracture force was done at the Technical Faculty of the University of Bihać.

The experiment used pure specimens of 20 mm thick spruce, 18 mm and 22 mm thick poplar, 16 mm, 20 mm and 24 mm thick beech, 18 mm and 22 mm thick oak and 20 mm thick ash, of different dimensions in length and width. The humidity of the samples was measured with an electric hygrometer, on the surface which was treated. Determination of wood density (bulk density) was done according to the standard BAS EN 13061-2: 2016, where small samples of dimensions 30 x 30 x d mm were taken Test methods for determining the mechanical properties as well as the dimensions, moisture content and wood density of the tested samples are determined according to BAS EN 789: 2004 (Figure 1). Methods using this standard are applied to wood-based panel constructions and glued laminated wood with permanent cross-sections. The tests must be carried out under conditions

where T = 20 °C at a relative humidity of 65%.
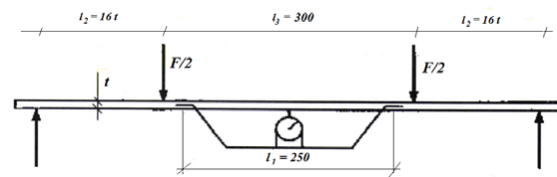
Figure 1. Arrangement for bending test according to BAS EN 789 standard, [4]

During the bending strength tests, the following values were constant:

- sample width $b = 300$ mm,
- sample length $l = 32\,d + 300$ mm,
- bending speed $v = 7$ mm/min,
- wood humidity $u = 8\%$.

The samples were cut from solid wood panels of 1800 x 1200 mm in thicknesses:

- 16 mm thick beech board,
- 18 mm thick poplar board,
- 20 mm thick beech board,
- 20 mm thick spruce boards,
- 20 mm thick ash board,
- 22 mm thick oak boards,
- 24 mm thick beech board.

From these plates, standard probes were cut longitudinally to stretch the fibers (13 pcs). In the case of beech, 5 samples measuring 980 x 300 x 20 mm were cut from two 20 mm thick solid boards, 1 sample was cut from one 16 mm thick solid board, and 1 sample was cut from one 24 mm thick solid board. The cutting was also done according to the standard BAS EN 789. The bending strength test was performed ion the machine SIL 50KNAG, manufactured by Shimadzu (Figure 2). With a central 2-factor experiment plan, an experiment with 8 or 13 replicates can be used.

Figure 2. Bending of wood according to BAS EN 789

In this case, an experimental design with 13 replicates, of which 5 are in the central point, has been chosen. The input parameters are set according to Table 1 [4].

Table 1. Values of experimental input factors

	-1.414	-1	0	1	1.414
Factor A Density ρ [kg/m³]	450	560	650	720	820
Factor B Thickness of panel[mm]	16	18	20	22	24

After the experiment was performed on all 13 tests, the results of plate fracture force were obtained according to the Table 2.

Table 2. Experimental values of fracture force

Number of experiment	Density of wood ρ [kg/m³]	Thickness of panel b [mm]	Force F [kN]
1	560	18	4.68
2	720	18	11.8
3	560	88	4.98
4	720	22	11.03
5	450	20	7.09
6	820	20	11.5
7	650	16	5.76
8	650	24	12.12
9	650	20	6.71
10	650	20	7.73
11	650	20	6.51
12	650	20	7.29
13	650	20	6.68

Table 3. Analysis of variance for the fracture force model of wood panels

Source of variation	SS	dF	MS	F	P	Significant
A	47.07	1	47.07	16.29	0.0023	Significant
B	9.08	1	9.08	3.44	0.093	Significant
Model	56.15	2	28.7	9.72	0.004	Significant
Error	28.88	10	2.88			
Lack of fit	27.84	6	4.64	1.80	0.296	Not significant
Pure error	1.042	4	0.26			
Total	85.04	12	7.08			

Once experimental results have been obtained, the processing of the mathematical model could be

proceeded. It could be obtained by the method of analysis of variance and by determining the significance of the influential parameters. Influential parameters are input factors, wood density and board thickness, and the interaction between these two factors. The variance analysis table (ANOVA) is shown in Table 3 [5].

The significance of the parameters can be determined using the Fisher Coefficient F or the parameter p. The Fisher calculated number is compared with the tabular one and if it is higher, the parameter is significant for a predefined level of significance. Using the parameter p, the significance of the parameters using the software R can be determined. With the command 1-pf (coefficient F, degree of freedom of the parameter, degree of freedom of error) numbers as shown in the following code are obtained [1,6].

```
> 1-pf(16.29,1,10)
[1] 0.0023761
> 1-pf(3.44,1,10)
[1] 0.0933194
> 1-pf(9.72,2,10)
[1] 0.0045217
> 1-pf(1.8,6,4)
[1] 0.29634
> 1-pf(1.8,6,4)
[1] 0.29634
```

First three lines of code represent the input factors A and B and the overall model. The numbers we obtained are less than 0.1 what means that the input parameters and the overall model are significant for the significance level $\alpha = 0.1$. The last row represents a deviation from the model that is greater than 0.1 what means that the deviation is not significant and therefore the model is adequate for application. Final expression of the model for determining the fracture force of a board, in which the stretching of wood fibers are parallel, is as follows:

$$F\text{max} = -21.97 + 0.029\rho + 0.53b, \qquad (1)$$

After obtaining the model equation, it is useful to check the homogeneity of the dispersions of the experiment at the point of replication using the Cochran criterion and the adequacy of the model by determining the multiple regression coefficient. Checking the homogeneity of dispersions according to the Cochran criterion showed that the Cochran coefficient of the model Kh = 0.533, which is less than the tabular value for the presented central plan of the experiment which is Kt = 0.544, so it can be concluded that the dispersion of experimental results is homogeneous. The value of the regression coefficient of the model was calculated and is R = 0.9288, which means that the linear model of the plate fracture force describes the accuracy of the experimental results with 92.88%, which is a very good accuracy of the model. The dependence of the fracture force on the interaction of the input quantities can be graphically represented by a contour two - dimensional diagram, Figure 3a, as well as by a three-dimensional representation, Figure 3b.
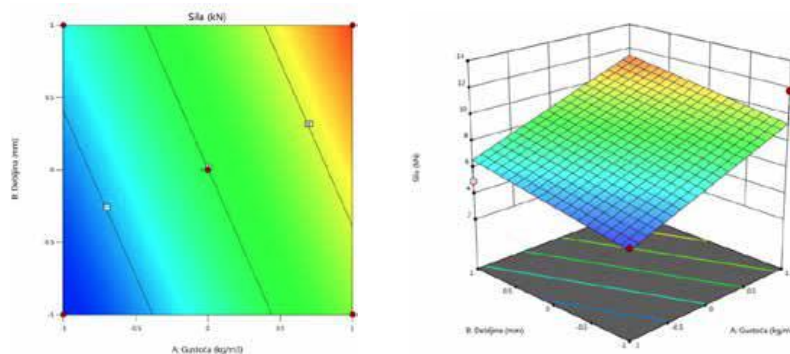
Figure 3. Graphical contour representation, a) two-dimensional, b) three-dimensional

3. Numerical simulation

Numerical analysis was carried out using the finite element method (FEM) with the commercial software Abaqus. This program enables three-dimensional nonlinear analysis of elements made of orthotropic materials, such as and analysis of solutions to constant problems. The simulation tool (basic concept illustrated in Figure 4) includes a geometrical model for the grain course and a micromechanical model for a density and moisture dependent characterization of the clear-wood material. The main goal of numerical modelling is to compare the results of numerical analysis and the results obtained experimental testing. All elements of the system are modelled using "solid" finite elements (C3D8) – spatial.

3D finite elements with 8 nodes. These elements in each node have 6 degrees of freedom, three displacements and three rotations. The deflection at the center of the girder and the reaction of the support are recorded for each increment in order to draw a load-deflection diagram, which best describes the behaviour of the girder.
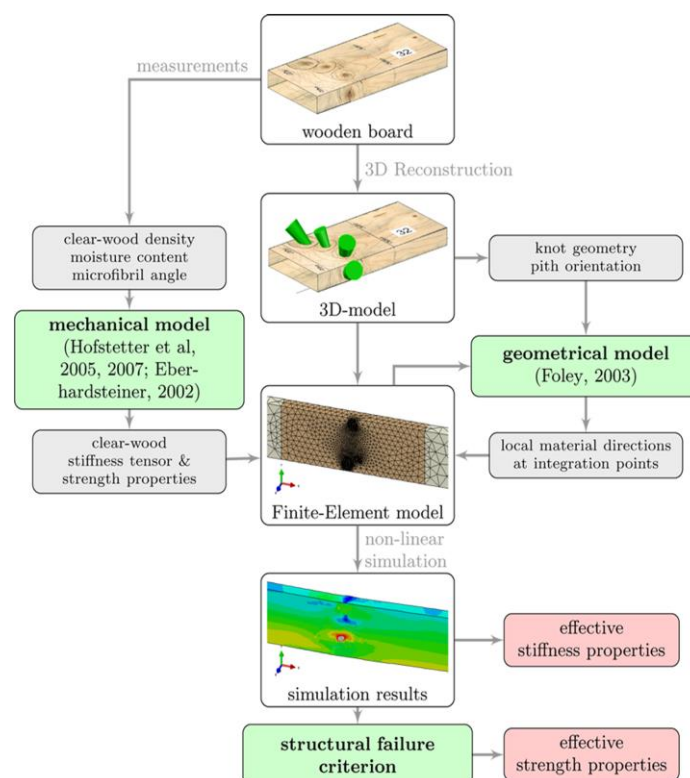
Figure 4.   Concept of the numerical simulation tool for timber elements [7]

Wood is considered as an orthotropic material, therefore it has independent mechanical characteristics in three mutually perpendicular directions (ie the longitudinal direction, parallel to the wood fibers, and two directions perpendicular to the longitudinal direction). The directions of the main axes are shown in Figure 5.
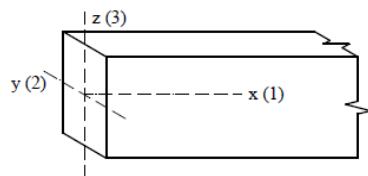
Figure 5.   The directions of the main axes of the samples

The material constants used in the numerical analysis are given in Table 4. Wood in tension, pressure and bending has a different modulus of elasticity in the direction and perpendicular to the direction of the fibers. Nevertheless, the differences are small, and for practical reasons it was adopted that the modulus of elasticity of wood has the same values regardless of the type of stress

Table 4.   Overview of characteristics of materials used in FEM simulation

	Wood
Elastic modulus E [MPa]	
E_1	11080
E_2	886
E_3	554
Poisson coefficients ν [-]	
ν_1	0.37
ν_2	0.42
ν_3	0.47
Slip modulus G[MPa]	
G_{12}	791
G_{13}	744
G_{23}	79

The values of deflection at break determined by numerical calculation are generally in good agreement with the average values obtained experimentally (Figure 6).
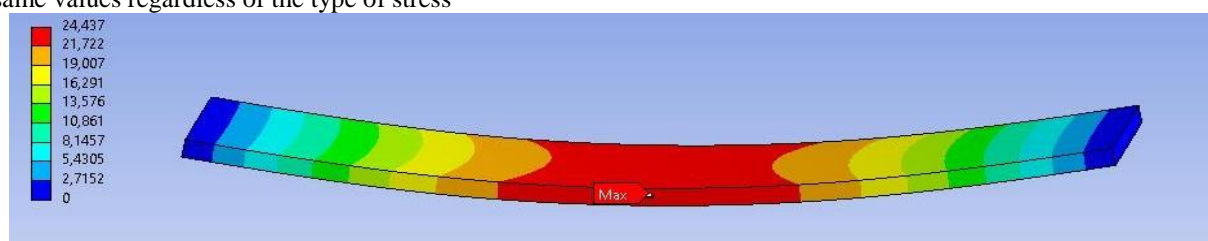
**Figure 6.**   Values of vertical displacement (mm) in FEM mode

The adopted stresses at the yield point necessary for defining the plastic behaviour of wood are shown in Table 5. The values were determined experimentally $(\bar{\sigma}_{11}, \bar{\sigma}_{12})$ and based on data available in the literature. For calculation purposes, it was assumed that the strengths in the transverse directions (radial and tangential) are the same.

Numerical analysis can also be very useful in interpretation experimental results and a better understanding of the mechanical behaviour of the supports.

Table 5.   Yield limits adopted in the numerical analysis

Yield stress[MPa]						
$\bar{\sigma}_{11}$	$\bar{\sigma}_{22}$	$\bar{\sigma}_{33}$	$\bar{\sigma}_{12}$	$\bar{\sigma}_{13}$	$\bar{\sigma}_{23}$	$\bar{\sigma}^0$
36.3	5.0	5.0	6.1	6.1	3.0	36.3

Figure 7 shows the distribution of stress in the wood at the limit load. The longitudinal section in the axis of symmetry enables simple monitoring of the voltage change along the support, as well as in cross sections. Based on the given representations of normal voltages, the area of maximum voltages can be clearly observed
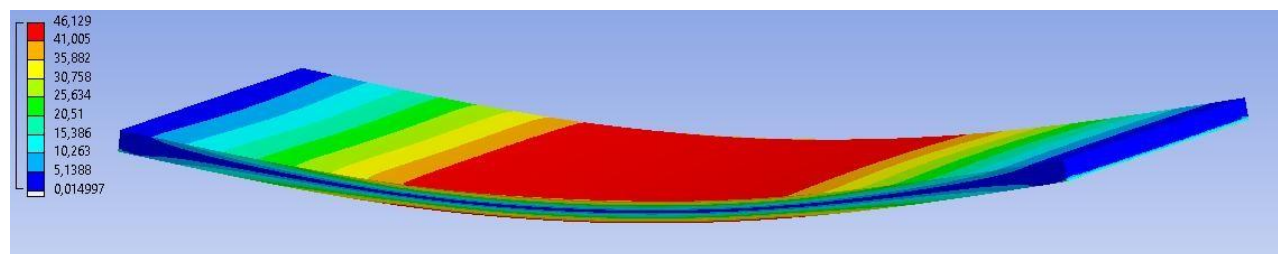
Figure 7.   Stress distribution in layers at cross-section of FEM model

While in the experimentally tested samples the fracture was predominantly due to reaching the limit shear stress, in the numerical model the fracture is a consequence of exceeding the limit tensile stress during bending. The breaking force obtained experimentally was used for the simulation. The obtained numerical result is slightly lower than the experimental one, with good agreement.

4. Conclusion

The model obtained and used in the numerical simulation of beam bending can be easily adapted to different geometries and material properties, and is therefore a useful tool for beam design optimization.The model can readily accommodate different geometries and material properties, and is therefore a useful tool to optimize the design of the beams. Due to the greater accuracy of the model with 13 repetitions was used. The regression coefficient of the model is over 90 %, so we can conclude that the accuracy of the model is good. The value of the maximum breaking force depends on the density of the wood and the thickness of the board, as both values increase, so does the value of the breaking force. A comparison of the values for the maximum load shows a good relationship between the experimental and numerical results.

REFERENCES

[1] Montgomery, D.C., 2015. *Design and Analysis of Experiment,* Arizone State University, John Wiley and Sons

[2] Jurković, M., 1999. *Matematičko modeliranje inženjerskih procesa i sistema*, Univerzitet u Bihaću, Mašinski fakultet, Bihać

[3] Hodžić, D., Džanić, A., 2020. *Planiranje eksperimenta*, Univerzitet u Bihaću, Bihać

[4] BAS EN 789 standard, 2005. *Konstrukcije od drveta – Postupci ispitivanja – Određivanje mehaničkih svojstava ploča od drveta*

[5] Hurem, N., Hodžić, D., Hodžić,A. 2020. *Application of Comparative Experiment in Analysis of Wood Strength*, International Conference of Applied Science ICAS 2020, Hunedoara, Romania

[6] Lawson, J., 2017. *Design and Analysis of Experiment with R*, Chapman and Halls CRC

[7] Lukačević, M., Füssl, J., 2014. *Numerical simulation tool for wooden boards with a physically based approach to identify structural failure,* European Journal of Wood and Wood Produc

Application of 3D scanning for deformation measurement for incremental sheet metal forming vessel bottom

Zlatan IŠTVANIĆ[1]**, Amra TALIĆ-ČIKMIŠ**[2]**, Aida IMAMOVIĆ**[3]

1) Metacomm, d.o.o. Bage 5, 70101 Jajce, **Bosnia and Herzegovina**
2) Faculty of Mechanical Engineering, Fakultetska 1, 72000 Zenica, **Bosnia and Herzegovina**
3) Faculty of Metallurgy and Technology of Zenica, Travnička 1, 72000 Zenica, **Bosnia and Herzegovina**

zlatan.istvanic@gmail.com
amra.talic.cikmis@unze.ba
aida.imamovic@unze.ba

Keywords

Incremental metal forming
Vessel bottom
3D Scanning
Deformation
Measurement

Original scientific paper
Abstract: Incremental forming is a die less metalworking process that is suitable for small lot productions for a wide variety of products. The advantages of this method include cost and lead time reduction in comparison to conventional metalworking processes (spinning or die casting). In the certification process, it is necessary to determine the deformations of the vessel. This paper presents the measurement procedure with the 3D scanning method using the geometry of a square grid engraved on steel plates (tori spherical head) obtained by gradual incremental deformation. The aim of the measurement is to use the results (measured lengths) to determine the permanent deformations in the vessel bottom after deformation treatment based on the known initial un-deformed dimensions of the net. Applicability and the results of the 3D scanning method for determining deformations of the vessel bottom after cold deformation are presented.

1. Introduction

When incremental forming is used in manufacturing large products, such as spherical tank ends, deformation phenomena has significant influence on the quality of the final product. Tori spherical heads are used in the construction of boilers and other thermal devices, and manufacturing pressure vessels [1].

Figure 1. shows the machine for incremental forming of spherical tank ends, up to 4 meters in diameter [1]. The initial shapes (roundels) are made from two parts for diameters greater than 1200 mm and shaped into the final form by the process of incremental deformation or hot forming.
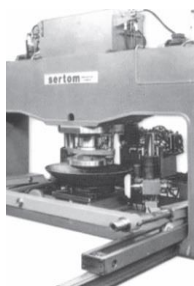
Figure 1.   Incremental forming press P2MF 200x4 - Sertom

The deformation distribution is not uniform and differs in the spherical part of the flooring, the torus part and the flat part of the flooring. Tori-spherical heads are made of steel S235 at the request of the customer are made of other materials according to EN 10025 and EN 10027-1 with the subsequent determination of the thickness.

Table 1.   Chemical composition of S235 steel sheet [1]

Material	chemical composition of [%]					
S235	Fe	S	P	Mn	C	N
JR	98.33 - 100	0 - 0.06	0 - 0.06	0 - 1.5	0-0.25	0-0.01
JO	98.34 - 100	0 - 0.05	0 - 0.05	0 - 1.5	0-0.19	0-0.01
J2G3						
JG4	98.36 - 100	0 - 0.04	0 - 0.04	0 - 1.5	0-0.019	-

Measuring the actual deformations on the final product-flooring is a demanding task that must be performed during the certification process. The procedure consists in carving the grid - squares measuring 10x10 mm on the rondel and the flooring according to AD 2000 MB. By applying digital photogrammetry 3D Scanner Artec Eva, it is possible to obtain much more data about the displacement - deformation of the outer surface of the floor.

Symbols

$Db(x)$ - diameter before processing, mm	$Fexp$ - deformation value determined on the basis of 3D scanning, %
De - outer diameters, mm	FEN_{13445} - deformation calculated according to standard, %
e - the thickness of the tiles, mm	$Deviation$ - deviation, %
F - deformation, %	

2. Measurement procedure

In the paper, measurements were made using the 3D scanning process of five samples for pressure vessels with incised meshes[3]. On the preparations (rounds), before deformation, grids of squares measuring 10 mm x 10 mm were cut. On the fourth vessel′s bottom, the net was etched on the outer surface, and on one on the inner surface. The aim of the measurement is to determine the dimensions after deformation in order to define local deformations after processing by deformation.

The labels that were written on them, for the sake of simplicity, will be replaced in further text with one-letter symbols according to Table 1. The Table 1. also includes photos of the vessel′s bottom.

Table 2. shows the basic measurements for each tile, the thickness of the tiles e, the diameters of the circular preparations (rounds) before processing by deformation $D_{b(x)}$ and the outer diameters of the finished tiles, after deformation, D_e.

Table 2. shows the calculated deformation values according to the expression from the standard EN 13445-5: 2014[3]:

$$F = 100 ln \frac{D_{b(x)}}{D_e - 2e} [\%] \tag{1}$$

Table 1. Labels and photos of the vessel bottom [2].

Name	Label	Photo
#6 Rundela ⌀1500	A	
#15 Rundela ⌀1500	B	
#10 Rundela ⌀2250	C	
#6 Rundela ⌀3000	D	
#15 Rundela ⌀3000	E	

Table 2. Geometry of vessel bottoms and calculated deformation according to EN 13345-4

| Label	$D_{b(x)}$ [mm]	D_e [mm]	e [mm]	F [%]
A	1500	1250	6	19.197
B	1500	1250	15	20.661
C	2250	1910	10	17.435
D	3000	2570	6	15.939
E	3000	2630	15	14.310

3. Experimental measurements

3D scanning was performed with a handheld Artec Eva 3D scanner that works on the principle of structured light (Figure 2).
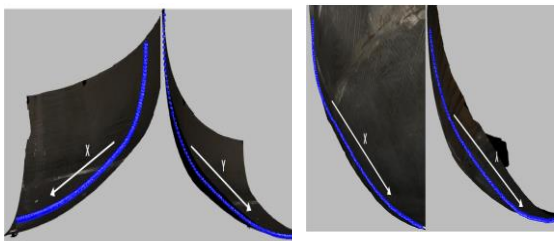

Figure 2. 3D scan of the vessel bottom

In order to more precisely register the incised mesh on the vessel bottom, a texture was subsequently added and recorded to the 3D models, because it was not possible to register the grooves of the mesh using only the geometry of the model obtained by scanning. In the same software, the measurements of the dimensions of the mesh were done after deformation using the distance measurement tool on the scanned models.

On the fourth vessel′s bottom, marked A, B, C and D, measurements of the mesh dimensions after deformation were made along the edges of the incised squares, in the 2nd radial direction (in which deformations are expected to occur), marked with X and Y, according to Figure 3 and Figure 4.
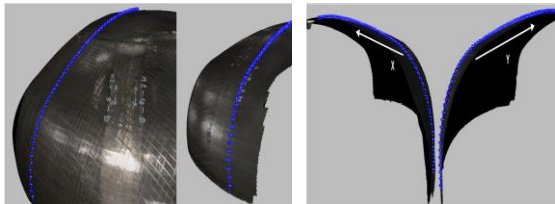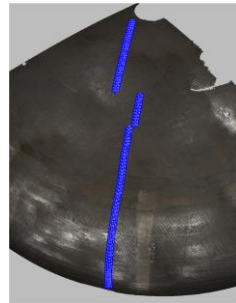

Figure 3. 3D model of vessel′s bottoms A and B with read grid points along two radial measurement direction [2]

Figure 4. 3D model of the vessel bottoms C and D with read grid points along two radial measurement directions [2]
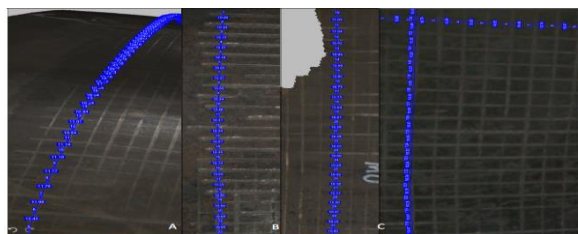
Figure 5. View of defining points and measuring lengths on grids of vessel bottoms A, B, C and D [2]

Figure 6. 3D model of vessel′s bottom E with read points on the grid along the three radial measurement directions [2]

Figure 7. View of definition of points and measurement of lengths on the network of the vessel bottom E [2]

The reading of the dimensions along the X and Y directions was done from the rim to the center of the vessel bottom. On vessel′s bottom C, the mesh was inbeded on the inner surface of the vessel bottom. The dimensions of the sides of the square were read using manually placed points. When placing the points, effort was made to maintain the linear direction of the dimension reading and to maintain the uniformity of the dimension values at adjacent edges, as shown in Figure 5.

It was not possible to register the points in two directions on the ridge E, as with the previously described vessel ends, due to the low visibility of the mesh in those parts. For this reason, the measurement of the dimensions was made along the diagonals of the squares in the grid, in the middle of the scanned part of the vessel bottom, where the diagonals have an approximately radial direction.

The reading was done on three close lines, which were chosen in the parts where the mesh was more visible, as shown in Figure 6. The results for all three lines were combined and ordered from the edge to the center of the vessel end. Figure 7. shows a detail of reading the measurements of the diagonals of the square.

4. Measurement results

By visual inspection, the parts of the net were separated into those located on the flat, tori spherical and spherical part of the vessel end, and for each of them, the mean deformation values were calculated, which in the attached results are marked as Sr1, Sr2 and Sr3, respectively. The measured strain values for all vessel bottoms are shown in the graph in Figure 8.

The obtained results for maximum and maximum average deformation values were compared with calculated deformation values according to the EN 13445-5 standard, where the deviation is calculated according to the expression:

$$Deviation = \frac{F_{exp} - F_{EN13445}}{F_{EN13445}} [\%]. \qquad (2)$$

where is F_{exp} deformation value determined on the basis of 3D scanning, and $F_{EN13445}$ is calculated according to standard.

The materials to be used in pressure vessels must be selected from Code-approved material specifications. This requirement is normally not a problem since a large catalogue of tables listing acceptable materials is available F[4].

Table 3. shows the average values of deformations for all vessel′s bottoms (in two directions X and Y for A, B, C, E and D), by their parts, as well as the maximum individual values.
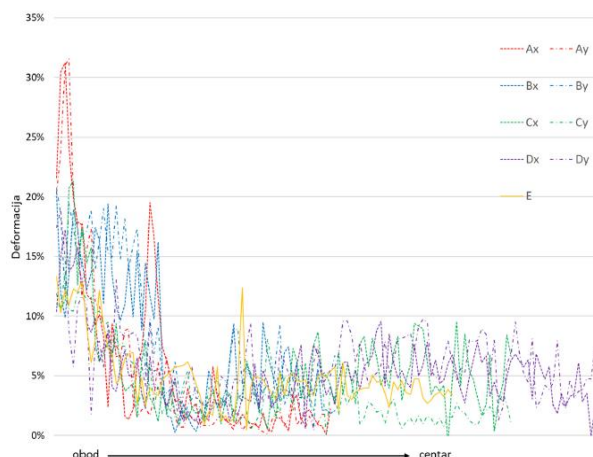
Figure 8. The results of the measured deformations for five tori spherical vessel bottoms.

Table 3. Average and maximum deformation values for 5 vassel bottoms and comparison with calculated values according to EN 13445

Vessel bottom		A		B		C		D		E
According to EN 13445, [%]		19.20		20.66		17.44		15.94		14.31
Reading direction		x	y	x	y	x	y	x	y	/
Average deform. values, [%]	Flat part	25.48	25.33	14.89	17.44	14.30	11.44	12.70	10.85	11.98
	Toro-spherical part	8.81	10.93	13.73	15.15	4.44	5.28	4.16	5.94	5.91
	Spherical part	3.27	1.64	3.77	4.13	4.49	2.50	4.56	5.52	3.91
Deviation max. average deformation values according to EN 13445, [%]		33	32	-28	-15	-18	-34	-20	-32	-16
Max. deformation, [%]		31.22	31.58	20.36	20.75	21.29	13.83	17.24	18.89	13.33
Deviation max. deformation values according to EN 13445, [%]		63	65	-1	0	22	-21	8	19	-7

5. Conclusion

For all vessel′s bottoms, the largest deformations were measured in the straight part. In the torispherical part deformation decreases by moving towards the spherical part. The deformations are the least in the spherical part. Deformations are not uniform, but there are minor deviations all over the bottom of the vessel.

The results of the measured deformations correspond to the expected deformations according to the calculation from the EN 13445 standard, with smaller or larger deviations.

Only for vessel′s bottom A are deviations from the values obtained according to the standard slightly higher, especially for the individual maximum value.

In purpose to determine the reason for this rather large deviation it would be perhaps necessary to perform additional analyses, the measuring procedure itself, as well as the geometry of dane A after processing by deformation. For the four vessel bottoms, markings B, C, D and E it can be said that the deviations are within acceptable limits.

For these four vessel′s ends, the deviations of the average values range from -34% to -15%, and the maximum from -21% to 22%. Such differences are acceptable and expected between the results obtained by the theoretical expression and the real, experimentally determined ones.

REFERENCES

[1] http://metacomm-bih.com/konstrukcije-oprema/ (accessed 13 March 2022).

[2] Tehnička dokumentacija Metacomm d.o.o., *Ekspertiza mjerenja deformacija postupkom 3D skeniranja u dancima nakon obrade deformacijom*, decembar, 2021.

[3] EN 13445-5:2014-Part 5, *Inspection and testing*

[4] Livingston, E., Scavuzzo, R.J., 2000. Pressure Vessels, The Engineering Handbook. Ed. Richard C. Dorf Boca Raton: CRC Press LLC.

Experimental device for measuring the thermal conductivity of metals

Zlatko JANKOSKI[1]*, Igor GABRIĆ*[1]

1) University Department of Professional
   Studies, University of Split
   Kopilica 5, 21000 Split, **Croatia**

zlatko.jankoski@oss.unist.hr
igabric@oss.unist.hr

Keywords

Thermal conductivity
Numerical modelling
Construction of experimental device
Experimental measurement

Original scientific paper

Abstract: In order to design and construct the didactic experimental device for measuring the thermal conductivity of metals, first the numerical modelling approach was applied. The numerical modelling was performed by implementing both the finite element method for transient heat flow and Python programming language. The conceptual design of device was confirmed based on the numerical results of thermal conductivity for three different metals (carbon steel, copper and aluminium). The didactic experimental device was constructed and tested by measuring the thermal conductivity of test specimens made of carbon steel, copper and aluminium. The experimental device proved to be easy to use and practical for educational purposes. The analysis of experimental results, together with the comparison of numerical and experimental results, have showed that the numerical model generally overestimates the rate of change of thermal conductivity. Finally, the reliability of experimental device still has to be confirmed by testing the certified material with known thermal conductivity.

1. Introduction

As a part of laboratory educational activities, devoted to implementation of practical sciences, an experimental device for measuring thermal conductivity of metals is constructed. Other authors have also researched and constructed similar devices for measuring thermal conductivity of different materials [1], ceramic coatings [2], insulating materials [3], etc. Although such apparatus can be easily purchased, the "in-house" designed and constructed experimental device can give students better theoretical and practical insights on thermal conductivity. Different specific requirements have been defined in order to optimise design and to construct the device to be as simple as possible. However, in this paper attention is given on the feasibility of the experimental device in measuring the value of thermal conductivity of different metals.

In order to identify the operating parameters of the experimental device, first the numerical modelling approach is applied. This has included the implementation of a finite element method for transient heat flow [4], and the development of an "in-house" numerical code written in the Python programming language [5]. The generated numerical results on thermal conductivity of carbon steel, copper and aluminium are presented, while the influence of operating parameters on the numerical results have already been discussed in the previous publication [6]. Based on the proposed model and numerical results, the experimental device for measuring thermal conductivity of metals is constructed.

The functionality and accuracy of experimental device are tested and presented by measuring the thermal conductivity of three test specimens made of carbon steel, copper and aluminium. Measured results are compared with the average values of thermal conductivity of respective metals, and also with the numerically obtained results.

Based on the achieved results, the experimental device for measuring thermal conductivity proved to be a valuable model for educational purposes.

2. Conceptual design

The experimental device for measuring thermal conductivity of metals is designed as cylindrical chamber having 50 mm thick layer of thermal insulation, shielded by 2 mm thick SAE 304 stainless steel (Figure 1). As thermal insulation, a calcium silicate ($\lambda = 0,12$ W/(m·K) @ 200°C) is selected. The test specimens for measuring thermal conductivity of metals were cylindrical in shape, 50 mm in diameter and 100 mm in length.

As a heat source, an electric resistance heater is located at the warm forehead of the test specimen. The heater is assumed as cylindrical in shape, with uniform heat distribution. The power of heater can be regulated from 0 to 60 W. A cooling chamber is attached at the cold forehead (heat sink). The cooling chamber is made of aluminium, and it was designed as a heat exchanger with fins in order to generate labyrinth flow and to increase the heat exchange between the cooling water and the specimen cold forehead (Figure 1).
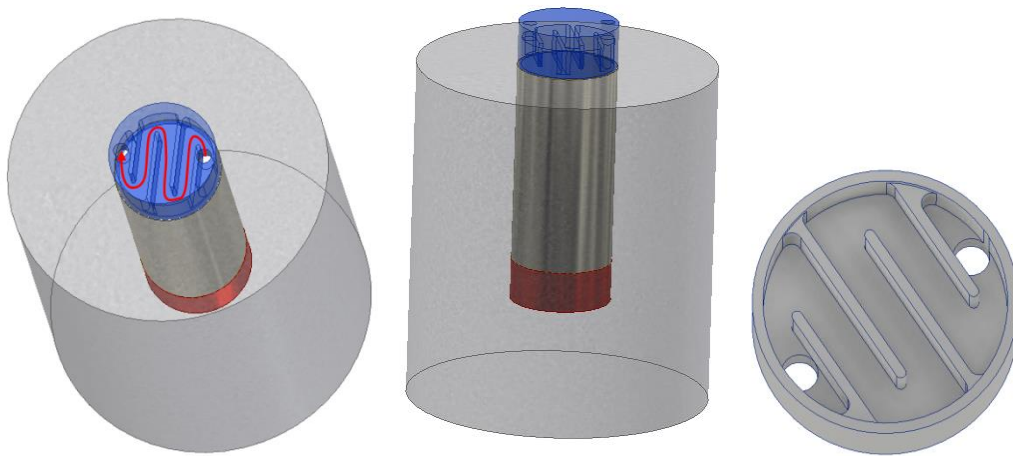
Symbols

t	- relative temperature, °C		**Greek letters**	
k	- thermal conductivity of material, W/mK	ρ	- density of material, kg/m³	
T	- absolute temperature, K	λ	- thermal conductivity of material, W/mK	
c	- specific heat capacity of material, J/kgK		**Subscripts**	
h	- convective heat transfer coefficient, W/m²K	1	- hot side of test specimen	
A	- area, m²	2	- cold side of test specimen	
T	- absolute temperature, K	s	- surface	
l	- distance, m	∞	- infinity	

Figure 1.   Experimental device for measuring thermal conductivity of metals – conceptual design

In order to maintain the controllable circulation of water, the system is equipped with the circulation pump with the variable flow. The circulating water is in the direct contact with the specimen forehead. So as to avoid the conductive heat transfer, the gap of 0,5 mm is assumed between the fins of the cooling chamber and the cold forehead.

The temperature difference between two foreheads (t_1-t_2) is measured at the distance Δl, which is nearly the length of the test specimen (Figure 2). Since the test specimen is surrounded by the thick layer of thermal insulation, it is estimated that the heat generated by electric resistance heater (E_{gen}) will mainly flow along the specimen length. Some of the heat will be lost, for heating the thermal insulation and due to the heat flow through the thermal insulation. Since the heat will be continuously removed from the cold forehead (Q_{water}), after some time the heat transfer will reach nearly stationary state.
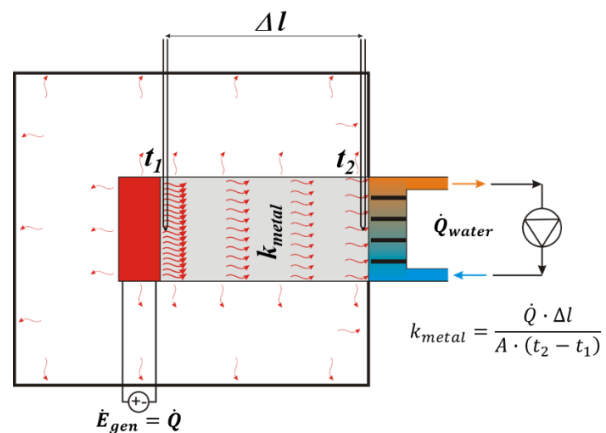
Figure 2.   Experimental device for measuring thermal conductivity of metals – schematic view

$$k_{metal} = \frac{\dot{Q} \cdot \Delta l}{A \cdot (t_2 - t_1)}$$

At that point, when the temperature difference (t_1-t_2) remains nearly constant, the value of thermal conductivity (k_{metal}) can be finally quantified. Radiative heat transfer is neglected due to the specific design of the experimental device, and the expected low temperature level of the surface of shielding stainless steel.

3. Numerical model and results

3.1. Numerical model

Numerical model is developed based on the proposed design and geometry of the physical model. The numerical grid is defined within the 2D area of numerical analysis, which is represented by one half of the longitudinal section (Figure 3), having dimensions 160 × 75 mm. The numerical grid is uniform, comprised of 16 × 12 cells, while the size of each cell is 10 × 6,25 mm. The additional analysis on sensitivity of the numerical results on grid density can be found in the previous publication [6], where the numerical grid was comprised of 32 × 24 cells and with cell size of 5 × 3,125 mm.
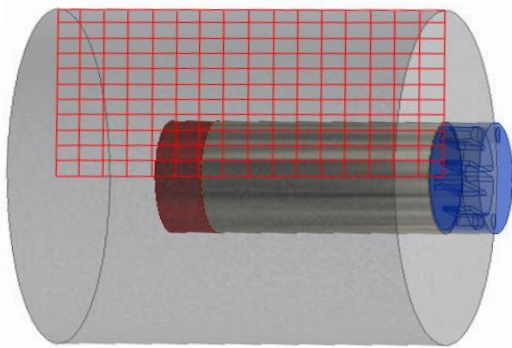

Figure 3.   Numerical geometry

Although the numerical grid is two-dimensional, the calculation of heat flows includes the cross section area of the physical model along the symmetry axis. The heat transfer considers the conduction through the test specimen and the thermal insulation. The following conduction coefficients are assumed:
- k_g = 100 W/mK for electric heater
- k_ms = 52 W/mK for carbon steel specimen
- k_mc = 390 W/mK for copper specimen
- k_ma = 190 W/mK for aluminium specimen
- k_i = 0,12 W/mK for thermal insulation

The above values, together with densities and specific heat capacities, were considered as constants within the operating temperature range. With this assumption the numerical model is simplified, which to some extent can affect the numerical results. However, due to the specific purpose of this numerical model, a certain level of inaccuracy of the results is considered acceptable.
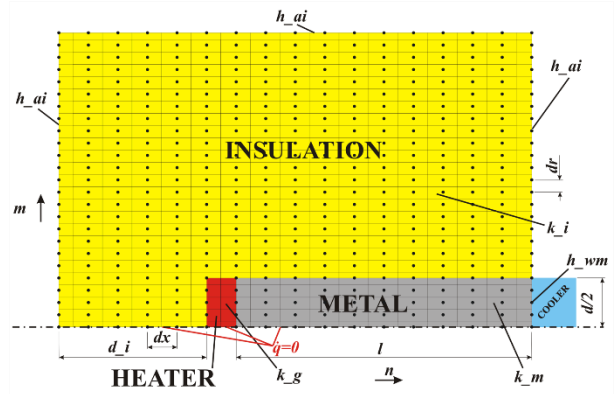

Figure 4.   Numerical grid and nods

The boundary conditions include the convection heat flow between the thermal insulation wall and the surrounding air, where the convective heat transfer coefficient h_ai = 6 W/m²K is used (Figure 4). The convection heat flow between the cold forehead and cooling water is dependent on the value of convective heat transfer coefficient h_wm. Based on the selected volume flow of cooling water, the convective heat transfer coefficient is calculated as 2.622 W/m²K.

Heat balance for each numerical cell (i, j) is based on the conductive (q_k) and the convective heat transfer (q_h) from/to adjacent numerical cell and the internally generated heat (q_{heater}) (Figure 5). The heat flow perpendicular to the symmetry line is assumed zero.

The equation for Fourier's law of two-dimensional heat conduction with heat generation can be written as [4]:

$$\frac{\partial}{\partial x}\left(k\cdot\frac{\partial T}{\partial x}\right) + \frac{\partial}{\partial y}\left(k\cdot\frac{\partial T}{\partial y}\right) + \dot{e}_{gen} = \rho\cdot c\cdot\frac{\partial T}{\partial t} \qquad (1)$$

$\frac{\partial T}{\partial x}$ - temperature gradient

$\dot{e}_{gen}$ - rate of heat generation

$\frac{\partial T}{\partial t}$ - rate of change of the temperature

The general relation for Newton's law of heat convection can be written as [4]:

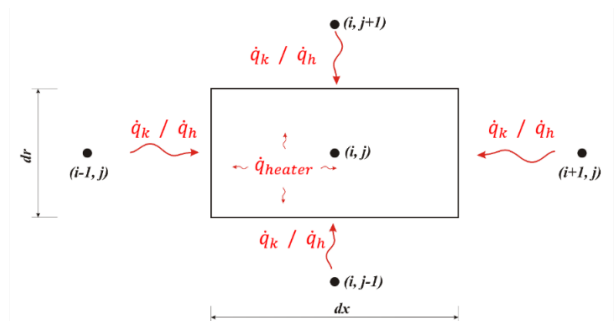$$\dot{Q}_{conv} = h\cdot A_s \cdot (T_s - T_\infty) \qquad (2)$$

**Figure 5.**   Numerical cell – heat balance

The governing equations include the heat balance of each cell where the sum of the conductive and the convective heat transfer, together with the internally generated heat, give the rate of total energy change. The calculations are time dependent, where each iteration considers the calculations of physical values at the specific time step. Detailed overview of governing equations and numerical parameters used, can be found in the previous publication [6].

3.2. Numerical results

The numerical simulations are undertaken in order to evaluate the validity of the proposed design of the experimental device for measuring thermal conductivity od metals. The resulting values of thermal conductivity for carbon steel, copper and aluminium are compared with their standard values for the specific temperaturerange. The maximum duration of numerical simulations was limited to 1800 s, while the power of electric heater was selected at 60 W.
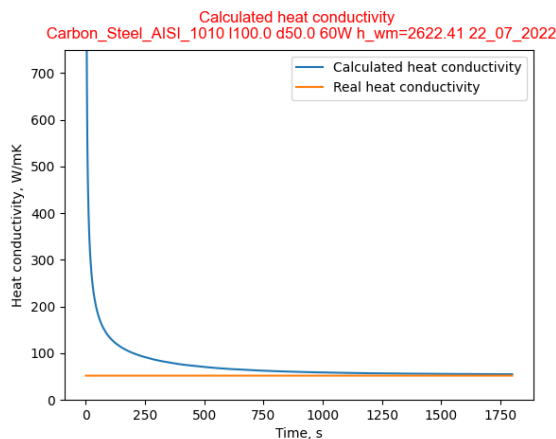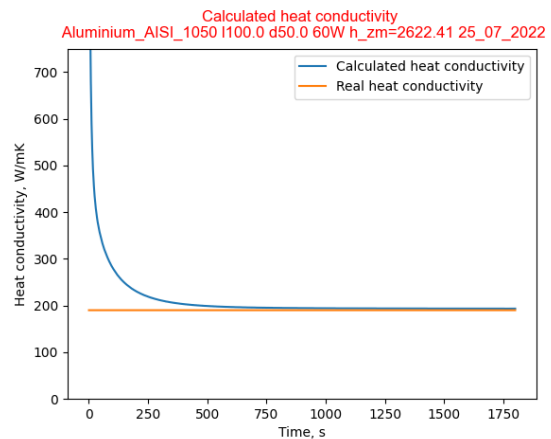

Figure 6. Numerical results – thermal conductivity of carbon steel
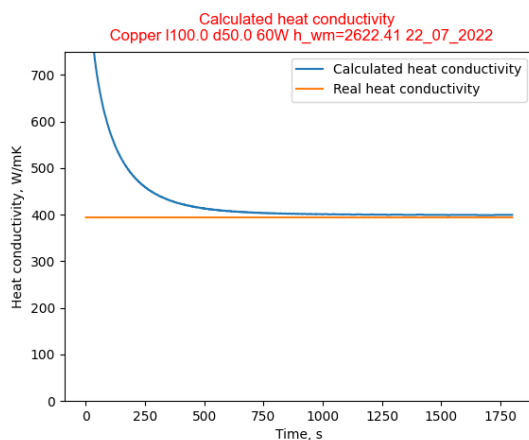
Figure 7. Numerical results - thermal conductivity of copper

Figure 6 shows the values of numerically calculated thermal conductivity for carbon steel as a function of time. At very beginning of the numerical simulation, as the temperature difference of foreheads is increasing, the value of thermal conductivity rapidly reduces. After some 500 s, the rate of change of thermal conductivity reduces, slowly converging to its standard value of 52 W/mK. After 1800 s, nearly stationary state is achieved with insignificant increase in temperature difference between the foreheads of the carbon steel test specimen. The final value of calculated thermal conductivity is almost equal to the standard value for carbon steel of 52 W/mK.

Figure 7 shows the rate of change of numerically calculated thermal conductivity for copper during the duration of numerical experiment, while Figure 8 shows the same for the aluminium test specimen. The same trends, as in case of carbon steel, can be noticed for the copper and aluminium test specimens, where after some 500 s the value of thermal conductivity slowly converges to its standard value of 390 W/mK and 190 W/mK respectively.

Figure 8. Numerical results - thermal conductivity of aluminium

However, compered to carbon steel, thermal conductivity of copper reduces slightly slower by time. This is due to the higher value of thermal diffusivity of copper $(114,11 \times 10^{-6}$ m^2/s) compared to the thermal diffusivity of carbon steel $(13,66 \times 10^{-6}$ m^2/s). For aluminium this effect is less evident, as the thermal diffusivity of aluminium was $78,19 \times 10^{-6}$ m^2/s. It can be concluded that the rate of transfer of heat from the hot end to the cold end of the test specimen affects the rate of change of thermal conductivity primarily in the early stages of experiment. After some 500 s, thermal diffusivity shows insignificant effect on thermal conductivity of the test specimens.

4.   Experimental device and results

4.1. Experimental device

The final design of the experimental device for measuring thermal conductivity is presented in Figure 9. The overall dimensions of the device are $450 \times 300 \times 700$ mm (w × d × h). The electrical heater is placed at the bottom of the main chamber, while the cooler is placed on the top. The cylindrical test specimen is placed between the heater and the cooler, being in direct contact with the source and sink of heat. The cooler is supplied with fresh tap water of constant temperature.

Three test specimens, made of carbon steel, copper and aluminium, were especially prepared to fit the experimental device (cylinders, $\varnothing$ 50 mm × 100 mm). The values of thermal conductivity of the test specimens are defined based on the average values for the selected materials as found in the literature. For placing temperature probes, two opening are made on the side surface of each cylinder, near the bottom and the top. The openings are located at distance of 82 mm. Temperature measurement is performed using two Pt100 temperature probes connected to MAX31865 Pt100 RTD module. The accuracy of the temperature probes is $\pm 0.5°C$.

Heater was made as a cylindrical aluminium block ($\varnothing$ 50 mm × 25 mm) with radially inserted five cylindrical electrical heaters ($\varnothing$ 6 mm × 20 mm) with the total power of 60 W. The power of the electric heater can be regulated from 0 to 60 W using a SSR relay (SSR-25 DD 25A DC-DC Solid State Relay 5V-60VDC output) and a potentiometer that controls the heater's operating time. The supply voltage of the heater is 12 V. The measurement of the power is indirectly enabled by current measurement, using an YHDC Hall Split core current sensor. The accuracy of measurement is ± 1 %.

The main chamber ($\varnothing$ 170 mm × 175 mm) is made of 2,8 mm thick SAE 304 stainless steel. Calcium silicate ($\lambda = 0.12$ W/(m·K) @ 200°C) is used as thermal insulation. The thickness of insulation is 50 mm while its density is 300 kg/m^3.

The cooler is made from cylindrical aluminium block. The fins inside the cooler are specifically arranged in order to generate labyrinth flow of the water and to increase the heat exchange between the cooling water and the specimen cold forehead. The water inlet and outlet are placed on the top of the cooler. Water supplied to the cooler is used directly from the tap. The water flow can be regulated by the valve, while the flow rate is measured by a water flow sensor FS300A G3/4". The water flow can be varied from 0 to 6 litres/min, which directly affects the value of convective heat transfer coefficient (based on calculations, from 0 to 16.000 W/m^{2}K).

Control unit is based on microprocessor technology (microcontroller Arduino Mega 2560). The control unit enables the storage of data measured by the electricity current sensors, temperatures, the flow of cooling water

and the position of the potentiometer for regulating the power of the heater. It is connected to a computer via an USB cable, where using the Python programme, the data read from the sensor are displayed in a diagram on the computer screen and stored in a csv file.

Figure 9.   Experimental device for measuring thermal conductivity

4.2. Experimental results

The measurements of thermal conductivity were conducted using the power of electric heater of 60 W, while the volume flow of cooling water was 3 litres/min. Based on the geometry of the cooler and selected volume flow, calculated value for convective heat transfer coefficient was around 2.622 W/m^{2}K.
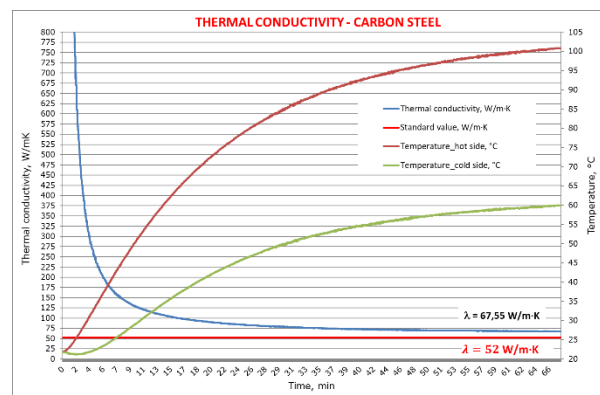

Figure 10. Experimental results – carbon steel

The measurement of main physical parameters in case of carbon steel is presented in Figure 10. Although the numerical experiments showed that the time scale of 1800 s (30 minutes) was sufficient for reaching the stationary state, in case of the physical experiments the duration of measurement was extended to more than 60 minutes. In Figure 10. it can be seen the rate of increase of the temperatures measured on the hot and the cold side of the test specimen. By the end of the experiment, after 60 minutes, the temperature on the hot side has reached some 99°C, while on the cold side it has reached 59°C, resulting in temperature difference of 40°C. The graph shows that the temperatures on the hot and the cold side did not reach the constant values, which applies to the temperature difference as well. Thus, the presented data for carbon steel do not represent the stationary state and further measurement is required. It can be seen that the value of thermal conductivity has decreased significantly until the tenth minute of the experiment, after which it slowly converged to the standard value. Although at the beginning carbon steel has showed high rate of change of thermal conductivity, at the end of experiment the value of measured thermal conductivity (67,55 W/mK) was around 30% higher compared to the standard value (52 W/mK).

The measurement for copper test specimen is presented in Figure 11. By the end of experiment, the temperature on the hot side has reached some 61°C, while on the cold side it has reached 54°C, resulting in temperature difference of 7°C. Compared to carbon steel, the temperatures on the hot and the cold side have almost reached the constant values after 60 minutes, suggesting that materials with higher thermal conductivity need less time for obtaining the stationary state. The value of thermal conductivity has decreased slower compared to carbon steel, due to the higher value of thermal diffusivity of copper. However, at the end of experiment, after 60 minutes, the value of measured thermal conductivity (423 W/mK) was around 8,5 % higher compared to the standard value (390 W/mK).
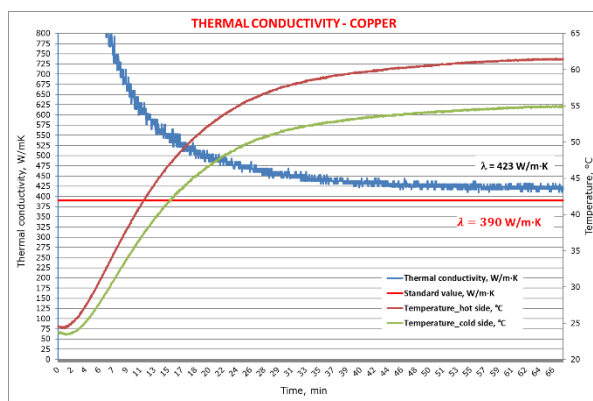

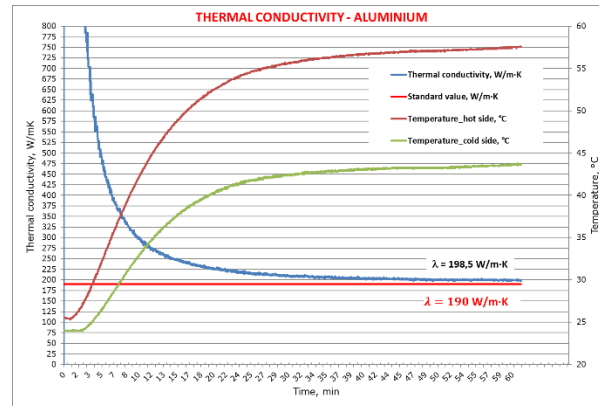**Figure 11.** Experimental results - copper

Figure 12. Experimental results - aluminium

Figure 12. presents the results for the aluminium test specimen. By the end of the experiment, the temperature on the hot side has reached some 57,5°C, while on the cold side it has reached 43,7°C, resulting in temperature difference of 13,8°C. In this case the temperatures on the hot and the cold side did not reach the constant values after 60 minutes, suggesting that further measurement is required in order to obtain the stationary state. The value of thermal conductivity has decreased slower compared to carbon steel but faster compared to copper, due to the intermediate value of thermal diffusivity of aluminium in relation to carbon steel and copper. At the end of experiment, the value of measured thermal conductivity (198,5 W/mK) was around 4,5 % higher compared to the standard value (190 W/mK).

Although it was expected that the discrepancy between the measured and standard value of thermal conductivity will be the smallest for copper, the results suggest that, apart from the thermal conductivity, the thermal diffusivity, density, specific heat capacity and other physical properties should be also considered. Furthermore, the specific technological processes of the metal production have to be taken into account as well.
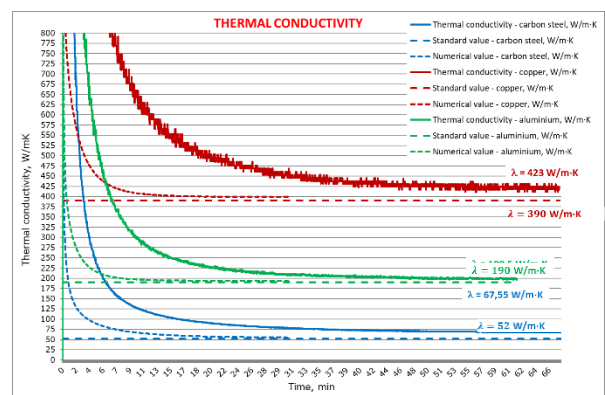

Figure 13. Comparison of experimental and numerical results

Figure 13. gives the overview of measured and numerically calculated thermal conductivity of carbon steel, copper and aluminium, and their relation to the standard values of thermal conductivity. Significant discrepancies are noticeable between numerically and experimentally obtained results suggesting that the existing numerical model underestimates the physical processes involved. This can be due to certain simplifications of the numerical approach, but also due to the physical properties of metals which could not be quantified in the numerical code. This can include the variability of metal structure due to machining and heat treatment of test specimens, and the variability of metal properties within the volume of the test specimen. It can be seen from Figure 13. that materials with higher conductivity exhibit more "noise" when measuring thermal conductivity due to the relatively smaller temperature difference and limited precision of temperature measurement. Finally, since the only purpose of the numerical code was to confirm the validity of the chosen approach in designing the experimental device for measuring the thermal conductivity, the numerical code will not be further developed.

5. Conclusions

The presented numerical analysis proved to be very useful tool in analysing the performance of theoretical experimental device for measuring thermal conductivity of metals, and for confirming the validity of the proposed conceptual design. The knowledge gained from the numerical analysis has been applied during the construction of the experimental device. The performance of the experimental device has met the expectations and it is already in use for educational purposes. In order to reduce the influence of thermal resistance, due to surface roughness and oxide layer formed on the surface of the metal, further analysis will include the application of a thermal paste on the contact surfaces between the test specimen and the heater and the cooler. The additional possible improvement can include the use of smaller temperature sensors and thus the smaller openings for inserting the sensors into the test specimen, in order to minimise the influence of thermal resistance of air.

Finally, the future perspectives will include the measurement of thermal conductivity of certified test samples in order to confirm the reliability of the experimental device for measuring thermal conductivity of metals.

REFERENCES

[1] Whaley, A. C., 2008. *Experimental Measurement of Thermal Conductivity of an Unknown Material*, Master's Thesis, University of Tennessee,

[2] Slifka, A. J., 2000. Thermal-Conductivity Apparatus for Steady-State, Comparative Measurement of Ceramic Coatings, Journal of Research of the National Institute of Standards and Technology. 105 (4), 591-605.

[3] Boulaoued, I., Amara, I., and Mhimid, A., 2016. Experimental Determination of Thermal Conductivity and Diffusivity of New Building Insulating Materials, International Journal of Heat and Technology, 34 (2), 325-331.

[4] Yunus, C., Afshin, G., 2015. *Heat and Mass Transfer: Fundamentals and Applications*, Fifth Edition in SI Units, McGraw-Hill Education, New York

[5] Python Software Foundation, www.python.org

[6] Gabrić, I., Jankoski, Z. 2020. The Numerical Modelling of Experimental Device for Measuring Thermal Conductivity of Metals, Contemporary issues in economy and technology – CIET 2020, Split, Croatia

The synthesis of microporous magnesium-based solids for reversible hydrogen storage

Jaroslav JERZ[1],
Arun GOPINATHAN[1, 2],
Jaroslav KOVÁČIK[1]

1) Institute of Materials and Machine
   Mechanics, Slovak Academy of Sciences,
   Dúbravská cesta 9/6319, 845 13 Bratislava,
   Slovakia

2) Faculty of Materials Science and
   Technology, Slovak University of
   Technology,
   Jána Bottu 2781/25, 917 24 Trnava,
   Slovakia

ummsjerz@savba.sk
arun.gopinathan@savba.sk
ummsjk@savba.sk

Keywords

Hydrogen storage
Additive manufacturing
Magnesium hydrides
Powder metallurgy
3D printing

Professional paper

Abstract: The technical concepts of building cladding structures used in the current construction industry are often associated with inappropriately chosen materials for façade and roofing systems. These environmentally unsuitable building solutions, therefore, causes excessive and uneven overheating of the earth's surface by the Sun and thus strongly supports the acceleration of the current rapid climate change.

However, thermochemical sorption long-term heat storage techniques have the great potential to store vast amounts of energy in the form of low potential heat obtained from summer solar energy surpluses.

This paper describes the practical applications of the system for storing summer solar energy surpluses based on the thermochemical reaction – dehydration of the mixture comprising metal halide hydrates and biomass, including the possibility to synthetize metal hydride powders characterized by an excellent ability to store reversibly hydrogen. The waste ash after the combustion of said mixture of dehydrated biomass and chemical compounds is used for this purpose as well. The ability to store reversibly hydrogen without structural degradation is sufficient by magnesium based hydrides, such as $Mg(BH_4)_2$, Mg_2CoH_5, $Mg(NH_2)_2$, $Mg(AlH_4)_2$, etc. The breakthrough solution proposed by this contribution is based on an innovative approach of metal hydrides synthesis by powder metallurgy, by which recycled waste ash from combustion of solid biomass enriched with dehydrated metal halide hydrates is admixed during preparation of industrially viable Mg-based microporous solids for reversible hydrogen storage using additive manufacturing technique.

1. Introduction

The global energy needs drastically increased from 5×10^3 TWh per year in 1860 to 1.6×10^5 TWh per year nowadays [1]. A fraction bigger than 93% of World's primary energy consumption originates from fossil fuels, such as oil, gas and coal (Fig. 1). The reserves of these fuels are depleting extremely quickly. The concentration of greenhouse gasses is due to their excessive compustion constantly increasing, therefore a varios a new energy concepts based on renewable sources and carriers are necessary.

Hydrogen seems to be a very promising energy carrier in a clean energy scenario. However, curently generally used hydrogen storage methods, such as compressed gas or liquefied hydrogen, cannot meet the target requirements set for the future use. Storage in the solid state, such as by means of metal hydrides, has great potential in comparison to other storage methods despite the fact that gravimetric and volumetric capacities are still some of the main issues for industrial applicatons of hydrogen storage technologies.

This contribution describes recent advancements resulting from the possibilities of using thermochemical storage of energy in combination with extremely efficient aluminium foam heat exchangers impregnated by Phase Change Materials (PCMs) repeatedly allowing to store latent heat of phase transformation during melting and to dissipate it during solidification of PCMs to the vicinity of the heat exchanger. The solar energy harvesting using a thermally active heat exchanger covering the entire sloping roof of the building allows to dissipate undesirable heat to the building's surroundings during cold summer nights when the need arises. Moreover, the use of interior ceiling panels made of aluminium foam impregnated with PCMs allows to reduce significantly the costs of maintaining sufficient thermal comfort.

The seasonal storage of summer solar energy surpluses based on the thermochemical reaction – dehydration of the mixture comprising metal halide hydrates and biomas allows to synthetize metal hydride powders characterized by ability to store reversibly hydrogen or methane. The waste ash after the combustion of said mixture of dehydrated biomass enriched with dehydrated metal halide hydrates is used for this purpose.

2. Innovative potential to increase energy efficiency

The energy efficiency, e.g. the amount of energy used per unit of product (building construction, materials, equipment, etc.), is determined by improvements in energy conversion and reductions in energy use for environmental control.

The energy efficiency of a building is the extent to which the energy consumption per square meter of floor area of the building measures up to established energy consumption benchmarks for that particular type of building under defined climatic conditions. Comparisons with simple benchmarks of annual energy use per square metre of floor area ($kWh/(m^2 \cdot annum)$) allow the standard of energy efficiency to be assessed and priority areas for action to be identified.

The annual energy use per square meter of floor area can be significantly reduced if:

- thermo-active roofing is capable of recovering the heat from solar gains as well as dissipating excessive summer heat surpluses,
- ceiling heat exchangers impregnated by Phase Change Materials (PCMs) are able to maintain sufficient thermal comfort in the interior in an energy-efficient way,
- collector working on the principle of thermochemical reaction incorporated into the air-handling system allows the seasonal storage of low-potential heat obtained from summer heat surpluses (Fig. 2). [7]

Thermochemical heat storage systems can provide very high energy densities. Various economic systems with the right choice of materials based on carbonation, oxidation, hydratation and hydrogenation reactions are therefore currently receiving a great deal of attention from scientific community.

3. Seasonal energy storage using a thermochemical reaction

Seasonal storage of summer solar energy surpluses is based on the thermochemical reaction – dehydration of the mixture comprising metal halide hydrates and biomass. The device for thermochemical storage of summer energy surpluses uses aluminum foam heat exchangers impregnated by paraffin wax-based PCM, which provide the ability short-term to store and release large amount of latent heat during their phase change from solid to the liquid stage and vice versa at a nearly constant temperature.

Waste ash from combustion of solid biomass enriched with dehydrated metal halide hydrates can be used as:

- an alkaline calcium-potassium fertilizer with a high biological value effectively reducing the undesirable acidification of agricultural land without excessively increasing the concentration of nitrates in the soil and groundwater,

- an additive during preparation of industrially viable magnesium-based hydrides, such as $Mg(BH_4)_2$, Mg_2CoH_5, $Mg(NH_2)_2$, $Mg(AlH_4)_2$, etc. for reversible hydrogen or methane storage.
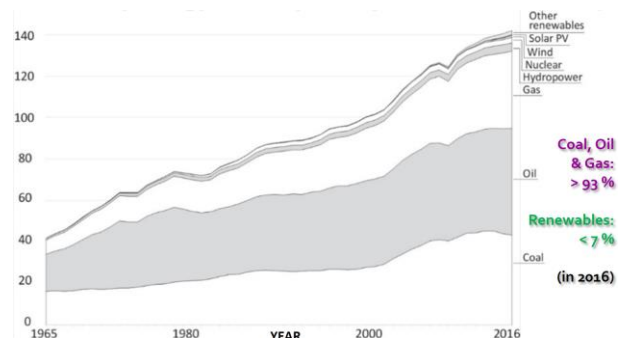
Figure 1. Primary energy consumption by source, World in PWh. [6]
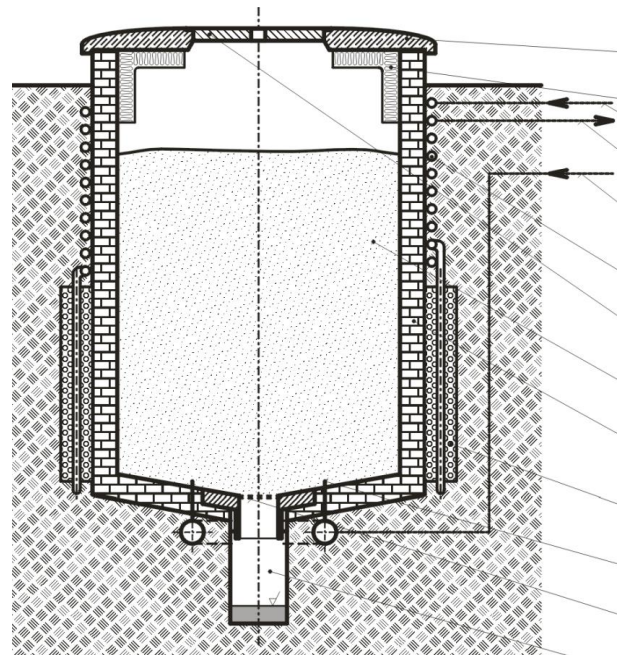
Figure 2. A device for seasonal energy storage using a thermochemical reaction of mixture containing metal halide hydrate and biomass [7].

4. Metal hydrides synthesis for hydrogen storage

Recently, alkali intercalated fullerides have been attracted some interest in the field of solid energy storage, for their ability to reversibly absorb hydrogen with favourable binding energies. The storage mechanism occurs through the chemical bond of H atoms on the C_{60} molecule (formation of the hydrofullerene $C_{60}H_x$).

Theoretical studies have shown [8] that metal-decorated fulleride $Li_{12}C_{60}$ may absorb up to 13.5 wt.% H_2. Practically $Li_{12}C_{60}$ is able to absorb ~ 4.5 wt.% H_2 at 225°C (5 wt.% H_2 at 350 °C).

Some common solid ammonia containing systems find direct use of hydrogen storage materials:

- ammonia borane (NH_3BH_3): 19.6 wt.% H_2
- ammonia complexes of borohydrides:
  $LiBH_4 \cdot nNH_3$: 18 wt.% H_2
  $Mg(BH_4)_2 \cdot nNH_3$: 16 wt.% H_2

The thermal decomposition usually causes in these compounds the recombination of the N–H and B–H groups (followed by H_2 emission), rather than the release of pure ammonia.

However, since all these methods of hydrogen storage are very expensive due to extremely high production costs of the mentioned chemical compounds, the ways of preparation materials capable of repeatedly storing hydrogen, which would be industrially feasible, are intensively investigated.

From this point of view the great application potential can be expected from powder-metallurgical approach to synthesis of magnesium-based hydrides for hydrogen or methane storage. This technique consist of admixing of recycled waste ash from combustion of solid biomass enriched with dehydrated metal halide hydrates and subsequent preparation of Mg-based microporous solids for reversible hydrogen storage using additive manufacturing technique, such as hot lithography. Obtained microporous polymeric matrix composite reinforced by particles of appropriate magnesium alloys and powders of alloying elements is subsequently sintern under inert argon atmosphere in order to prepare suitable microporous solid for repeatable hydrogen storage.

5. Conclusions

- Development of a system based on solid-state hydrogen storage materials has been actively undertaken in order to solve a current low volume storage density problem of a high-pressure gaseous hydrogen storage system.
- Various complex hydrides based on a metal hydride are excellent in reversibility of hydrogen release and storage reaction, but have a difficulty in practical usage because they are operated at a high temperature and need a continuous heat supply for the hydrogen release.
- The improvements in minimizing the amount of heat needed to operate the solid-state hydrogen system and improving the weight storage capacity are required.

Acknowledgments

REFERENCES

[1] Jepsen, J., et al., 2020. Fundamental Material Properties of the 2LiBH$_4$-MgH$_2$ Reactive Hydride Composite for Hydrogen Storage: (I) Thermodynamic and Heat Transfer Properties. Energies, 11(5), 1081.

[2] Jerz, J., Simančík, F., Španielka, J., Šebek, J., Kováčik, J., Tobolka, P., Dvorák, T., Orovčík, Ľ., 2018. Energy demand reduction in nearly zero-energy buildings by highly efficient aluminium foam heat exchangers. Materials Science Forum. 919, 236-245.

[3] Jerz, J., Simančík, F., Kováčik, J., Španielka, J., *Aluminium foam for thermo-active pitched roofs of nearly zero-energy buildings*. 2017. 7th International Conference Mechanical Technologies and Structural Materials 2017. – Split: Croatian Society for Mechanical Technologies, 49-58. Split, Croatia

[4] Jerz, J., Gopinathan, A., Kováčik, J, 2021. *Phase Change Materials Reinforced with Aluminium Foam for Latent Heat Storage.* In: Vid. Proc. Adv. Mater., Volume 2, Article ID 2021-0146, DOI: 10.5185/vpoam.2021.0146. (https://www.proceedings.iaamonline.org/article/vpoam-2021-0146)

[5] Gopinathan, A., Jerz, J., Kováčik, J., Dvorák, T., 2021. Investigation of the Relationship between Morphology and Thermal Conductivity of Powder Metallurgically Prepared Aluminium Foams. Materials. 14, no. 3623.

[6] https://ourworldindata.org/energy-production-and-changing-energy-sources (accessed 13 March 2022).

[7] Jerz, J., 2021. SK Patent Application PP 61-2021, A device for seasonal energy storage using a thermochemical reaction and the use of the obtained dehydrated mixture containing metal halide hydrate and biomass.

[8] Aramini, A. et al., 2013. Addition of transition metals to lithium intercalated fullerides enhances hydrogen storage properties. Int. J. of hydrogen energy. 39, 2124-2131.

Selection of optimal die casting process parameters based on simulation and genetic algorithms

Sonja JOZIĆ[1), **Dražen BAJIĆ**[1), **Ivana DUMANIĆ**[1), **Brigita LJUBA**[1)

1) Faculty of Electrical Engineering,
   Mechanical Engineering and Naval
   Architecture, University of Split
   Ruđera Boškovića 32, 21 000 Split,
   Croatia

Sonja.Jozic@fesb.hr
Drazen.Bajic@fesb.hr
Ivana.Dumanic.00@fesb.hr
Brigita.Matic.01@fesb.hr

Keywords

High-pressure die casting
Mould
Optimization
Simulation
Aluminum alloy

Abstract: High pressure die casting is a common process for manufacturing structural components from non-ferrous metals with a low melting point. Process is particularly suitable for large-scale castings production with complex geometry. There are many features affecting the complexity of the process. It is of great importance for engineers to optimize process parameters and improve casting quality. In this paper, design and implementation of predictive models developed for improving the quality of aluminum die castings are presented. The goal is minimizing material shrinkage and solidification time. Design of experiments were obtained using the Box-Behnken method, and experiments were made in virtual environment, i.e. in NovaFlow&Solid software. Regression analysis and analysis of variance were used for obtaining mathematical models. Optimization of mathematical models was performed using genetic algorithms. Optimal values of input parameters are preheating mould temperature of 150 °C, velocity of piston of 2.5 m/s and injection pressure of 49.2 MPa.

1. Introduction

High pressure die casting (HPDC) is a process of molten metal injecting at high speed and high pressure into permanent mould. The pressure in the mould is maintained until the casting solidification is completely finished. The mould is made of material that is highly resistant to heat and wear, and is designed to allow the production of geometrically complex castings with a high degree of dimensional accuracy. High pressure die casting is used in a serial and mass production of castings. Excellent surface quality and high precision are the main features of castings produced by high pressure die casting. The process is very productive; the price of one casting is acceptable even though the mould is very expensive. Due to the above characteristics, more than 50 % of all castings of aluminium alloys are produced by HPDC. In order to obtain a quality casting, it is necessary to properly design the mould and its components as well as to adjust the technological parameters that affect the final properties of the casting, [1]. Those parameters are: alloy and mould materials, mould preheating temperature, ejection force and time, injection speed in the first phase, injection pressure in second phase, piston diameter etc. The temperature of the mould and the temperature of the molten metal that flows into it have a very important influence on the mould life during the process, [2]. The high temperature of the mould prolongs the solidification process, which prolongs the cycle itself, while the cold mould will cause surface defects. Based on the research in the literature, the optimal preheating temperature of the mould for aluminium alloys is from 180 °C to 300 °C, [3], [4].

If the mould temperature is less than the optimal range, the probability of errors and pore appearance increases. Aghion et al. [5] investigated the relationship between the characteristics of high-pressure die casting and the mechanical properties of casting. They reported about the close connection between microstructure and properties of alloy and process parameters as well. The greater the wall thickness, the lower the tensile strength and yield strength, while the elongation increased proportionally. The wall thickness of the casting also affects the porosity and grain size, the thicker wall reduces the occurrence of porosity and increases the grain, but also prolongs the cooling time. Molten metal flow velocity has a significant influence on the alloy microstructure, and consequently on mechanical properties of the casting, [6], [7]. In order to achieve the best possible properties of high-pressure die castings, it is necessary to adjust the parameters that affect the quality of the casting, namely: casting alloy, die casting machine, pouring temperature, melt pressure, molten metal flow velocity in all stages of the process etc [8], [9].

2. Parameters of high pressure die casting process

In order to obtain a satisfactory quality casting, the proper dimensioning of the gating system was performed in this paper. After investigating the influences of technological parameters and properties of aluminium alloys, three input parameters were selected, the action of which was monitored through the conduction of virtual experiments, i.e. simulations in program NovaFlow&Solid. Simulations were carried out according to the adopted Box-Behnken design of experiments and three input parameters were: mould preheating temperature, velocity of piston in second phase and injection pressure (melt pressure in third phase). NovaFlow&Solid is designed to simulate high pressure die casting process and many others commercial casting method. As output process values, obtained by the simulations, were chosen the material shrinkage and solidification time. Regression analysis was used to achieve mathematical models, and then optimal values of the input parameters that will ensure the production of high-quality castings has been determined. Based on the obtained simulation results, the influence of individual parameters will be explained and the conclusion of the conducted process will be made.
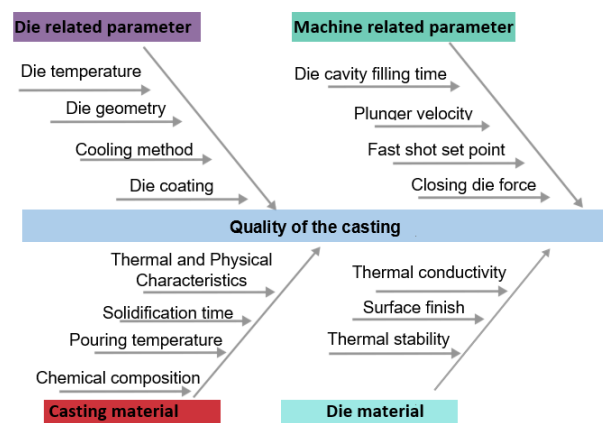
The high pressure die casting process consists of the following operations: closing the mould, filling the pressure chamber with melt, starting the piston, pushing the melt into the mould, opening the mould and ejecting the casting. The HPDC process, in the narrow sense, can be divided into three phases in which the action of the speed and pressure of the molten metal will be described. Their dependence is shown in Figure 1., and all phases will be explained below.
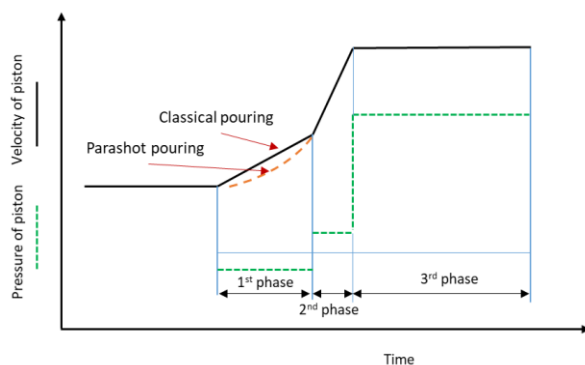
Figure 1. Schematic representation of the piston pressure dependence on the process flow by phases, [10]

In the first phase of HPDC process, it is necessary to expel air from the pressure chamber, so the piston must move at relatively low speeds. The speed in this phase ranges from 0.05 m/s to 0.5 m/s. At higher speeds, there would be a turbulent flow of molten metal that would draw air into the mould causing a danger of the melt splashing through the pouring hole and later the porosity in the casting. In order to avoid this problem, the so-called „parashot pouring" is applied in which no shock wave is created because the speed of piston gradually increased and followed the speed of the molten metal. In addition to the piston speed, the formation of the wave and the trapping of air inside the pressure chamber are also influenced by the filling of the pressure chamber with melt, and dimensions of the gate cross-section, [11]. The second phase of HPDC process is called the "fast phase" because the molten metal must fill the mould cavity through the gate as soon as possible. In the second phase, it is necessary to determine the maximum speed that will ensure the required properties of the casting. High speeds are mainly used for the production of thin-walled castings to achieve better surface quality and result in less porosity. Increasing the speed increases the dynamic pressure of the melt on the tool, which damages it, and increasing the pressure can cause the mould to open, which leads to the spraying of the molten metal.

When the mould cavity is filled with melt, the third phase of the high-pressure casting process begins. In this phase, a controlled increase in pressure occurs in order to obtain better mechanical properties, lower porosity and better surface quality of the casting. The parameters that affect the pressure at this stage are the type of casting, the closing force of the machine and the type of alloy. In order to avoid undesirable reactions during the process, the beginning of the third phase must be 0.1 to 0.6 seconds after filling the mould with molten metal.

Figure 2 Ishikawa diagram of technological parameters

In the HPDC process, one of the main elements is the mould and its temperature is one of the basic parameters that ensure safe operation. The mould temperature for high-pressure die casting depends on the molten temperature and specific heat of the alloy being poured, the productivity of the machine, the ratio of melt mass to mould mass, and the cooling efficiency of the mould. Ishikawa diagram, showed in figure 2., containing all the

features that can lead to the consequence/problem being analysed, all with the aim of improving and enhancing the process in an organization or experiment. Diagram graphically illustrates the relationship between a given output and all the factors that affect the output. The visual representation of the causes, which this method provides, facilitates the analysis of their mutual relationship and significance.

3.   Virtual experiments and methodology

In this paper importance is given to the parameter design stage. The basic steps to investigate the role of process parameters and mould geometry in level of shrinkage defects and solidification time, are summarized as follows:

- selection of the most significant die casting parameters influencing on the shrinkage and solidification time,
- selection of the appropriate design of experiments,
- performing simulation of the die casting process under the experimental conditions dictated by the chosen design of experiments,
- collection and analysis the data and
- making decisions regarding optimum setting of control parameters.

Solid modelling of the two castings, showed in Figure 3., was conducted by means of CATIA V5, commercial modelling program. The other necessary parts for HPDC process such as biscuit, runners, gates and overflows were also modelled and showed in figure 3. The casting material is aluminium alloy AlSi12 (Fe) or according to the European standard EN AC - 44300. The mentioned alloy is an eutectic alloy with excellent casting properties with high chemical resistance.

Design of experiments is carried out using the Box-Behnken design. The number of required experimental points is given by Equation 1.

$$N = 2k \cdot (k - 1) + n_0 \qquad (1)$$

k - number of different experimental factors,

n_0 - number of repetitions of the experiment at the intermediate level.

The experimental design for three controllable variables with their maximal and minimal values are presented in Table 1, and is organized by the Box-Behneken design of experiments.

Table 1.   The experimental factors and their levels

| Levels of input variables	Preheating mould temperature [°C] **A**	Velocity of piston, v_{II} [m/s] **B**	Injection pressure, p [MPa] **C**
1	150	2.5	40
2	200	5.25	60
3	250	8	80

Experimental runs with results are given in Table 2.

Two process variables were read from the report obtained at the end of the simulation, i.e. after each virtual experiment. Experimental results were inputted into computer software Design-Expert. Statistical processing of data was carried out resulting in mathematical models for shrinkage and solidification time.

Linear mathematical model for material shrinkage, was suggested and analysis of variance (ANOVA) indicated that all three input variables are insignificant model terms. R-Squared, Adj R-Squared, Pred R-Squared and Adeq Precision were obtained as 0.9496, 0.68, 0.51 and 10.2, respectively.

Table 2.   Design of experiments and experimental results

Nr	A [°C]	B [m/s]	C [MPa]	MS [%]	ST [s]
1	200	5.25	40	1.98	8.04
2	200	5.25	40	1.98	8.04
3	150	5.25	20	2.35	7.32
4	150	2.5	40	1.82	7.75
5	200	5.25	40	1.97	8.04
6	200	5.25	40	1.97	8.04
7	200	8	60	1.66	8.04
8	250	5.25	20	2.41	9.09
9	200	2.5	20	1.99	8.44
10	150	8	40	2.00	7.18
11	200	5.25	40	1.97	8.04
12	200	8	20	2.39	7.91
13	250	2.5	40	1.91	9.54
14	200	2.5	60	1.51	8.49
15	250	5.25	60	1.64	9.12
16	250	8	40	2.05	9.11
17	150	5.25	60	1.63	7.51
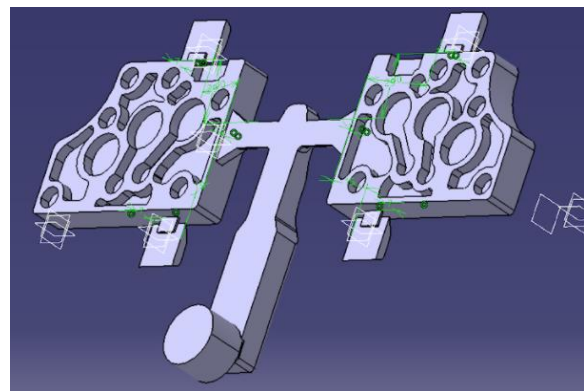
**Figure 3.**   Model of castings made in CATIA V5

Mathematical model for material shrinkage, MS

Linear mathematical model was adopted in a form:

$$MS = 2.32648 + 4.97500E\text{-}004 \cdot A + 0.039727 \cdot B - 0.016906 \cdot C \qquad (2)$$

In Figure 4, it can be noticed that at the lowest values of mould preheating temperature and velocity of piston (in the second phase) is the lowest percentage of material shrinkage. and in proportion to their growth. the percentage of material shrinkage increases, reaching its maximum value of 2.41%.

Figure 5, showed that at the lowest values of the velocity of piston and the highest value of the injection (third phase) pressure results in the lowest percentage of material shrinkage. The lowest injection pressure and the highest velocity of the piston, results in the reaching maximum value of material shrinkage, 2.41%.
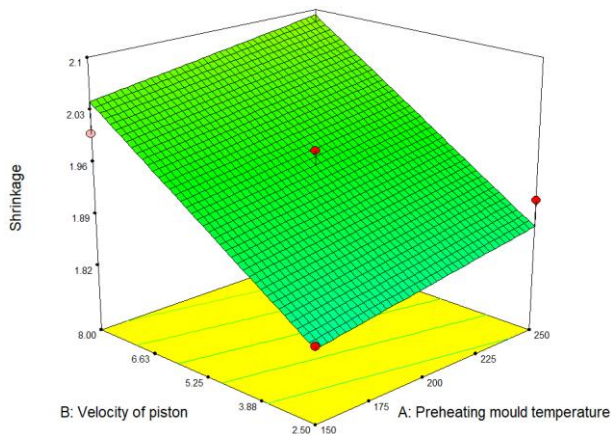
Figure 4.   Influence of velocity of piston in second phase and preheating mould temperature, injection (third phase) pressure constant [40 MPa]
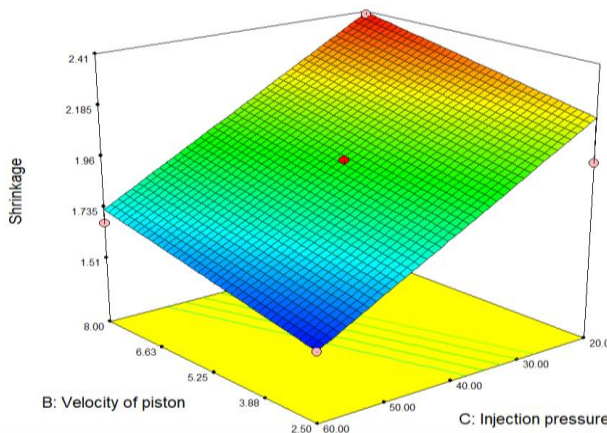
Figure 5.   Influence of velocity of piston in second phase and injection (third phase) pressure, constant preheating mould temperature [200 °C]

In Figure 6, it can be seen that at the lowest values of the injection pressure and the mould preheating temperature is the lowest percentage of material shrinkage, and with their growth, the percentage of material shrinkage increases to its maximum value of 2.41%.

Mathematical model for solidification time, ST

Quadratic mathematical model was suggested for solidification time *ST,* and ANOVA showed that A, B, C, A^2 and B^2 are significant factors model terms.

Figure 6.   Influence of preheating mould temperature and injection (third phase) pressure, constant velocity of piston in second phase [5.25 m/s]

After insignificant factors were excluded equation for prediction of solidification time, ST, was adopted in a form:

$$ST = 8.82226 - 0.015550 \cdot A - 0.3511 \cdot B + 5.77330E - 003 \cdot C + 8.47500E - 005 \cdot A^2 + 0.019322 \cdot B^2 \qquad (3)$$

R-Squared. Adj R-Squared. Pred R-Squared and Adeq Precision were obtained as 0.9968. 0.9926. 0.9482 and 51.448. respectively.

Figures 7. 8. and 9. show the dependence of the mathematical model of three input variables.

Figure 7.   Influence of velocity of piston in second phase and preheating mould temperature, injection (third phase) pressure constant [40 MPa]
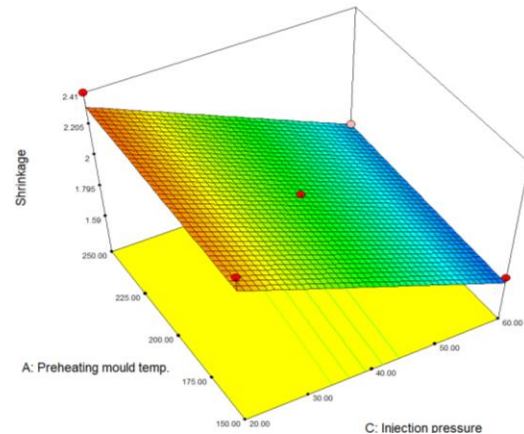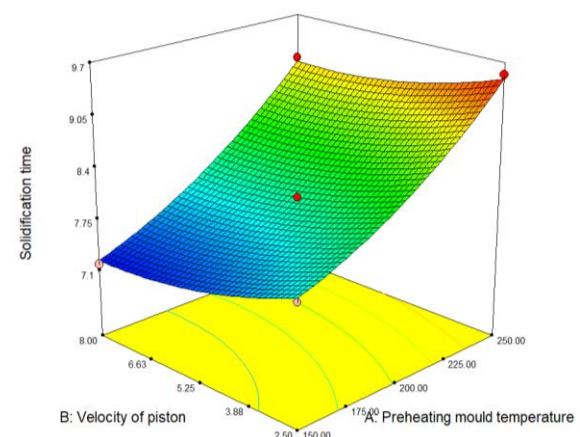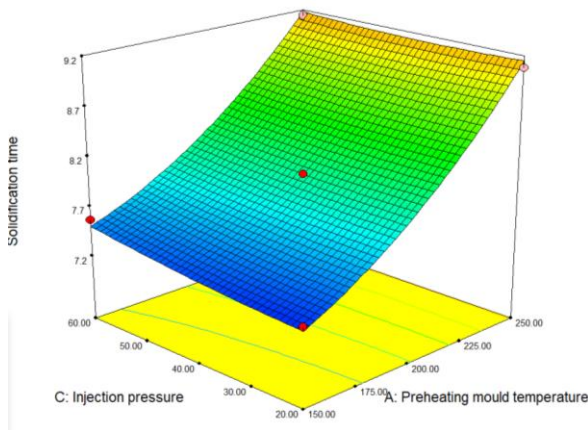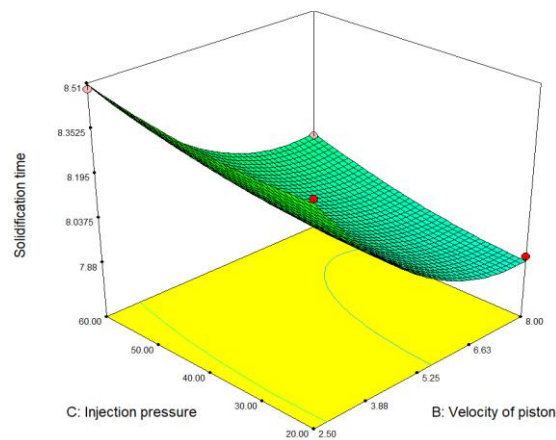
Figure 8. Influence of preheating mould temperature and injection (third phase) pressure, constant velocity of piston in second phase [5.25 m/s]

Figure 9. Influence of velocity of piston in second phase and injection (third phase) pressure, constant preheating mould temperature [200 °C]

After the mathematical models of the observed output quantities have been obtained, it is necessary to optimize and determine the values of the input parameters that will give the smallest material shrinkage and the shortest solidification time.

The objective function for a given problem is shown as follows:

$$\min(fx) = \sum \frac{w_i \sqrt{f_i^2}}{c} \qquad (4)$$

where are:

w_i- weight factor
$f(x)$ - objective function
f_i - i-th mathematical model
C – target value of the i-th mathematical model

The optimization was performed using genetic algorithm in software package MATLAB 2021. The subject of optimization are two mathematical models that describe the dependence of material shrinkage and solidification time on mould temperature, velocity of piston in second phase and injection (third phase) pressure. The goal of optimization is to obtain optimal process input parameters (Table 3) which would provide the smallest shrinkage of material and shortest solidification time.

Table 3. Optimal values input parameters

Optimal values of input parameters	
Preheating mould temperature [°C]	150
Velocity of piston. v_{II} [m/s]	2.5
Injection pressure. p [MPa]	49.2

The simulation provides useful information about the casting process and it is possible to monitor the movement of the melt and check the correctness of the mould construction. After the simulation. performed with the optimal parameters given in Table 3. the values of the output parameters were obtained: material shrinkage 1.60% and solidification time 7.746 s.

In Figure 10. the shrinkage of the material. after filling the mould cavity. is shown. Figure 11. shows the simulation predictions about the places of probable porosity occurrence. It can be seen that both shrinkage and porosities mostly occur in added parts i.e. overflows, (marked in red) which should be removed after the process.
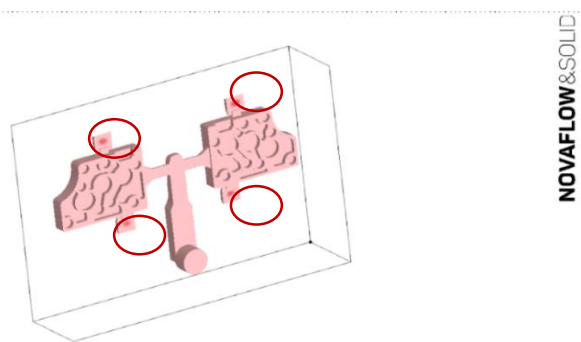
Figure 10. Shrinkage of material
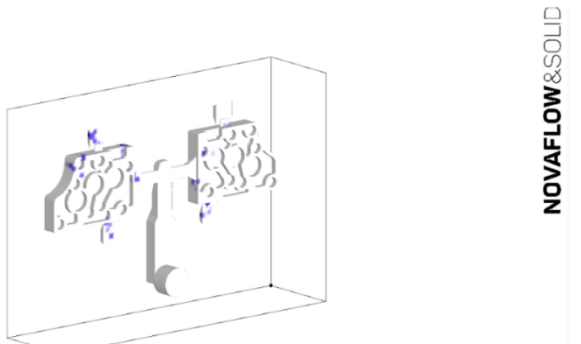
Figure 11. Porosities in the castings

4. Conclusions

Nowadays, the general requirements are for the products to be as high quality as possible and the production process to be as short as possible. Therefore, optimizing the production process and applying computer simulations is very important to achieve better productivity. To perform the casting process, it was first necessary to model the casting in some 3D modelling software such as CATIA program (V5). Dimensions and geometry of casting, together with the entire inflow system, are determined by calculating. Subsequently, the input parameters of the casting process were selected based on research in the literature, which were considered to have a significant impact on the final properties of the casting. Simulations were then performed to confirm the correctness of the inflow system. The mentioned simulations were performed in the NovaFlow&Solid program. During the simulations, the whole casting process was monitored and the occurrence of errors was monitored, after which two output variables were selected whose values were recorded. The output parameters that were monitored were material shrinkage (MS) and solidification time (ST). Experimental results were processed by regression analysis and mathematical models were obtained to predict the two mentioned output variables.

After that, optimization was performed in order to determine the input parameters that will ensure the lowest material shrinkage and the shortest solidification time. The optimal input parameters were: preheating mould temperature 150 °C, velocity of piston 2.5 m/s and injection pressure 49.2 MPa. The values of the output parameters were obtained by process simulation with mentioned input parameters as: material shrinkage 1.60% and solidification time 7.746 s. According to the simulation results, it was observed that the geometry of the inflow system and the limit values were chosen correctly because most of the errors occurred in the overflows which have to be removed when the process is finished.

REFERENCES

[1] Anglada, E., Meléndez, A., Vicario, I., Arratibel, E., Cangas, G., 2015. Simplified Models for High Pressure Die Casting Simulation. Procedia Eng., 132, 974–981, doi: 10.1016/j.proeng.12.585.

[2] Gunasegaram, D., R., Finnin, B., R., Polivka, F., B., 2007. Melt flow velocity in high pressure die casting: Its effect on microstructure and mechanical properties in an Al-Si alloy. Mater. Sci. Technol., 23(7), 847–856.

[3] Sadeghi, M., Mahmoudi, J., 2012. Experimental and theoretical studies on the effect of die temperature on the quality of the products in high-pressure die-casting process, Adv. Mater. Sci. Eng., doi: 10.1155/2012/434605.

[4] Suraj, R., Marathe, D., Carmo Quadros, D., R., 2020. Thermal Factor of Aluminium High pressure Die Casting Container (Mould) to achieve Six Sigma Quality of Castings, Int. J. Eng. Res., 9(4), 59–68.

[5] Aghion, E., Moscovitch, N., Arnon, A. 2007. The correlation between wall thickness and properties of HPDC Magnesium alloys, Mater. Sci. Eng. A, 447(1–2), 341–346.

[6] Ma, C., Zhang, W., YU., Zhang, Z., Ma, Y., Xiong, S., 2021. The effect of slow shot speed and casting pressure on the 3D microstructure of high pressure die casting AE44 magnesium alloy, J. Magnes. Alloy.,
doi: 10.1016/j.jma.2021.09.011.

[7] Li., Z., Li., D., Zhou, W., Hu, B., Zhao, X., Wang, J., Qin, M., Xu, J., Zeng, X., 2021. Characterization on the formation of porosity and tensile properties prediction in die casting Mg alloys, J. Magnes. Alloy,
doi: 10.1016/j.jma.2020.12.006.

[8] Jadhav, A., R., Hujare, D., P., Hujare, P., P., 2021. Design and optimization of gating system, modification of cooling system position and flow simulation for cold chamber HPDC machine, Mater. Today Proc, 46, 7175–7181.

[9] Li, H., 2020. Towards intelligent design optimization: Progress and challenge of design optimization theories and technologies for plastic forming, Chinese J. Aeronaut., 34(2), 104–123.

[10] Mikell P. Groover, 2020. *Fundamentals of Modern Manufacturing Materials, Processes, and Systems Seventh Edition*, Wiley

[11] Mehtedi, M. El., Mancia, T., Buonadonna, P., Guzzini, L., Santini, E., Forcellese, A., 2020. Design optimization of gate system on high pressure die casting of AlSi13Fe alloy by means of finite element simulations, Procedia CIRP, 88, 509–514.

The solidification sequence and microstructure development of secondary EN AC 46100 alloy

Franjo KOZINA[1], *Zdenka ZOVKO BRODARAC*[1], *Mario STJEPANOVIĆ*[2]

1) University of Zagreb Faculty of Metallurgy
    Aleja narodnih heroja 3, 44000 Sisak,
    Croatia
2) Lipovica d.o.o.
    Lipovečka 22, 44317 Popovača, **Croatia**

fkozin@uizg.simet.hr
zovko@unizg.simet.hr
mario.stjepi@gmail.com

Keywords

EN AC 47100
Secondary material
Recycling
Microstructure development
Solidification sequence

Original scientific paper

Abstract: The main challenges in the production and utilization of secondary aluminum alloys are achieving the targeted chemical composition and controlling the level of impurity elements. Those challenges originate from the accumulation of trump elements such as silicone, magnesium, nickel, zinc, lead, chromium, iron, copper, vanadium, and manganese during recycling. The inability to achieve targeted chemical composition negatively impacts the secondary alloy properties and hinders its use in the safety-critical applications. Despite the fact that there are a variety of solutions to lower the negative impact of trump elements, each of them represents a trade-off between the coast and the recycling potential. The research was performed to estimate the influence of excess Mg and Zn on solidification sequence and microstructure development of secondary EN AC 46100 alloy. The investigation comprehended determination of chemical composition, equilibrium and non-equilibrium solidification sequence using Thermo-Calc software support as well as metallographic analysis. Based on the obtained results, it was concluded that the excess amounts of magnesium and zing led to the solidification and precipitation of complex phases, mainly Q-$Al_5Cu_2Mg_8Si_7$, π-$Al_8FeMg_3Si_6$ and $Al_5(Cu,Zn)_6Mg_2$ that are not characteristic for EN AC 46100 type alloy.

1. Introduction

The increasing global demand for aluminum (Al) alloys has led to the significant growth of secondary Al production and emphasized the importance of sustainable management of Al scrap [1]. Compared to the other high-volume materials, such as copper (Cu), zinc (Zn), magnesium (Mg) and steel, the Al production has one of the widest energy differences between the primary and secondary routes [2]. When compared to the primary Al production, the Al recycling allows for the 95 % energy reduction and emits only 5 % greenhouse gases [3]. Furthermore, one ton of recycled Al saves up to 8 metric tons of bauxite, 14 000 kWh of energy, 6 300 liters of oil, 7.6 cubic meters of landfill with the average total exhaust emission of 350 kg of carbon dioxide (CO_2) [4]. However, the share of secondary Al production with respect to the total one is about 35 %. Today, the materials with the highest recycled fraction are Cu and steel at about 40 % [5].

The main challenges in the production and utilization of secondary Al alloys are achieving the targeted chemical composition and controlling the level of impurity elements. Those challenges originate from the recycling of different Al alloys containing different alloying elements in different amounts, as well as the accumulation of trump elements such as silicone (Si), Mg, nickel (Ni), Zn, lead (Pb), chromium (Cr), iron (Fe),

copper (Cu), vanadium (V), and manganese (Mn) [6]. Inability to achieve targeted chemical composition results in the alteration of secondary alloy properties hindering its use in the safety-critical applications [7]. As a major alloying elements, Si, Mg, Cu and Zn have the highest solid solubility in Al solid solution (α_{Al}) and a strengthening effect obtained through the solid solution hardening and second phase precipitation. Silicone is used in the majority of cast Al alloys to influence casting characteristics, such as fluidity, resistance to hot tearing, solidification shrinkage and feeding [8]. However, increase in Si content can lead to the eutectic (α_{Al} + β_{Si}) coarsening and transformation of primary β_{Si} phase from fine star-like to massive plate-like morphology followed by decrease in tensile strength, ductility and elongation [9, 10]. In the Al-Si and Al-Si-Cu alloys Mg is used to increase strength, hardness and ductility through the solid solution strengthening and solidification of metastable β' phase. The negative impact of Mg on mechanical properties, thermal and electrical conductivity is a consequence of hard and brittle Al_8Mg_5 (β) phase precipitation at the grain boundaries [11, 12]. The negative impact of elevated Cu content manifests through the coarsening of Al_2Cu (θ) phase [13]. Since this phase often appears as a part of two-phase heterogeneous structure (α_{Al} + θ) forming at the terminal stages of solidification sequence [14, 15, 16], coarsening of its

morphology decreases ductility by acting as a void/crack initiation site or enabling preferred crack propagation direction [17]. Although Zn is considered as a neutral element with no significant influence on the Al properties, its accumulation above 1 wt.% in Al-Cu-Mg-Si type alloys can result in the formation of a thin film along the grain boundaries with a negative impact on the mechanical properties, weldability, and surface quality of the casting. Nickel, V, Cr and Fe are considered as impurity elements with negative impact on electrical conductivity, cold working properties, corrosion resistance and causing fabrication defects and hot cracking in Al alloys [18]. Among all of the impurity elements, Fe has the most detrimental effect on the alloy properties. In combination with other alloying elements, Fe forms numerus intermetallic phases whose size, morphology and volume fraction can have a pronounced effect on as-cast properties [19, 20, 21].

The downgrading and diluting represent two possible solutions to reduce the content of trump elements. By downgrading, the low-alloyed scrap is used to produce alloys with higher alloying content, while diluting of molten scrap with primary Al allows for the reduction of trump elements below critical levels [22].

Despite the fact that there are a variety of solutions to lower the negative impact of trump element accumulation during recycling, each represents a trade-off between the coast and the recycling potential [23]. Furthermore, in the absence of the better solution, these strategies will gradually lead to a non-recyclable scrap surplus [24]. A grater standardization of the commercial alloys allowing for the wider range of alloying elements and acceptable impurity levels may represent an alternative [25].

For this purpose, the research was performed to determine the influence of excess Mg and Zn on solidification sequence and microstructure development of secondary EN AC 46100 alloy used in the production of radiators by high-pressure die casting technology.

2. Experimental work

In order to determine solidification sequence and microstructure development the secondary EN AC 46100 alloy was produced using melting furnace with three gas burners (Figure 1 a). The secondary raw material, consisting of Al scrap of different qualities (Figure 1 b) and own return material (Figure 1 c), was melted in the melting chamber of the furnace heated by two gas burners. The own return material represents the pouring system, risers and previously produced castings with the same or similar quality. The chemical composition was corrected by diluting the molten scrap with the addition of EN AB 46100 and Si-based master alloys. After the melt was transported into a temperature holding furnace, the sampling was performed by manual casting into a permanent steel mold.

The chemical composition was determined using optical spectrometer SPECTROMAXx Stationary Metal Analyser.

Based on the results of chemical composition, the Thermo–Calc 2022a software support was used to calculate the equilibrium and non-equilibrium solidification sequence and reactions in liquid and solid states. The solidification sequence was calculated using the TCAL68: Al-Alloys v8.1 technical sheet for Al.
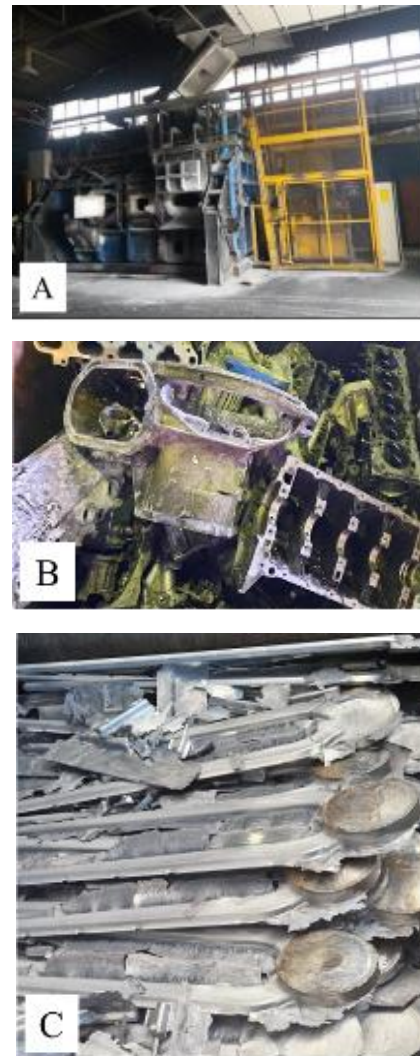
Figure 1. The production of EN AC 46100 alloy: a) Gass melting furnace with two chambers, b) Al scrap, c) own return material

The prediction of non-equilibrium solidification sequence was based on the classic Scheil–Gulliver model assuming that:

- Diffusion in the liquid state is infinitely fast,
- Diffusion in the solid state is zero,

- The liquid/solid interface is in thermodynamic equilibrium.

The aforementioned assumptions are only valid for systems without fast diffuser components or solute trapping. Both, equilibrium and non-equilibrium calculations were performed considering the weight percentages of Si, Fe, Cu, Mn, Mg and Zn in the temperature range between 0 and 780 °C at the default pressure of 100 000 Pa.

The samples for metallographic analysis were prepared using standard grinding and polishing techniques. In order to obtain better distinction between the intermetallic phases, the samples were etched using:

- Keller etching solution (2.5 ml nitric acid (HNO_3), 1.5 ml hydrochloric acid (HCl), 1.0 ml hydrofluoric acid (HF) and 95 ml water),
- Wecks etching solution (100 ml H_2O, 1 g sodium hydroxide (NaOH) and 4 g Potassium permanganate ($KMnO_4$)),
- Poulton etching solution (2 ml HF, 3 ml HCl, 20 ml HNO_3, 175 ml water).

The Olympus GX51 inverted metallographic microscope equipped with Stream Motion software support was used to perform light microscopy. The identification of intermetallic phases was based on the comparison of their morphology with data available in literature [10, 12, 15, 20].

Correlating the results of thermodynamic calculations with microstructure analysis enabled the assessment of the influence of the excess Mg and Zn on EN AC 46100 alloy solidification sequence and microstructure development.

3. Results

The results of chemical composition analysis show the deviation in Mg and Zn content with respect to the standard EN AC 46100 alloy (Table 1). Considering that the Mg content is higher than its solid solubility in $α_{Al}$ matrix, the formation of Mg-containing intermetallic phases is expected. Furthermore, the lower amount of Mg compared to the stochiometric ration Mg:Si=1.73 points to the possibility of Mg_2Si phase solidification [20]. Regardless of the increased Zn content (Table 1), the formation of its intermetallic phases is not expected due to the small atomic radii mismatch of only 7 % between Al and Zn atoms. Instead, the $α_{Al}$ solid solution has extended composition range [21]. The produced alloy is hypoeutectic with Si content of 10.17 wt.% (Table 1) indicating transformation of primary $α_{Al}$ dendritic network followed by the solidification of eutectic ($α_{Al}$ + $β_{Si}$). The Mn/Fe ration of 0.25 points to the preferred precipitation of $β$-Al_5FeSi intermetallic phase with needle-like morphology [22].

The equilibrium and non-equilibrium phase diagrams are illustrated in Figure 2 a and b, while the corresponding reactions are given in Table 2 and 3.

Table 1. The results of chemical composition analysis

	Chemical composition, wt.%										
	Si	Fe	Cu	Mn	Mg	Cr	Ni	Zn	Pb	Sn	Al
Sample	10.17	0.85	1.89	0.213	0.89	0.022	0.069	2.01	0.094	0.020	Balance
EN AC 46100	10.00-12.00	0.0450-1.00	1.50-2.50	<0.55	<0.300	<0.150	<0.450	<1.70	<0.250	<0.150	Balance

Table 2. The equilibrium solidification sequence according to the Thermo-Calc calculations

Reaction No.	Reaction	Temperature, °C
1	Liquid (L) → $Al_9Fe_2Si_2$ ($β$-Al_5FeSi)	586.1
2	L → $β$-Al_5FeSi + FCC_A1 ($α_{Al}$)	578.5
3	L → $β$-Al_5FeSi + FCC_A1 + DIAMOND_A4 ($α_{Al}$+$β_{Si}$)	564.3
4	L → Al_9Fe_2Si ($α$-$Al_{15}(Mn,Fe)_3Si_2$) + $β$-Al_5FeSi + ($α_{Al}$+$β_{Si}$)	562.3
5	L → $α$-$Al_{15}(Mn,Fe)_3Si_2$ + $β$-Al_5FeSi + ($α_{Al}$+$β_{Si}$) + $Al_{18}Fe_2Mg_7Si_{10}$ ($π$-$Al_8FeMg_3Si_6$)	535.9
6	$β$-Al_5FeSi +$α_{Al}$ + $α$-$Al_{15}(Mn,Fe)_3Si_2$ → $π$-$Al_8FeMg_3Si_6$ + $Al_5Cu_2Mg_8Si_6$ (Q-$Al_5Cu_2Mg_8Si_7$)	493.3
7	$α_{Al}$ → Q-$Al_5Cu_2Mg_8Si_{7+}$ + Al_2Cu_C16 (Al_2Cu)	407.1
8	$α_{Al}$ + Q-$Al_5Cu_2Mg_8Si_7$ → Al_2Cu + V_PHASE ($Al_5(Cu,Zn)_6Mg_2$)	72.2

Table 3. The non-equilibrium solidification sequence according to the Thermo-Calc calculations

Reaction No.	Reaction	Temperature, °C
1	L + β-Al$_5$FeSi	586.2
2	L + β-Al$_5$FeSi + α$_{Al}$	578.5
3	L + β-Al$_5$FeSi + (α$_{Al}$+β$_{Si}$)	564.4
4	L + α-Al$_{15}$(Mn,Fe)$_3$Si$_2$ + β-Al$_5$FeSi + (α$_{Al}$+β$_{Si}$)	562.8
5	L + α-Al$_{15}$(Mn,Fe)$_3$Si$_2$ + β-Al$_5$FeSi + (α$_{Al}$+β$_{Si}$) + π-Al$_8$FeMg$_3$Si$_6$	536.8
6	L + (α$_{Al}$+β$_{Si}$) + π-Al$_8$FeMg$_3$Si$_5$	356.6
7	L + (α$_{Al}$+β$_{Si}$) + π-Al$_8$FeMg$_3$Si$_6$ + Mg$_2$Si_C1 (Mg$_2$Si)	534.2
8	L + (α$_{Al}$+β$_{Si}$) + π-Al$_8$FeMg$_3$Si$_6$ + Mg$_2$Si + α-Al$_{15}$(Mn,Fe)$_3$Si$_2$	532.8
9	L + (α$_{Al}$+β$_{Si}$) + α-Al$_{15}$(Mn,Fe)$_3$Si$_2$ + Q-Al$_5$Cu$_2$Mg$_8$Si$_6$ + π-Al$_8$FeMg$_3$Si$_6$ + Mg$_2$Si	520.7
10	L + (α$_{Al}$+β$_{Si}$) + α-Al$_{15}$(Mn,Fe)$_3$Si$_2$ + Q-Al$_5$Cu$_2$Mg$_8$Si$_6$	519.9
11	L + (α$_{Al}$+β$_{Si}$) + α-Al$_{15}$(Mn,Fe)$_3$Si$_2$ + Q-Al$_5$Cu$_2$Mg$_8$Si$_7$ + Al$_2$Cu	493.8

a)   b)
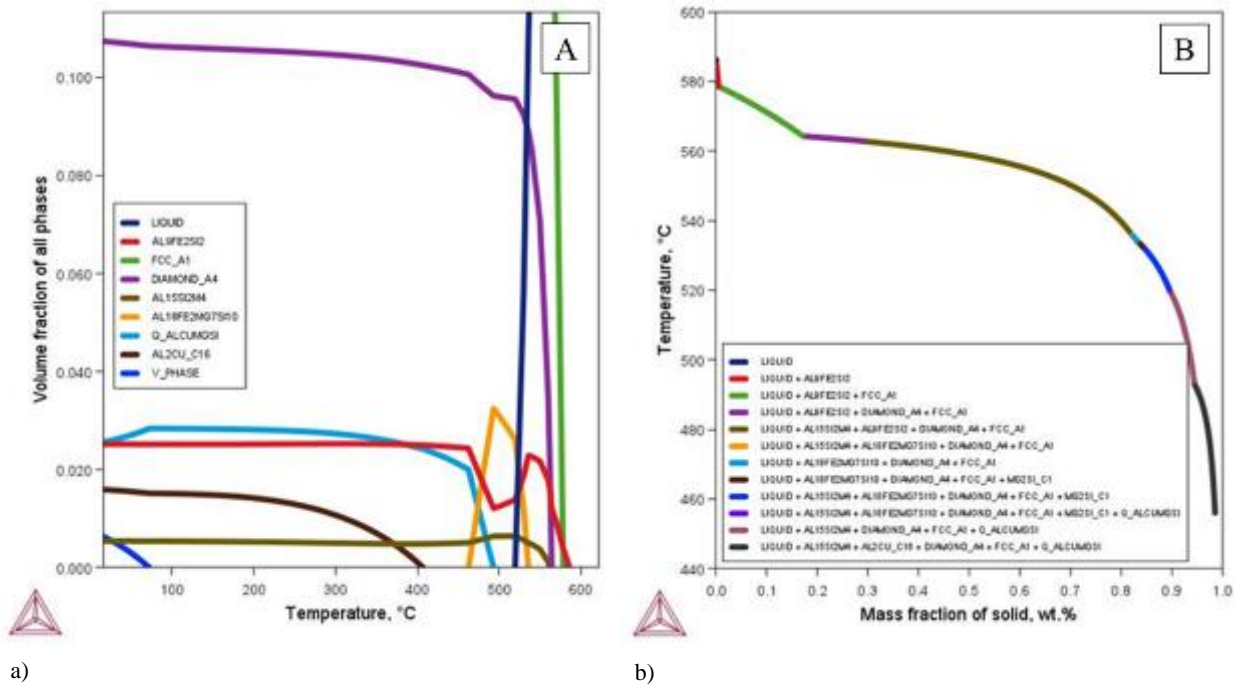
Figure 2.   The phase diagram of: a) equilibrium, b) non-equilibrium solidification

The microstructure development under equilibrium conditions initiates with solidification of β-Al$_5$FeSi phase with needle-like morphology at 586.1 °C (Table 2, Reaction No. 1) followed by transformation of primary α$_{Al}$ dendritic network at 578.5°C (Table 2, Reaction No.

2). The solidification of compact α-Al$_{15}$(Mn,Fe)$_3$Si$_2$ phase with Chinese script morphology at 562.3 °C (Table 2, Reaction No. 4) is preceded by the eutectic reaction and solidification of (α$_{Al}$+β$_{Si}$) at 564.3 °C (Table 2, Reaction No. 3). The quaternary π-Al$_8$FeMg$_3$Si$_6$ phase

with narrow homogeneity range and high thermal stability is last to solidify at 535.9 °C (Table 2, Reaction No. 5). According to the Thermo-Calc calculations the Cu-containing phases precipitate during solid state reactions (Figure 2 a, Table 3) beginning with the precipitation of Q-$Al_5Cu_2Mg_8Si_7$ at 493.3°C C. Increase in the amount of π-$Al_8FeMg_3Si_6$ phase leads to the decrease in the ratio of β-Al_5FeSi and α-$Al_{15}(Mn,Fe)_3Si_2$ phases in the total amount of Fe-based precipitates (Table 2, Reaction No. 6). High amount of π-$Al_8FeMg_3Si_6$ phase is a consequence of high Fe content and precipitation in solid state. The precipitation of Al_2Cu phase initiates at 407.1 °C from the super saturated solid solution of α_{Al} (Table 2, Reaction No. 7). The solidification sequence ends with precipitation of $Al_5(Cu,Zn)_6Mg_2$ phase at 72.2 °C from the super saturated solid solution of α_{Al} and previously precipitated Q-$Al_5Cu_2Mg_8Si_7$ phase (Table 2, Reaction No. 8).

Unlike equilibrium, the nonequilibrium solidification sequence takes place in the temperature interval between 586.2 and 493.8 °C (Table 3) and recognizes solidification of Mg_2Si phase at 534.2 °C (Table 3 Reaction No. 7). The solidification of Fe-based intermetallic phases initiates at higher temperatures (Table 3 Reaction No. 1-5), while solidification of Cu-containing phases is suppressed towards the end of non-equilibrium solidification with Al_2Cu as a last solidifying phase (Table 3 Reaction No. 9-11). The solidification of $Al_5(Cu,Zn)_6Mg_2$ phase is not covered by Scheil–Gulliver calculations.

As indicated by Tables 2 and 3, the formation of Zn-containing phases is limited to the precipitation of $Al_5(Cu,Zn)_6Mg_2$ phase at the end of equilibrium solidification sequence (Table 2, Reaction No. 8). The results of thermodynamic calculations referring to the amount of components in individual phases, indicate that the changes in the amount of Zn are related to solidification of β-Al_5FeSi phase, development of primary α_{Al} dendritic network and solidification of $Al_5(Cu,Zn)_6Mg_2$ phase (Figure 3).

The results of metallographic analysis are given in Figure 4.
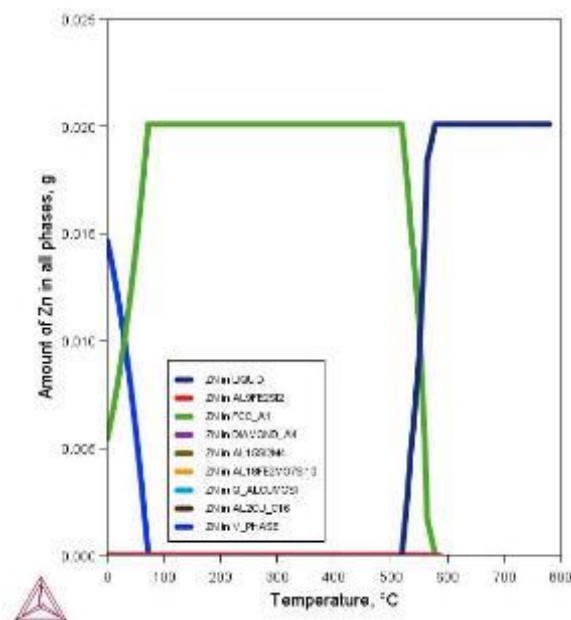
Figure 3.   The amount of Zn in all phases during equilibrium solidification
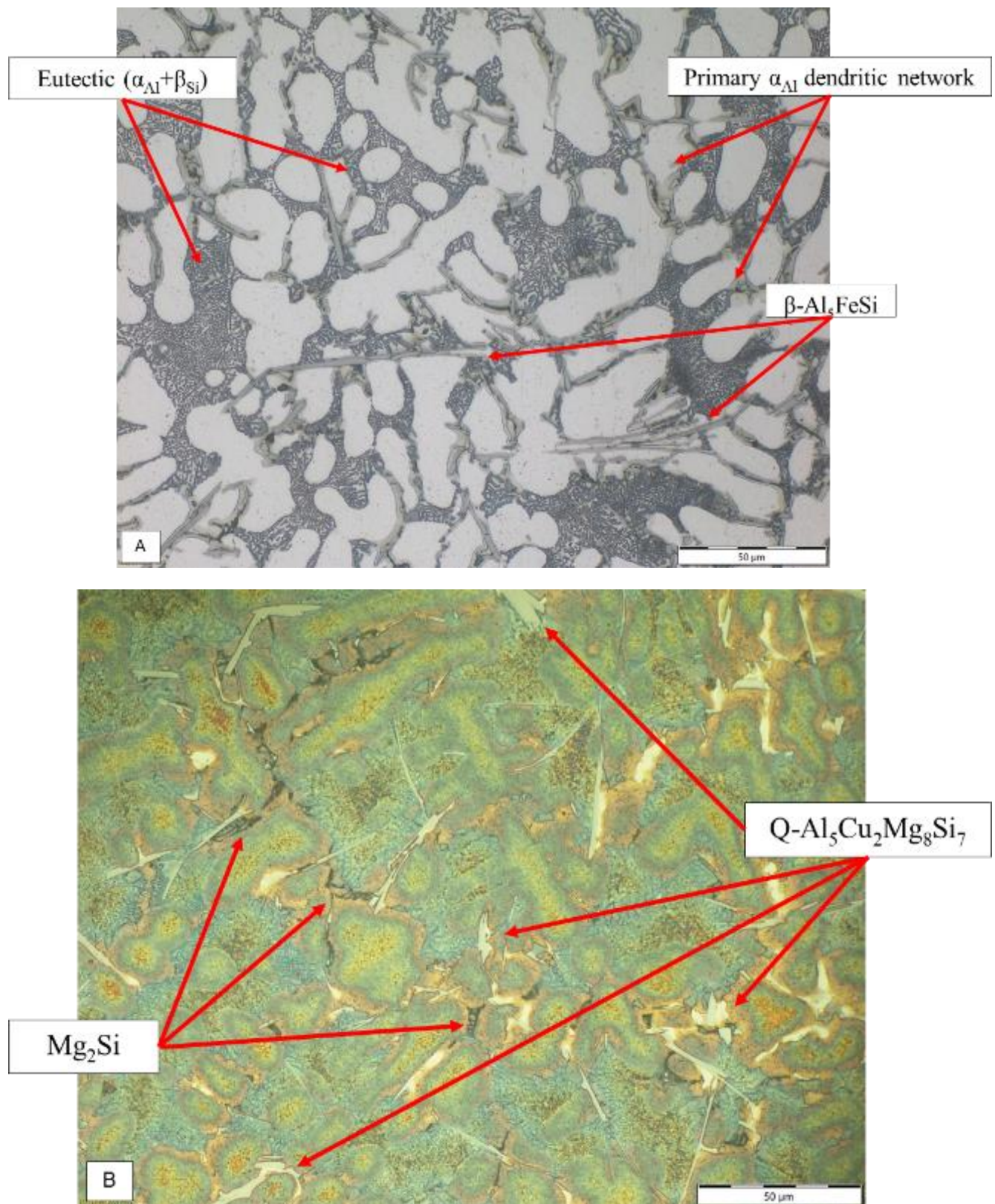
Figure 4.   The microstructure of secondary EN AC 4600 with indicated intermetallic phases

Figure 4.   Continuation - The microstructure of secondary EN AC 4600 with indicated intermetallic phases

The results of metallographic analysis confirmed the presence of primary α_{Al} dendritic network, eutectic ($\alpha_{Al}+\beta_{Si}$), β-Al_5FeSi, Q-$Al_5Cu_2Mg_8Si_7$, Mg_2Si, π-$Al_8FeMg_3Si_6$, Al_2Cu, and $Al_5(Cu,Zn)_6Mg_2$ phases in the microstructure of secondary EN AC 46100 alloy (Figure 4). The needle-like β-Al_5FeSi phase was found between the branches of primary α_{Al} dendrites (Figure 4 a), while the modified eutectic ($\alpha_{Al}+\beta_{Si}$) with fine fibre morphology was located in the interdendritic areas (Figure 4 a). The rest of the intermetallic phases were found at the grain boundaries, with Cu-containing phases showing a tendency to pile up. The Al_2Cu phase with lamellar morphology was found near the π-$Al_8FeMg_3Si_6$ phase with irregular complex morphology (Figure 4 c and d), while spherical $Al_5(Cu,Zn)_6Mg_2$ phase was found in proximity to Q-$Al_5Cu_2Mg_8Si_7$ phase with rod-like morphology (Figure 4 b and d). The α-$Al_{15}(Mn,Fe)_3Si_2$ phases with Chinese script morphology was not found.

4. Conclusions

The research was performed to estimate the influence of excess Mg and Zn on solidification sequence and microstructure development of secondary EN AC 46100 alloy. The alloy was produced by remelting secondary raw material and own return material followed by the chemical composition correction by diluting with EN AB 46100 and the addition of Si-containing master alloy. The investigation comprehended determination of chemical composition, equilibrium and non-equilibrium solidification sequence using Thermo-Calc software support as well as meta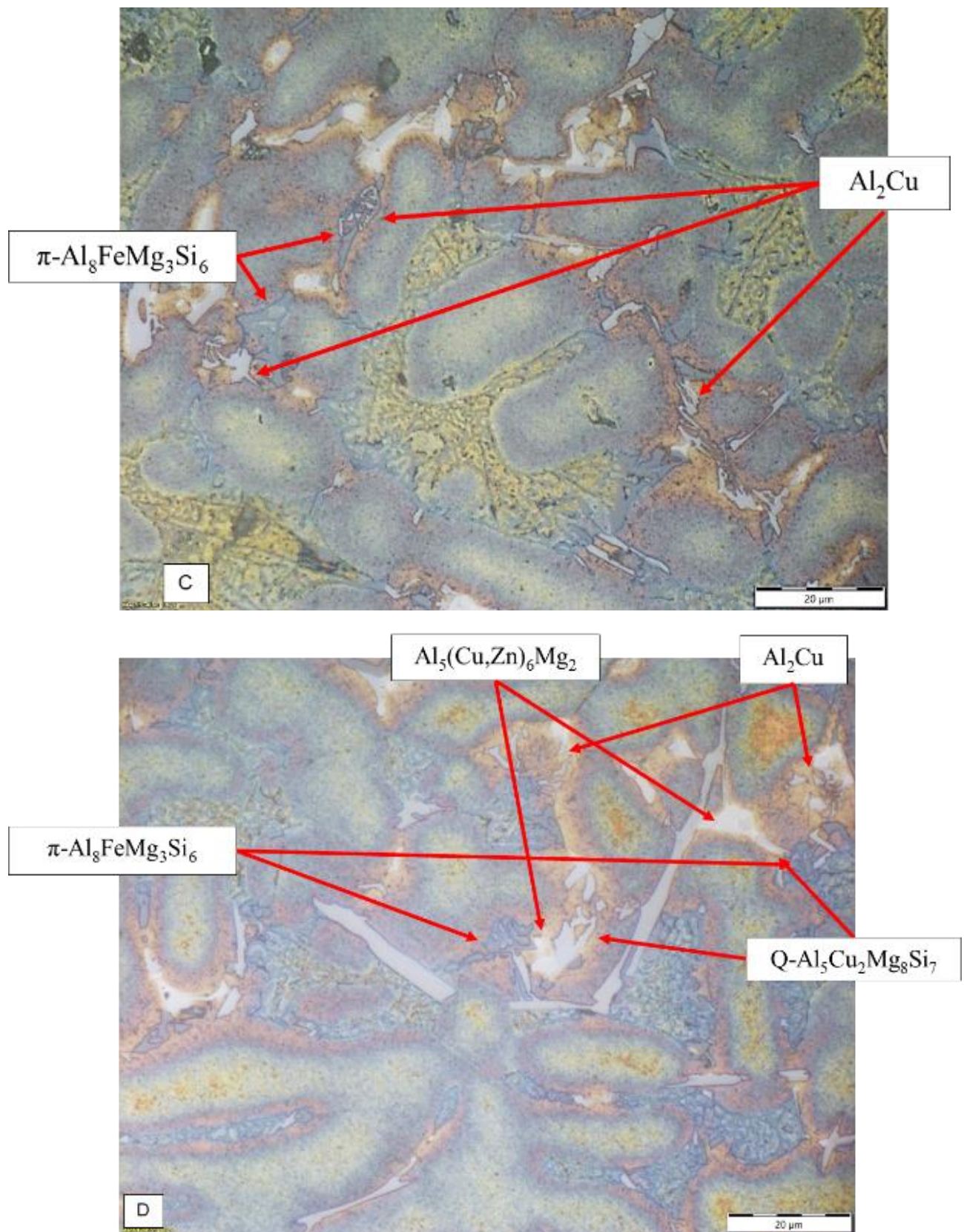llographic analysis. Although, the results of thermodynamic calculations show a similar phase development during equilibrium and non-equilibrium solidification, they differ in width of temperature range, solidification mechanism of Cu-containing phases as well as the appearance of Mg_2Si and $Al_5(Cu,Zn)_6Mg_2$ phase. The comparison of the metallographic analysis results with data available in the literature enabled identification of primary α_{Al} dendritic network, eutectic ($\alpha_{Al}+\beta_{Si}$), β-Al_5FeSi, Q-$Al_5Cu_2Mg_8Si_7$, Mg_2Si, π-$Al_8FeMg_3Si_6$, Al_2Cu, and $Al_5(Cu,Zn)_6Mg_2$ phases. While β-Al_5FeSi and eutectic ($\alpha_{Al}+\beta_{Si}$) were found in the interdendritic areas of primary α_{Al} dendrites, the rest of intermetallic phase were located at the grain boundaries.

Based on the obtained results, it can be concluded that the excess amounts of Mg and Zn led to the solidification and precipitation of complex thernary and quarternary phases such as Q-$Al_5Cu_2Mg_8Si_7$, π-$Al_8FeMg_3Si_6$, $Al_5(Cu,Zn)_6Mg_2$ that are not characteristic for EN AC 46100. Further research needs to be conducted in order to confirm microstructure characterization and estimate the influence of intermetallic phases on the mechanical properties of the secondary EN AC 46100 alloy.

REFERENCES

[1] Soo, V.K., Peeters, V.J., Compston, P., Doolan, M., Duflou, J.R., 2019. Economic and environmental evaluation of aluminium recycling based on a belgian case study. Procedia Manuf. 33, 639–646.

[2] Capuzzi, S., Timelli, G., 2018. Preparation and melting of scrap in aluminum recycling: A review. Metals (Basel). 8.

[3] Sopha, M.B, Ma'mun, S., 2021. Economic analysis and environmental assessment of aluminum debris power generator for deployment to communal-scale disaster areas. Heliyon. 7, e07264.

[4] Cui, J., Roven, H.J., 2010. Recycling of automotive aluminum. Trans. Nonferrous Met. Soc. China. 20, 2057–2063.

[5] Bireau of International Recycling, BE, 2022, ANNUAL REPORTS. https://www.bir.org/ (accessed Jun. 29, 2022).

[6] Nakajima, K., Takeda, O., Miki, T., Matsubae, K., Nakamura, S., Nagasaka, T., 2010. Thermodynamic analysis of contamination by alloying elements in aluminum recycling. Environ. Sci. Technol. 44, 5594–5600.

[7] Cinkilic, E., Ridgeway, C.D., Yan, X., Luo, A.A., 2019. A formation map of iron-containing intermetallic phases in recycled cast aluminum alloys. Metall. Mater. Trans. A Phys. Metall. Mater. Sci. 50, 5945–5956.

[8] Barrirero, J., Engstler, M., Ghafoor, N., De Jonge, N., Odén, M., Mücklich, F., 2014. Comparison of segregations formed in unmodified and Sr-modified Al-Si alloys studied by atom probe tomography and transmission electron microscopy. J. Alloys Compd. 611, 410–421.

[9] Nikanorov, S.P., Osipov, V.N., Regel, L.I., 2019. Structural and mechanical properties of directionally solidified Al-Si alloys. J. Mater. Eng. Perform. 28, 7302–7323.

[10] Zovko Brodarac, Z., Holjevac Grgurić, T., Burja, J., 2016. Thermodynamic stability of AlSi11 alloy microstructure. J. Therm. Anal. Calorim.127, 431-438.

[11] Asghar, G., Peng, L., Fu, P.,. Yuan, L., Liu, Y., 2020. Role of Mg2Si precipitates size in determining the ductility of A357 cast alloy. Mater. Des. 186, 108280.

[12] Zovko Brodarac, Z., Unkić, F., Medved, J., Mrvar, P., 2012. Determination of solidification sequence of the AlMg9 alloy. Kov. Mater.50, 59-67.

[13] Stanić, D., Zovko Brodarac, Z., Li, L., 2020. Influence of copper addition in AlSi7MgCu alloy on microstructure development and tensile strength improvement. Metals (Basel). 10, 1–16.

[14] Zhang, Y., Li, R., Chen, P., Li, X., Liu, Z., 2019. Microstructural evolution of Al2Cu phase and mechanical properties of the large-scale Al alloy components under different consecutive manufacturing processes. J. Alloys Compd. 808, 151634.

[15] Zovko Brodarac, Z., Dolić, N., Unkić, F., 2014. Influence of copper content on microstructure development of AlSi9Cu3 alloy. J. Min. Metall. B. 50, 53-62.

[16] Manasijević, S., Dolić, N., Zovko Brodarac, Z., Radiša, R., 2015. Analysis of piston microstructure in the most critical zones. Kov. Mater.53, 357-363..

[17] He, H., Yi, Y., Huang, S., Zhang, Y., 2018. Effects of cold predeformation on dissolution of second-phase Al2Cu particles during solution treatment of 2219 Al-Cu alloy forgings. Mater. Charact.. 135, 18–24.

[18] Dewan, M.A., 2011. Control and removal of impurities from Al melts: A review. Mat. Scien. For.

693, 149–160.

[19] Puncreobutr, C., Phillion, A.B., Fife, J.L., Rockett, P.,. Horsfield, A.P., Lee, D.P., 2014. In situ quantification of the nucleation and growth of Fe-rich intermetallics during Al alloy solidification. Acta Mater. 79, 292–303.

[20] Kozina, F., Zovko Brodarac, Z., Drobnjak, D., Jukić, I., *Investigation of iron containing intermetallics in AlSi12 alloy with w(Mn/Fe)=0.99*, 18th international foundrymen conference 2019, Sisak, Crosatia.

[21] Kozina, F., Zovko Brodarac, Z., Petrič, M., Penko, A., 2020. The impact of iron impurities on the compression behavior of Al-2.24Mg-2.09Li alloy. J. Min. Metall. B. 56, 425-433.

[22] Modaresi, R., Müller, D.P, 2012. The role of automobiles for the future of aluminum recycling. Environ. Sci. Technol. 46, 8587–8594.

[23] Gaustad, G., Olivetti, E., Kirchain, R., 2012. Improving aluminum recycling: A survey of sorting and impurity removal technologies. Resour. Conserv. Recycl. 58, 79–87.

[24] Das, S.K., Green, J.A.S. & Kaufman, J.G., 2007. The development of recycle-friendly automotive aluminum alloys. JOM 59, 47–51.

[25] Source for standards, engineering specifications, manuals and technical publications, SAD, 2022, EN 1676:2010 - Aluminium and aluminium alloys - Alloyed ingots for remelting - Specifications. https://standards.iteh.ai/catalog/standards/cen/0662 4bd9-ce86-48d1-8870-cc3abb0bb613/en-1676-2010 (accessed Jul. 06, 2022).

Analysis of the tube hydroforming by numerical simulation and Response Surface Methodology

Jure KROLO[1], *Branimir LELA*[1],
Nikolay BIBA[2], *Domagoj ŠAKOTA*[1]
1) Faculty of Electrical Engineering,
   Mechanical Engineering, and Naval
   Architecture, Split, **Croatia**
2) MICAS Simulations Limited, Temple
   Court, 107 Oxford Road, Oxford, **U.K.**

jkrolo@fesb.hr
blela@fesb.hr

Keywords

Tube hydroforming
Finite element analysis
Design of experiments
Optimization

Original scientific paper

Abstract: In this research mathematical model was developed utilizing the 3D finite element method and response surface methodology to describe the tube hydroforming production process. This paper is an example of the relatively simple analysis of the influence of the technological parameters on hydroformed T-shaped tube protrusion height, diameter, and thickness utilizing statistical analysis and 3D finite element analysis in the QForm UK 10.2 commercial software. Therefore, this paper could be beneficial for both researchers and engineers interested in tube hydroforming design guidelines and simple optimization methods. The influence of the hydroforming die radius filler, axial tool displacement, and counter punch force on the T tube protrusion height, diameter, and thickness was described and optimized.

1. Introduction

In the last few decades hydroforming has become the standard method to produce more complex parts with fewer operations than traditional cold forming methods. The other advantages can be better surface finish, production of parts with fewer components, and better thickness control. Hydroforming is usually divided into a tube, sheet, and shell hydroforming. It is well known that the tube hydroforming process (THF) has wide application in the automotive industry, but also can be found in the aerospace industry and piping manufacturing processes [1]. Hydroforming can be found in the latest automotive parts production due to the increased demand for a lightweight solution on due to production of the electric vehicles with relatively heavy batteries. Furthermore, weight reduction in next-generation vehicles can be achieved by the replacement of stamped and spot-welded steel assemblies [2]. Many of the structural members of the automobile are now made via a hydroforming manufacturing method that includes such as cradles [3] and pillars, [4]. Therefore, through the THF process, manufacturers are able to produce complex-shaped parts with lightweight and fewer welds than through alternative metal forming techniques [5]. Hydroforming can increase designed part complexity and quality due to the uniformly distributed working fluid pressure inside workpiece material. For certain geometries, hydroforming technology permits the creation of parts that are lighter weight, have stiffer properties, are cheaper to produce and can be manufactured from fewer blanks which produce less material waste [6]. Some authors investigated the hydroforming process parameters influence on

hydroformed parts utilizing the finite element method and statistical analysis. Reddy P.V. investigated tube hydroforming utilizing the finite element method and Taguchi analysis. Results showed that axial feed, hydroforming pressure, and friction coefficient have an influence on formed bulge height and thickness. Taguchi optimization showed that optimized bulge height can be obtained if 6 MPa pressure, 3 mm axial feed, and 0.05 friction coefficient were used [7]. Rakesh A. S. researched the influence of die corner radius, length of the tube, the thickness of the tube, and internal pressure on hydroformed tube thickness reduction. In this case, simulation was performed in combination of the FEM and Taguchi methods [8]. Koc M. used FEA and the low-cost response surface method to optimize the height of the "T shaped" tube protrusion height. Input parameters were left and right tube edge distance from protrusion, die opening diameter for protrusion part, and die fillet radius. According to the authors, these parameters should have a significant influence on protrusion height. Increased protrusion die diameter, and die fillet radius increased protrusion height. Also, reduced edge distance contributed to the protrusion height increment [5]. In this research, motivated by increasing interest in hydroforming in the automotive industry over the last few years, a simple method for tube hydroforming 3D numerical simulation and statistical optimization was presented. 3D finite element analysis has the advantage to provide a unique insight in the production process. The advantage of the numerical simulation approach is well known because it is possible to avoid costly and time-consuming multiple experiments. Statistical analysis utilizing response surface methodology was employed in

combination with FEM. Statistical analysis of the influence of hydroforming parameters on hydroformed tube shape enabled the development of the mathematical model which can be useful to describe and optimize the mentioned process. Selected input hydroforming parameters were axial punch tool displacement, the radius of the "T shaped" tube forming die, and counter punch force. Punch displacement, die radius, and counter force were in a range from 20 mm to 30 mm, 2 mm to 10 mm, and 8 kN to 12 kN, respectively. Output parameters were protrusion height and diameter, and thickness of the protrusion upper part. Utilization of the commercial software QForm UK 10.2 enabled 3D simulation with simultaneous axial tool movement, counter punch movement and force regulation, and pressure change according to the optimized pressure load diagram. The ability to simulate all mentioned parameters and tools kinematics is important due to the aim to describe the realistic production parameters more accurately.

2. Simulation and process

In the tube hydroforming process, a blank tube, straight or preformed, is shaped in a die cavity through the application of hydraulic internal pressure and simultaneous axial compressive forces from both ends. One of the most important parameters to be considered is the optimized pressure load step which should be carefully selected in accordance with the side punches displacements. By simultaneously increasing the fluid pressure on the inside of the tube while feeding new material, axial feeding can reduce material thinning. For better process control counter punch should also be used to prevent excessive thinning and unwanted shape of the protrusion part in the T-shaped hydroformed tube. Other influence parameters are workpiece material properties, friction coefficient, die geometry, workpiece size, axial punch feed speed and amount, counter punch pressure, etc. Successful numerical simulation or experiment of the hydroforming process can be performed only if all influence factors are taken into consideration. Therefore, hydroforming can be considered as a complex manufacturing process. The main aim is to avoid possible failures such as wrinkling, buckling, necking, or bursting and to achieve good dimensional accuracy [1]. Firstly, material description is of the main importance. Both experimental data and mathematical material hardening models can be used to describe the used material. In this paper, flow stress curves for aluminum alloy AA 1050 obtained with different strain rates were taken from the database available in the numerical simulation software QForm UK 10.2. Experimental data should provide a better material description than material hardening models which are usually used in previous research. An aluminum alloy workpiece was considered an isotropic material. The workpiece was meshed into 62138 volumetric tetrahedral finite elements, which is considered sufficient relative to the work volume and

previous researches [9]. The mesh was automatically re-meshed if the elements became too distorted during the forming process simulations. The aluminum tube was 200 mm in length with 50 mm diameter and 2.5 mm wall thickness. Tools were considered to be a rigid body. In previous research, the Coulomb friction coefficient was used for lubricated conditions 0.03 [10]. In other research was determined to be around 0.05 in expansion zone for 20 MPa pressure [11]. Some researchers reported that the friction coefficient in a range from 0.06 to 0.23 was dependent on hydroforming pressure [12]. To describe friction behavior in this research Levanov friction model was used with a 0.1 friction coefficient which should be appropriate for aluminum steel contact with lubrication conditions. The used model is similar to the hybrid model of the classic Coulomb friction model and Shear friction model [13]. Selected input hydroforming parameters were axial punch tool displacement, fillet radius of the hydroforming die, and counter punch force. According to the reviewed literature, there is a lack of investigation of the counter punch force influence on part shape. Output parameters were protrusion height and diameter, and thickness of the protrusion upper part. Figure 1. a shows hydroforming pressure versus axial tool displacement diagram. This diagram is usually called loading path diagram and it has great influence on the thickness uniformity of the product [9, 14]. Diagram was optimized according to the preliminary simulations where the aim was to find a range of the input parameters and pressure load diagram for successful simulation. The main criteria for successful simulation were the ability to create protrusion with some minimal height or to avoid protrusion bursting. Figure 1. b shows used tools and hydroformed aluminum tube sample. Furthermore, after initial simulations selected range to vary counterpunch force was from 8 kN to 12 kN. When a smaller force was used, for the selected hydroforming pressure load path diagram, a burst of the tube occurred. In the case that pressure or material were changed, this counterpunch pressure should be selected accordingly. The radius of the fillet at the die channels intersection was very influential on the shape of the formed tube protrusion, but using to high radius useful part of the T shaped tube protrusion is smaller, so in this case, the fillet radius was selected in a range from 2 mm to 10 mm. This parameter can be easily changed according to the possible application or tube geometry. The third parameter was axial punch feed (displacement). Intending to achieve good tube protrusion shape and thickness (to avoid possible bursting) it is necessary to simultaneously control punch axial feed, hydroforming pressure, and counter punch force. Therefore, mathematical modelling utilizing response surface methodology can be a useful tool for selected process optimization. The same analogy can be easily used for other process parameters, material, geometry, etc.
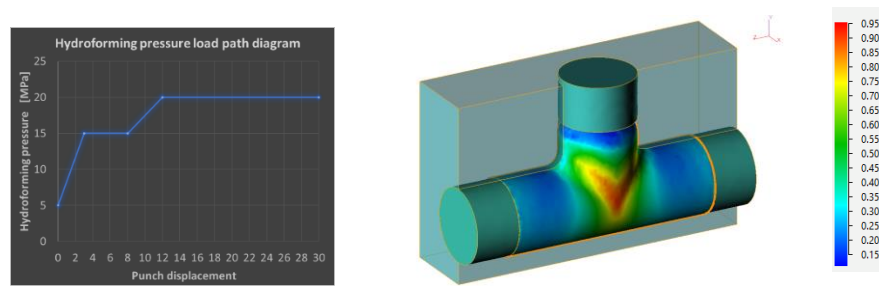
Figure 1. a) Hydroforming pressure versus axial tool displacement b) hydroforming tools and formed workpiece plastic strain

3. Design of experiments

Box Behnken experimental design was used to derive mathematical models which can describe the influence of the input process parameters on tube protrusion height, diameter, and thickness. Design-Expert software was used to create the experimental plan. According to the Box Behnken design usually 17 experiments are necessary for three input numerical factors. But in this case, due to the 5 central points which are the same in the numerical simulation, only 13 simulations were performed. Used input parameters for simulation and simulation results are presented in Table 1. For easier writing of the mathematical models punch displacement will be denoted with A, tool radius with B, and counter force with C.

Table 1. Input parameters according to the experimental plan and simulation results

Exp.	Punch displacement	Tool radius	Counter force	Protrusion height	Protrusion diameter	Protrusion thickness
	mm	mm	kN	mm	mm	mm
1	25	6	10	74,3	49,4	2,2
2	20	10	10	72,04	49,68	2,18
3	20	6	8	72,27	49,23	2,09
4	25	10	8	79,42	49,88	2,05
5	20	6	12	67,85	48,67	2,28
6	25	2	8	74,27	49,34	2,19
7	30	10	10	81,08	49,99	2,18
8	25	2	12	69,56	46,64	2,32
9	30	6	12	75,9	49,59	2,26
10	30	2	10	75,9	49,21	2,28
11	25	10	12	74,29	49,76	2,22
12	30	6	8	81,29	49,69	2,09
13	20	2	10	67,74	46,65	2,28

4. Results and discussion

4.1. Protrusion height

According to the regression analysis and ANOVA quadratic model was suggested to describe the influence of the input parameters on the T-shaped tube protrusion height. R Squared was 0.99, the same as Adj and Pred R Squared. The mathematical model was derived as follows:

$$PH = + 56.93987 + 1.20351 * A + 0.46125 * B$$
$$- 1.09247 * C + 0.011 * A + B - 0.0245250 * A$$
$$* C - 0.013125 * B * C - 3.40526 * 10^{-3} * A^2 +$$
$$0.027467 * C^2 \quad (1)$$

The graphical presentation of equation 1 is presented in Figure 2. According to Figure 2. a. and b. increased punch displacement, radius, and reduced counter force contributed to increased protrusion height. According to the results achieved protrusion height was in a range from 67.74 to 81.29 mm.

Figure 2.   a) Influence of the die fillet radius and punch axial displacement on protrusion height

Figure 2.   b) Influence of the die counter force and punch axial displacement on protrusion height

Figure 3. a)   Influence of the die fillet radius and punch axial displacement on protrusion diameter
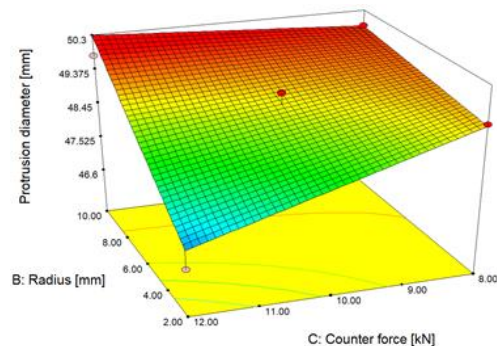
Figure 3. b)   Influence of the die counter force and die fillet radius on protrusion diameter

4.2. Protrusion diameter

According to the regression analysis and ANOVA 2FL model was suggested to describe influence of the input parameters on the T shaped tube protrusion diameter. R Squared was 0.88. Adj and Pred R Squared were 0.827 and 0.595, respectively. Mathematical model was derived as follows:

$$PH = +47.88358 + 0.27480 * A + 0.12791 * B - 0.70163 * C - 0.028075 * A * B + 0.080719 * B * C \quad (2)$$

The graphical presentation of equation 2 is presented on Figure 3. According to Figure 3. a. and b. increased punch displacement, radius, and reduced counter force contributed to increased protrusion diameter. For a lower counter punch force of 8 kN, die radius doesn't have pronounced influence, as for 12 kN counter force. Similarly, for punch displacement of 30 mm die radius change does not influence protrusion diameter as for punch displacement of 20 mm. This indicated that proper selection of the tool displacement and counter force can reduce negative influence if too small die fillet radius was used. According to the results achieved protrusion diameter was in a range from 46.66 to 49.99 mm.
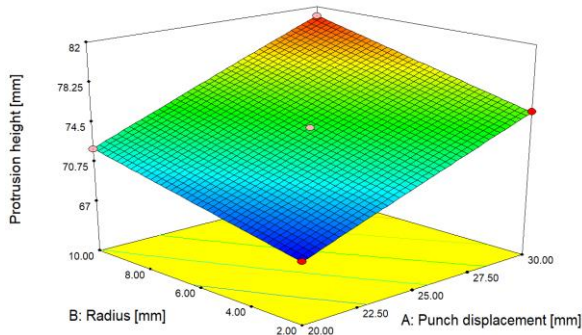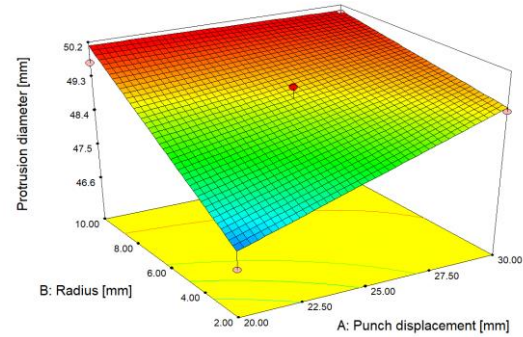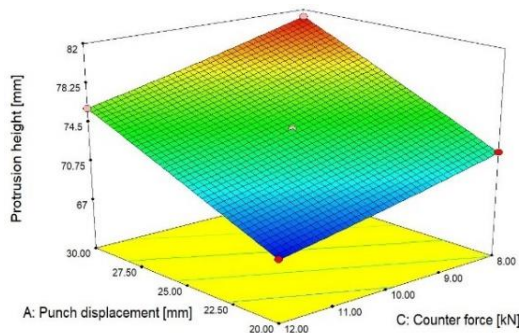
4.3. Protrusion thickness

According to the regression analysis and ANOVA quadratic model was suggested to describe the influence of the input parameters on the T-shaped tube protrusion thickness. R Squared was 0.98. Adj and Pred R Squared were 0.98 and 0.93, respectively. The mathematical model was derived as follows:

$$PT = +1.34134 - 5.50000E\text{-}004 * A - 0.043204 * B + 0.16810 * C + 1.25000E\text{-}003 * B * C + 1.41283E\text{-}003 * B^2 - 6.72368E\text{-}003 * C^2 \quad (3)$$

The graphical presentation of equation 3 is presented on Figure 4. According to Figure 4 counter force has a significant impact on T-shaped protrusion thickness. Increased counter punch force contributed to increased protrusion wall thickness. Counter punch force had the most influence on workpiece thickness. Workpiece thickness was selected as the output parameter to avoid possible protrusion bursting due to extensive thinning. Increased die radius slightly reduced protrusion wall thickness. It seems that axial tool displacement does not have a pronounced influence on protrusion upper part thickness. According to the results achieved protrusion thickness was in a range from 2.05 to 2.32 mm.
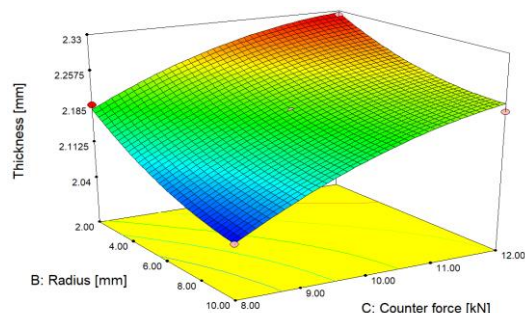
Figure 4. Influence of the die counter force and die fillet radius on protrusion thickness

5. Conclusion

Numerical simulation of T shaped tube hydroforming process was performed for different process parameters. Utilizing statistical analysis those parameters were described both graphically and mathematically. According to the results increased punch displacement, radius and reduced counter force contributed to increased protrusion height. Protrusion diameter was increased with increased radius when 12 kN counter punch force was applied, while for 8 kN force, die radius does not have pronounced influence. For punch displacement of 20 mm increased radius was beneficial to achieve a higher protrusion diameter, while at 30 mm punch displacement radius did not have a pronounced influence. On the other hand, punch displacement did have a statistically significant influence on protrusion thickness. On the protrusion thickness, counter punch force had the most influence, and for higher counter punch force higher thickness was achieved. It is important to preserve tube wall thickness to prevent protrusion bursting. According to the results, it is clearly visible that interaction between parameter is very dependent based on which values for each parameter is selected. Therefore, numerical analysis in combination with the statistical approach used in this research could be beneficial in the selection of the process manufacturing parameters to optimize the process before expensive trial-error experiments. Mathematical models derivation allowed optimization of the process presented in this research. Hydroforming process optimization was performed in Design-Expert software. Optimization was performed to achieve the highest possible protrusion height, diameter, and thickness. Optimal punch displacement, counter punch force, and die fillet radius were 30 mm, 11.84 kN, and 10 mm, respectively. Selection of those input parameters should result in protrusion height of 78.64 mm, protrusion diameter of 50 mm, and thickness of 2.22 mm. After numerical simulation of the hydroforming process with optimized input parameters, output for protrusion height, protrusion diameter, and thickness were 78.72 mm, 49.95 mm, and 2.24 mm, respectively. These results are in fair agreement with those predicted with optimization.

REFERENCES

[1] Hartl, C., (2020), *Mechanics of hydroforming*. LTD.

[2] Darlington, R., (2003), *Tube hydroforming of steel for automotive applications*. Swansea University.

[3] Koç, M., Altan, T., (2001), *Overall review of the tube hydroforming (THF) technology*. Journal of Materials Processing Technology, 108 (3), 384–393.

[4] Tolazzi, M., (2010), *Hydroforming applications in automotive : a review Centro Ricerche Fiat – Trento Branch*. Journal of Materials, 3, 307–310.

[5] Koç, M. et al., (2000), *Use of FEA and design of experiments to establish design guidelines for simple hydroformed parts*. International Journal of Machine Tools and Manufacture, 40 (15), 2249–2266.

[6] Bell, C. et al., (2020), *A state of the art review of hydroforming technology: Its applications, research areas, history, and future in manufacturing*. International Journal of Material Forming, 13 (5), 789–828.

[7] Venkateshwar Reddy, P. et al., (2018), *A Numerical Study on Tube Hydroforming Process to optimize the Process Parameters by Taguchi Method*. Materials Today: Proceedings, 5 (11), 25376–25381.

[8] Shinde, R.A. et al., (2016), *Optimization of Tube Hydroforming Process (without Axial Feed) by Using FEA Simulations*. Procedia Technology, 23, 398–405.

[9] Hwang, Y.M., Tsai, Y.J., (2020), *Movable die and loading path design in tube hydroforming of irregular bellows*. Metals, 10 (11), 1–16.

[10] Liu, G. et al., (2015), *Analysis on critical conditions of sidewall wrinkling for hydroforming of thin-walled Tee-joint*. International Journal of Machine Tools and Manufacture, 97 (February), 42–49.

[11] Yi, H.K. et al., (2011), *Experimental investigation of friction coefficient in tube hydroforming*. Transactions of Nonferrous Metals Society of China (English Edition), 21 (SUPPL. 1), 194–198.

[12] Ghorpade, S.S., (2017), *Mathematical Model for Estimation of Hydroform Pressure & Coefficient of Friction in Tube Hydroformed Parts*. IOSR Journal of Mechanical and Civil Engineering, 17 (03), 29–

38.

[13] QForm UK 10.2 Manual, *Friction at plastic deformation*.

[14] Imaninejad, M. et al., (2005), *Loading path optimization of tube hydroforming process*. International Journal of Machine Tools and Manufacture, 45 (12–13), 1504–1514.

Improvement of resistance to sliding wear by nitriding the bearing steel EN DIN 100Cr6

Darko LANDEK[1], **Josip CEROVEČKI**[1]

1) University of Zagreb, Faculty of Mechanical Engineering and Naval Architecture, Ivana Lučića 5, 10000 Zagreb, **Croatia**

dlandek@fsb.hr

Keywords

Sliding wear
Steel EN DIN 100Cr6
Tenifer salth bath nitriding
Plasma nitriding
Block on ring test method

Professional paper

Abstract: The paper investigates the resistance to adhesive wear of sliding bearings consisting of a nitrided ring made of steel EN DIN 100Cr6 and a bearing pad made of lead bronze. The tested rings were nitrated in a Tenifer salt bath at 580 °C/2h and in plasma of ionized gases N_2/H_2 at 500 °C/4h. Roughness measurement and surface hardness testing were performed on the all-test samples. On tribocouples composed of a nitrided ring and a lead bronze prism, the increase in temperature, and the width of the wear track on the contact surface of the prism were determined after 30 s of wear using the "prism on ring" sliding method under the conditions of dry friction and lubrication with SAE 5W engine oil during 30 s of wear under load with a normal force of 6.31 N and with ring speed 1200 rpm, 1740 rpm and 2500 rpm

1. Introduction

During operation, the surfaces of sliding and rolling bearings are exposed to static and dynamic loads, contact pressures, wear and corrosion. The sliding bearing cushion, which is usually made of a softer and tougher material compared to the material of the shaft, wears out more and is damaged by the shaft sleeve. Due to the differences in the hardness of the cushion and the shaft and the variable friction factor, vibrations, noise and heating of the bearing occur [1]. The design of the sliding bearing is prescribed by standards (DIN 50282, ISO 76-1978, etc.). They emphasize the importance of selecting the lubricant, cushion material and shaft sleeve for certain conditions of speed, rotation speed and bearing load. Due to the increased wear of the plain bearing cushion, the maintenance code of the plain bearings is usually changed. The cushion materials are bearing bronzes, bearing alloys, sintered materials, ceramic materials or composites. In conditions of dry and marginal friction, where intense wear occurs, it is recommended to modify or coat the surface of the sleeve, and if possible also the surface of the cushion. Gloves are coated with sliding surface layers (oxides, nitrides, oxynitrides, suflonitrides), tribological coatings (Sn, Pb, MnS, DLC, TiN coatings, etc.), or with coatings of solid lubricants (graphite, MoS2) [2,3]. The long-lasting range of high-load bearings is achieved with the condition that the zone of action of contact pressures is within the hardening zone of the surface layer or within the thickness of the coating. Also, the dynamic durability of

the sleeve material must necessarily be greater than the dynamic load of the bearing [1, 3].

From the all mentioned procedures for modifying and coating the bearing surface, the application of nitriding stands out due to its favorable combination of mechanical and tribological properties. The application of the nitriding process achieves a combination of properties favorable for application in highly loaded sliding bearings. A diffusion zone is formed under the nitrided surface, which increases the resistance to contact pressures and the dynamic durability of the steel, while the thin compound zone formed on the nitrided surface prevents microwelding, increases resistance to adhesion and microabrasion, lowers the dry friction factor, increases corrosion resistance, tolerates elevated temperatures and binds to itself a boundary layer of lubricating oil [3, 4, 5]. Disadvantages of the application of nitriding refer to the reduction of the hardness of the core of hardened and tempered steel for bearings, if the tempering temperature was lower than the nitriding temperature; a change in the dimensions of the bearing rings (at least to double the thickness of the compound zone) and an increase in the cost of manufacturing the bearing. Nitriding is carried out in a salt bath, gas or plasma. Nitriding in a salt bath (with a thicker compound zone) is suitable for highly loaded sliding surfaces with lower sliding speeds and higher permitted values of the friction factor, compared to finely ground or polished steel. Gas nitriding is suitable for highly loaded sliding surfaces with medium sliding speeds and medium friction factor values. Plasma nitriding (with or without a

thin compound zone) is suitable for high-load and high-speed sliding bearings where a low friction factor is required under all conditions. [3, 6, 7].

Nitriding in a salt bath is the simplest of the listed nitriding procedures. For its implementation, the nitriding time must be determined depending on the nitrided steel and the required depth of the nitrided layer. To carry out nitriding in a salt bath, it is necessary to control the chemical composition of the bath at the beginning of the process and the temperature (around 580 °C) and the time during the process (from 1 h to 5 h). Although the process of nitriding in salt baths is relatively simple to manage, during nitration it is necessary to carry out ventilation and neutralization of dangerous vapors and drops of the bath above the working area of the furnace. After nitriding, it is necessary to wash the workpiece, neutralize salt residues and dispose of them. Nitriding in gas is a more complex procedure for automation and implementation, which additionally requires a cleaner surface of the parts than nitriding in a salt bath. In order to carry out gas nitriding of a certain steel, it is necessary to select the optimal temperature (between 550°C to 580 °C) and nitriding time (from 2 h to 48 h) and the appropriate flow rate of ammonia, nitrogen and possibly carbon dioxide and water vapor. During gas nitriding, the spent gases from the furnace are burned on a burner before being released into the environment. After gas nitriding, the surface of the workpiece is clean and dry and can be immediately installed in the structural assembly. Plasma nitriding is the most complex of the mentioned procedures, which also requires a finely ground surface of the workpiece, cleaned of metal dust, and a drop of liquid for cooling and lubrication from machining. After cleaning the workpiece surface in aqueous solutions of alcohol or industrial detergents, the dried parts are placed in the vacuum chamber of the nitriding device. Before plasma nitriding, ion sputtering is carried out with the aim of completely removing organic impurities and oxide from the surface of the metal material. Then, on the degreased and ionically cleaned surface, plasma nitriding is carried out with the appropriate combination of temperatures

(between 350 °C and 650 °C) and nitriding time (from 2 h to 30 h), voltage, current and power of the plasma and the flow of gases: nitrogen, hydrogen and argon. By choosing plasma nitriding parameters, it is possible to achieve a nitrided layer with and without a junction zone. It is also possible to achieve a homogeneous compound zone with a certain type of nitride or their combination. The plasma nitriding process is carried out in a vacuum furnace with a cooled outer wall , and without significant impact on the environment. Output and cooled gases from the vacuum chamber are released into the environment as water vapor and carbon dioxide. After plasma nitriding, the surface of the parts is clean and dry, and they can be immediately installed in the assembly [7].

The paper compares the influence of the nitriding process (in a salt bath or plasma), lubrication (dry friction or lubrication with SAE 5W-30 oil) and the bearing rotation speed on the resistance to adhesive wear in a tribocouple composed of a rotating nitrided ring and a prism made of bearing bronze.

2.   Materials and methods

Tribocouples consisting of NTN 2U1708 bearing rings made of hardened and tempered steel EN DIN 100Cr6 and prisms made of copper-lead bronze were tested in the work. The dimensions of the ring were Dia 30/35 mm, width 17 mm. The initial ring hardness was 56 ± 2 HRC, which corresponds to the hardened and low-temperature softened state of steel EN DIN 100Cr6. Non-nitrided rings are marked as "NN00". The dimensions of the prism were 7x7x14 mm. Six rings were nitrided in a Tenifer salt bath (sample designations "TF580"), while six rings were plasma nitrided (sample designations "PN500"). The parameters of nitriding processes are listed in Table 1. Six prisms are made by milling and grinding from the bearing pad of the sliding bearing of the diesel engine crankshaft. Manual sanding of the surface of the prism was carried out with P600 and P1200 grit sandpapers. Figure 1 shows the nitrided rings and prisms before the start of the test. All samples were tested for: surface roughness and hardness, as well as resistance to adhesive wear by sliding the prism on the ring

Table 1. Nitriding parameters of EN DIN 100Cr6 steel rings

Sample label	Nitriding process	Proces parameters
NN00	Not nitrated (initial condition)	-
TF580	Nitriding in salth bath Tenifer	1. Pre heating450 °C /1 h 2. Nitriding 580 °C / 2 h / Cooling: stil water, 20 °C
PN500	Plasma nitriding in a vacuum furnace Rübig PC 70/90 S	1. Surface cleaning by sputtering process: 420 °C /3 h (2 mbar; 1000 W; 90 % H_2, 5 % N_2, 10 % Ar) 2. Plasma nitriding: 500 °C / 4 h (2 mbar; 2000 W; 22 % H_2, 67 % N_2, 11 % Ar) 3. Cooling in vacuum: 2 mbar, 100% N_2

The surface roughness test was carried out according to ISO 4287 and ISO 4288 standards. The surface roughness test was carried out on the Perthen Mahr device with five repetitions at different points of the sample. The hardness test on the surface of the samples was carried out using the Vickers method (HV0.5) on a Wilson-Wolpert Tukon 2100B hardness tester with five repetitions per sample.

Figure 1.   Nitrided rings and prism before testing

The adhesive wear test was performed on the adapted device shown in Figure 2 by sliding a prism pressed against a rotating ring. The prism was pressed onto the ring with a normal force of 6.31 N. The ring is attached to the chuck of the Proxxon DB 250 model lathe and rotated at a constant speed for 30 s. The influence of ring rotation speed on adhesive wear and wear effects was tested, with the specified rotation speeds: 1200 rpm, 1740 rpm and 2500 rpm. Before starting the test, the ring rotation speed was checked with a laser tachometer UNI-T UT373.
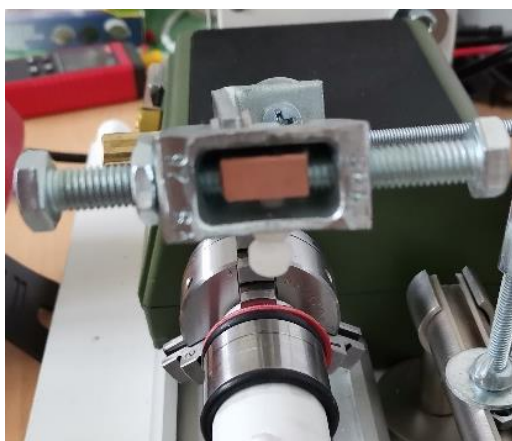
Figure 2.   Device for testing adhesive wear by sliding a prism on a ring

Two groups of tests were performed: (1) wear without lubrication, (2) wear with lubrication with synthetic engine oil INA Ultra Sint SAE 5W-30. Lubrication is carried out by adding oil to the contact point of the prism and the ring with a flow rate of 10 mL/s. The wear test was carried out with the same tribocouple and under the same conditions with three repetitions, where by moving the prism along the ring in each new wear, contact between the prism and the unworn surface of the ring was achieved. All tests were carried out at a constant room temperature of 30 °C. After 30 s, the temperature rise on the worn surface of the prism was measured by K-type contact thermocouples connected to the UTI-T UT320D measuring device. The width of the sputtering track on the prism is then measured using a TOOLCRAFT light microscope with a magnification of 50:1 and the computer program for image analysis Micro Capture Plus.

3.   Results and discussion

3.1. Surface roughness and hardness

The roughness profiles of the test samples are shown in Figure 3. The mean values of the roughness parameters are listed in Table 2. By comparing the values of the roughness parameters from Table 2, it can be seen that both nitriding procedures increase the roughness of the ring surface by about 1.5 times compared to the initial state. The roughness of the surface of the prism is created by sanding with sandpaper and differs slightly from the roughness of the ring. By comparing the roughness profile shown in Figure 3a, a typical profile of the ground surface on the non-nitrided sample "NN00" with a series of pits and a uniform ridge height can be observed. The roughness profile of sample "TF580", in Figure 3b, which is nitrated in the Tenifer salt bath, shows a larger number of ridges and micro-pits, and a smaller number of depressions. This type of surface topography is characterized by a microporous part of the junction zone composed of epsilon-nitride ($Fe_{2,3}N$) and gamma-prime nitride (Fe_4N), which is formed during nitriding in a salt bath. The compound zone grows on the surface of the nitrided steel by the diffusion of iron atoms from the interior of the material, the melting of ridges on the starting surface and the diffusion of nitrogen atoms from the salt bath. This growth of the compound zone creates its own characteristic surface topography, which, as a rule, increases the roughness of the initial surface. During the initial wear (running-in) of the tribocouple, the ridges on the roughness profile rapidly wear and the surface is smoothed. If the lubricant is present in the tribocouple, it remains in the micropores of the compound zone, which gives the nitrided surfaces the property of self-lubrication. Figure 3c shows the profile of the plasma nitrided surface on the "PN500" samples. Due to the short duration of the nitriding process (4 h) and the ratio H_2/N_2 = 1:3, the number of depressions and ridges on the

roughness profile is uniform. The reason for this change in the initial topography of the surface is the application of ion dusting by bombarding the sample with N^+, Ar^+ and H^+ ions in a vacuum, which smoothes the roughness profile and removes the oxide layer. Then, in the plasma nitriding phase, nitrogen diffuses into the surface layer and the formation of a very thin and compact zone of compounds composed mainly of iron gamma-nitride (Fe_4N). On the profile of the surface of the prism in Figure 3d, microgrooves and ridges characteristic of a surface sanded with sandpaper can be observed.

Table 2. Mean values of roughness parameters of test rings and prisms

Paramether	NN00	TF580	PN500	Prism
R_a, μm	0,050 ± 0,003	0,132 ± 0,025	0,127 ± 0,060	0,171 ± 0,031
R_z, μm	0,400 ± 0,039	1,040 ± 0,340	0,894 ± 0,215	1,401 ± 0,578
R_p, μm	0,150 ± 0,003	0,598 ± 0,360	0,587 ± 0,201	1,079 ± 0,683
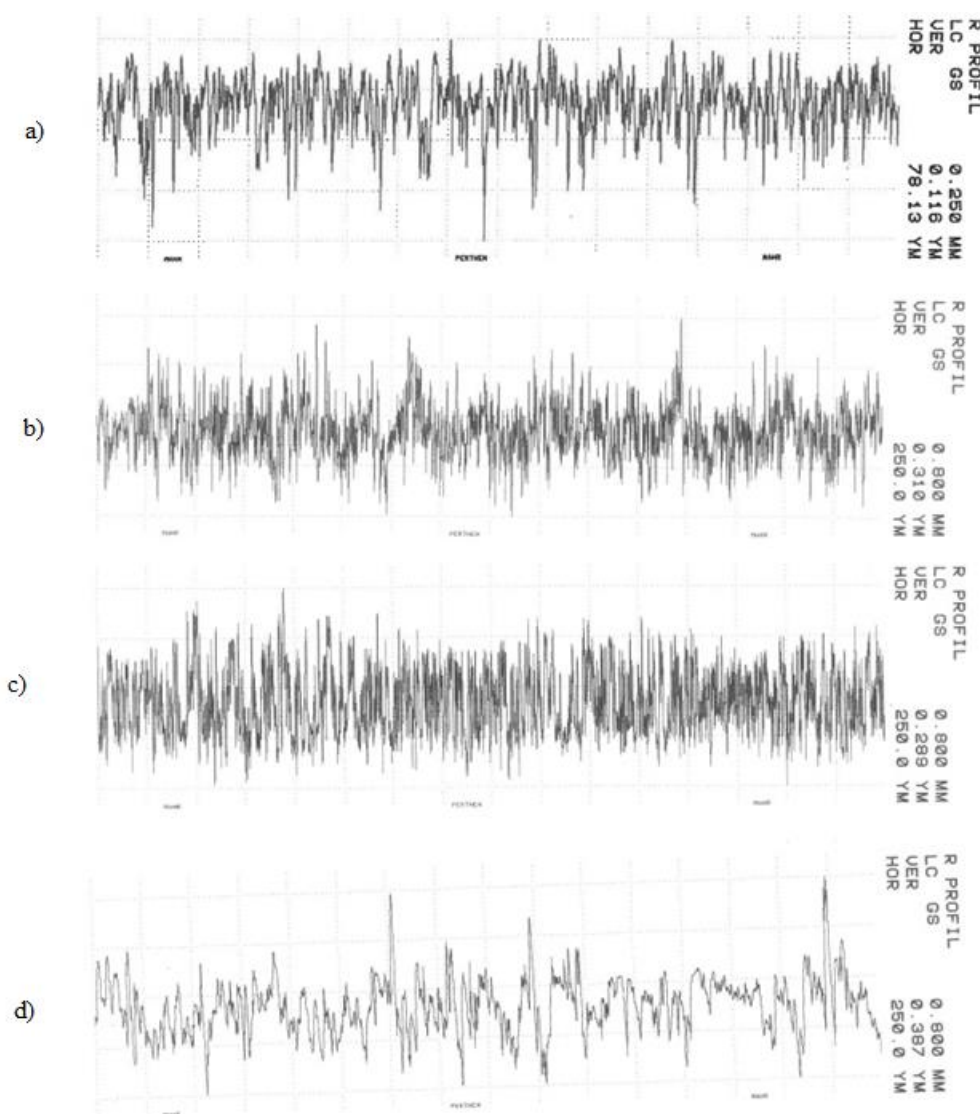
Figure 3.   Roughness profiles of test samples: a) NN00, b) TF580, c) PN500, d) prism

The surface hardness values of the test samples are listed in Table 3. Samples "NN00" made of hardened and low-temperature tempered steel EN DIN 100Cr6 showed the highest hardness value, 860 HV0.5. Nitriding with the TENIFER process (on "TF580" samples) and plasma nitriding (on "PN500" samples) results in a decrease in surface hardness due to additional softening at elevated temperature. The higher the temperature of the nitriding process, the stronger the softening of steel EN DIN 100Cr6. The hardness of the sample nitrided in plasma at 500 °C still remains at high values around 700 HV0.5.

However, nitriding in the Tenifer salt bath leads to a significant decrease in surface hardness to 510 HV0.5. This decrease in hardness is the result of the action of two influential factors: (1) elevated nitriding temperature, which reduces the hardness of the hardened steel core, and (2) deeper penetration of the indenter of the microhardness test device into the porous part of the compound zone created after nitriding in the salt bath. The hardness of the prism of 82 HV0.5 is ten times lower than the hardness of the non-nitrided ring and corresponds to the usual hardness values of lead bronze.

Table 3. Surface hardness of test samples determined by the Vickers method

	NN00	TF580	PN500	Prism
HV 0.5	860±35	510±30	700±50	82±18

3.2. Testing resistance to adhesive wear

Figure 4 shows the average temperature increase on the surface of the prism after sliding wear with and without lubrication. In the conditions of sliding contact between the prism and the ring without lubrication, the temperature rises two to four times higher than in sliding contact with lubrication. Also, with an increase in the ring's rotation speed, there is a greater heating of the surfaces in contact. The increase in temperature in the sliding contact between the prism and the ring without lubrication is the result of frictional forces, plastic deformation and separation of lead bronze particles that stick to the surface of the ring. Figure 5 shows the surfaces of the ring after 30 s of wear without lubrication. All the ring samples showed adhesion of lead bronze

wear particles from the prism. The greatest adhesion of the prism material was observed on the ring nitrided with the Tenifer process. This result can be explained by the higher mean surface roughness and the higher heights of the roughness ridges on the "TF580" sample, which causes the occurrence of a greater number of microwelds between the prism and the ring, compared to the other samples. In the non-nitrided sample "NN00" and the plasma-nitrided sample "PN500", smoothing of the surface of the ring appears at the point of contact with the prism, with practically no transfer of lead bronze from the prism to the ring. In the adhesive wear experiments with lubrication, no significant sticking of the lead bronze from the prism to the ring occurred, but the wear particles were carried away in oil droplets that continuously flowed through the tribocouple.

a)   b)
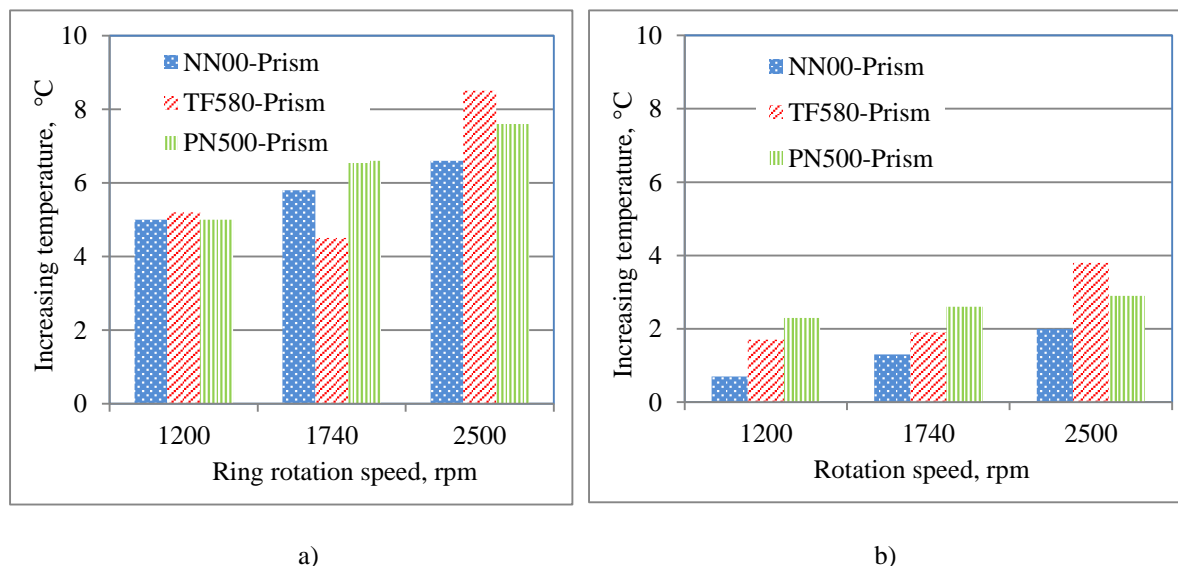
Figure 4. Temperature increase on the surface of the lead bronze prism after 30 s of adhesive wear: a) without lubrication, b) lubrication with synthetic motor oil SAE 5W-30
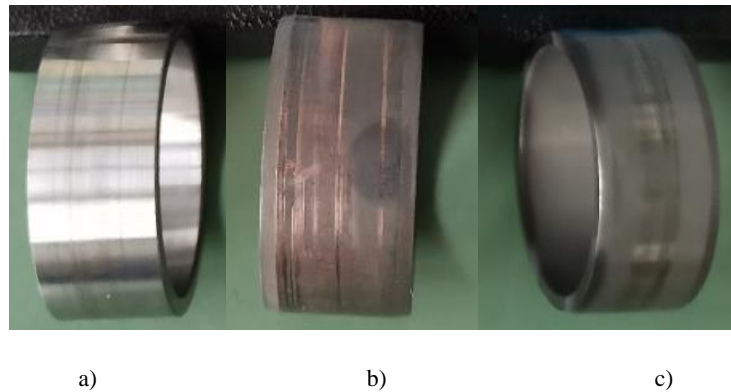
Figure 5. Adhesion of the prism material to the surface of the ring after 30 s of adhesive wear without lubrication on the sample: a) NN00, b) TF580, c) PN500

Figure 6 shows the change in the width of the wear track on the prism after 30 seconds of sliding contact with and without lubrication. In experiments without lubrication, the width of the wear track on the prism is greater than in experiments with lubrication. Figure 6a shows that in experiments with a tribocouple composed of a prism and a non-nitrided ring ("NN00") and a prism and a ring nitrided in Tenifer salt bath ("TF580"), the wear mark on the prism increases with increasing rotation speed ring. The wear trace on the prism in tribocouples with a plasma nitrided ring ("PN500") is higher than the wear trace in tribocouples with a salt bath nitrided ring for the same ring rotation speed. The increased width of the wear track on the prism, under conditions of dry friction between the nitrided ring and the prism, can be explained by intense microadhesive and microabrasive wear of the soft surface of the lead bronze on the prism by the action of the hard nitride zone from the surface of the ring.

In experiments with tribocouple lubrication with SAE 5W-30 engine oil, shown in Figure 6b, an increased wear mark is formed on the prism in contact with a non-nitrided ring at all tested ring rotation speeds. Also, a wide wear track was formed on the prism in the tribocouple with the sample nitrated in Tenifer salt bath at the highest rotation speed of 2500 rpm. In these cases, it can be assumed that there was boundary or mixed friction between the prism and the ring with intensive removal of lead bronze particles from the prism. In the experiments with a lubricated tribocouple composed of lead bronze and a ring nitrided in plasma ("PN500"), a small wear track was formed on the prism, at all tested rotation speeds of the ring. For these experiments, it can be assumed that hydrodynamic lubrication was achieved between the prism and the ring with the small adhesive wear.

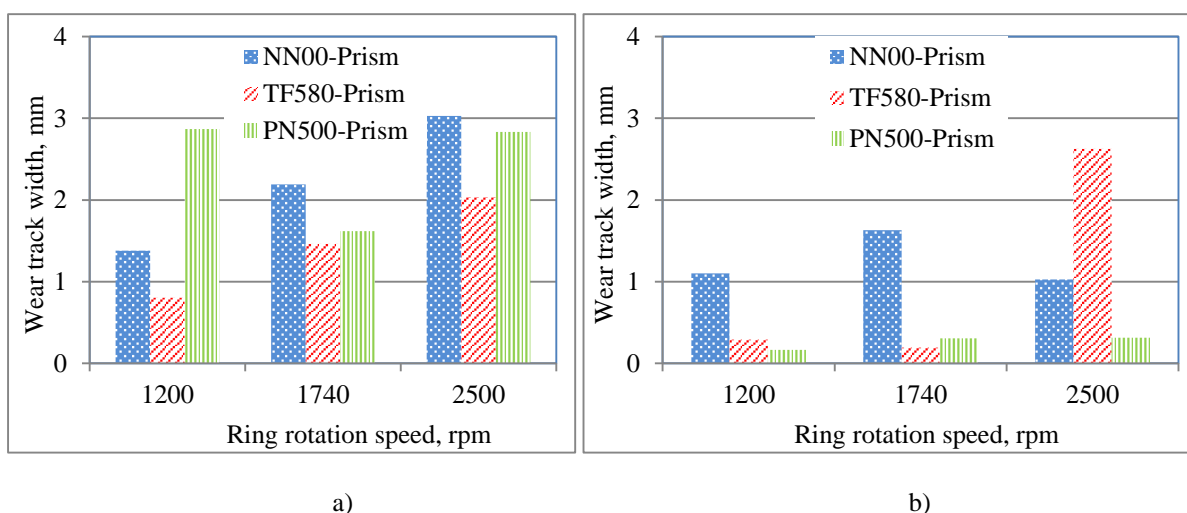**Figure 6.** Width of the wear track on the surface of the lead bronze prism after 30 s of adhesive wear: a) without lubrication, b) with lubrication with synthetic engine oil SAE 5W-30

4. Conclusion

Based on the tests of surface roughness, microhardness and resistance to adhesive wear under conditions of dry and mixed friction using the method of prism sliding on the ring, the following is concluded.

Nitriding of the surface increases the roughness of the surface due to the formation of a nitrided layer, the compound zone. The increase in the value of the mean roughness parameters Ra is about 1.5 times compared to the initial state. The nitrated layer creates its own surface topography, which depends on the chemical composition and compactness of the layer. After plasma nitriding, a more compact surface layer is formed with smaller horizontal gaps between ridges and depressions compared to the nitrated layer formed after nitriding in a salt bath.

In dry friction conditions, with the action of a small normal pressure force of the prism on the rotating ring of 6.31 N, after 30 seconds of adhesive wear, the surface of the prism heats up by 4 °C to 8 °C and the lead bronze removed from the prism sticks to the surface of the ring. The greatest adhesion of lead bronze appears on rings nitrated in salt water.

Using SAE 5W-30 motor oil significantly reduces the heating of the tribocouple and the width of the wear track on the prism. In all experiments with lubrication, after 30 s of adhesive wear, the temperature increase of the prism was less than 4 °C. The smallest heating of the prism with lubrication was achieved in the sliding contact with the non-nitrided ring, which can be explained by its smallest roughness and good wetting of the surface with SAE W-30 motor oil. The smallest wear trace on the prism, without material transfer from the prism to the ring, with engine oil lubrication, at all ring rotation speeds, was achieved in tribocouples with a plasma nitrided ring.

Nitriding of the bearing ring in plasma and continuous lubrication with engine oil achieved the least adhesive wear of the prism and the ring. So, this procedure can be recommended for improving the wear resistance of sliding bearings in a wide range of rotation speeds up to 2500 rpm.

In future research, it is recommended to examine the influence of the choice of lubricating oil, rotational speed and bearing load on the width of the bearing pad wear track, heating, vibration and noise of the bearing

Acknowledgements

REFERENCES

[1]   Khonsari, M. M., Booser, E. R 2017. *Applied tribology: bearing design and lubrication*, 3rd edition, John Wiley & Sons Ltd, New Delhi, India

[2]   Farleya, J., Wrobela, L.C., Maob, K. 2010. *Performance evaluation of multilayer thin film coatings under mixed rolling–sliding dry contact conditions*, Wear 268, 269–276

[3]   Bhadeshia, H.K.D.H., 2012. *Steels for bearings*, Progress in Materials Science 57, 268–435

[4]   Pinedo, C.E. 2003., *The use of selective plasma nitriding on piston rings for performance improveme*nt, Materials and Design 24, 131–135

[5]   Podgornik, B.,. Vižintin, J.,. Leskovšek, V., 1998. *Tribological properties of plasma and pulse plasma nitrided AISI 4140 steel*, Surface and Coatings Technology 108–109, 454–460

[6]   Landek, D., Jakopčić, M. 2019. *Povišenje otpornosti na trošenje čelika za visokoopterećene klizne ležajeve*, Zbornik radova MTECH 2019, Poreč, 57-64

[7]   Pye, D. 2003. *Practical Nitriding and Ferritic Nitrocarburizing*, ASM International, Metals Park, OH, USA

Comparison of macro and micro abrasive wear of hard PACVD coatings on tool steel EN DIN X37CrMoV5-1

Darko LANDEK[1], *Jurica JAČAN*[1]
Suzana JAKOVLJEVIĆ[1]

1) University of Zagreb, Faculty of
   Mechanical Engineering and Naval
   Architecture, Ivana Lučića 5, 10000
   Zagreb, **Croatia**

dlandek@fsb.hr
jjacan@fsb.hr
sjakovljevic@fsb.hr

Keywords

Micro-abrasive wear
Calotest
Steel X37CrMoV5-
PACVD TiN/TiCN
PACVD TIN/TIBN

Original scientific paper

Abstract: Abrasion resistance of thin hard coatings is a key property for their application. The paper compares the abrasion resistance of two coatings produced by plasma-assisted chemical vapor deposition (PACVD): gradient coatings TiN/TiCN and multilayer coatings TiN/TiBN, which were applied to tool steel EN DIN X37CrMoV5-1. The coatings were tested for roughness, microhardness, and adhesion. Abrasion resistance was tested using the "dry sand - rubber wheel" method according to ASTM G-65 and micro-abrasion wear was tested using a calotester device. In the calotest, the coating is worn by rotating a hardened steel ball made of steel EN DIN 100Cr6 coated with diamond paste. At the place of calotest wear, a spherical crater with a circular rim on the outer edge and the bottom of the crater is formed in the substrate material. The ratio of the outer and inner diameter of the circular rim around the crater determines the thickness of the coating. The outer diameter of the crater can also be an indicator of resistance to micro abrasion. By carrying out a series of calotests of different duration, from 10 s to 60 s, craters are created in coating and substrate. The diameter of craters were increased with the prolongation of the test. The paper compares the rate of wear on the same samples, determined according to both methods of abrasion resistance testing.

1. Introduction

Coating the surfaces of tool steel significantly increases wear resistance and extends the service life of the tool. Coating is usually carried out with thin tribological coatings composed of nitrides (TiCN, TiN, AlTiN, TiAlCN, CrN), borides (TiB, TiB2), carbides (TiC, SiC), carbonitrides (TiCN), oxides (Al2O3), carbon, etc. Coatings are applied as single-layer, multi-layer, with a gradient change in chemical composition, and as composite and multi-component (duplex layers). Physical vapor deposition (PVD), chemical vapor deposition (CVD) and plasma-assisted chemical vapor deposition (PACVD) procedures are used for their formation. In these coatings, a thin hard coating with a thickness between 1 μm and 10 μm is applied to the finely processed, polished, cleaned and degreased surface of the metal material. The properties of the coating (hardness, modulus of elasticity, fracture toughness, surface roughness, thermal expansion coefficient, residual stresses, wear resistance, corrosion resistance, etc.) depend on its chemical composition and microstructure, process parameters, and the properties of the metal substrate. The usual hardness of the coating is 2 to 5 times higher than the hardness of the substrate, which enables good resistance to abrasive wear. The type and parameters of the crystal lattice of the coating are usually different from the crystal lattice of the workpiece

material, which achieves good resistance to adhesive wear. Hard tribological coatings of nitrides, carbonitrides, carbides and borides are usually resistant to oxidation and elevated temperatures up to 500°C [1, 2, 3]. The characterization of the properties of tribological coatings usually consists of testing surface roughness and topography, thickness and adhesion of the coating, micro- or nano-hardness, fracture toughness, residual stresses and resistance to one or more wear mechanisms. The topography and roughness of surfaces are tested according to ISO 4288:1996 (Geometrical Product Specifications - surface texture profile method - rules and procedures for the assessment of surface texture).. The coating thickness is tested by destructive methods: calotest, light or electron microscopy, chemical analysis on a metallographically prepared section of the coating, and non-destructive methods, using ultrasound, eddy currents, etc. Residual stresses in the coating are usually examined by X-radiation according to the $\sin^2\psi$ method. The mechanical properties of hard tribological coatings are tested according to ISO 15787 (Technical product documentation – Heat treated ferrous parts), ISO 6507-1 (Vickers hardness test). The Palmqvist test is used to test the fracture toughness of hard coatings. Adhesion of the coatings is tested with the scratch test according to the ASTM D907-93c norm or with the Rockwell C indenter indentation test according to the VDI 3198 norm.

Symbols			
d	- inner diameter of the wear track, mm	R_a	- arithmetical mean height, μm
D	- outer diameter of the wear track, mm	R_z	- maximum profile peak height, μm
e	- coating thickness, mm	R	- radius of the calotest ball, mm
F	- normal force, N	s	- penetration depth in supstrate, mm
n	- rotation speed of the calotest ball, rpm	t	- wear time, s
P	- total penetration depth of the ball, mm	x_s	- wear path, m
P_p	- plasma power, W		

The micro-abrasion was tested according to the ISO 26424:2008 (resistance to micro-abrasion), ASTM D273, ASTM G99 (resistance to adhesion) and others [4, 5, 6]. In the international project EuropeAid - 131920/M/ACT/HR- ARISE – Advanced Research, Innovation and technology transfer in Surface Engineering (2013-2015) at the Faculty of Mechanical Engineering and Naval Architecture at the University of Zagreb, the technology of applying tribological coatings TiN, TiCN, TiBN was adopted by the PACVD process. The mentioned coatings are used in die casting tools and moulds, forging and pressing tools, polymer processing tools, etc. [7, 8, 9]. The particularity of the properties of tribological coatings investigated in the ARISE project and applied in industry is their good adhesion to the base of tool steels for hot and cold work, high hardness and good wear resistance. The hardness of the TiCN coating is from 1600 to 2200 HV0.01, while the hardness of the TiBN coating is from 2000 to 2500 HV0.01, depending on the microstructure and composition of the coating. The average coefficient of thermal expansion of the coating is: for the TiN coating, $9.35 \cdot 10^{-6}\,K^{-1}$, for the TiC coating $7.60 \cdot 10^{-6}\,K^{-1}$, for the TiB_2 $7.80 \cdot 10^{-6}\,K^{-1}$ [10, 11, 12].

The two most commonly used methods of testing the resistance to abrasive wear of hard coatings are the "dry sand-rubber wheel" method (standard ASTM G-65) and the micro-abrasion wear method with a rotating ball. Micro-abrasive wear of single-layer or multi-layer coatings with a thickness of 0.1 to 50 μm by rotating a hardened steel ball coated with abrasive paste over the coating was proposed and mathematically modelled in paper [13] in the nineties of the last century. In later works [14, 15], a mathematical model was developed to determine the speed of micro-abrasive wear of the coating and substrate depending on the diameter and speed of rotation of the ball, the size of the abrasive grain and the amount of added suspension and wear time. Two variants of micro-abrasive wear are proposed: (a) with a ball attached to a rotating shaft that presses against the coating with a certain force (b) with a freely rotating ball of a certain diameter (between 15 and 30 mm) that rests on one side of the rotating shaft, and on the other side to the test sample. The conditions under which abrasion occurs by scratching the coating with hard particles (so-called two-body abrasion) and abrasion of the smoothing coating (so-called three-body abrasion) are also determined [16]. Devices for the micro-abrasive wear method are relatively simple and inexpensive to manufacture. They can be used in laboratory and operating conditions to determine wear resistance, coating thickness (calotest) and preparation of the coating for analysis of the chemical composition by coating depth. The influencing parameters on the results of the micro-abrasion test are the following [13, 16, 17]: type, size and shape of abrasive; type and flow of abrasive slurry; material, load, rotational speed, diameter and surface texture of the ball.

The mentioned advantages of using the device and the conducted research on the reproducibility of the micro-abrasion wear test enabled the standardization of the method in the ISO 26424:2008 standard [17, 18]. Further development of the micro-abrasive wear method is aimed at improving the calotester by adding a sensor for determining the pressure force of the ball on the test sample and the friction force between the ball and the coating [19], the construction of a device with a ball and sample immersed in an electrolyte for determining tribocorrosion [20] and performance device with complex ball motion (rotation with oscillation) [21]. This paper investigates the influence of the duration of the calorimeter test and the speed of rotation of the ball

on the outer diameter of the calorimeter formed on PACVD coatings of TiN/TiCN, TiN/TiBN of test samples made of hardened and tempered tool steel for hot work EN DIN X37CrMoV5-1. The selectivity of the applied micro-abrasion test was compared with the wear resistance test results of the same coating/substrate systems tested with the conventional "dry sand/rubber wheel" abrasive wear method according to the ASTM G-65 norm.

2.   Materials and methods

The chemical composition of test samples made of tool steel EN DIN X37CrMoV5-1 is listed in Table 1. The samples were made by milling and grinding to dimensions of 50 x 25 x 10 mm. Sample markings and heat treatment parameters are listed in Table 2. In the hardened and tempered state, the hardness of the sample was 51±2 HRC. The mean coefficient of thermal expansion of steel EN DIN X37CrMoV5-1 upon cooling from 600 °C to 20 °C is 13.2 x 10^{-6} K^{-1}. After hardening and tempering, the samples were finely ground and

polished, cleaned and degreased in an ultrasonic bath with 95% ethanol, dried in air and additionally ionically cleaned of oxides in the plasma of the PACVD device by ion sputtering.

"TiCN" and "TiBN" samples were plasma nitrided in separate procedures, but with the same parameters. On the nitrated sample "TiCN" a basic coating of TiN with a thickness of about 1 μm was first applied, and then the growth of coating continued with a gradient transition of from TiN to the TiCN, with a change in the proportion of nitrogen, methane and precursor $TiCl_4$ per thickness of the coating. This resulted in a TiN layer at the bottom of the coating, while a TiCN layer was formed at the top of the coating. On the nitrated sample "TiBN" the basic TiN coating was applied analogously to the "TiCN" sample, and then by changing the proportion of nitrogen, methane and $TiCl_4$ and BCl_3 precursors, 43 layers of TiN/TiBN and the final layer of a multi-layer coating of the chemical composition TiB_2 were applied.

Table 1. Chemical composition of tool steel X37CrMoV5-1 according to the certificate of the manufacturer Uddelholm

wt, %	% C	% Si	% Mn	% Cr	% Mo	% V
X37CrMoV5-1	0.38	1.0	0.4	5.0	1.30	0,40

Table 2. Designations of samples and heat treatment parameters of tool steel EN DIN X37CrMoV5-1

Sample label	Hardening + tempering	Ion sputtering	Plasma nitriding	PACVD TiN/TiCN	PACVD TiN/TiBN
TiCN	400°C/870°C/ 1010°C/20 min/N_2 + 500 °C/2 h; +570 °C/2 h	500 °C/2 h; 4% Ar, 9% N_2, 87% H2; p = 2 mbar P_p = 1000 W	500 °C/6 h; 5% Ar, 5% N_2, 90% H_2; p = 2 mbar P_p = 1000 W	TiN: 500°C/1.5 h 4% Ar, 9% N_2, 85% H_2; 2% $TiCl_4$ TiCN: 500°C/6.5 h 4% Ar, 8% N_2, 83% H_2; 2% $TiCl_4$; 3 % CH_4 p = 2 mbar P_p = 2000 W	
TiBN					TiN: 500°C/2 h 4% Ar, 9% N_2, 85% H_2; 2% $TiCl_4$ TiBN: 500°C /7,5 h 4% Ar, 8% N2, 83% H_2; 5% BCl_3; p = 2 mbar P_p = 1650 W

After PACVD coating, a roughness test was carried out using a Perthometer S8P measuring device with a Gaussian filter lenght 0.8 mm and a probe radius 5 μm. An evaluation length of roughness profile was 4.0 mm. Based on 5 repeated measurements, the roughness parameters were determined: R_a and R_z, as well as the values of the estimated standard deviations.

According to the recommendations of the VDI 3198 norm, the adhesion test of the coatings was carried out. The Insize hardness tester and coating penetration force of 1471 N were used for the test. The appearance of the coating around the indentation point is evaluated according to the six classes shown in Figure 1. Classes HF1, HF2, HF3, HF4 show an acceptable appearance of the coating. Even and uniform microcracks are observed with minor indications of delamination. Unacceptable quality of the coating (grades HF5, HF6) will have a very pronounced delamination along the entire circumference of the indenter impression with many microcracks.
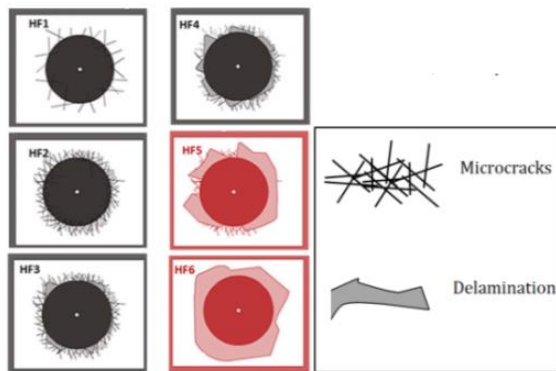
Figure 1.   Coating adhesion quality classes according to VDI 3198 test [22]

Resistance to abrasive wear was tested by the "dry sand - rubber wheel" method using an apparatus manufactured according to the ASTM G-65 standard, as shown in Figure 2. Samples with dimensions of 50x20x10 mm were subjected to a normal load of $F = 45$ N on a wear path of 358 m. The mass loss was measured after every 100 turns of rubber wheel. The diameter of wheel was 0.227 m. The quartz sand B35S with grain sizes of 0.063 to 0.355 mm was used as an abrasive jet with flux of 2.3 g/sec. Resistance to the abrasive wear was determined by measuring the mass loss of test samples in the Toledo mass balance with precision of ±0.0001 g.

Coating thickness determination and micro-abrasive wear tests were carried out on a TRIBOtechnic calotester with a freely rotating ball. The principle of the test and the main measures of the crater after wear are shown in Figure 3. The coating was worn by rotating a ball of example 15 mm made of hardened steel EN DIN 100Cr6,

onto which an emulsion with diamond grains with a mean diameter of 1 μm was dripped every 10 s.

For short-term wear, a spherical crater with diameter b is formed under the rotating ball. After longer wear, in which the coating is broken, a spherical crater with a circular rim on the outer edge is formed.
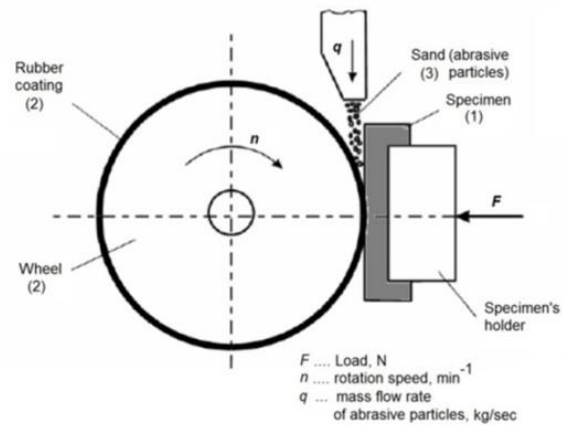
Figure 2.   Working principle of abrasion and erosion wear testing: (a) a tribosystem "rubber wheel – test sample – dry sand particles"
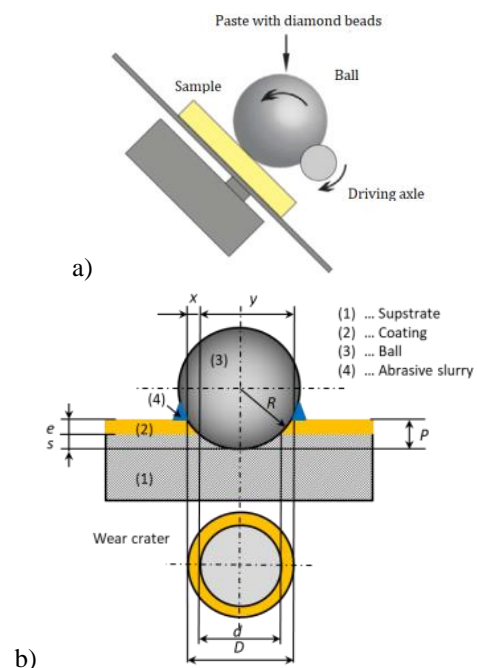
Figure 3.   Calotest: (a) working principle, (b) the principle of determining coating thickness after wear crater measurement

The inner diameter of the circular rim in Figure 3b is marked with d, while the outer diameter is marked with

D. The bottom of the crater is located in the base material at depth *P*, and the ratio of the outer and inner diameter of the circular rim determines the coating thickness.

The samples were placed at an angle of 45° in relation to the horizontal plane. Each sample was tested three times with a series of six calotests of different test durations (t_1 = 10 s, t_2 = 20 s, t_3 = 30 s, t_4 = 40 s, t_5 = 50 s, t_6 = 60 s), with with constant ball rotation speed n = 300 rpm. During this test a steel ball coated with diamond paste rotates at a constant speed on the coating's surface. The wear path (x_s, [m]) is determined based on the product of the ball circumference ($2R\pi$, [m]), rotation speed (*n*, [rpm]) and wear time (*t*, [s]):

$$x_s = 2 \cdot R \cdot \pi \cdot n / 60 \cdot t \qquad (1)$$

The thickness of the coating (*e*, [mm]) on a sample with a flat surface is determined as the difference between the total penetration depth of the ball (*P*) and the depth of penetration of the ball into the substrate material (*s*):

$$e = P - s \qquad (2)$$

From equation (2) and the geometric relations of the outer (*D*) and inner diameter of the wear track (*d*) and the radius of the ball (*R*), equation (3) follows for determining the thickness of the coating:

$$e = \frac{1}{2}\left(\sqrt{4\,R^2 - d^2} - \sqrt{4\,R^2 - D^2}\right) \qquad (3)$$

In the case when the conditions are met: $d < R$ and $D = R$, the thickness of the coating is determined by the simpler equation (4):

$$e = \frac{xy}{2R} = \frac{D^2 - d^2}{8R} \qquad (4)$$

The precision of coating thickness measurement depends on the roughness of the surface, the contrast of reflected light from different layers of the coating and the accuracy of the optical measuring system. The thickness of the tested coatings was determined from the wear marks formed after 60 s. The diameters of the wear marks formed after 10 s to 60 s of wear were measured using a TOOLCRAFT light microscope at a magnification of 200:1 with image analysis using the Micro Capture Plus computer program. The imprint of the indenter when determining the adhesion of the coating was analyzed on a TESCAN VEGA 5136 mm scanning electron microscope.

3. Results and discussion

3.1. Surface roughness

Test results of the surface roughness before and after the PACVD deposition are shown in Table 3 using the parameters R_a, and R_z. On samples made with the gradient coating TiN/TiCN the initial roughness was increased by about two times after sputtering and PACVD coating with layer TiN/TiCN. This can be explained by sputtering of ions from carbide and matrix which roughens its surface. Additional increasing in surface roughness is caused by the growth of the coating TiCN which form own surface topography. In samples

with a multi-layer TiN/TiBN coating, the roughness of the flat surface decreased. This can be explained by a good wetting of the surface by microdroplets of the TiN coating and filling of micro-pits in the surface when applying a new coating layer.
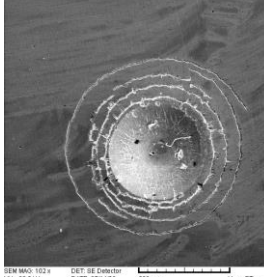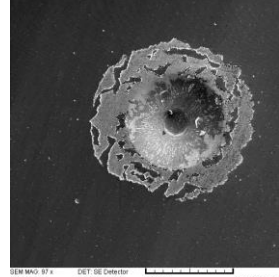
Table 3. Roughness parameters of steel test samples made from the tool steel EN DIN X37CrMoV5-1

	Non coated sample	Sample TiN/TiCN	Sample TiN/TiBN
R_a [µm]	0.047±0.003	0.086±0.013	0.042 ±0.003
R_z [µm]	0.528±0.089	1.222 ± 0.304	0.180 ± 0.021

3.2. Coatings thickness and adhesion

The adhesion of the coatings TiN i TiBN was tested with 6 prints on each sample. The results showed in Table 4 refer to good adhesion of the TiN/TiCN gradient coating compared to the TiN/TiBN multilayer coating.

Table 4. Thickness and adhesion quality of the PACVD coatings TiN/TiCN and TiN/TiBN deposited on tool steel EN DIN X37CrMoV5-1

Sample TiN/TiCN	Sample TiN/TiBN
e = 3.81 ± 0.55 µm	e = 3.55 ± 0.32 µm
HF 2	HF 5

The coating TiN/TiCN showed only microcracks, but without the appearance of delamination. The multilayer coating TiN/TiBN showed significant delamination around the edge of the impression site Delamination of the coating is probably a consequence of the difference in the coefficients of expansion of the coating and the substrate, due to which elevated residual stresses occur after cooling the TiN/TiBN coating from the application temperature. When cooling the TiN/TiCN gradient coating, the differences in the coefficient of expansion between the substrate and the coating are smaller and the coefficient of expansion of the coating continuously changes with the depth of the coating due to the change in chemical composition.

3.3. Coatings wear resistance

Figure 4 shows the mass loss in abrasion wear experiments using the "dry sand - rubber wheel" method. Wear experiments were performed on two samples measuring 50x20x10 mm which were heat-treated and coated in the same conditions. Reference samples for determining the increase in abrasion resistance were hardened and tempered samples of uncoated steels, labelled as "Non-coated". Comparing hardened and tempered uncoated samples, six times lower weight loss is observed in samples with the TiN/TiBN mulitlayer coating and fifty six times lower weight loss was determined in samples with the TiN/TiCN gradient coating. Such a small loss of mass on the gradient coating can be explained by its high hardness and good adhesion to the substrate (HF = 2). On the other hand, the weaker adhesion of the multi-layer TiN/TiBN coating and the occurrence of delamination during the test resulted in a weaker resistance to abrasion wear.

Figure 5 shows the increase in the diameter of the crater depending on the wear path after a micro-abrasion test lasting from 10 s to 60 s. In this test, the penetration of the coating occurred after 15 s of the test, that is, after 3.5 m of wear. Further wear is carried out with an increase in the diameter and depth of the crater that includes the coating and the substrate.
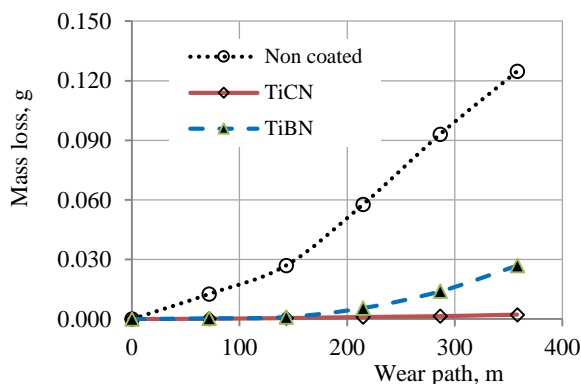
Figure 4.   Mass loss in abrasion wear test by "dry sand - rubber wheel" method on non-coated and coated steel samples

From the test results, a smaller increase in crater diameter can be observed on samples with a multi-layer TiN/TiBN coating compared to samples with a gradient TiN/TiCN coating. This wear result is consistent with the higher hardness and better micro-abrasion resistance of the TiN/TiBN coating compared to the TiN/TiCN coating. The wear test by micro-abrasion is carried out by gradually removing the layers of the coating with a very small normal pressure force of the ball on the coating (between 0.1 and 1 N). In these conditions, the wear of the coating can be tested independently of the wear of the

substrate and the adhesion of the coating to the substrate [13, 14].

Figure 6 shows the surface of the crater after 20 s of microabrasion testing on both coatings. Both images of wear show furrows directed parallel over the crater created by the action of abrasive diamond grains stuck to the surface of the ball, which indicates uniform micro-abrasive wear with the contact of only two bodies (abrasive and sample material) described in the paper [16].
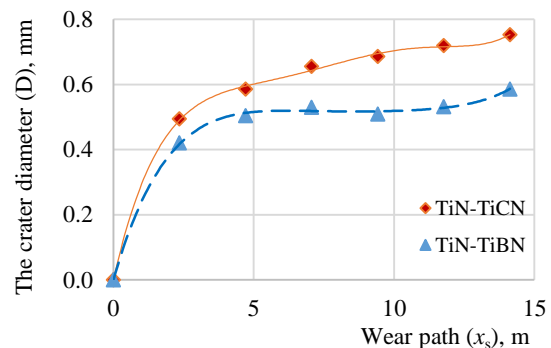
Figure 5.   Diameter of spherical cups after micro-abrasion tests on the PACVD coatings on tool steel X37CrMoV5-1.
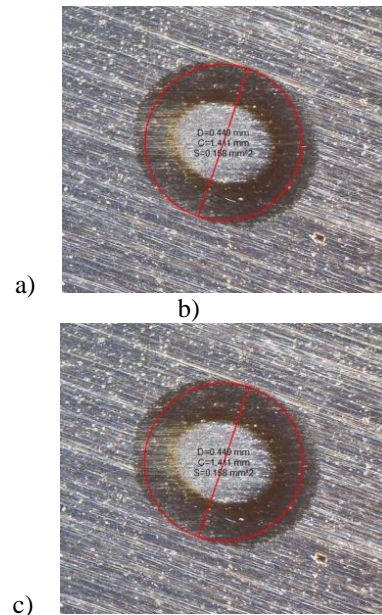
Figure 6.   Appearance of the crater surface after 20 s of micro-abrasion test on the PACVD coatings on tool steel X37CrMoV5-1: gradient coating TiN/TiCN, b) multilayer coating TiN/TiBN.

4. Conclusion

The application of hard tribological PACVD coatings TiN/TiCN and TiN/TiBN significantly increased the resistance to abrasive wear of tool steel for hot work X37CrMoV5-1. The application of the TiN/TiCN gradient coating increased the surface roughness by two times, while the TiN/TiBN multilayer coating kept the roughness similar to the uncoated surface. The TiN/TiCN gradient coating performed better on the X37CrMoV5-1 steel surface, while the TiN/TiBN multi-layer coating showed worse adhesion and delamination in tests according to the VDI 3198 method. In the tribological test using the "dry sand-rubber wheel" method, both coatings showed an increase resistance to abrasion compared to uncoated samples. At the same time, the TiN/TiCN coating showed significantly better resistance to abrasion with 12 times less mass loss compared to the TiN/TiBN coating. In the micro-abrasion test, the TiN/TiBN coating showed 28% better wear resistance than the TiN/TiCN coating.

From the above, the application of gradient PACVD coating TiN/TiCN can be recommended for tools for hot work tools in which coarser abrasive particles appear, such as tools for pressure casting or aluminum extrusion. The multi-layer PACVD TiN/TiBN coating can be recommended for tools for hot work tools with smaller abrasive particles in the workpiece material, such as tools for hot pressing powder materials, tools for glass casting, etc.

Further research will be aimed at searching for an optimal combination of the PACVD process parameters that would increase the adhesion of the tested coatings and their application to the dies and molds in exploitation conditions. Also, in the conducted tests, it was not possible to investigate the beginning of wear (on the wear path from 0 to 1.5 m) due to the parameters of the device, and in future research it is necessary to investigate the initial micro-abrasive wear in more detail.

REFERENCES

[1] Burakowski, T., Wierzchon, T., 1999. *Surface Engineering – Principles, Equipment, Technologies*, CRC Press, Boca Raton, London, New York

[2] Bunshah, R.F. (ed), 2001. *Handbook of hard coatings - Deposition Technologies, Properties and Applications*, Noyes Publications / William Andrew Publishing, LLC, Norwich, New York, USA

[3] Filetin, T., Grilec, K., 2004. *Postupci modificiranja i prevlačenja površina*, Hrvatsko društvo za materijale i tribologiju, Zagreb

[4] Kuhn, H., Medlin, D. (ed.), 2000. *ASM Handbook, Mechanical Testing and Evaluation*, Vol. 8, ASM International, Metal Park, OH, USA

[5] LI, J. Beres, W. 2007. *Scratch test for coating/substrate systems – a literature review*, Canadian Metallurgical Quarterly, Vol 46, No 2, 155-174

[6] Hawk, J.A., Wilson, R.D., Tylczak, J.H., Dogan, O .N. 1999. *Laboratory abrasive wear tests: investigation of test methods and alloy correlation*, Wear 225–229, 1031–1042

[7] Cajner, F., Landek, D., Kovačić, S., 2015 I*ntroduction and application of new tehnologies of plasma nitriding and PACVD coating*, Proceedings of the International conference "Mechanical Technologies and Structural Materials", Split

[8] Mitterer, C. Holler, F. Reitberger, D., et.all., 2003. *Industrial applications of PACVD hard coatings*, Surface and Coatings Technology 163 –164, 716–722

[9] Davis, J.R. (ed.), 2001. *Surface engineering for corrosion and wear resistance*, ASM International, Materials Park, OH, USA

[10] Bull, S.J., Bhat, D.G,. Staia, D.G, 2003. *Properties and performance of commercial TiCN coatings. Part 1: coating architecture and hardness modelling*, Surface and Coatings Technology 163 –164, 499–506

[11] Bull,S.J., Bhat, D.G,. Staia, D.G. 2003. *Properties and performance of commercial TiCN coatings. Part 2: tribological performanc*e, Surface and Coatings Technology 163 –164, 507–514

[12] Pfohl, C., Rie, K.T., 1999. *Wear-resistant PACVD coatings of the system Ti–B–N*, Surface and Coatings Technology 116–119, 911–915

[13] Kassman, A., Jacobson, S., Erickson, L., Hedenqvist, P., Olsson, M. 1991. *A new test method for the intrinsic abrasion resistance of thin coatings*, Surface and Coatings Technology, 50, 75—84

[14] Rutherford, K. L., Hutchins, I. M., 1996., *A Micro-Abrasive Wear Test, with Particular Application to Coated Systems*, Surface and Coatings Technology, Vol 79, 231–239.

[15] Matthew T. Siniawski , S. Harris, J., Wang, Q. 2007. *A universal wear law for abrasion*, Wear 262, 883–888

[16] Trezona, R.I., Allsopp, D.N., Hutchings, I.M. 1999. *Transitions between two-body and three-body abrasive wear: influence of test conditions in the microscale abrasive wear test*, Wear 225–229, 205–214

[17] Gee, M.G., Gant, A. et. all. 2003. *Progress towards standardisation of ball cratering*, Wear 255, 1–13

[18] ISO 26424:2008, *Fine ceramics (advanced ceramics, advanced technical ceramics)—Determination of the abrasion resistance of coatings by a micro-scale abrasion test*, Technical Committee:ISO/TC 206 Fine ceramics

[19] Cozza, R.C., 2013. *A study on friction coefficient and wear coefficient of coated systems submitted to micro-scale abrasion tests*, Surface & Coatings Technology 215, 224–233

[20] Bello, J.O., Wood, R.J.K., Wharton, J.A. 2007. *Synergistic effects of micro-abrasion–corrosion of UNS S30403, S31603 and S32760 stainless steels*, Wear 263, 149–159

[21] Resendiz-Calderon, C.D., Cabrera,L.I.F, C´azares-Ramírez, I. 2021. *A novel tester to examine micro-abrasion of materials in oscillating sliding contact – The case study of a total knee replacement biomaterial*, Wear, https://doi.org/10.1016/j.wear.2021.203661

[22] Vidakis, N., Antoniadis, A., Bilalis, N., 2003. *The VDI 3198 indentation test evaluation of a reliable qualitative control for layered compounds*, Journal of Materials Processing Technology 143–144, 481–485

Determination of critical temperature for pitting corrosion occurrence at welded 2205 duplex-duplex steel

Petar LJUMOVIĆ[1]*, Marko JAKOVAC*[2]*, Teo UGRINA*[2]*, Zvonimir DADIĆ*[1]

1) Faculty of Electrical Engineering, Mechanical Engineering and Naval Architecture, Rudjera Boskovica 32, 21 000 Split **Croatia**
2) Brodosplit d. d. Put Supavla 21, 21 000 Split, **Croatia**

petarlj@fesb.hr
jakovac.ma@gmail.com
teo.ugrina@brodosplit.hr
zdadic@fesb.hr

Keywords

Stainless steel
Duplex
*Pitting corrosion*
Welding
Seawater

Original scientific paper

Abstract: The aim of this paper was determination of the critical temperature at which pitting corrosion occurs in welded 2205 duplex-duplex steel. Its chemical composition and properties are given. Pitting corrosion and the conditions of its occurrence as well as the measures for protection against it have been specially treated. Also, duplex steel welding preparation procedures are described. The welding process of the specimen as well as its properties after welding is given as well. The microstructure of the specimen and its austenite-ferrite ratios were obtained and analyzed. Susceptibility to pitting corrosion was tested in simulated seawater atmosphere. Pitting corrosion resistance tests through conducted surface roughness analysis were performed and discussed for each set of parameters, which included time and temperature. The results showed that temperature elevation has a significant influence on pitting corrosion occurrence. Measured critical temperature value for pitting corrosion occurrence at welded 2205 duplex-duplex steel in simulated seawater conditions was 40 °C.

1. Introduction

Considering the fact that both, austenite and ferrite phase influence the duplex steel properties, it is useful to determine their ratio. The heat introduced during welding process can deteriorate the duplex steel structure, so it is of a great importance to control the temperature during welding. The difficulty with duplex steels welding is the heat affected zone, where lower corrosion resistance, decreased toughness or post-welding cracks may occur. To avoid this, defining of proper welding technology is needed by reducing time duration in critical temperature interval. It is necessary to control the heat input for every layer [1]. During welding processes at elevated temperatures, the whole microstructure in heat affected zone becomes ferritic. If certain ferrite-austenite transformation should not occur, negative influences on material properties emerge, toughness and corrosion resistance reduce. Therefore, different nickel-based added materials (3-4 % nickel) are used, which favour austenite forming in weld with keeping the austenite/ferrite ratio in balance. In heat affected zone, this control is not possible; moreover, achieving the relevant phase balance depends on certain skills and welding conditions [2, 3]. By increasing the temperature during welding, ferritic area expands. There, just beside the melting line in heat affected zone, rough ferrite grains

form surrounded by austenite matrix. By inducing a small amount of heat in welding process, quick cooling occurs which results in forming of mostly ferrite phases in heat affected zone. Slow cooling may lead to carbide, nitride or iron-nickel intermetallic compounds extraction, and brittleness at 475 °C [3]. Therefore, optimal temperature at which these two phases will be in balance should be found.
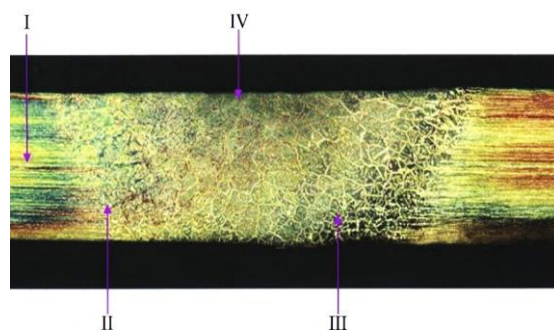
Figure 1. Macrostructure of welded 2205 duplex-duplex steel consists of: I. – base metal macrostructure; II. – low - temperature heat affected zone macrostructure; III. – high - temperature heat affected zone macrostructure; IV. – weld macrostructure [4]

Due to the low carbon content, occurrence of inter-crystal corrosion is reduced. Duplex steels in general have very good resistance to pitting corrosion due to low carbon content and high content of chromium, molybdenum and nickel. If the microstructure of duplex steel contains increased level of ferrite phase, or nitride precipitations occur in large ferrite grains, this will have a negative influence on materials pitting corrosion resistance. Welding behaviour of duplex 2205 stainless steel was analyzed, where comprehensive study was done right on the effect of welding on corrosion, mechanical properties and subsequently on the microstructure of 2205 stainless steel, pointing out the necessary parameter balance for the purpose of providing certain corrosion resistance, moreover showing primary pitting corrosion occurrence at HAZ [5]. Corrosion behaviour of duplex steel welds after short-time heat treatment was also analysed. In the tested range from 1020 to 1150 °C with holding time of 3 minutes, the highest pitting corrosion of the welds was obtained while heat treating at 1080 °C [6]. It was also established that the ferrite phase in the HAZ was the weaker phase, which confirms the thesis how much the HAZ in the 2205 duplex steels is sensitive structure wise and how it affects its corrosion resistance. Furthermore, ambient temperature pitting corrosion on 2205 duplex steels was analysed with the use of bipolar electrochemistry method, where corrosion pits formed by selected dissolution of ferrite phase [7]. The observations also showed that pit nucleation typically occurred at the ferrite–austenite interface, with pit growth via dissolution of the ferrite phase. The pitting corrosion occurrence of duplex 2205 steel welded by filler metal 2209 was also tested, after exposure to service temperatures [8]. The results showed that severe pitting corrosion and the largest metal loss occurred while heat treating at 850 °C, with holding times of 1 and 3 h. This reason for this is the presence of large amounts of intermetallic phases within the matrix at this temperature, which point out the importance of the particular intermetallic compound occurrence in 2205 duplex steel weld joint and their influence on 2205 duplex steel corrosion resistance or susceptibility. Corrosion behaviour of laser beam welded 2205 duplex steel in simulated body fluid was analysed as well. The results indicated that laser-welded AISI 2205 duplex stainless steel showed enough corrosion resistance in case of using it as a short-term implant in human body, which emphasise the usage possibilities of welded 2205 duplex steels in potential corrosive (organic) environment [9]. Duplex steels are commonly used in shipbuilding industry, so base metal and welded joints can be in direct contact with seawater. Nevertheless, poorly machined surfaces are generally not recommended for the marine exposure due to their grooved surface profiles which will endanger the

material's life drastically. Shot peening, laser shock peening and friction stir processing are significantly enhancing the surface properties of duplex 2205 steels which are strongly recommended in the corrosive environment [10].

The possibility of corrosion occurrence in these steels would significantly influence the stability and endurance of vessels, moreover maritime constructions in general. In experimental work, the susceptibility of welded duplex-duplex steel to pitting corrosion was tested, in simulated seawater conditions.

2. Experimental work

The experimental work was conducted in chemical laboratory at Brodosplit d.d. Shipyard Company. The specimen was previously welded at manufacturing plant at Brodosplit, with delta-ferrite content determination. The macrostructure of duplex steel welded joint consists of characteristic areas, showed in Figure 1. Specimen was then prepared and submerged into simulated seawater atmosphere solution.

After being kept in a solution for a certain time, measurements and determination of pitting corrosion existence were done.

2.1. Welding of steel plate

As the base material for specimen making, duplex stainless-steel 2205 (UNS S31803) was used, which chemical composition is given, Table 1.

Table 1. Chemical composition of 2205 duplex steel by mass proportion [11]

wt	C	Mn	Si	P	S	Cr	Mo	Ni	N
						min: 21.0	min: 2.5	min: 4.5	min: 0.08
2205 (S31803)	max: 0.03	max: 2.0	max: 1.0	max: 0.03	max: 0.02				
						max: 23.0	max: 3.5	max: 6.5	max: 0.20

Sheet thickness from which specimen was made was 12 mm. Welding was done by MAG process with powder-filled cored wire according to EN ISO 4063:2012. Wire diameter was 1.2 mm, and gas flow rate 18 l/min. The weld form was "V", in horizontal position. Inert gas mixture argon with 18 % carbon dioxide was used. For quality root welding purposes ceramic backing was used. This way, weld root could be welded with higher current which insured better weld quality. Steel plate was welded in eight layers, Figure 2.
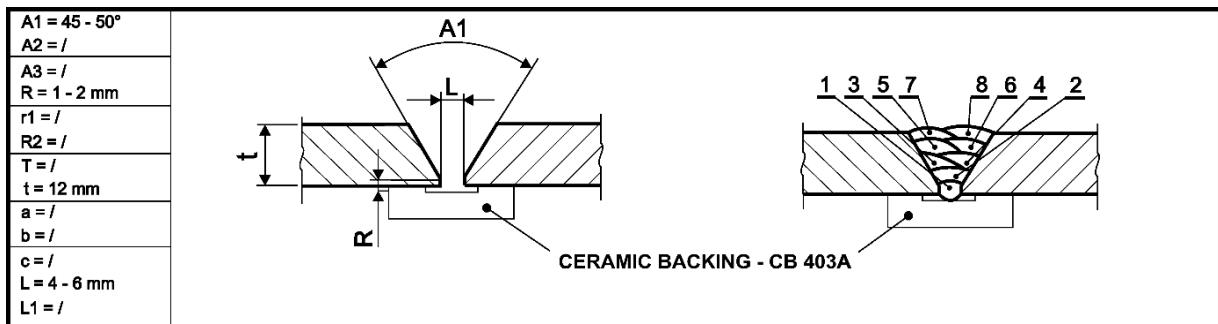
Figure 2. Welding preparation parameters with welded layers' scheme

2.2. Surface preparation of welded specimen

After the welding was completed, the specimen was cut out of the welded plate with the use of Struers LABOTOM-5 manual cut-off machine with coolant. Since no additional heat has been introduced, no apparent changes in microstructure have occurred. Specimen surface was then treated for rough edges, grease, dust and other impurities. Surface was then treated mechanically, to obtain smooth finish in order to remove any possible pits caused by pitting corrosion. For mechanical treatment, grinding and polishing device with rotating discs was used. To avoid specimen overheating, water was used. Grinding was done with grit designation P60. Then, finer grinding papers were used to a final P1500 grit designation, Figure 3.

Figure 3. Polished specimen prepared for further testing After all rough edges were eliminated, further testing and analysis of polished specimen were conducted.

2.3. Determination of delta-ferrite phase in welded specimen

If welding procedure was not done properly and the material is left with too much ferrite content, toughness decreases as well as corrosion resistance. This way stainless steel loses its primal properties. Therefore, it is necessary to determine the ferrite content after the welding is done. Ferrite content at welded duplex steel materials should be between 30 % and 65 %. The range

can be somewhat wider or narrower but never outside the interval 20-70 %. To make communication easier worldwide, internationally used term Ferrite Number [12] (FN, e.g. FN 30), is accepted for the purpose of marking the delta-ferrite content in stainless steel welded joints. Ferrite Number is commonly used as an indicator for certain welding characteristics, among which is weld resistance to hot cracking. Ferrite Number is not equal to volumetric content of ferrite (%). Although real content of ferrite cannot be measured precisely, relevant estimate of ferrite content can be obtained by dividing the Ferrite Number with factor f (% ferrite = FN/f), which is dependable on iron content in weld metal, Figure 4.
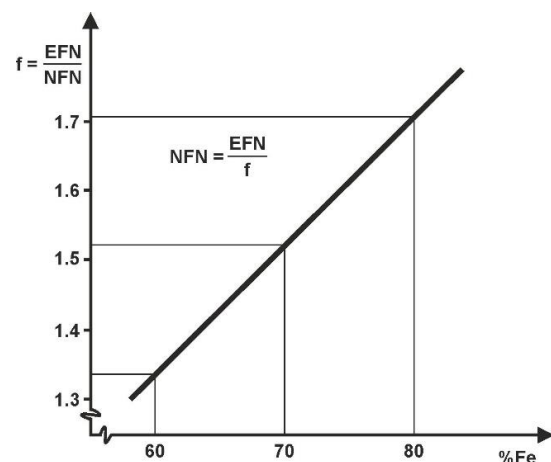
Figure 4. Factor f dependence on Fe percentage in weld metal [13]

Measuring surface must be thoroughly prepared and flat enough to ensure proper connection of the test probe. In this regard, weld area must be smooth, which was done by brushing. During the brushing process, no micro structural changes (martensite forming, colouring) should take place. Measuring area distance should be 40 mm with minimal width of 5 mm. There should not be

any leftovers from welding arcs, as well as impurities, magnetic particles, dust or lubricants.

Determination of delta-ferrite was done by FERITSCOPE FMP30 instrument. Prior to measuring, the instrument was calibrated by secondary standard in relation to EN ISO 8249. As ferrite is not evenly distributed in the material, the obtained results from one welded joint can vary from one measuring point to another. Therefore, measuring was done at 6 evenly distanced points distributed on the central line of measuring area.

Ferrite Number is an arithmetical mean of 6 individual measures, rounded to the next whole number. Measuring was done at room temperature of 21 °C. Measuring surface should not be exposed to any shocks or vibrations during measuring process. Welded specimen was submitted to ferrite content determination, and it fulfilled the condition of minimum, therefore maximum content. The results were presented for base metal, heat affected zone and weld. The microstructure was developed by etching in solution prepared by adding 5g of iron (III) chloride in the mixture of 10 ml of hydrochloric acid and 100 ml of water. After welding, mechanical treatment and ferrite phase measuring of the specimen, it was submitted to surface etching by the solution that simulates seawater atmosphere. Magnetic mixer that was used is IKA C-MAG HS 7. Pitting corrosion occurrence detection was conducted by MarSurf PS1 instrument made by Mahr GmbH Company.

3. Results and discussion

In base metal of prepared specimen, two-phase microstructure of duplex steel is clearly visible, with equal phase ratios, Figure 5. Average measured value of ferrite on the left side of the weld was 53.8 %, and 53.1 % on the right side. Values are satisfactory considering the optimal ferrite phase interval of 30-65 %. Unlike the microstructure in base metal, phases in heat affected zone are not clearly and evenly distributed. Temperature influence on material microstructure is visible, Figure 6. Larger grouping of phases occurred with consequently larger grains. The microstructure is not homogenous as it is in the base metal, which leads to the conclusion that mechanical properties in this zone are reduced as well as the corrosion resistance. The line that divides heat affected zone from the base metal is visible. Since duplex steels (austenite phase especially), are poor heat conductors, this line is particularly expressed. Measured ferrite values in the heat affected zone are 46.7 % on the left side and 45.8 % on the right side of the weld. The values are, as in base metal, in optimal range.

In weld microstructure, a clear difference in relation to base metal is visible, Figure 7.

The grain growth is obvious, and the measured ferrite content is somewhat lower. The ferrite average value is 40.9 % which is still satisfactory. Moreover, in weld zone, as well as in heat affected zone, grain growth

consequently brings reduced mechanical properties and corrosion resistance.

The measurements of ferrite phase are done in all three zones of the material.

The optimal ferrite value is established in every zone. In base metal, as well as in heat affected zone, measurements were done on both sides of the weld to be sure that the ferrite content is satisfactory through the whole specimen area. In both zones, the ferrite content was almost the same on every side.
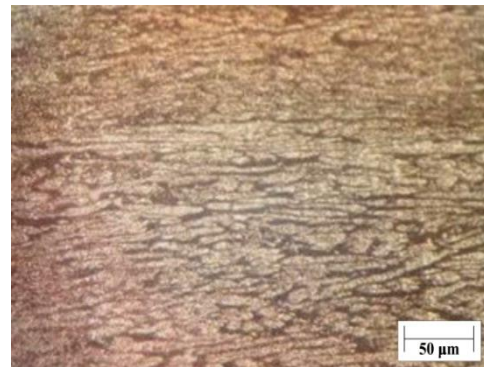

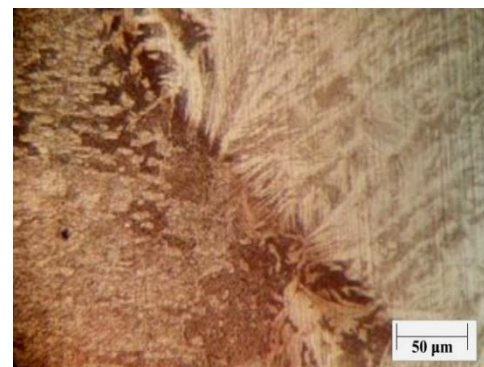**Figure 5.** Base metal microstructure

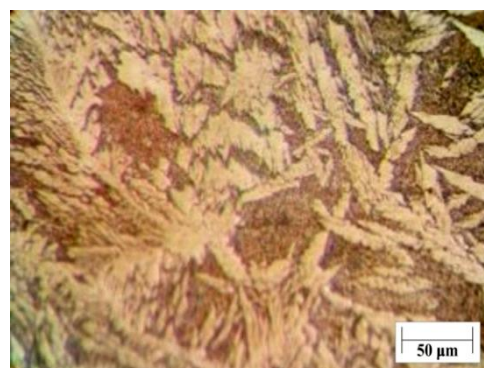**Figure 6.** Heat affected zone microstructure

Figure 7. Weld microstructure

Specimen was submitted to surface etching by the solution that simulates seawater atmosphere. Iron (III) chloride was used [14]. The solution contained 5 g of dissolved iron (III) chloride in 10 ml of hydrochloric acid and 100 ml of water, as it did for microstructure development shown earlier in the paper. The specimen was put into chemical container with prepared solution. The aim was to submit the specimen to simulated seawater conditions at three different temperatures. Test was conducted at 25 °C, 30 °C and 40 °C for the period of 72 hours, Figure 8.
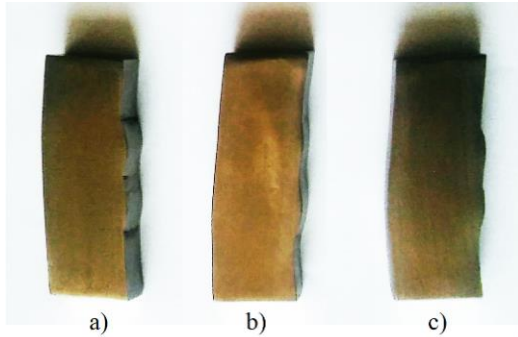
Figure 8. Specimen images after surface treatment for 72 hours with iron (III) chloride at temperatures a) 25 °C, b) 30 °C, c) 40 °C

Due to the relevance of the obtained results, after each testing regime was conducted, specimen was grinded to a final P1500 grit designation, polished then rinsed with 96 % ethanol and dried to its initial state. Moreover, roughness measurements were repeated as well, to ensure that specimen is brought to its original state and ready for the next testing cycle.

MarSurf PS1 instrument enabled simple surface roughness measurement. Path distance includes starting length "run up" which enables feeler carrier on measuring instrument to accelerate to certain constant velocity, and final length "run out" at which the feeler stops. Only the part of the Lt distance is measured therefore used for roughness grading and determination. Ln, in general, is mostly consisted of several referent distances Lr [15], Figure 9.

As it was pointed before, pitting corrosion is expected to occur in heat affected zone first, therefore in large-grained structure. Determination of critical temperature for pitting corrosion occurrence was initiated with specimen treated at 25 °C. MarSurf PS1 instrument has a measuring console which is its standard equipment as well as the integrated calibration block. Measuring feeler (2 μm in diameter) is made from diamond. It pressures the measuring area with the force of 0.7 mN.

Surface roughness has been the subject of experimental and theoretical investigations for many decades [16, 17]. Surface roughness measurements are expressed by parameters Ra, Rz, Rx or Tp. Parameters are obtained by measuring profiles from deepest valley to their highest peak with the combination of peak frequency mark in certain area. All roughness parameters that were used are defined by the ISO 4287 standard.

Referent distance or plain is a chosen dimension on which surface roughness is established, where no other imperfections are considered; such as chamfers, cavities, form deviations and others. Referent distances values are standardized [15] and they are: 0.08, 0.25, 0.80, 2.5, 8.00 and 25.00. Referent distance used in this work was 0.80 mm, due to the specimen characteristics.

Selection of instrument parameters was done in relation to the tested specimen. The finer surface finish was; the lower instrument border values were chosen. Furthermore, measuring distances depend on testing specimen distance itself. For this particular testing, chosen border values were 0.8 mm, with measuring distance 2.4 mm. The instrument was positioned on the specimen; roughness was measured by feeler movement on referent distance Lt which was 2.4 mm. After the feeler had passed the referent distance, roughness measurements were ready for analysis. As it was mentioned earlier in the paper, the occurrence of pitting corrosion is expected in heat affected zone, so that area was particularly surveyed.
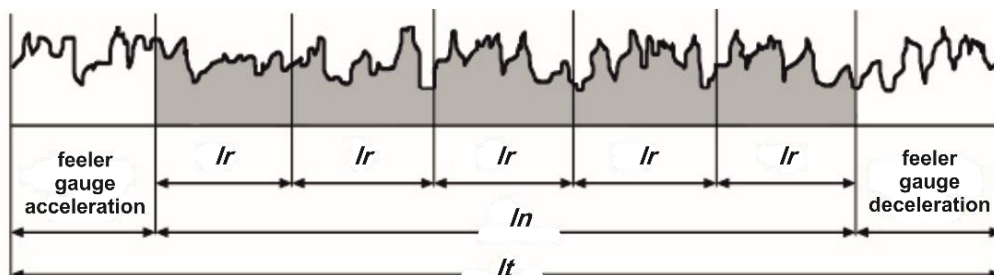
Figure 9. Characteristic distances of 2D roughness profile [15]
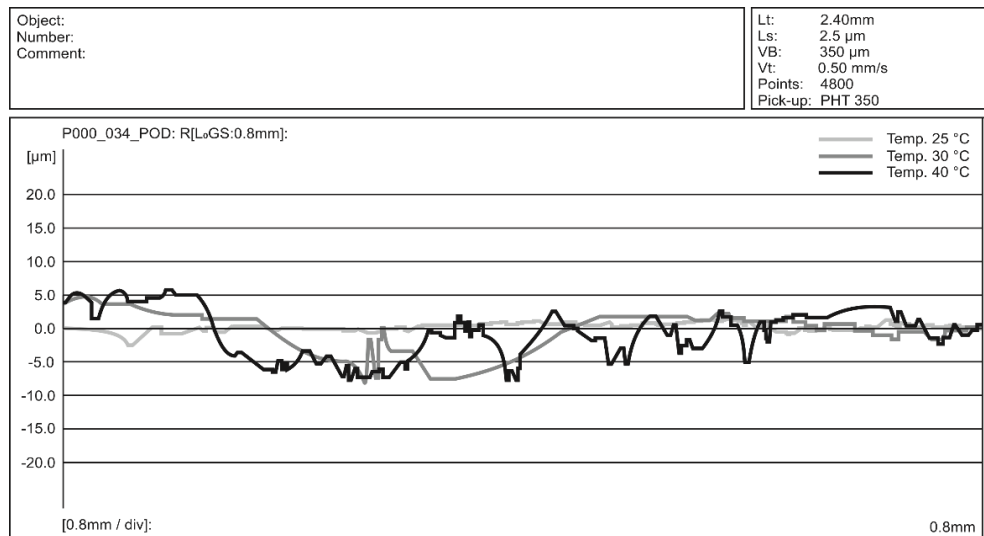
Figure 10. Surface roughness of the specimen treated in iron (III) chloride solution for 72 hours at 25, 30 and 40 °C

With no surface anomalies detected by visual inspection, neither the testing provided any anomalies in terms of pitting corrosion. The surface roughness measurement diagram for the specimen treated in iron (III) chloride solution for 72 hours at 25, 30 and 40 °C was obtained, Figure 10.

On Figure 10, it can be perceived that the biggest surface roughness deviation is noted at T = 40 °C. The deviations at this temperature are present regardless of specimen measuring position; base metal, weld zone or heat affected zone, with somewhat different, but nevertheless critical values.

MarSurf PS1 instrument read an arithmetic mean deviation of the assessed profile Ra, and maximum depth of the profile irregularity Rx, according to the instrument nomenclature. Ra value was 0.438 μm, while Rx was 5.3 μm. These results do not point out any pitting corrosion occurrence, according to ASTM G48. It can be stated that welded duplex 2205 steel treated in iron (III) solution for the period of 72 hours at 25 °C is pitting corrosion resistant. After bringing the specimen to initial state, testing was continued with same parameters apart from the temperature, which was elevated to 30 °C. Surface roughness results for the specimen submerged in iron (III) chloride solution for the period of 72 hours at 30 °C did not show any substantial occurrence of pitting corrosion. However, significant increase of Rx value was noted, which was 19.4 μm, and more than 3.5 times greater than in the first cycle. As it was expected, biggest peak values appeared in heat affected zone in which grain growth took place due to the welding process heat input. Values are not critical, but they do point out that temperature has a significant impact to surface roughness increase, therefore pitting corrosion occurrence.

The values measured at 40 °C pointed that pitting corrosion developed significantly. Rx value was 28.6 μm, which is, according to ASTM G48 standard, considered as pitting corrosion presence. This standard suggests that border value of Rx for pitting corrosion occurrence is 25 μm. Therefore, all values beyond 25 μm are considered as pitting corrosion existence. Surface anomalies are clearly noticeable from the diagram. Even before the specimen was taken out of the solution, by visual inspection it was clear that the surface did not stay smooth; moreover, the elevated temperature effect was noted, Figure 11. Pitting corrosion development is noticeable at the weld edges in heat affected zone, as it was expected.

Figure 11. Specimen image after iron (III) chloride solution treatment for 72 hours at 40 °C

4. Conclusion

In this paper, critical temperature for pitting corrosion occurrence at 2205 welded duplex-duplex steel was determined. According to the ASTM G48 standard,

border value of *Rx* for this type of corrosion occurrence is 25 μm. All values below the proposed one are not considered as pitting corrosion occurrence, which does not mean that they should be neglected. This type of corrosion is very hazardous because it is hardly visible. Once it evolves, then it is mostly too late for reparations. Therefore, it is important to survey every change in surface roughness since it is a parameter for potential pitting corrosion development. The testing was done in simulated seawater atmosphere. Considering the fact that average sea temperature is below 40 °C, it can be concluded that welded duplex steels are resistant to pitting corrosion in real conditions. From the diagrams obtained by Marsurf PS1 instrument, it is visible that temperature has a significant influence on pitting corrosion occurrence. At treatment with iron (III) chloride at 25 °C, surface roughness was almost negligible. With temperature increase by only 5 °C, significant increase in surface roughness is perceived; therefore, potential spots for pitting corrosion occurrence are noted. By elevating the temperature to 40 °C, definite occurrence of pitting corrosion phenomenon is recognized. From conducted experiments, it can be concluded that temperature has a significant influence on pitting corrosion occurrence and that the critical temperature value for pitting corrosion occurrence at welded 2205 duplex-duplex steel in simulated seawater conditions is 40 °C.

REFERENCES

[1] TMR Stainless, (2014), *Practical guidelines for the fabrication of duplex stainless steel*, International Molybdenum Association, London.

[2] D. Seferijan*, Metalurgija zavarivanja*, (1969), Građevinska Knjiga, Beograd.

[3] D. Kudumović, (1997), *Zavarivanje i termička obrada*, Fakultet elektrotehnike i mašinstva, Tuzla.

[4] V. Rede, (2004), *Utjecaj mikrostrukture zavara dupleks čelika na otpornost prema trošenju*, Fakultet strojarstva i brodogradnje, Zagreb.

[5] A. N. Chaudhari, K. Dixit, G. S. Bhatia, B. Singh, P. Singhal, K. K. Saxena, (2019), *Mater. Today*, Volume 18 (Part 7), 2731.

[6] Z. Zhang, H. Zhao, H. Zhang, J. Hu, J. Jin, (2017), *Corros. Sci.,* Volume 121, 22.

[7] Y. Zhou, D. L. Engelberg, (2020), *Electrochem. Commun.*, Volume 117, 1388.

[8] M. A. Elsaady, W. Khalifa, M. A. Nabil, I. S. El-Mahallawi, (2018), *Ain Shams Eng. J.*, Volume 9, 1407.

[9] C. Köse, (2020), *J. Mater. Sci.*, Volume 55, 17232.

[10] A. V. Jebaraj, L. Ajaykumar, C. R. Deepak, K. V. V. Aditya, (2017), *J. Adv. Res.*, Volume 8 (Issue 3), 183.

[11] Penn stainless inventory, (2021), *Duplex 2205 Specifications*, Penn Stainless Products, Quakertown .

[12] J. C. M. Farrar, (2013), *Weld. World.*, Volume 49, 13.

[13] EN ISO 17655, (2003), *Destructive tests on welds in metallic materials - Method for taking samples for delta ferrite measurement*, International Organization for Standardization.

[14] Diaz, David D., Miranda, Pedro, O., Padron, Juan, I., Martin. Victor. S., (2006), *Curr. Org. Chem*, Volume 10 (Number 4), 457.

[15] N. Zaimović-Uzunović, A. Softić, (2005), presented at *KVALITET 200*, Fojnica, B&H, pp. 371-374.

[16] E. S. Gadelmawla, M. M. Koura, T. M. A. Maksoud, I. M. Elewa, H. H. Soliman, (2002), *J. Mater. Process. Technol.*, Volume 123 (Issue 1), 133.

[17] M. Sedlaček, B. Podgornik, J. Vižintin, (2009), *Wear*, Volume 266 (Issues 3-4), 482.

Fatigue behavior of flash butt welds of high-strength aluminum alloy with high zinc content

Sviatoslav MOTRUNICH[1], **Ilya KLOCHKOV**[1], **Vitaliy KNYSH**[1], **Konstantin GUSHIN**[1], **Massimo ROGANTE**[2], **Anatoliy ZAVDOVEEV**[1]

1) Paton Electric Welding Institute of NAS of Ukraine, 03150 Kyiv, **Ukraine**

2) Rogante Engineering Office, Contrada San Michele n. 61, I-62012 Civitanova Marche, **Italy**

paton.testlab@gmail.com
main@roganteengineering.it
avzavdoveev@gmail.com

Keywords

Flash butt welding
Aluminium alloy
Microstructure
Mechanical properties
Fatigue

Original scientific paper

Abstract: The main purpose of this work is to investigate mechanical properties and microstructure peculiarities of flash butt welding (FBW) joints of high-strength heat treatable AA7056 with Zn content up to 9.8%. FBW technology shows good quality of welded joints of Al-Zn-Mg-Cu alloying system alloy, so the range of alloys that can be welded by FBW can be expanded.

A microstructural analysis of the metal in the welded zone of Al alloys has been carried out. Results of hardness measurements and tensile testing show the prospects of application of FBW technology for heavy loaded structural elements. FBW joints show tensile strength up to 90% of the values related to the base metal.

The fatigue behavior of Al welded joints under 0.1 stress ratio has been studied, showing that fatigue limit at $2 \cdot 10^6$ cycles of sound welded joints reaches the value of 150 MPa.

1. Introduction

High-strength thermally hardened Al alloys have found wide application in industry in the production of critical elements and structures in aircraft and rocketry. These alloys are strengthened by heat treatment, while acquiring high mechanical properties and maintaining sufficient technological ductility. Currently, for example, high-strength heat treatable aluminium alloys of 2XXX and 7XXX series are used for the principal structural elements of aircrafts and rockets and space shuttles manufacturing. Commonly, riveted joints are used, as alloys with complex alloying systems belong to the groups of hard-to-weld or until recently not welded alloys.

At the same time, a significant disadvantage of riveted joints is the increase in weight of the structure, due to the appearance of auxiliary elements when riveting the joined elements. Riveting is a time-consuming and costly operation associated with difficult working conditions. A careful surface treatment of the rivet hole is required to securely connect the product [1]. During long-term operation, the riveted joint is prone to loosening, which affects the service life of the products.

An effective way to solve the problem of increasing strength and quality of joints and improving the tactical and technical characteristics of aircraft (including reducing the structure weight and, accordingly, increasing the aircraft payload) is the use of welding instead of riveting. Various welding technologies are used for common aluminium alloys [2-7]. For hard-to-weld alloys such as AA7056, some complex and pricy welding methods like electron beam welding can be used [8]. FBW is widely used for low-alloyed and railway steels [9-12]. FBW, nevertheless, is also used for Al alloys [13-15], thus it is one of the promising ways to obtain high-quality welded joints with high mechanical properties for such tasks.

It is known that thermally strengthened alloys are sensitive to heat, the degree of their softening depending on heating temperature and holding time at a given temperature. In welding, the highest mechanical properties can be obtained when the duration of heating to temperatures above those critical does not exceed certain limits. This temperature cycle is difficult to ensure in welding of aluminium alloys, due to their high thermal conductivity. In this regard, it is necessary to provide intensive highly concentrated heat input into the heating zone, which can be implemented using the so called solid phase welding technologies. One of the promising methods of such welding procedure is the butt fusion welding.

Most welded structures are exposed to cyclic loads during operation. These loads lead to the formation of fatigue cracks in the metal structures, which, under certain conditions, lead to the rapid fracture of structures. Fatigue cracks in the welded joints could initiate from defects. The cause of such defects can be: inadequate design, high stress, incorrect choice of welding materials, unability to provide the required viscosity and weldability of joints, unsatisfactory performance of thermal cutting, poor penetration, undercuts, vibration, corrosive environment, operating loads. Fatigue fracture occurs without noticeable increase in deformations and it has the character of brittle fracture; in fact, it occurs in the area of plastic landslides. It is preceded by a long period of preparation and development, during which in some crystallites the sliding lines of mutually moving parts turn into intracrystalline cracks that damage individual crystallites. Damage from fatigue, thus, is local in nature; between cracks, the material retains its properties. As the number of cycles of damage increases, they move to neighboring crystallites, turning into a fatigue crack. Damage begins on the surface of the sample, often uneven and therefore often with significant stress concentrations.

In this regard, main aim of the study is the weldability of high-strength heat treatable aluminium alloys using FBW method. In order to demonstrate the prospects of this method, joints of AA7056 were obtained. This paper considers the formation of the structure, mechanical properties and fatigue life of high-strength heat treatable joints of AA7056.

2.   Research methods

The FBW process takes place in an automatic mode, which provides a stable high-quality connection. The design of welding equipment and technological equipment provides a combination of assembly and welding operations in a single cycle and high accuracy of the geometric dimensions of the welded joint. A prerequisite for obtaining high-quality welded joints from Al alloys is the formation of joints with extrusion of metal during settling in the gap between the forming devices. The degree of deformation increases as the knives converge. The scheme of the process of FBW with extrusion is shown in Figure 1. Forming devices perform two important functions - during deposition, they form joints in terms of volumetric-plastic deformation and perform the function of knives for cutting the grate. As a result, a welded joint is formed, which requires virtually no further mechanical stripping of the lattice (Figure 2).

Welding was performed on a laboratory machine type K724 equipped with a DC power supply with a capacity of 180 kVA and a drive with a deposition force of 160 kN. The total allowance for welding was 26 mm; welding voltage was 5.0-6.7 V; the final melting rate was 16 mm/s, the deposition rate was more than 150 mm/s.

Annealing of prismatic blanks with a cross section of 40×12 mm was performed at 450 °C for 1-5 hours.

Mechanical testing study was performed using the universal servohydraulic complex nanoBISS with a maximum force of 25 kN and MTS 318.25 with a maximum force of 250 kN. Samples for mechanical testing (Fig.3 a) were produced from obtained welded joints (250x40x12 mm) after heat treatment (HT).

Fatigue testing were performed under constant amplitude tensile loading with frequency 20 Hz and at stress ratio 0.1, which is one of most common for aerospace structures [16]. Specimens where tested either to fracture or up to $2 \cdot 10^6$ cycles.
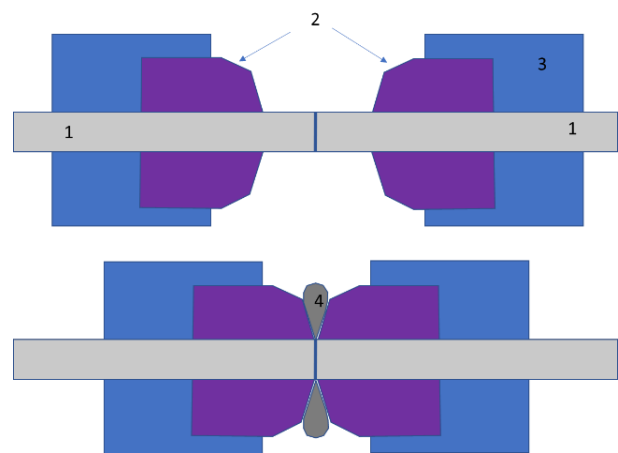
Figure 1.   Scheme of butt welding with the formation of the connection: 1 - parts; 2 - forming devices; 3 - current supply ; 4 - extruded metal

Figure 2.   Welded joint of AA7056 obtained by FBW

Specimens for fatigue testing was machined from the center part of welded plate (Figure 3 b) according to requirements of ISO 1099: 2017.

For structural analysis, several methods were used: microhardness, scanning electron microscopy (SEM, with a Tscan Mira 3 LMU facility), electron backscattering diffraction (EBSD from Oxford Instruments), and energy dispersive spectroscopy (EDS

from Oxford Instruments). The preparation of the metallographic specimens for microstructural studies was carried out according to standard methods using grinding papers of different roughness (P240, P400, P600, P1200, P2000). Final polishing was carried out on a diamond suspension with a polish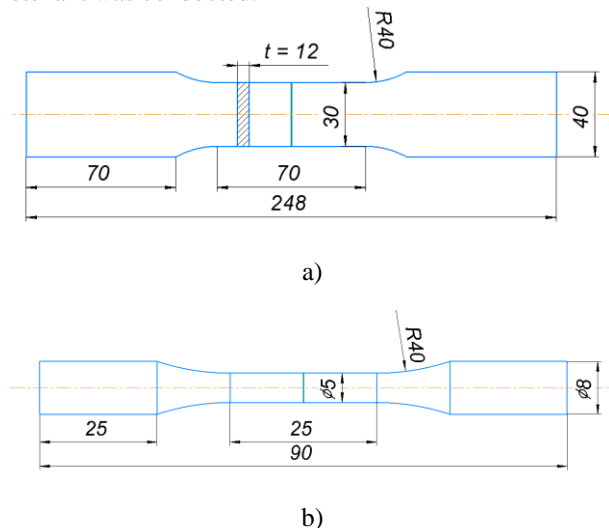ing particle size of 1 μm. To reveal and identify the morphology of the microstructure of the specimen, etching with a Keller's etchant was conducted.

a)

b)

Figure 3.   Geometry of samples made of welded plates of the AA7056, obtained by FBW, for tensile testing (a) and fatigue testing (b)

To assess the level of softening of the metal in FBW, hardness was measured on the prepared surface of the welded joint, by adopting the Rockwell method, i.e. indentation of a steel ball with a diameter of 1/16 inch with a force of 600 N. Measurements were performed in the direction perpendicular to the seam, the interval between measurement points being ≈ 1,5 mm.

3.   Results and discussion

3.1. Welded joint

The structure of the base material of the AA7056 is fine-grained with the location of excess non-equilibrium phases along the grain boundaries of the solid solution and in its middle. Zn, Mg and Cu form with Al and between them solid solutions and various metal compounds - phases M ($MgZn_2$), S (Al_2CuMg), T ($Al_2Mg_3Zn_3$), which play an important role in strengthening the alloy during its heat treatment. Since the alloy is high-alloy, its structure is thermodynamically unstable and inhomogeneous, which causes reduced ductility and, as a consequence, difficulties in its welding by FBW.
Previous studies of butt welding of the AA7056 on welding modes, which were tested for a similar alloy

(B95) did not allow obtaining high-quality welded joints. Oxide films were observed in the weld along almost the entire cross section of the weld, which were easily detected after the fracture of the samples under static loading. This is due to the much higher content than the B95 alloy of the main alloying element - Zn, which oxidizes much faster on the melting surface than Al.
In order to eliminate the structural features that complicate welding, namely reduced ductility, annealing was used to eliminate the non-equilibrium state of the alloy. At this temperature and under slow cooling, the supersaturated solid solution is completely decomposed, when the dissolved alloying components are again separated from the solid solution in the form of secondary phases. As a result, the ductility of the alloy increases, which improves weldability.
During welding, additional protection of the melting zone from air was used. The welding area was isolated from the environment by a disposable fiberglass chamber. As a result of melting, metal vapours with excess pressure were formed in the chamber, which prevented the access of air on the melting surface.
The selection and subsequent correction of welding modes were performed experimentally. Also, in the process of testing the welding modes, an express analysis of the quality of welded joints was carried out - bending of samples with an incision along the joint to fracture. The quality of the joints was assessed by the presence or absence of defects on visual inspection of the fractured sample at the weld (oxide films, etc.). According to the above mentioned method, effective modes have been identified that ensure the absence of defects in the connection line.
To improve the mechanical properties, joints samples of AA7056 were subjected to heat treatment (HT), i.e. quenching (465 °C 6 hours) + two-stage aging (120 °C 3 hours + 160 °C 3 hours).
To determine the structural features of the obtained compounds, metallographic studies were performed before and after HT. In the case of FBW in the deposition process as a result of metal extrusion between the forming devices, the texture of the weld is formed with a characteristic reversal of the fibers of the base metal at an angle close to 90° (Figure 4). During the aging of Al alloys, submicroscopic particles of the secondary phase are released, which form an irregular dislocation structure. The microstructure of the joint zone of the AA7056 is characterized by deformed elongated grains of solid solution with a high density of intermetallic phases in the form of elongated chains formed during heat treatment. In approaching the fusion zone, the intermetallic inclusions are crushed.
The weld metal has a characteristic fine-grained structure, contains grains of solid solution of Mg, Zn, Cu in Al and crushed intermetallic phases $MgZn_2$, T_{phase} ($Al_2Mg_2Zn_3$), S_{phase} (Al_2CuMg), size from 1 to 2 μm, oriented

in the direction of the metal flow during deposition.

It is possible to observe that in places of turn of fibers on 90°, there is a higher concentration of the alloying elements Zn, Mg, Cu, (according to energy dispersion analysis) due to partial melting, and significant efforts of metal deposition during welding. According to the results of studies of the welded joints' hardness distribution, it can be concluded that the total value of the softening zone is 14 to 16 mm, and the maximum value of weld softening does not exceed 5% (Figure 5).
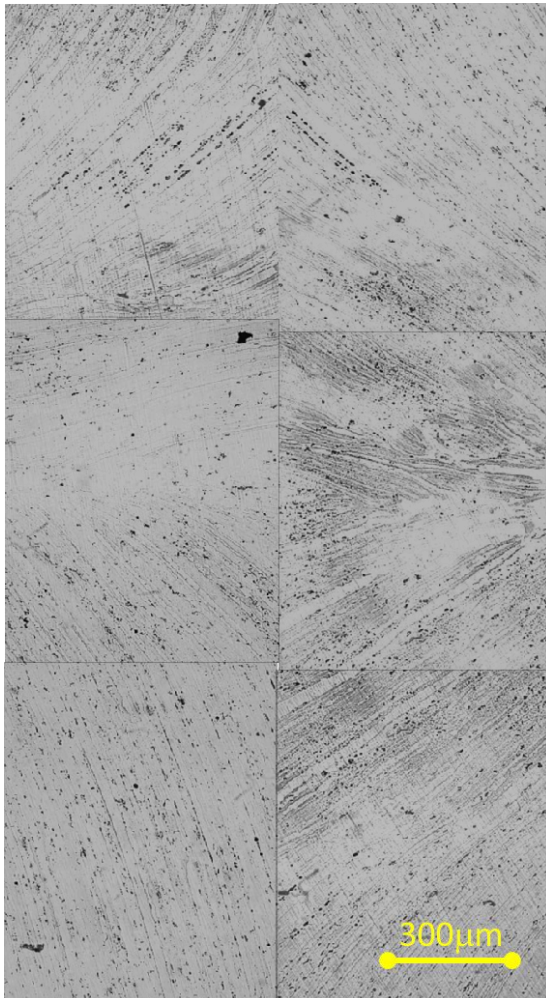
Figure 4. Macrostructure of the fusion zone of welded joints of the studied alloys obtained by FBW

Hardness measurement in the alloy zones and thermal zones showed that it is at the level of the corresponding values for the base material and it is 112 HRB for the investigated alloy. It is established, therefore, that the welded joints of the AA7056 obtained by FBW have high performance compared to the base material
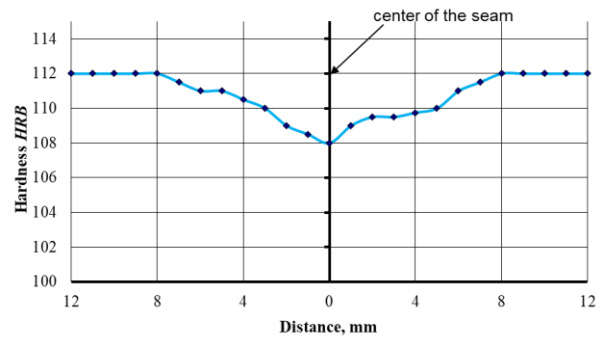
Figure 5. Distribution of metal hardness in the welded joint of the AA7056, made by FBW

The values of the tensile strength (Table 1) of the joints reach 524 MPa, which is about 90% of the corresponding values of the parent metal (UTS$^{o.m. 7056o}$=^{o}590MPa).

Table 1. Mechanical properties of welded joints of AA7056, made by FBW and after HT

Width	Thickness	E	YS	UTS	δ
mm	mm	GPa	MPa	MPa	%
29.3	12.4	72.9	501.5	519.1	2.3

3.2. Fatigue resistance of welded joints (BM + HT)

Fractures that occur at different stages of deformation, interatomic, intermolecular and other bonds, lead to some damage to the material, i.e. to its degradation. In the working process, sometimes, there is an intensive growth of macrodefects in the material, which can lead to premature fracture of individual elements and, as a consequence, to the loss of bearing capacity of the entire structure.

There are the following mechanisms for the development of cyclic hardening of steels and alloys: local adjustment within the sliding strips; dissolution of coherent and semi-coherent particles of secretions at reciprocating motion of dislocations through the particles of the second phase; weakening of the dispersed phase by repeated cutting dislocations of secretion particles; diffusion dissolution of release particles within stable bands slip; reconstruction of the dislocation structure near the particles of secretions.

The accumulation of fatigue damage in metals occurs as follows. From the first cycles of loading, deformation is observed. At the stage of cyclic microfluidity, as well as at the stage of microfluidity at static tension, microplastic deformation takes place on all metal volume, generally connected with the increase in density of dislocations on grain borders, generation of separate dislocations by initial sublimits and formation of dislocations. The most important feature of the metal's behavior at the incubation

period stage is that during the first load cycles there is more intense plastic deformation of the surface layer of the metal depth of the order of grain size. In the surface layers of the cyclically deformed sample at the cyclic microfluidity stage, sliding bands may be formed, the length of which is limited by the size of one grain. The stage of cyclic hardening completes the incubation period of the fatigue process associated with significant changes in the dislocation structure of the metal and its physical and mechanical properties and the emergence of the first surface submicroscopic cracks. During the emerging and development of submicroscopic cracks, there is a gradual increase of stable sliding bands in the surface, with the expansion of these bands and the merger of individual submicrocracks in the sliding strips in microcracks.

In the second period of fatigue, new volumes of metal are gradually attracted to the intense plastic flow until the entire metal surface is covered with a large number of relatively evenly spaced coarse sliding strips, which are actually microcracks equal in grain size. Thus, until the end of the cyclic microfluidity stage (stage length from 10^2 to 10^4 cycles, at maximum cycle stress equal to the fatigue limit), the entire metal cross section receives a small microplastic deformation and a layer of metal with high dislocation density is formed in surface grains. With a certain number of cycles, there is an avalanche-like macroscopic deformation of the entire cross section of the metal.

The beginning of the stage of cyclic fluidity is associated with macroscopic weakening, i.e. with a sharp increase in the intensity of "opening" of the hysteresis loop. "Tired" microstrips are usually located perpendicular to the propagation direction of fatigue microcracks. There are plastic and fragile fatigue microstrips. The first are the alternation of ridges and depressions. There are three types of plastic fatigue microstrips: intragrain non-crystallographic, intragrain crystallographic and intergranular non-crystallographic. The most common type of fatigue microstrips is the intragranular non-crystallographic.

Cyclic deformation at the stage of cyclic fluidity leads to changes in some physical and mechanical properties of the metal: increasing of micro-hardness, reducing of the metal ductility. It should be noted that with the onset of plastic deformation under cyclic loading, depending on the structure of the metal, the type of load and the test temperature, any change in the physical and mechanical properties of the metal can be observed. The total damage to the metal increases relatively intensively during the first 10% of durability, then in the range of 10-50% of durability comes a period of stabilization, followed by a new period of damage. This ends the period of accumulation of irreversible damage in the metal and begins the period of nucleation of microcracks.

Under tensile constant amplitude loading at stress ratio 0.1, 9-12 samples of each batch of samples were tested at different stress range values. Figure 6 shows the S-N curve of the base metal of the AA7056 after HT and the corresponding boundaries of the 95% confidence interval of the experimental data. For comparison, the previously obtained results of the fatigue test of the AA7056-T351 base metal are also given. The fatigue limit at $2 \cdot 10^6$ cycles of AA7056-T351 and AA7056 after HT is near the same shows 200-205 MPa.

However, fatigue limit at 10^5 cycles, shows that the base metal AA7056+HT is 24% lower than the corresponding values of AA7056-T351 in the initial state which gives 240 MPa. The fatigue curve slope in the double logarithmic coordinate system of the AA7056-T351 base metal in the initial state is m = 6.55, and after HT it is m = 16.43.

The S-N curves of the welded joints obtained by FBW is lower than curves of the base metal after HT in the entire region $10^5...2 \cdot 10^6$ cycles. The fatigue limit, at 10^5 and $2 \cdot 10^6$ cycles, of welded joints made FBW is 163 MPa and 120 MPa, respectively, which is about 60% to 68% of the corresponding base metal.
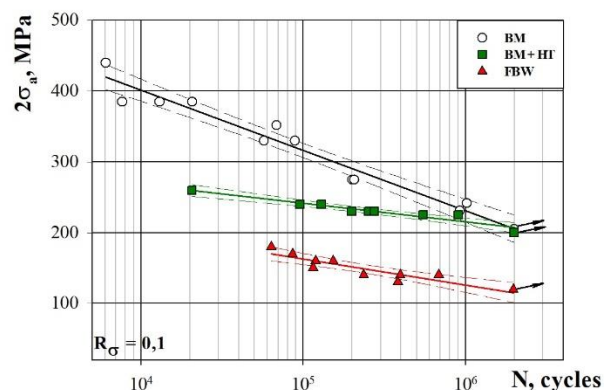
Figure 6. S-N curves at stress ratio 0.1 of the welded joints and base metal of AA7056-T351 alloy and the base material AA7056 after HT

3.3. Fractographic analysis of fractures of samples after fatigue tests

It is known that the nucleation of a fatigue crack during fracture occurs in local volumes of metal and its development takes place under conditions of constant increase in the amplitude values of the stress intensity factor. At the same time, there is a metal structure change in the area of accumulation of fatigue damage and there are characteristic features of the fracture surface. Fractographic analysis of micro-relief of fatigue fractures of laboratory samples allows determining the causes and foci of microcracks, to establish the nature of their development under cyclic loading, which creates a basis for physical and practical interpretation of fatigue processes occurring during fracture of materials and their welds.

Based on the conducted experimental studies of fatigue resistance of welded joints of the AA7056 obtained by FBW, it was found that nature of the samples fracture in the regular and studied process of random loading is significantly similar. The fracture of the samples during uniaxial stretching takes place on the weld metal, where structural changes and significant metal hardening are observed.

According to the visual analysis data of the fracture surface of welded joints samples of AA7056 after fatigue testing, all fractures have three characteristic zones: fatigue crack initiation ("b"), fatigue fracture with plastic deformation ("a") and fracture zone ("c", "d"), formed by the brittle-viscous fracture mechanism (Figure 7).
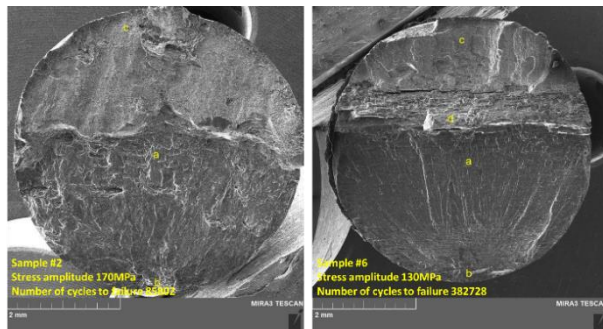
Figure 7.   Electronic image of the fracture of the samples of welded joints of AA7056 made by FBW (visible field 10 mm)

The presence of different topography of the fracture's relief sections indicates the heterogeneity of plastic deformation that accompanies the growth of the main fatigue crack during the testing of the sample. The area of the fracture where the fatigue crack arises is shiny, and the fracture zone is matte. On its relief there are cracks formed on the sample's surface. The origin of the fatigue crack and the destruction of sample #2 occurred in the fusion zone. In sample #6, the origin and development of the fatigue crack occurred in the fusion zone and the fractures sample occurred with the transition to the parent metal, as shown in Figure 7. In the fracture zone of sample #6 we can distinguish two characteristic zones, which are denoted by the letters "c" and "d" in Figure 7.

Images of the fatigue crack initiation zone are shown in Figure 8. Using fractographic studies performed by scanning electron microscopy, it was found that the topography features of the structural components of the fracture surface: i.e. the nuclei of fatigue cracks, associated with the nature of the microstructure of the activation energy when reaching the critical value of the stress range in the conditions of fatigue testing.

Chemical analysis of the metal was performed on the fracture surface of Sample # 6 (Figure 8) at the crack origin. The generalized results of the spectra are presented in Table 2.
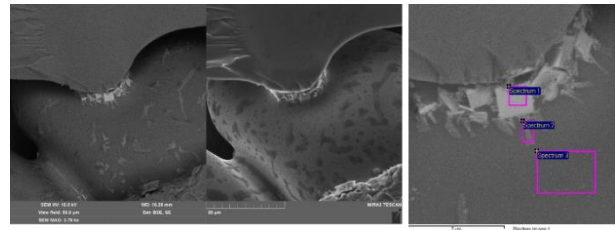

Figure 8.   Occurrence of fatigue crack in zone "b"

Table 2.   Chemical composition in the areas, wt.%

Spectr	O	Mg	Al	Ti	Zn	Zr
1	3.17	1.63	69.26	1.10	2.31	22.53
2	2.42	3.08	88.57		5.92	
3	3.45	2.39	90.15		4.02	

Analyzing the chemical composition of the spectra, we can say that the chemical element Zr is concentrated at the grain boundaries in the metal and its absence on the fracture surface is observed. The appearance of a fatigue crack and the nature of its development are usually due to the concentration of plastic shear in some of the most intense crystallites or grains of the parent metal. The localization of such shifts under cyclic loading usually occurs in the structural components of the surface layer of the sample. As a result, intense sliding bands are formed and a fatigue crack is formed along equally oriented crystallographic surfaces. The crack is a flat surface that grows in the radial direction, usually from the oxide film, near which the initial concentration of deformation under cyclic loads took place. Microcracks mainly originate from the sample's surface or in the sub-surface layers at the microdefects sites and they are oriented perpendicular to the axis of the sample.

It should be noted that the processes of fatigue crack initiation and growth till fracture occurs in Al alloys are as follows. Their essence is that the formation of the main fatigue crack occurs at high stress (above the critical values) by merging the germinal micro-cracks, and at low stress by developing one of them. Welded joints of Al alloys have a set of complex multiphase structures, so the mechanism of their destruction is quite complex and requires further special studies.

4. Conclusions

For the first time, the peculiarities of fusion butt welding of high-strength heat-strengthened AA7056 with high Zn content (> 9%) are considered.

The high mechanical properties of welded joints obtained by FBW give grounds to recommend this technology to produce joints of modern Al alloys. It is shown that in the

deposition process, as a result of extrusion of metal between the forming devices, a texture of the welded joint is formed with a characteristic reversal of the base metal's fibers at an angle close to 90°. It is established that HT leads to grinding of the structure of the fusion zone and to achieving maximum strength of welded joints. It has been found that in the AA7056 welded joints obtained by FBW: the metal hardness of the alloying zone is 5% lower than the corresponding values of the base material; static tensile strength reaches 90% of the strength of the base material.

Fractographic studies of specimens fractures tested under static tension were performed, which indicate the mixed nature of fracture. Areas with oxide films are observed in the fracture due to the high content of Zn in the welding alloy, which oxidizes much faster than Al on the melting surface.

S-N curves at constant amplitude loading at stress ration 0.1 of AA7056 welded joints made by FBW have been obtained. It is shown that the fatigue limit at 10^5 and 2×10^6 cycles, of the joints made by FBW is 163 MPa and 120 MPa, respectively, which is about 60% to 68% of the corresponding values of the base metal after heat treatment.

Fractographic analysis of weld metal fractures revealed signs of both viscous transcrystalline and brittle transcrystallite nature of joint fracture and showed that microcracks mainly originate in the subsurface layers at microdefects that are oriented perpendicular to the sample axis.

REFERENCES

[1] Saniuk, A., Cagáňová, D., Čambál, M., 2013. Performance Management in metalworking processes as a source of sustainable development. METAL 2013, Brno, Czech Republic

[2] Sahul, M., Turňa, M., Šugárová, J., Sahul, M., 2013. Influence of laser welding aluminium alloy on mechanical properties of welded joints. Manuf. Technol. 13, 526–530.

[3] Vyskoč, M., Sahul, M., Dománková, M., Jurči, P., Sahul, M., Vyskočová, M., Martinkovič, M., 2020. The Effect of Process Parameters on the Microstructure and Mechanical Properties of AW5083 Aluminum Laser Weld Joints, Metals 10/11, 1443.

[4] Motrunich, S., Klochkov, I., Poklaytsky, A., 2020. High cycle fatigue behaviour of thin sheet joints of aluminium-lithium alloys under constant and variable amplitude loading. Weld. World 64, 1971–1979.

[5] Sahul, M., Sahul, M., Haršáni, M., Dománková, M., 2020. On the microstructure and mechanical properties of AW2099 aluminium lithium alloy

[6] Motrunich, S., Poklatsky, A., Klochkov, I., Rogante, M., Zavdoveev, A., 2021. Basic advantages of thin-sheet AA5056 alloy joints produced by friction stir welding. MTSM2021, Split, Croatia

[7] Lukinenko, A.O., Motrunich, S.I., Bajić, D., Kuleshov, V.A., Pokliatskyi, A.G., Labur, T.M., 2021. Noise level assessment and mechanical properties of welded joints of aluminium alloys of the Al-Cu-Li system in FSW and TIG welding. FME Trans. 49, 220–224.

[8] Nesterenkov, V.M., Motrunich, S.I., Berdnikova, O.M., Klochkov, I.M., Polovetskyi, E.V., 2021. Elevation of the Fatigue Resistance of the Joints of 7056-T351 Aluminum Alloy Obtained by Electron-Beam Welding. Mater. Sci. 56, 830–836.

[9] Li, M., Xu, P., Zhou, L., Wei, Z., Liang, Y., 2020. Better mechanical properties via uniform microstructure architecture in flash-butt welded TA19 joints. Mater. Sci. Eng. A. 788, 139545.

[10] Sheng, X.W., Zheng, W.Q., Yang, Y., 2020. Tensile and high-cycle fatigue performance of HRB500 high-strength steel rebars joined by flash butt welding. Constr. Build. Mater. 241, 118037.

[11] Ribeiro, H.V., Lima, M.S.F., Marcomini, J.B., Pinto, F.C., Baptista, C.A.R.P., 2022. Fatigue Crack Growth on Flash Butt Welded and Laser Beam Welded Joints in a High-Strength Low-Alloy Steel. J. Mater. Eng. Perform.https://doi.org/10.1007/s11665-022-06795-4

[12] Shajan, N., Arora, K.S., Asati, B., Sharma, V., Shome, M., 2018. Effects of Post-Weld Heat Treatment on the Microstructure and Toughness of Flash Butt Welded High-Strength Low-Alloy Steel. Metall. Mater. Trans. A 49, 1276–1286.

[13] Bi, Y., Luo, Z., Guo, J., Yang, Y., Su, J., Zhang, Y., 2022. Joint formation mechanism and performance of resistance butt spot welding for AA 5754 aluminum alloy sheet. Mater. Lett. 319, 132279.

[14] Kuchuk-Yatsenko, S.I., Chvertko, P.N., Semyonov, L.A., 2010. Peculiarities of flash butt welding of high-strength aluminium alloy 2219. Pat. Weld. J. 3, 7–9.

[15] Kuchuk-Yatsenko, S.I., Hushchyn, K.V., Ziakhor, I.V., Samotryasov, S.M., Zavertannyi, M.S., Levchuk, A.M., 2021. Structure and mechanical properties of 2219-t87 aluminium alloy joints produced by flash butt welding. Pat. Weld. J. 8, 27–32.

[16] Yıldırım, H.C., 2014. Fatigue strength assessment of HFMI-treated butt welds by the effective notch stress method. Weld. World. 58, 279–288.

joints produced with electron beam welding. Mater. Lett. 276, 128276.

Stress-corrosion cracking of steels for main gas pipelines

Lyudmila NYRKOVA[1]*, Larysa GONCHSRENKO*[1]*, Pavlo LISOVYI*[1]*, Svetlana OSADCHUK*[1]*, Anatoly KLYMENKO*[1]*, Valery KOSTIN*[1]

1) E.O. Paton Electric Welding Institute of the National Academy of Sciences of Ukraine, **Ukraine**

lnyrkova@gmail.com
larikgon153@gmail.com
lisovyi.pavel@gmail.com
svetlanaosadchuk@meta.ua
aklimenko@meta.ua
valerykostinepwi@gmail.com

Keywords

Stress-corrosion cracking
Cathodic protection
Maine gas pipeline
Steel

Original scientific paper

Abstract: Comparative studies of the susceptibility to stress-corrosion cracking of steels for main gas pipelines (09G2S, 17G1S and 10G2FB) in the conditions of cathodic protection in the model soil electrolyte NS4 were carried out. The borders of polarization potentials outside which the mechanism of stress-corrosion cracking of these steels changes are determined. It is established that the concentration of hydrogen, penetrating into these steels under cathodic polarization varies nonlinearly depending on the polarization potential and differs for steels of different chemical composition. The obtained regularities indicate the possibility of the development of stress-corrosion cracking with different rates and patterns under other identical conditions.

1. Introduction

Stress corrosion cracking (SCC) is the most dangerous type of corrosion-mechanical failure of main gas pipelines. The origin and development of corrosion crack, which leads to the emergence of this phenomenon, continues to study [1]. During operation on the outer cathodically protected surface of the pipe SCC develops as single and multiple cracks [2].

Last 10 years' researching's is aimed to determine the factors of SCC from the influence of variable parameters, in particular the polarization potential, alternating current, temperature, etc. Many studies are devoted to the study of the behavior of high-strength steels of the new generation categories X70, X80, X90, X100 [3-6].

The susceptibility of steel to SCC depends on the microstructure, chemical and mechanical influences, external and internal factors. In some cases, SCC can be initiated by hydrogen, which is formed under cathodic polarization. Using polarization curves method, it was shown that the sensitivity to SCC of the samples of welded joint of X90 pipe steel with the straight seam is higher than the base metal in NS4 solution [7]. There are three mechanisms of SCC for this steel (anodic dissolution at corrosion potential; mixed mechanism – at potential from -850 mV to -1000 mV; hydrogen embrittlement – at potentials from -1000 mV to -1200 mV).

A critical factor that increases the sensitivity to SCC of X70 steel in model seawater is alternating current (including its frequency), which accelerates the mass transfer and generation of O_2 in situ as well as the hydrogen reduction [8].

For X80 steel, the susceptibility to SCC cracking, which occurs by mixed mechanism (anodic dissolution and hydrogen embrittlement), in neutral NS4 solution increases with increasing alternating current density [9, 10].

Of interest there are the results presented in [11] about the presence of a synergistic effect of cyclic loading and cathodic protection in the soil environment under the exfoliated cover on the initiation of corrosion cracking of steel X65. It is noted that increasing the tests duration and the maximum stress increases the probability of cracking in the potential areas in which susceptibility to local anodic dissolution is high.

In work [12] noticed that the effect of plasticity of X70 steel in neutral solution induced by hydrogen in a certain range of cathodic potentials, which reduces the probability of SCC due to reduced concentration and stress intensity at cracks' initiation.

Unstable cathodic polarization by the method of rectangular polarization compared to the potentiostatic mode of polarization of X80 steel at a slow strain rate in acidic soil solution accelerates both anodic dissolution and cathodic hydrogen reduction, causing to increasing of susceptibility to SCC [13].

SCC mechanism of X80 steel is associated with anodic dissolution. The steel demonstrates lower susceptibility

---

Symbols

C_H	- the hydrogen concentration, which penetrate through the steel membrane at cathodic polarization, mole/m^3	ψ_{air}	- relative narrowing of samples in the air, %
E	- electrode potential, V	ψ	- relative narrowing of samples, %
E_{pol}	- polarization potential, V	ψ_s	- relative narrowing of the samples in solution, %
i	- current density, A/m^2		**Subscripts**
$i_{res.cor.}$	- residual corrosion rate, mm/year	H	- hydrogen
K_S	- dimensionless coefficient for estimation of susceptibility to SCC	us	- ultimate strength
P	- stressб Ь3ф	y	- yield strength
S	- cross-sectional of the specimen, mm^2 A/m^2	S	- cross-sectional area of the specimen
		res. cor.	- residual corrosion
	Greek letters	*s*	- solution
δ	- relative elongation, %	air	- air
σ_{us}	- ultimate strength, MPa	pol	- polarization
σ_y	- yield strength, MPa		

to SCC than it welded joints at polarization potential of -900 mV (chloride-silver electrode, c.s.e.), and show a higher sensitivity to SCC at -1200 mV (c.s.e.), while due to the synergistic effect of stress and hydrogen influence, the mechanism of crack prolongation is hydrogen cracking. Welded joint is usually more sensitive to SCC than the base metal at the same potential, and cracking occurs in the heat affected zone due to metallurgical phase transformations and residual stresses arising during the welding process [14].

It is established that the susceptibility to corrosion cracking of X52 steel at a slow strain rate 10^{-6} inches/s in the soil electrolyte at room temperature increases with increasing plasticity and strength. The highest susceptibility of steel to SCC was obtained at a polarization of -400 mV (from the corrosion potential), and the fracture is brittle and has transcrystalline character, which was explained by the hydrogen mechanism [15].

Laboratory simulation of degradation in the operation of pipe steels of different strength mode, the essence of which is in the combined action of axial loading and hydrogenation, showed that 17G1C and X60 steels tested in NS4 solution saturated with CO_2, at corrosion potential showed a tendency to corrosion cracking [16]. This is confirmed by the deterioration of mechanical properties. Degraded X60 steel showed higher resistance to SCC than degraded 17G1C steel. Fractographic studies have

confirmed the hydrogen embrittlement of these steels caused by hydrogenation. Failure studies of the breakdown of pipeline $\varnothing$457.2 mm with spiral seam made of X52 steel laying in the soil with pH ~9-10 revealed intergranular type cracks. It has been suggested that the stresses caused by laying the pipe into the pipeline trench of the gas pipeline contributed to SCC [17].

Main gas pipelines are built of steels of different grades and have different microstructures. But the requirements of regulations on the level of protection potential are the same. Taking into account the results of our previous investigations [18-20], in which was showed that, in other conditions being equal, the susceptibility to SCC X70 and X80 steels with maximum protective potential differs, a study of the complex properties of low-carbon and low-alloy steels, on the base of that the conclusion regarding their susceptibility to SCC can be made. For Ukraine, as a gas transporter country, the issue of susceptibility to SCC of steels, from which the pipes of the main gas pipelines of the gas transmission system are made, is relevant. Therefore, a study of the susceptibility to stress-corrosion cracking of steels 09G2S, 17G1S and 10G2FB.

2. Research methods

The study was performed in a model soil electrolyte NS4, g/l: 0.122 + 0.483 NaHCO$_3$ + 0.181 CaCl$_2$ + 0.131 MgSO$_4$ [21].

The research objects are low-carbon and low-alloy steels for pipelines grade 09G2S, 17G1S and 10G2FB. Mechanical properties and chemical composition of these steels are given in Table 1, 2.

Table 1. Mechanical properties of the studied steels

Steel	σ$_y$, MPa	σ$_{us}$, MPa	δ, %
09G2S	325	470	21
17G1S	345-355	510	23
10G2FB	440	590	20

Table 2. Chemical composition of the studied steels

Steel	C	Mn	Si	S	P	Al	Ni	Mo	Ti	V	Nb	Cr	Cu	B
09G2S	0.08	1.65	0.68	0.034	0.019	-*	0.10	-*	-*	0.007	-*	0.10	0.27	-
17G1S	0.16	1.32	0.47	0.023	0.016	-*	0.06	-**	-*	-**	-**	0.04	-	-
10G2FB	0.096	1.71	0.208	0.009	0.007	0.035	0.03	0.03	0.015	0.06	0.052	-	-	0.002
*The content of the element was not determined														
** The element was not present														

Corrosion-mechanical studies were performed by the method of slow strain rate (10^{-6} s^{-1}) using a machine AIMA-5-1 in solution with periodic immersion: 50 minutes in the solution, 10 minutes in the air [22]. The shape and dimensions of the samples are shown in Figure 1.

Corrosion cracking studies were performed on samples that were catholically polarized in the potentiostatic mode in the potential range from -0.75 V to -1.2 V (relative to the chloride-silver comparison electrode) with a step of 0.05 V using the potentiostat PI-50-1.1, thus modeling the cathodic protection used on the underground gas pipeline. Specimens for metallographic research were made according to standard methods. The microstructure of the samples was detected by etching in nital (solution of 4% nitric acid in ethyl alcohol) and studied using a NEOPHOT 21 microscope and a Sigeta digital camera.

Figure 1. Sketch of a sample for corrosion-mechanical tests at a slow strain rate [23].

Examination of the surface of the samples after rupture was performed on a scanning electron microscope JSM 840 (JEOL, Japan) in the mode of secondary and backscattered electrons at a voltage of 20 kV accelerating and electron beam current (10^{-7}-10^{-10}).

3. Experimental results

3.1. Microstructure

All studied steels belong to the ferritic-pearlitic class, but have some differences in structure. In the structure of steel 09G2S (Figure 2, a) the number of ferritic and

pearlitic grains is equal to 70 and 30%, respectively. Part of the perlite has the form of strips. Ferrite grains correspond to 6-7 sizes in accordance with GOST 5639. The hardness of steel is (160-170) HV_5. Non-metallic inclusions are brittle silicates and small round oxides. Microstructure of steel 17G1S (Figure 2, b) – a mixture of fine-grained ferrite and perlite with ferrite grain numbers 9-10 (according to GOST 5639). Striping line is estimated by a score of 4-5 on a scale of 3 according to GOST 5640. The microstructure of 10G2FB steel (Figure 2, c) is dispersed ferrite-pearlite mixture with elongation of the grains in the direction of rolling. Ferrite grain corresponds to (10-11) number according to GOST 5639; striping line corresponds to (3-4) points, row B in accordance with GOST 5640. The hardness of steel is in the range (180-190) HV_5.

3.2. Electrochemical studies of the mechanism of SCC

Using the theoretical model proposed in [24] and using for determining the potential regions in the changing of the mechanism of SCC [25-27], it was found that the length and boundaries of these areas differ for low-carbon steels 09G2S and 17G1S and low-alloy steel of controllable rolling 10G2FB (Figure 3). That potentials' areas are: for 09G2S steel is from -0.85 V to -1.0 V, for 17G1S is from -0.8 V to -0.98 V, for 10G2FB is from -0.75 V to -1.05 V [28].

In the range of potentials less negative than the lower level (i.e. -0.85 V, -0.80 V and -0.75 V for steels 09G2S, 17G1S and 10G2FB), region I, there are two anode branches of polarization curves obtained with small and high potential sweep rate [28]. This means that in such a potential area the crack tip is under anode polarization. The current density of the anodic dissolution curve of the fast potential scanning (which characterizes the state of the crack tip) is greater than on the curve of the slow potential scanning (which characterizes the state of the surface far away from the crack tip).

The results show that the mechanism of SCC at potentials more positive than the above level is anodic dissolution.

a   b   c
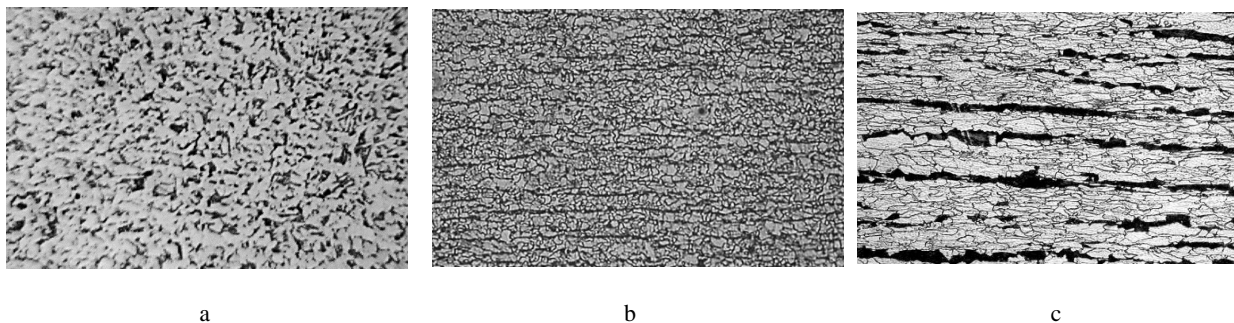
Figure 2. Steels' microstructure: a – 09G2S, ×100; b – 17G1C, ×200; c – 10G2FB, ×400

a   b   c
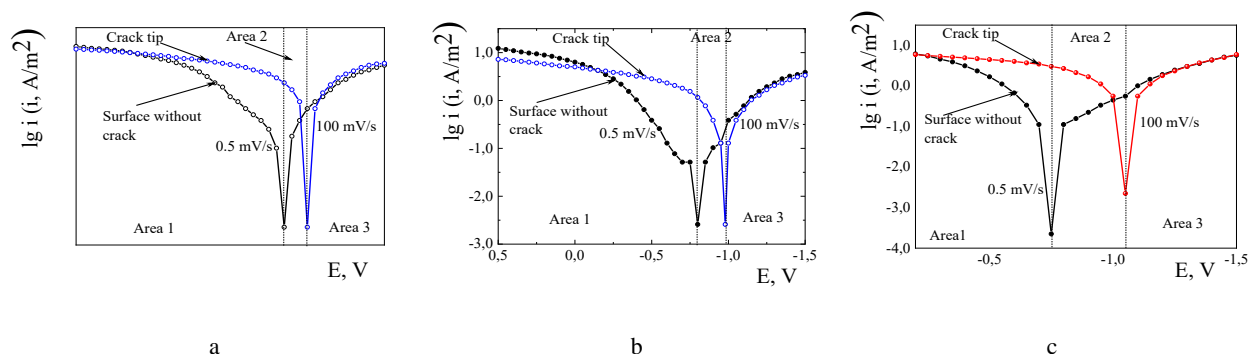
Figure 3. Polarization curves of pipe steels 09G2S (a), 17G1S (b), 10G2FB (c) in NS4, obtained with different potential scanning rate: 1 – 0.5 mV/s; 2 – 100 mV/s. Area 1 – local anodic dissolution mechanism, area 3 – hydrogen embrittlement mechanism, area 2 – local anodic dissolution and hydrogen embrittlement mechanism.

For the potential range from -0.85 V to -1.0 V for 09G2C steel, from -0.8 V to -0.98 V for 17G1C steel and from -0.75 V to -1.05 V for 10G2FB steel (area 2) the slow rate scan potential curve is located in the cathodic region, and the fast scan curve is located in the anodic potential region. This means that the crack tip stays in the conditions of anodic polarization, and the other surface stay under influence of cathodic polarization, i.e., SCC occurs by a mixed mechanism of anodic dissolution and hydrogen embrittlement. At more negative potentials as -1.0, -0.98 and -1.05 V (for the steels 09G2S, 17G1C and 10G2FB, respectively) (area 3), both polarization curves are in the cathodic region, which indicates on the hydrogen embrittlement

mechanism of SCC. Depending on the level of protective potential, either anodic dissolution or a hydrogen embrittlement mechanism may be predominant.

3.3. Investigation of stress-corrosion cracking

The degree of susceptibility to stress-corrosion cracking was assessed by the dimensionless coefficient proposed in our previous work [29, 30]:

$$K_S = \frac{\psi_S}{\psi_{air}} \qquad (1)$$

Breaking diagrams of steels in air and in solution at different cathodic polarization potentials are shown in Figure 4. It is not unexpected that in the corrosive environment the process of rupture of samples in solution occurs faster than in air. Cathodic polarization accelerates the destruction process and promote changes in the specimens' nature sharp bend (Figure 4).

Samples of all investigated steels that are breaking in the air have signs of viscous fracture: characteristic tightening near the break edge, the formation of areas that have undergone to plastic deformation. But there are differences in the indicators of relative elongation (Figure 4, a) and narrowing for those specimens (Table 3). In the morphology of fractures, the viscous (pit) character prevails (Figure 5).

After breaking the samples at the minimum protective potential of -0.75 V, the largest relative elongation was observed for 09G2C steel, the smallest elongation was observed for 10G2FB steel. In compare with the relative elongation of samples in the air, this criterion decreased as follows: for 09G2S steel by ~3.3%, for 17G1S steel – by ~18.4%, for 10G2FB steel – by ~1.8% respectively. The relative narrowing also decreased: by ~2.1% for 09G2S steel (from 52.5% to 51.4%), for 17G1S steel by ~9.7% (from 57% to 51.6%), for 10G2FB steel – by ~8,3% (from 53.1% to 48.7%).

a

b

c

d
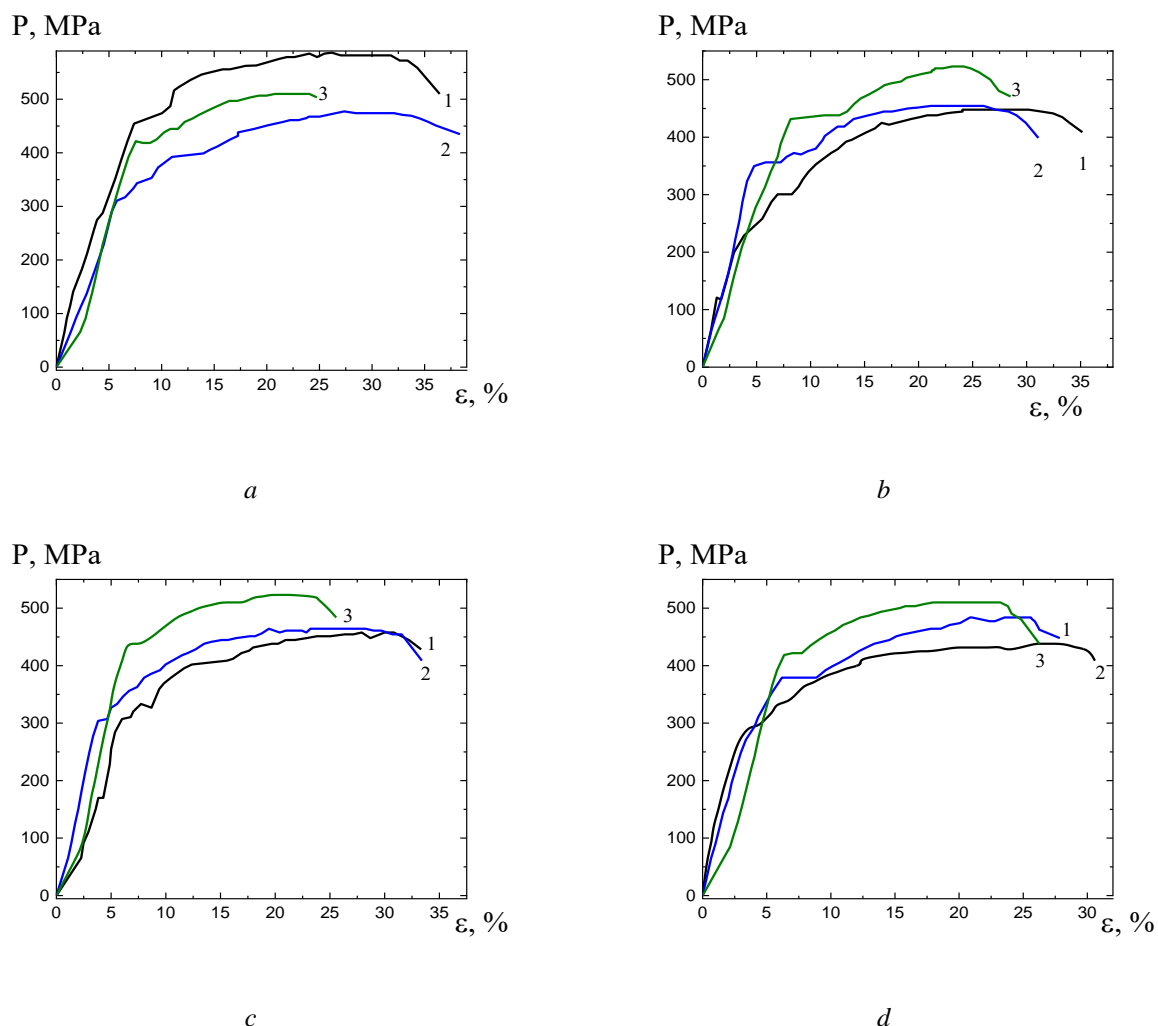
Figure 4. Fracture diagrams of samples of the steels 09G2S (1), 17G1S (2) and 10G2FB (3) during corrosion-mechanical tests in NS4 solution under different conditions: a – in air; at polarization potentials: b – -0.75 V; c – -1.05 V; d – -1.20 V/

Table 3. Mechanical properties of the studied steels in air and corrosion-mechanical properties in the NS4 at different polarization potentials

Criteria	Steel mode	Test conditions, polarization potential			
		Air	- 0.75 V	- 1.05 V	- 1.2 V
δ, %	09G2S	36.4	33.9	35.0	31.0
	17G1S	38.0	31.0	33.0	48.0
	10G2FB	28.0	28.5	25.6	24.8
S, мм^2	09G2S	14.26	14.6	17.8	17.3
	17G1S	12.9	14.5	16.2	26.2
	10G2FB	14.8	15.4	15.9	17.4
ψ, %	09G2S	52.5	51.4	40.7	42.3
	17G1S	57.0	51.6	47.0	13.0
	10G2FB	53.1	48.7	47.0	42.0
K_S	09G2S	-	1.02	1.25	1.21
	17G1S	-	1.1	1.21	4.38
	10G2FB	-	1.09	1.13	1.26

The part of pit fractures of 09G2C steel, depth and number of holes also decreases compared to fractures of samples in the air (Figure 5). It was observed an increase in the proportion of sheared surfaces, which shows agreement with decreasing in plasticity [23].

Signs of viscous fracture (retraction) around the rupture area of the 17G1C steel sample remain, the nature of the fracture remains viscous (Figure 5).

For 10G2FB steel, as in the case of fracture in air, the nature of fracture is viscous, but visually visible enlargement of the size of the holes and reducing their depth (Figure 5) [31].

The values of the coefficient of susceptibility to SCC were equal for steels 09G2S, 17G1S and 10G2FB, respectively 1.02, 1.1 and 1.09.

At the maximum protective potential -1.05 V, the relative elongation decreases more intensively compared to air, namely: by about ~7.9% for 09G2C, by ~13.1% for 09G2C and by ~8.8% for 10G2FB. There was decreasing in relative elongation also: for steel 09G2S by ~3.3%, for 17G1S – by ~18.4%, for 10G2FB – by ~1.8% compared to the relative elongation in air. This indicates on the development of brittle destruction. For 09G2S steel signs of viscous fracture near the rupture line are less pronounced, the proportion of pit fracture, depth and number of holes also decreases (Figure 5). There is an increasing in the proportion of chips, which is consistent with decreasing in plasticity. In the fracture of 17G1S steel samples signs of brittle fracture occur: flat areas and stratification, along with the viscous nature areas of the destruction of most parts of the surface (Figure 5). On the breaking surface of 10G2FB steel almost the flat fracture sites with a larger area of 10 to 30 μm in length than on the samples

destroyed at less negative potentials are dominated (Figure 5).

The coefficient of susceptibility to SCC for the steels 09G2S, 17G1S and 10G2FB is equal 1.25, 1.21 and 1.13, respectively. In the potentials' region negatively than -1.2 V, the relative elongation of 09G2S steel samples' decreases more intensively compared to the relative elongation of that samples in air – by about ~7.9% (Figure 4, d) and rather sharply decreases the relative narrowing ~24.7% (Table. 3). Relative elongation of 17G1S steel decreased by about ~26.1%, relative narrowing to ~13% (Figure 4, b). Signs of viscous fracture (retraction) around the rupture area of the specimen persist, but the rupture line has a complex zigzag shape. A larger share of flat areas of destruction was found in the fracture, the pits have a smaller depth and diameter (Figure 5).

For 10G2FB steel at negatively than -1.2 V potentials the part of brittle fracture increases, which correlates with decreasing in relative narrowing. The rupture line is a complex stepped polyline, the number of flat areas of destruction and their area on the surface of destruction increases, the share of holes and their depth decreases (Figure 5).

The coefficient of susceptibility to SCC increased for the steels 09G2S, 17G1S and 10G2FB, respectively 1.21, 4.38 and 1.26 (Table 3).

3.4. Investigation of the susceptibility of steels to electrolytic hydrogenation

Studies of the susceptibility of pipeline steels to electrolytic hydrogenation in the model soil electrolyte NS4 showed that the dependence of the concentration of hydrogen penetrating to the steel membrane during

cathodic polarization on the polarization potential is nonlinear and differs for steels of different chemical composition.

For 09G2S steel hydrogen begins to penetrate through the steel membrane at -0.95 V, at the potentials' range from -0.95 V to -1.1 V slowly increases and reaches a concentration of 0.00114 mole/m^3 to 0.00218 mole/m^3. The most intense hydrogenation observed at -1.2 V – hydrogen concentration was riches 0.00396 mole/m^3.

For steel 17G1S hydrogen begins to penetrate at -0.95 V, its concentration at this potential is 0.00056 mole/m^3. In the potential range from -0.95 V to -1.05 V, the amount of hydrogen varies from 0.00118 mole/m^3 to 0.00086 mole/m^3, then monotonically increases to a potential of -1.2 V, and reaches the value 0.00366 mole/m^3.

For steel 10G2FB steel hydrogen penetration begins at a potential of -1.0 V, its concentration in steel equal to 0.0023 mole/m^3, and then changes by jumps at potentials area from -1.05 V to -1.2 V from a minimum of 0.000518 mole/m^3 to a maximum of 0.0135 mole/m^3.

3.5. Investigation of the influence of the protective potential on the residual corrosion rate of pipeline steels

An important characteristic of the degree of protection of the pipeline is the residual corrosion rate. According to the normative documents of different countries [32, 33] technically sufficient protective effect is considered to be achieved if the corrosion rate of the pipeline metal is less than 0.01 mm/year.

World experience shows that even if the above indicators are within the standardized values, it is difficult to prevent the development of corrosion, including SCC completely. Investigation of the residual corrosion rate of the above steels in NS4 in the range of protective potentials from -0.75 to -1.05 V showed that technically sufficient protective effect is achieved at a minimum protective potential of -0.75 V (Figure 6, curves 1). When the potential of cathodic polarization is shifted to more negative values, at which the reduction of hydrogen on the surface will take place, under certain conditions the hydrogen is able to penetrate into the steel and contribute to its brittle destruction.

4. Discussion

According to the results of electrochemical, corrosion-mechanical and fractographic studies, it was found that in the range of the mixed mechanism (-0.85 V to -1.0 V)

for 09G2C steel in NS4 solution, the susceptibility to corrosion cracking and hydrogenation change nonmonotonically: hydrogen penetration increased (Figure 6, a, curve 2), the tendency to SCC has increased slightly compared to the potential range more positively -0.85 V, and remains almost constant (Figure 6, a, curve 1). In the region of potentials (less than -1.0 V), in which the concentration of hydrogen penetrating through 09G2C steel in NS4 solution increases intensively, there is a sharp increase in the tendency to SCC (Figure 6, a, curve 3).

For 17G1S steel in NS4 solution it was found that in the area of action of the mixed mechanism of corrosion cracking (from -0.8 V to -0.98 V) the concentration of hydrogen, which is able to penetrate back through the steel membrane, increases. 6, b (curve 2). In this area of potentials, the tendency to corrosion cracking of 17G1S steel also grows (Figure 6, b, curve 3).

Sharp increase in the concentration of hydrogen, and a corresponding increase in susceptibility to SCC was observed for potentials more negative than -0.98 V (Figure 6, b). For 10G2FB steel in NS4 solution at potentials more positive than -0.75 V hydrogen penetration is not observed (Figure 6, curve 2), the susceptibility to corrosion cracking does not exceed 1.1 (Figure 6, c, curve 3). In the potential range from -0.75 to -1.05 V, a significant increase in hydrogen penetration and a nonmonotonic increase in K_S coefficient (Figure 6, c, curve 3), due to shifting in the equilibrium of the destruction process from anodic dissolution to hydrogen embrittlement was established. In the potential range (negatively than -1.05 V), in which the concentration of hydrogen, penetrating the steel, changes abruptly from 0.002 mole/m^3 to 0.006 mole/m^3, the susceptibility to corrosion cracking continues to increase from 1.11 to 1.25.

Thus, according to the results of research, it is established that in general for steels of pipe assortment there are three areas of potential in which the nature of fracture changes, which indicates on the change in SCC mechanism. The range of the mixed fracture mechanism for pipe assortment steels may shift depending on the chemical composition of the steels, which led to changing of the value of potential at which the tendency to brittle fracture increases. Naturally, in the potentials' range of hydrogen embrittlement mechanism, there is a sharper decrease in relative elongation and relative narrowing of samples.

09G2S   17G1S   10G2FB

Air

E = -0.75 V

E = -1.05 V

E = -1.2 V
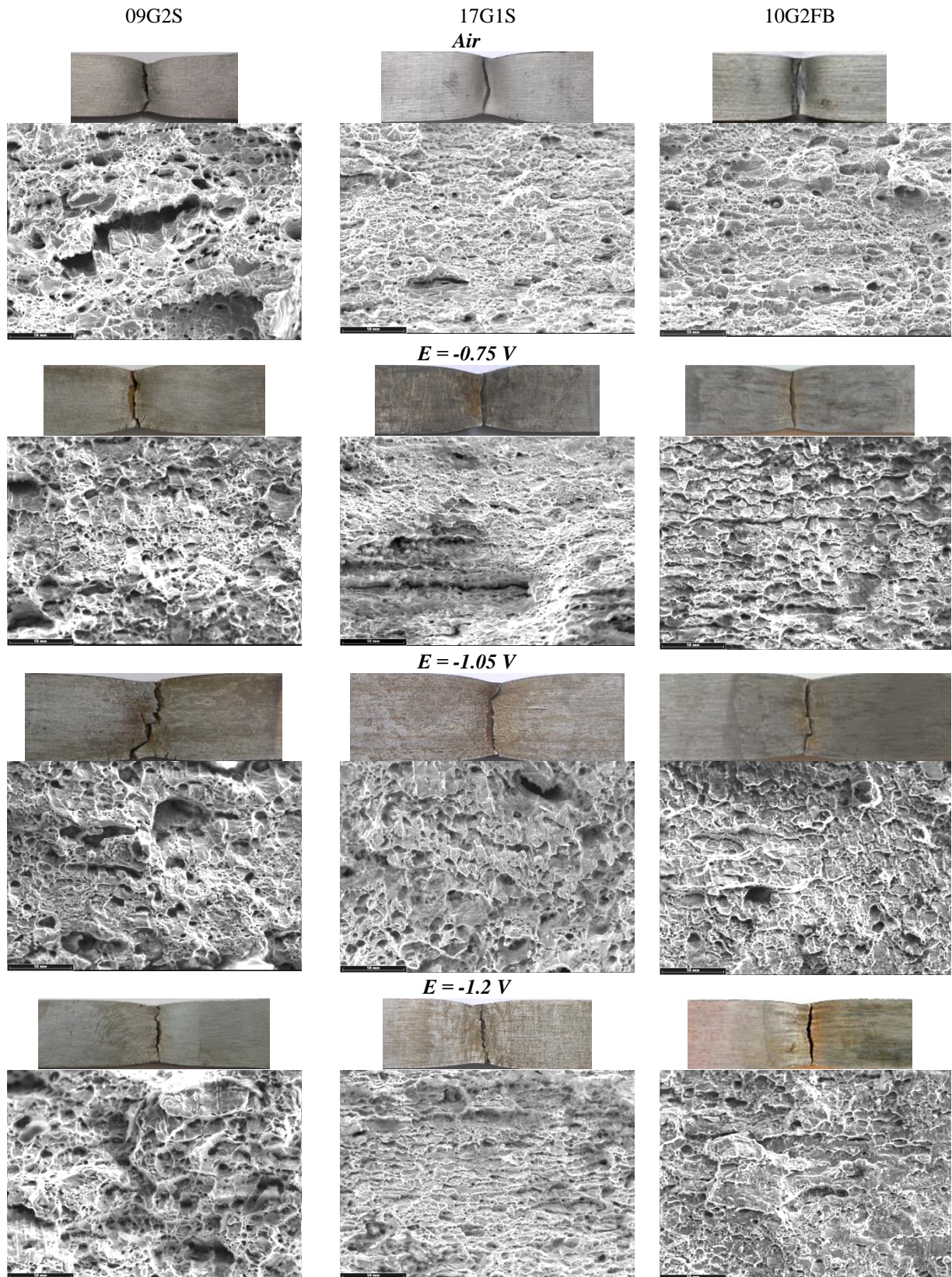
Figure 5. View of the fracture region and fractogram of fracture surfaces of tubular steel samples in air and after corrosion-mechanical tests in NS4 solution under different conditions, ×500
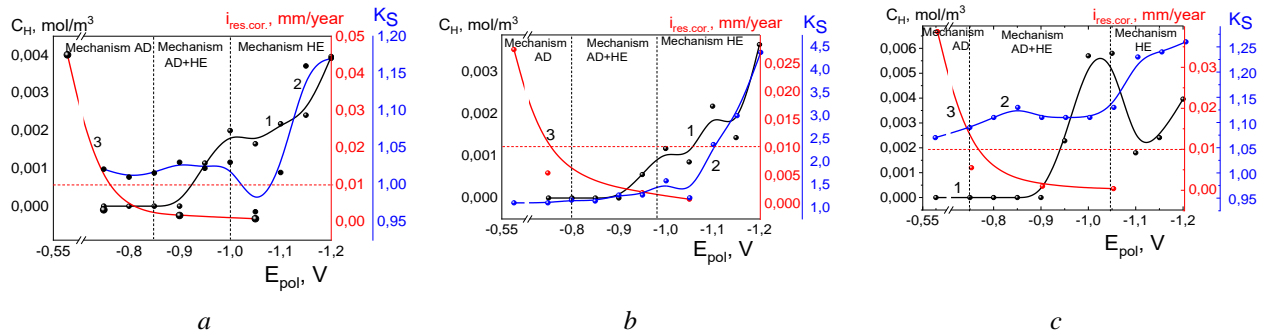
Figure 6.   Dependence of the indicators influencing the corrosion cracking of 09G2C steel on the potential of cathodic polarization in NS4 solution: 1 - concentration of hydrogen penetrating through the steel membrane; 2 - susceptibility to corrosion cracking; 3 - residual corrosion rate

5.   Conclusions

1. By the investigation results of electrochemical, corrosion-mechanical and fractographic studies it was established and experimentally confirmed the existence of three potential areas in which corrosion cracking of pipeline steels in the model soil electrolyte NS4 occurs due tu different mechanisms.

2. For steel 09G2S at potentials more positive than -0.85 V the mechanism of local anodic dissolution operates. Hydrogenation of steel does not occur at those potentials, the coefficient K_S values are low, the dominated morphology of the fracture is preferably viscous (pit) nature. In the potential' range from -0.85 V to -1.0 V SCC occurs by both mechanisms – local anodic dissolution and hydrogen embrittlement proceed simultaneously: the tendency to stress-corrosion cracking and hydrogenation changes non-monotonically, both viscous and fragile components present in the morphology of destruction surface. At potentials' from -1.0 V and less – hydrogen cracking prevails: the concentration of hydrogen penetrating the steel increases rapidly, the tendency to corrosion cracking increases sharply, which is confirmed by an increase in the proportion of sheared surfaces on the fracture surface. This is consistent with decrease in plasticity.

3. For 17G1S steel in the potentials' region more positive than -0.8 V SCC occurs by the mechanism of local anodic dissolution, hydrogen penetration through steel does not occur, the values of K_S coefficient vary from 1.1 to 1.16, the fracture surface morphology is viscous. In the potential range from -0.8 V to -0.98 V SCC occurs by the mechanisms of local anodic dissolution and hydrogen cracking: the concentration of hydrogen capable to penetrate through the steel membrane increases, the susceptibility to SCC increases from 1.16 to 1,58, in the morphology of destruction there are areas of fragile breaking. In the potentials' region less than -0.98 V, hydrogen embrittlement predominates: the concentration of hydrogen penetrating the steel and the coefficient of susceptibility to corrosion cracking from 1.56 to 4.38,

which correlates with increasing in the proportion of brittle areas on the fracture surface.

4. For 10G2FB steel cracking by the mechanism of local anodic dissolution occurs in the range of potentials more positive than -0.75 V, hydrogen penetration through the steel does not occur, the values of K_S coefficient vary from 1.01 to 1.09, the fracture is viscous. For the potential range from -0.75 V to -1.05 V, in which the mixed mechanism of SCC runs, the following breaking features are characteristic: significant increase in hydrogen penetration, non-monotonic increasing of the coefficient of susceptibility to SCC 1.09 to 1.13, formation of areas of brittle fracture on the fracture surface. In the potentials' region negatively than -1.05 V, hydrogen cracking prevails, which is confirmed by the sharp increase in the concentration of hydrogen, penetrating to the steel, increase the value of the coefficient of susceptibility to SCC from 1.13 to 1.26 and fracture morphology, in which signs of fragile destruction is dominated.

5. The obtained regularities testify to the possibility of development of stress-corrosion cracking of main gas pipelines made of investigated steels with different rate and regularities under other identical conditions, including the level of electrochemical protection

Acknowledgements

REFERENCES

[1]   Baker M., (2005), Stress Corrosion Cracking Study. FINAL REPORT. *Integrity Management Program Delivery Order* DTRS56-02-D-70036. 201p.

[2]   Otegui J. L., (2014), *Challenges to the integrity of old pipelines buried in stable ground*, Engineering Failure Analysis 42, p. 311–323

[3] Wu T., Yan M., Yu L., Zhao H., Sun Ch., Yin F., Ke W., (2019), *Stress corrosion of pipeline steel under disbonded coating in a SRB-containing environment* Corrosion Science 157, No. 15. p. 518-530

[4] Wang L. W., Du C. W., Liu Z. Y., Wang X. H., Li X. G., (2013), Influence of carbon on stress corrosion cracking of high strength pipeline steel. *Corrosion Science*. Vol. 76. P. 486-493

[5] Song L., Liu Zh., Li X., Du C., (2020), *Characteristics of hydrogen embrittlement in high-pH stress corrosion cracking of X100 pipeline steel in carbonate/ bicarbonate solution* Construction and Building Materials 263 No 10, 120124

[6] Fu A. Q., Cheng Y. F., (2010), *Electrochemical polarization behavior of X70 steel in thin carbonate/bicarbonate solution layers trapped under a disbonded coating and its implication on pipeline SCC* Corrosion Science 52, No. 7, p. 2511-2518

[7] Luo J., Luo Sh., Li L., Zhang L., Wu G., Zhu L., (2019), *Stress corrosion cracking behavior of X90 pipeline steel and its weld joint at different applied potentials in near-neutral solutions* Natural Gas Industry B 6, No. 2, p. 138-144

[8] Liu , Wu , Pan , Liu Z.Y., Zhou X.C., Li X.G., (2018), *Electrochemical mechanism of stress corrosion cracking of API X70 pipeline steel under different AC frequencies* Construction and Building Materials 171, No. 20, p. 622-633

[9] Wan H., Song D., Liu Z., Du C., Zeng Z., Wang Z., Ding D., Li X., (2017), *Effect of negative half-wave alternating current on stress corrosion cracking behavior and mechanism of X80 pipeline steel in near-neutral solution* Construction and Building Materials 154, No.15, p. 580-589

[10] Wan H., Song D., Liu Z., Du C., Zeng Z., Yang X., Li X., (2017), *Effect of alternating current on stress corrosion cracking behavior and mechanism of X80 pipeline steel in near-neutral solution* Journal of Natural Gas Science and Engineering 38, p. 458-465

[11] Eslami A., Fang B., Kania R., Worthingham B., Been J., Eadie R., Chen W., (2010), *Stress corrosion cracking initiation under the disbonded coating of pipeline steel in near-neutral pH environment* Corrosion Science 52, No, 11, p. 3750-3756

[12] Liu Z. Y., Wang X. Z., Du C. W., Li J. K., Li X. G., (2016), *Effect of hydrogen-induced plasticity on the stress corrosion cracking of X70 pipeline steel in simulated soil environments* Materials Science and Engineering: A 658, No. 21, p. 348-354

[13] Zhiyong L., Zhongyu C., Xiaogang L., Cuiwei D., Yunying X., (2014), *Mechanistic aspect of stress corrosion cracking of X80 pipeline steel under non-*

stable cathodic polarization Electrochemistry Communications 48, p. 127-129

[14] Xu Ch., Ming W., Chuan H., Jun X., (2010), *Effect of applied potential on scc of x80 pipeline steel and its weld joint in ku'erle soil simulated solution* Acta Metall Sin 46, No. 8, p. 951-958

[15] Contreras A., Hernández S. L., Orozco-Cruz R., Galvan-Martínez R., (2012), *Mechanical and environmental effects on stress corrosion cracking of low carbon pipeline steel in a soil solution.* Materials & Design 35. P. 281-289

[16] Zvirko O. I., Savula S. F., Tsependa V. M., Gabetta G., Nykyforchyn H. M., (2016), *Stress corrosion cracking of gas pipeline steels of different strength* Procedia Structural Integrity 2, p. 509-516

[17] Saleem B., Ahmed F., Rafiq M. A., Ajmal M., Ali L., (2014), *Stress corrosion failure of an X52 grade gas pipeline* Engineering Failure Analysis 46, p. 157-165

[18] Nyrkova L., Rybakov A., Melnychuk S., Osadchuk S., (2016), *Influence of increase of characteristics of durability of pipe steel on corrosion properties of the main pipelines in the conditions of complex anticorrosive protection.* Physico-chemical mechanics of materials: XIII International Conference "Problems of corrosion and corrosion protection of materials" Lviv, June 14-15, 2016, special issue No. 11, p.312–318

[19] Nyrkova L. I., Melnychuk S. L., Borysenko Y. V., (2017), *Influence of strength properties of pipe steel on its corrosion resistance and electrochemical characteristics in solutions of different corrosivity* Promising Materials and Processes in Technical Electrochemistry: Monograph, Kyiv: KNUTD, p. 110–118

[20] Nyrkova L., Gavryishina O., Borysenko Y., (2018), *Electrochemical and corrosion-mechanical properties of pipe steel of different strength level in model soil electrolyte* Bulletin of the Kyiv National University of Technology and Design: Series "Technical Sciences" 126, No. 5, p. 99–105

[21] R Antunes de Sena, I. Napoleão Bastos, G. Mendes Plat, (2012), *Theoretical and Experimental Aspects of the Corrosivity of Simulated Soil Solutions* International Scholarly Research Notices Article ID 103715, 6 pages

[22] Nyrkova L., Rybakov A., Osadchuk S., Melnychuk S., Gapula N., Yakovenko G., (2014), *Device for studying the susceptibility of pipeline steels to stress-corrosion cracking*: UA Pat. for the invention 107229 Ukraine: IPC G01N 17/00, G01N 17/02 - 201 a20124719; stated 21.12.2012, publ. 12.10.2014, Bull. № 23. 4 p.

[23] Nyrkova L.I., Lisovyi P.E., Goncharenko L.V., Osadchuk S.O., Kostin V.A., Klymenko A.V.,

(2021), *Regularities of Stress-Corrosion Cracking of Pipe Steel 09G2S at Cathodic Polarization in a Model Soil Environment* Physics and chemistry of solid state 22, No.4, p. 828 – 836

[24] Liu Z.Y., Li X.G., Cheng Y.F., (2012), *Mechanistic aspect of near-neutral pH stress corrosion cracking of pipelines under cathodic polarization*, Corrosion Sciences 55, p. 54-60

[25] Murakami Y., Kanezaki T., Mine Y., (2010), *Hydrogen Effect against hydrogen embrittlement*. Metall. Mater. Trans. A 41A, p. 2548-2562

[26] Miresmaeili R., Liu L., Kanayama H., (2012), *A possible explanation for the contradictory results of hydrogen effects on macroscopic deformation* Inter. J. Pres. Ves. Pip. 99-100, p. 34-43

[27] Ren X.C., Chu W.Y., Su Y.J., (2008), *The effects of atomic hydrogen and flake on mechanical properties of a tyre steel* Mater. Sci. Eng. A 491, p. 164-171

[28] Nyrkova L., Osadchuk S., Lisovyi P., Prokopchuk S., (2021), *Methodical approach to the study of corrosion cracking mechanism of pipe steel under cathodic protection by voltammeter method* Scientific Bulletin of Ivano-Frankivsk National Technical University of Oil and Gas. Technical sciences series 51, No. 2, p.7-15

[29] Nyrkova L., (2020), Stress-corrosion cracking of pipe steel under complex influence of factors. *Engineering Failure Analysis*. Vol. 116. 104757

[30] Nyrkova L. I., Osadchuk S. O., Rybakov A. O., Mel'nychuk S. L., (2020), *Methodical approach and a criterion for the evaluation of the susceptibility of pipe steel to corrosion cracking* Materials Science 55, No. 5, p. 625–632

[31] L. Nyrkova, P. Lisovyi, L. Goncharenko, S. Osadchuk, A. Klymenko, Y. Borysenko, Bratochkin O., (2021), *Regularities of stress corrosion cracking of 10G2FB pipeline steel in near neutral soil environment at cathodic polarization* Bulletin of the Kyiv National University of Technologies and Design (Technical sciences series) , No. 2, p. 29-39

[32] DSTU 4219-2003 Steel pipe mains. General requirements for corrosion protection. Kyiv, 86 p.

[33] NACE SP0169-2013 Control of External Corrosion on Underground or Submerged Metallic Piping Systems

Comparison of determined theoretically and experimentally critical speed of a ball mill

Miglena PANEVA[1]*, Nikolay STOIMENOV*[1]*, Peter PANEV*[1]

1) Institute of Information and Communication Technologies – Bulgarian Academy of Sciences, bl. 2, ac. G. Bonchev str, 1113 Sofia, **Bulgaria**

m.paneva7@gmail.com
nikistoimenow@gmail.com
panevv@gmail.com

Keywords

Critical speed
Laboratory ball mill
Grinding bodies
3D additive technology
3D materials

Professional article

Abstract: In the present work, a comparative analysis of the critical speed values calculated theoretically and experimentally is made. The research was done with the help of a laboratory ball mill with transparent lids and a high-speed camera. The chamber of the mill and the grinding bodies are made by using 3D additive technology. The chamber is made of PLA material without lifters and several types of material are used for the grinding bodies - PLA, SteelLike, CarbonFil, and SteelFil. The study was performed with 20% infill of the laboratory ball mill with grinding bodies, without added material for grinding. The reported results from the theoretical and experimental determination of the critical speeds show that the specified formula is not applicable in the established experimental research and the critical speed depends on the properties of different types of materials.

1. Introduction

Grinding mills are divided into three types - autogenous, semi-autogenous, and ball mills. The first two types are in the initial stage of crushing. Ball mills are used when the output production must be milled in finer particles. Ball Mills are mainly used in metallurgy, chemical industry, cement, and other industrial and mining business. The main characteristics are strong adaptability to raw materials, excellence in continuous production, high crushing ratio and easy to adjust the fineness of the milled product. There are available two types of systems- open or closed, according to the production model- dry or wet process production can be adopted. The grinding and drying operations can be completed at the same time. Laboratory mills are used to establish the best milling process using different grinding bodies and grinding environments (liners and lifters). Through the research of different combinations of materials, the presence of lifters with various shapes and numbers contributes to the optimization of the grinding process by decreasing the time for milling and increasing the energy efficiency [1, 2]. When the speed of a ball mill increases, the intensity of the grinding process and representatively the productivity of the mill increases. According to literature data [3], the spheres should not exceed 60% of the total volume of the mill. A fixed number of spheres are placed in the cylinder and then the cylinder is closed. The mill starts and begins rotating. At low speeds, the mass of the balls will slide or pile on top of each other and this will only lead to a slight reduction in size. At high speeds, the balls are thrown against the wall of the cylinder due to centrifugal force and no grinding will occur. The speed must be calculated precisely because, at speeds above a certain value, the contents of the mill adhere to the wall of the mill and begin to centrifuge, whereby the grinding effect is reduced and the electricity consumed by the mill is increased. For this reason, the speed at which the mill operates at maximum power and above which the load begins to centrifuge is defined as the critical speed [4, 5]. Ball mills operate at a rotational speed below the critical speed of about 2/3 of the centrifugal speed. At this speed, the balls are raised almost to the top of the mill and after that start falling in a cascade along the diameter of the mill. In this way, the maximum reduction in size is achieved by hitting the particles between the balls and by milling the material by the balls [6].

The present work aims to determine the critical speed in motion and interaction of grinding bodies and grinding media in different additive materials and to compare with the calculated theoretical.

Symbols

D	- diameter, m		R	- inner radius of mill, m
V	- Volume, m³		r	- radius of the ball, m
F_g	- force of gravity, N		n	- frequency of rotation, rpm
Fc	- centrifugal force, N		d	- diameter of ball, m
m	- mass of the ball, kg		n_c	- critical speed, rpm
g	- acceleration of gravity, m/s²			
	Greek letters			
v	- linear speed of rotation, m/s			

2. Parameters of laboratory ball mill and grinding bodies

Studies to determine the critical velocity in the movement and interaction of grinding bodies and grinding media have been experimentally established in a laboratory ball mill with intelligent control with a 1.1 kW motor with controllable speed (Fig. 1). The used mill is constructed with options for quick changing the mill drum produced from different materials, length, size and inserting different grinding bodies. The lids of the ball mill are available in two types: transparent and dense.

The transparent lids are made of Plexiglass, on which a transparent foil (scratch resistant) is placed and thus allows to observe the movement, trajectory, the interaction of the grinding bodies, the grinding media and the grinding material; determination of the angle of the shoulder, toe; speeds; displacement, accelerations. [7]. The percentage of filling with grinding bodies is 20% with a spherical shape and a diameter of 9 mm. The number of spheres has been experimentally established. The parameters of the mill are the following:

Outer diameter - 0.269 m
Inner diameter - 0.235 m
Length - 0.013 m
Volume- 0.000563 m³ = $5.63 \cdot 10^{-4}$ m³
Sphere volume, 9 mm - 381.51 mm³ = $3.82 \cdot 10^{-7}$ m³

Figure 1. Filling of the mill with grinding bodies at 20%

3. Theoretical determination of the critical speed of rotation of the mill drum

The critical speed of rotation depends on the diameter of the ball mill and the diameter of the grinding bodies. In Figure 2, position A shows an isolated metal ball in the process of rotation, on which the force of gravity Fg and the centrifugal force Fc act. Position B means the center of gravity of the entire load of the mill, where the action of physical forces is similar to that in position A, but here the unknown friction forces between the particles of the material and the grinding medium also influence [4, 5].
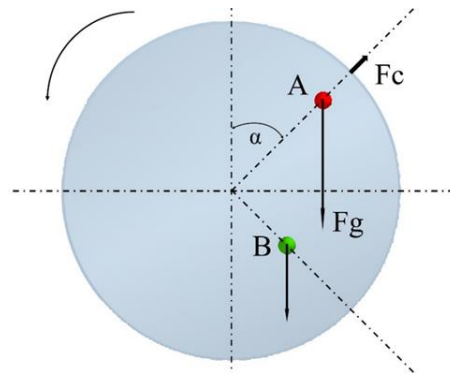
Figure 2. Forces acting on grinding bodies

The values of Fg and Fc are respectively:

$$F_g = mg, \tag{1}$$

where m is the mass of the ball and g is the ground acceleration,

$$F_c = \frac{mv^2}{(R-r)}, \tag{2}$$

where R is the inner radius of the mill, r is the radius of the ball, and v is the linear speed of rotation along the inner diameter of the mill.

The radial component of gravity is:

$$F_r = F_g \cos\alpha, \tag{3}$$

and the value of *v* in m/s can be expressed as:

$$v = 2\pi(R-r)\frac{n}{60}, \qquad (4)$$

where *n* is the speed in rpm. Provided that the value of the centrifugal force is greater than the maximum value of the radial component of gravity, the ball from position A will centrifuge on the inner surface of the mill. Since *Fr* reaches its maximum value at *Fr* = *Fg*, ie. for α = 0 and respectively cosα = 1, then from the equality of the two forces:

$$F_g = F_c, \qquad (5)$$

determine the critical rotation speed:

$$v_c = \sqrt{(R-r)g}. \quad , \qquad (6)$$

From (4) and (6) the corresponding critical speed is determined:

$$n_c = \frac{42,3}{\sqrt{(D-d)}}, \qquad (7)$$

where *D* is the inner diameter of the mill and *d* is the diameter of the ball.

The derived formula (5) clearly shows that the variable parameter is the inner diameter of the mill and the diameter of the sphere, which means that they are constant in all experiments.

After replacing the formula with the parameters of the mill, the following equation is obtained:

$$N_c = \frac{42,3}{\sqrt{(0.235-0.009)}}. \qquad (8)$$

It follows that the critical velocity *nc* = **88,98 rpm.**

4. Experimental determination of critical speed in motion and interaction of grinding bodies and grinding media

The experiments were made with grinding bodies with 4 types of material: three of them are made of additive material - PLA, SteelLike, and CarbonFil, and the fourth type is purchased steel spheres - Steel. The number of spheres with a diameter of 9 mm is 142 pcs. at 20% filling of the ball mill. The manufactured spheres are made using a 3D printer Tevo Tornado, 3D Printer Ultimaker S5 [7, 8]. The digital laser tachometer and high-speed camera NAC MEMRECAM HX6 [7]

determine the critical speed of interaction and movement of the grinding bodies. When using the tachometer, specialized markers are placed on the shaft, which transmits the rotational movement of the drum to the laboratory ball mill to identify the movement. The measurement is made with the help of the laser beam reflected by the marker, whose power is less than 1 mw. The device is capable of measuring speeds in the range of 2.5 to 99 thousand revolutions per minute. The weight of the spheres was measured with an analytical balance with an accuracy of ± 0.00001. 10 pieces of each type were measured and the values were averaged. The average values and total weight of all spheres are presented in Table 1.

Based on the developed methodology for experimental determination of critical speed in the interaction of grinding bodies [9], it is established that the correct critical speed is obtained after starting the engine and gradually reaching critical speed. To check the critical speed, it is recommended that after reaching a critical speed, the mill must be switched off, then switched on again and the specified critical speed be reached smoothly. The same is recommended when determining the percentage of critical speeds for use in cataract mode. Based on these features, the following experimental results have been established in Figure 3. From the obtained results, it is clear that in the study with different types of material the speed of the critical speed is different.
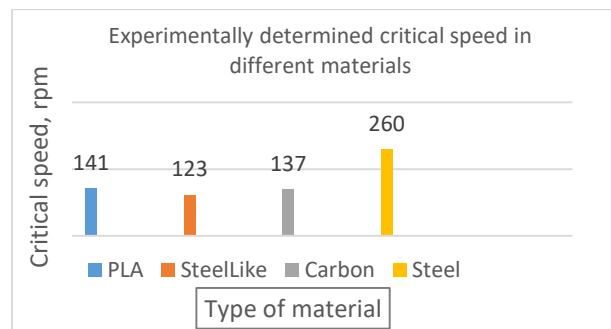

Figure 3. Graph with the experimentally determined critical speed in different materials

Table 1. Mass of 1 and 142 spheres in different materials

|	Type of material			
	PLA	SteelLike	Carbon	Steel
Mass, [gr.] for 1 pcs	0,40905	1,08856	0,41310	2,97675
Mass, [gr.] for 142 pcs	58,085	154,576	58,660	422,699

By using a high-speed camera and specialized software, it is possible to accurately determine the critical speed (Fig. 4). It is necessary due to the impossibility to see with an unarmed eye the moment when all the spheres stick to the lining of the drum, namely the resulting centrifugation. The high-speed camera can record from 2000 to 370,000 frames per second.
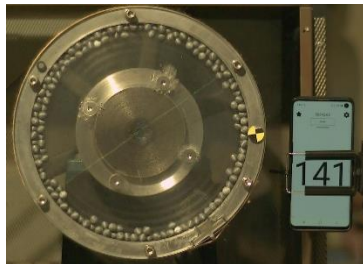
a) PLA
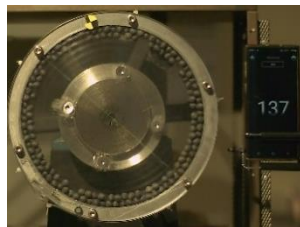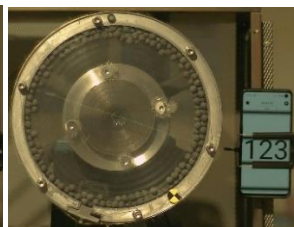
b) CarbonFil™　　　　c) SteelFill

Figure 4. Photos of critical speed of ball mill with different materials

As is seen from the Figure 4, for the differences in the mass of the spheres, as well as their coefficient of friction are needed different rotational speeds. For additive materials with approximately the same coefficients of friction and restitution [10, 11, 12], the greater the weight of the grinding bodies, the lower the critical speed is. While in steel spheres, the coefficient of friction is very low and despite its significantly higher weight, the critical speed is much higher. The experiment with the sphere balls was not completed due to the possibility of breakage of the PLA shell material of the ball mill.

5.　Future steps

The results obtained from the experimental determination of the critical speed for different types of materials in a laboratory ball mill will be used to determine 70, 75, and 80% of the critical speed and it will determine the shoulder angle and the toe angle. A comparison of the experimentally obtained results with a simulation made using EDEM software will be made. The results obtained will be verified.

6.　Conclusions

This experimental research presents a laboratory ball mill, which determines the revolutions of the critical speed in the interaction and movement of grinding bodies. Critical speed calculations have also been made theoretically by formula (7), in which the variable value is the inner diameter of the mill and the diameter of the spheres. In this case, regardless of the type of material, the values of the critical value are the same - 89 rpm. After the printing of the spheres by using 3D additive technology of the grinding bodies of different materials - PLA, Steellike, and Carbon, their weights were measured by an analytical scale. The experimental results of determining the revolutions of the critical speed show different values: PLA-141 rpm; SteelLike-123 rpm; Carbon-138; Steel>260. The construction of the mill is not suitable for more than 260 rpm. From the analysis, it is established that the main factors are the weight and the coefficient of friction.

The reported results from the theoretical and experimental determination of the critical speeds show that the specified formula is not applicable in the established experimental research. The properties of different types of materials in a laboratory experiment must be taken into account. For this research, the most accurate result can be determined experimentally by using the described experimental determination method for the laboratory ball mill.

The used laboratory mill is functional and can be composed of different types of materials of drum, liner and grinding bodies.

Acknowledgments

REFERENCES

[1]　Wang T., Zou W., Xu R., Xu H., Tao L., Zhao J., He Y., Assessing load in ball mill using instrumented grinding media, Materials Engineering, Vol. 173, 2021.

[2] Stoimenov N., Karastoyanov D., Klochkov L., Study of the Factors Increasing the Quality and Productivity of Drum, Rod and Ball mills, 2nd Int. Conf. on Environment, Chemical Engineering & Materials, ECEM '18, Malta Sliema, June 22-24, 2018, AIP (American Institute of Physics) Publishing house, Vol. 2022, Issue 1, ISBN: 978-0-7354-1740-3, pp. 020024-1 - 020024-6

[3] WCleary P., *Charge behaviour and power consumption in ball mills: sensitivity to mill operating conditions, liner geometry and charge composition*, International Journal of Mineral Processing, Volume 63, Issue 2, August 2001, Pages 79-114

[4] Jultov A., Machines for construction materials, Sofia, Technika, 1980 (in Bulgarian)

[5] Gupta, A., D. Yan, *Mineral Processing Design and Operations: An introduction*, 718 pages, Elsevier, May 2006.

[6] Karastoyanov D., Mihov M., Sokolov B.., *Optimization of the Control System by Milling Processes.*, John Atanasoff Celebration Days, International Conference RAM 2012, Sofia, 15-17 October 2012, pp m15 – m20, ISSN 1314-4634

[7] SMART Lab IICT-BAS, https://rius.iict.bas.bg/smart_lab.html#1 (accessed May 2022).

[8] 3D printer Tevo, https://www.tevousa.com/products/tevo-tornado-3d-printer-kit(accessed May 2022).

[9] Paneva M., Stoimenov N., Panev P., *Methodology for Experimental Determination of a Ball Mill Critical Speed*, 11th International Scientific Conference "TechSys 2022" – ENGINEERING, TECHNOLOGIES AND SYSTEMS, Technical University of Sofia, Plovdiv Branch, 26-28 May 2022, AIP Conference Proceedings (e-ISSN:1551-7616), accepted for publication

[10] Stoimenov N., Gyoshev S., Paneva M. Panev P., Determination of the friction coefficient of 3D printed materials - Part I - Rolling friction, 10th International Conference on Mechanical Technologies and Structural Materials (MTSM 2021), Split, Croatia, September 23-24, 2021, Croatian Society for Mechanical Technologies, Croatia, ISSN: 1847-7917, pp. 149-152.

[11] Gyoshev S., Stoimenov N., Paneva M., Determination of the friction coefficient of 3D printed materials - Part II - Sliding friction, 10th International Conference on Mechanical Technologies and Structural Materials (MTSM 2021), Split, Croatia, September 23-24, 2021, Croatian Society for Mechanical Technologies, Croatia, ISSN: 1847-7917, pp. 43-46.

[12] Stoimenov N., Gyoshev S., Restitution Coefficient Determination of 3D Printed Materials, Part of the Lecture Notes in Networks and Systems book series (LNNS, volume 465), Proceedings of Seventh International Congress on Information and Communication Technology pp. 663–669, Springer, Singapore DOI: 10.1007/978-981-19-2397-5_59

The use of high strength steels in the manufacture of building welded structures

Massimo ROGANTE[1], **Valeriy POZNIAKOV**[2], **Alexandr GAJVORONSKIY**[2] **Anatoliy ZAVDOVEEV**[2]

1) Rogante Engineering Office, Contrada San Michele n. 61, I-62012 Civitanova Marche, **Italy**
2) Paton Electric Welding Institute of NAS of Ukraine, 03150 Kyiv, **Ukraine**

main@roganteengineering.it
avzavdoveev@gmail.com

Original scientific paper

Abstract: The influence of welding thermal cycles on structure and mechanical properties of the metal of the welded joints' heat affected zone (HAZ) was investigated.

It was established that, as a result of welding thermal cycles: the HAZ metal structure of most microalloyed steels of strength classes C350 to C490, except for the 09G2SYu (S275ML - EN10025-4) steel, remains stably bainitic in a wide range of cooling speeds, and mechanical properties do not change significantly; the HAZ metal structure of the 09G2SYu steel can change from bainitic at moderate cooling rates to bainitic-martensitic and martensitic, as the cooling rate of the metal increases; static strength and toughness of the metal increase, and its plastic properties decrease.

1. Introduction

One of the main tasks of the modern industrial development is to increase the technical and economic performances of machines, mechanisms and engineering structures on the basis of reducing their specific metal content and increasing operational reliability and durability. In world practice, this is achieved by using in the manufacture of welded metal structures high-strength steels with a yield strength of 350 MPa and more. In particular, low-alloy high-strength steels of strength class C355 - C490 are widely used, e.g., in bridge construction, in the production of tanks for storage and processing of gas and oil and in the manufacture of building structures. Since the vast majority of these metal structures are welded, there are certain requirements for such steels, namely, they must be satisfactorily welded. High ductility and uniformity of welded joints should be provided, as well as impact strength at the level of requirements regulated by the state construction norms that, in recent years, have undergone some changes. First of all, these changes concern the indicators of impact strength and relative narrowing of rolled products in the Z-direction. According to modern requirements of steel, respectively the weld metal and heat affected zone (HAZ) of welded joints must have an impact strength of KCV-20 $\geq$ 25 J/cm^2 for steels with yield stress (YS) from 290 to 390 MPa and KCV40 $\geq$ 25 J/cm^2 for steels with YS $\geq$ 390 MPa and relative narrowing in the Z-direction (Ψz) not less than 35, 25 and 15% for the first, second and third groups of structures, respectively.

To date, in the manufacture of building structures low-alloy steels of strength class C350 - C390 such as 09G2S, 10HSND, 15HSND and others are still widely used. They were developed 30 years ago (Table 1).

Low-alloy structural steels fully meet the modern requirements for static strength and plastic properties of steels along and across the rolling (Table 2).

In most of these steels, toughness is also at the level of these requirements. Nevertheless, to maintain the required level of KCV for the HAZ metal, the cooling rate of welded joints in the temperature range of 600-500 °C ($W_{6/5}$) should be in the range of 15-20 °C/s. This requires a significant restriction of welding modes, which complicates the technological process and makes it unproductive. In addition, Ψz in such steels does not exceed 15%, which limits their use in welded elements that work in the direction of rolled thickness. Since the 1990s, certain changes have taken place in the metallurgical industry as a result of significant economic and technical transformations. .

Symbols

HAZ	- heat affected zone	$W_{6/5}$	-	cooling rate (600÷500ºC range), ºC/s
I	- welding current, A	$W_{8/5}$	-	cooling rate (800÷500ºC range), ºC/s
KCU	- impact strength with curve radius, J/cm^2	*WTC*	-	welding thermal cycle
KCV	- impact strength with sharp cut, J/cm^2	*YS*	-	yield stress, MPa
Q	- heat input, kJ/cm	**Greek letters**		
U	- voltage, V	δ_5	-	elongation for failure, %
UTS	- ultimate tensile strength, MPa	ψ_z	-	narrowing in the z direction, %
V	- welding speed, m/hour	ψ	-	reduction factor, %

Table 1. Requirements for the chemical composition of high and high strength steels for building structures

Steel grade	Chemical composition, wt %										
	C	Si	Mn	Cr	Ni	Mo	V	Al	Cu	S	P
09G2S	≤0.12	0.5-0.8	1.3-1.7	<0.3	<0.3	-	-	-	<0.3	<0.035	<0.03
15KhSND	0.12-0.18	0.4-0.7	0.4-0.7	0.6-0.9	0.3-0.6	-	-	-	0.2-0.4	<0.035	<0.03
17G1S	0.15-0.20	0.4-0.6	1.15-1.6	<0.3	<0.3	-	-	-	<0.3	<0.035	<0.03
10G2S1	≤0.12	0.8-1.1	1.3-1.65	<0.3	<0.3	-	-	-	<0.3	<0.035	<0.03
10KhSND	≤0.12	0.8-1.1	0.5-0.8	0.6-0.9	0.5-0.8	-	-	-	0.4-0.6	<0.035	<0.03
06GB	0.04-0.08	0.25-0.50	1.1-1.4	≤0.08	≤0.05	0.01-0.03	0.02-0.05	-	<0.3	<0.01	<0.025
06G2B	0.04-0.08	0.25-0.50	1.3-1.6	≤0.10	0.02-0.05	0.03-0.05	0.03-0.07	-	<0.3	<0.01	<0.025
09G2SY	0.08-0.11	0.3-0.6	1.9-2.2	-	0.035-0.065	-	-	0.002-0.005	0.3-0.6	<0.015	<0.02
10G2FB	≤0.15	≤0.35	≤1.7	≤0.3	0.02-0.03	≤0.08	≤0,1	-	-	<0.01	<0.02

Table 2. Requirements for mechanical properties of high and high strength steels for building structures (not less)

Steel grade	YS	UTS	δ_5,	KCU^{-40},
	MPa		%	J/cm^2
09G2S	350	500	21	34
15KhSND	350	500	21	29
17G1S	350	500	22	29
10G2S1	390	520	19	29
10KhSND	390	530–660	19	29
06GB	390	490	22	98
06G2B	440	540	22	98
09G2SY	450	570	19	29
10G2FB	490	565	22	29

The mass transition of enterprises to economic independence has prompted the creation of steels, the production of which is most economically advantageous for the specific economic conditions of the plants.

Intensive integration of domestic metallurgy into the world economy has necessitated a revision of steel quality assessment standards.

First of all, it concerns the evaluation of their impact strength. A generally accepted approach, to determine the impact strength in the domestic industry, is the examination of samples with a U-shaped notch. The usage of V-shaped notch samples instead of U-shaped also started. Their use in tests allows a more accurate assessment of the ability of steels to resist failure. At the same time, this approach revealed certain shortcomings of domestic steels. There is a need, therefore, to modernize existing and create new steels that would meet the ever-increasing demands of production. As a result, in recent years, domestic metallurgical plants have mastered the production of new steels with high strength, which are manufactured according to domestic and international standards and fully meet the Euronorms requirements.

These modern high-strength structural steels, manufactured at the metallurgical enterprises of Ukraine, have exceptionally high mechanical properties.

Consequently, they were all recommended and included in the State Building Regulations as those that can be used in the manufacture of metal structures. To justify this possibility in the Institute of Electric Welding Є.О., comprehensive studies have been performed at the Paton Electric Welding Institute, which have shown the good ability of these steels to weld and to determine the welding conditions under which the joints of these steels will fully meet the modern requirements for metal structures.

2. Experimental setup

Evaluation of the ability of steels to weld is to determine the optimal welding conditions, which excludes the possibility of forming cold cracks in joints and metal zones of thermal influence of structures that will reduce strength, ductility and cold resistance.

In contrast to rolled steel, the structure formation in the HAZ metal of welded joints of high-strength steels is significantly influenced by the welding thermal cycle (WTC) [1-9]. The most significant changes in the structure of steel during welding occur in the area of overheating of the HAZ metal, i.e. in its zone closely adjacent to the weld and heated to a temperature of 1150–1300 oC. In arc welding, WTC parameters depend on several factors, the most important being the running energy of the weld, the initial temperature of the metal and its thickness, the type of welded joint. By increasing the welding linear energy and the initial temperature of the metal, the cooling rate of the HAZ metal in the temperature range 600-500 °C ($W_{6/5}$, °C/c) decreases. By increasing the metal thickness, such cooling rate increases. In view of this, we have chosen $W_{6/5}$ as a criterion that allows comparing the reaction of steels to TCP and determining how the heating and cooling conditions of the metal affect its structure and mechanical properties. To determine the toughness of the "roller test", samples were obtained by cutting blanks, having a $10\times10\times55$ mm cross section (type VI with a round cut and type IX with a sharp cut). Tests of the samples were performed at a temperature of −40 °C.

The studies have been performed in relation to heat-treated samples and samples obtained from surfacing on a plate. The influence of thermal welding cycles on the HAZ metal structure was studied by dilatometric analysis and optical microscopy [10]. Mechanical tests for static tension and impact bending have been carried out by using standard samples.

To determine the influence of the chemical composition and cooling conditions of the metal on its structure, austenite conversion diagrams were used, taking into account the processes occurring during welding. In this case, to ensure a high resistance of austenite to welding, the following heating conditions were chosen in creating the conversion diagrams, under which the individual features of steels related to the tendency to grain growth begin to appear quite clearly. Typically, during the dilatometric analysis, the heating rate of the samples is set in the range of 150–300 °C/s [11]. In our experiments it was 150 °C/s. The cooling rates of the dilatometric samples were chosen based on the need to ensure in the temperature range the lowest stability of austenite cooling conditions, which will be as close as possible to the cooling conditions of the metal in the overheating area of the thermal zone of joints made with arc welding. The heating rate was regulated by changing the current flowing through the sample according to a given program. The cooling rate was regulated by cooling devices that transmit current from the heating machine to the sample with water, blowing the samples with inert gas.

Due to the rigid fixation of the samples in the heating machine, the processes of internal deformations are simulated in the area of uniform heating.

3. Results and discussion

The dependences on the change of structural components occurring at different cooling rates in the overheating area of the HAZ metal of new high-strength microalloyed steel structures are presented on the basis of the austenite transformation diagram (Figure 1).

In contrast to low-alloy steels 09G2S, 10HSND, 15HSND - in which the austenite conversion largely depends on the metal cooling rate and it can occur in ferrite (at moderate cooling rate, up to 10 °C/s) and in bainite and martensitic areas at high speeds -, in microalloyed steels of grades 06GBD, 06G2B and 10G2FB it occurs very differently. In almost the entire studied range of cooling rates, the transformation of austenite in the metal overheating area of HAZ occurs mainly with the formation of bainite concerning the 06G2B and 10G2FB steels, and ferrite, perlite and bainite concerning the 06GB steel [1, 2].

An exception among the studied microalloyed structural steels is the grade 09G2SYu [5], in which, as in most low-alloy high-strength structural steels, the transformation of austenite occurs with the formation of bainite and martensite. In the future, we are considering how the cooling conditions of the metal under the influence of TCC affect its mechanical properties.

To obtain information on the TCZ effect on static strength and plastic properties of the HAZ metal, standard tensile samples are used, obtained from thermal pre-treated welding bars of the considered metal. This is due to the fact that usually the size of the HAZ and its individual components is much smaller than that of the samples being tested. In this case, therefore, studies on changes in yield strength, elongation and relative narrowing that occur in the metal HAZ steels under the influence of WTC are obtained adopting the above mentioned approach. Bars with a size of $13\times13\times150$ mm^3 were used, thus, processed by the thermal cycle of welding on the installation MCP-75 [12].

The results indicate that when the metal is cooled in the area of HAZ overheating with a cooling rate of $W_{6/5}$, which does not exceed 10 °C/s, it may weaken. This is caused by the fact that the values of its yield strength decrease in relation to the base metal by 10–25%. In the range of velocities from 3–10 °C/s, the values of YS and ultimate tensile stress (UTS) of HAZ metal increase rapidly and then increase rather slowly.
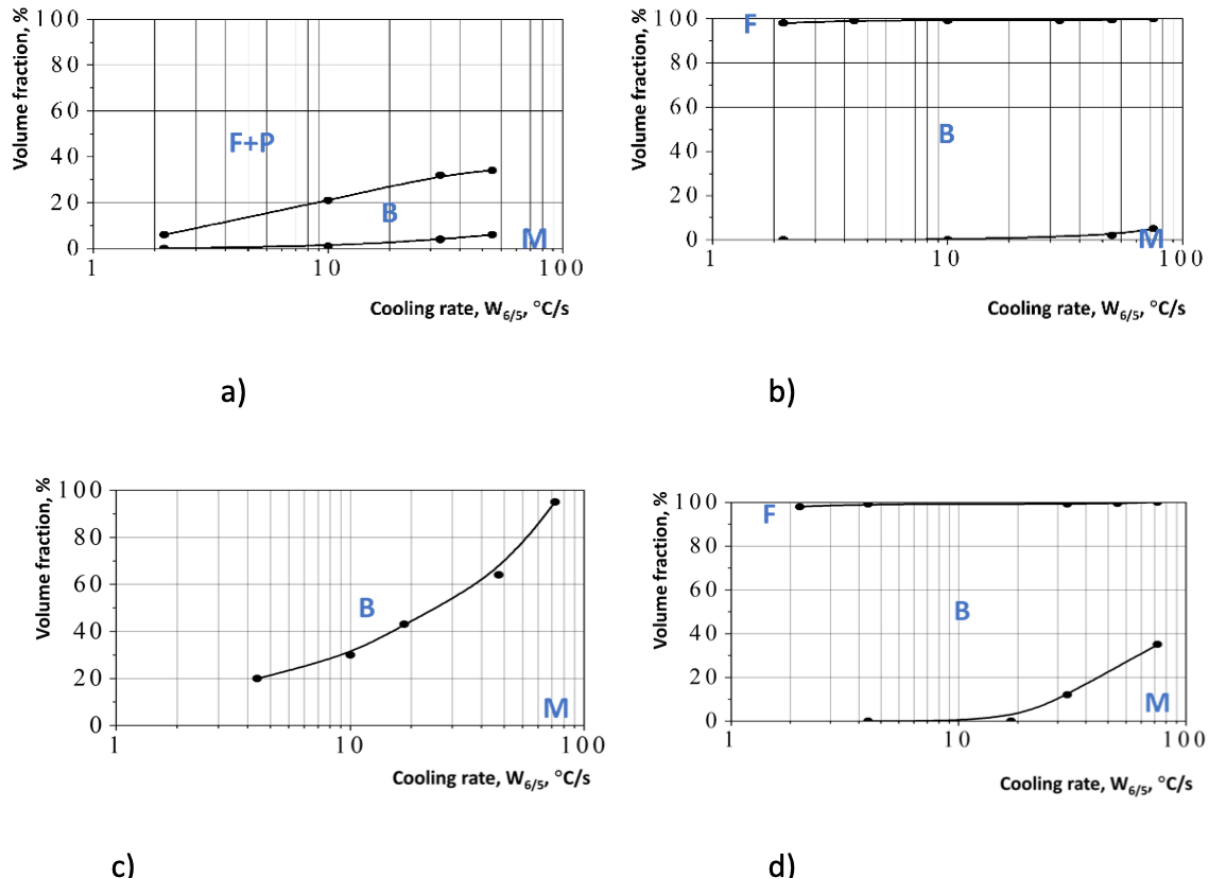
Figure 1. Diagrams of structural transformations of austenite in the overheating area of HAZ metal of low-alloy high-strength steels of type: (a) 06GBD; (b) 06G2B; (c) 09G2SYuch; (d) 10G2FB

This is quite natural because, as evidenced by the data shown in Figure 2, the HAZ metal structure of high-strength microalloyed structural steels in a wide range of cooling rates is stable. The plastic properties of the HAZ metal of these steels are also somewhat reduced but they remain quite high and stable over a wide range of cooling rates.

The WTC influence on the impact strength of the HAZ metal of the considered structural steels was studied using a "roller test", performed in accordance with GOST 13585-68.

To provide cooling conditions for welded joints with characteristics of manual, mechanized in shielding gases and automatic under the flux layer of arc welding processes of metal of different thickness - namely in the range from 3.0 °C/s to 5.0 °C/s -, deposition on 20 mm thick plates was performed with a wire of solid cross section having a diameter of 4.0 mm under a layer of flux in the modes shown in Table 3.

The results reported in Figure 2 show that, under the HAZ welded joints cooling conditions with a speed of $W_{6/5}$ more than 5.0 °C/s, metal impact strength (KCV-40) in the area of overheating is provided at a level that significantly exceeds modern requirements for building metal structures. With slower cooling speed, KCV-40 values may decrease to critical levels.

In general, studies have shown that the new microalloyed structural steels of strength classes C350-C490 in mechanical properties are dominated by low-alloy structural steels of strength classes C350-C390, which were developed in the USSR.

Table 3. Modes in which the surfacing was performed on the plates.

№	I A	U V	V m/hour	Q kJ/cm	$W_{6/5}$ °C/c
1	580…600	34…38	9.8	62.7	3
2	580…600	34…38	14.7	41.8	6
3	580…600	34…38	17.3	35.7	10
4	580…600	34…38	21.7	28.6	20
5	380…400	30…32	15.2	23.0	30
6	380…400	30…32	20.1	16.7	50

The latter are more technological and provide a set of welds properties at the level of modern world requirements for metal building structures. This was the impetus for the fact that from the beginning of the current millennium such steels began to be gradually introduced in Ukraine for the manufacture of welded metal structures for the needs of the construction industry in bridge construction, mechanical engineering, etc.

In particular, the technological processes of arc welding developed on the basis of the above reported results have been introduced in the manufacture of unique building structures, in particular during the construction of an oil storage tank with a volume of 75,000 m^3 made of rolled steel 06G2B of strength class C440 in Brody (Figure 3).

The experience gained in performing this work was exploited, subsequently, during the manufacture of metal structures of tanks with a capacity of 50,000 m^3 in the modernization of the tank farm in Mozyr (Republic of Belarus) on the section of main oil pipelines. These structures are made of rolled steel 06GB strength class C390 with a thickness of 20-30 mm, using mechanized welding in a mixture of gases (82% Ar + 18% CO$_2$) wire of solid cross sectionIn the year 2006, the steel 06GBD strength class C390 and welding technology were used in the manufacture of metal structures at the plant. I.B. Babushkina (Dnipro) of metal structures for the Podolsk bridge over the Dnieper River in Kyiv (Figure 4).

In preparation of the European Football Championship EURO 2012 in Ukraine, technologies for automatic welding under a layer of flux were developed and certified, mechanized in shielding gases and manual arc welding of 16-100 mm thick steel S355J2 (analogue steel 10G2FB strength class C355). In the period 2010-2011, they were introduced during the manufacture and the installation of box metal structures for the canopy over the NSC "Olympic" (Kyiv) during its reconstruction. The welded metal structure with a total weight of 40 thousand tons consists of 80 lower and front columns with a length of 23.0 to 25.5 m, each weighing from 25 to 30 tons, as well as beams of the lower and upper compressed rings of Figure 5.

The experience gained during the reconstruction of the NSC "Olympic" contributed to the successful completion of a new task in 2013, namely, the development of welding technology for the manufacture and installation of tubular steel structures made of steel 10G2FBYu strength class C490 for a football stadium for 45,000 spectators.

An advanced nano(micro)-characterization of the studied samples is planned by using neutron beam techniques (NBT), which has been already adopted to analyse wire samples made of low-alloyed quality structural steel Grade 08G2S GOST 1050 [13, 14]. Such additional investigation would supplement the information achieved from the other characterization methods, providing significant data helping to estimate the effect of the welding process on:

− residual stresses (RS), by using neutron diffraction [15]

− nano(micro)-structure, by using small angle neutron scattering [16], studying the morphology of grains and monitoring anisotropy and other key parameters of eventual nanocracks, nanopores and other nanosized defects, responsible for mechanical properties.

Welding processes, indeed, involve very high temperature gradients that can induce elevated RS. It is essential to know these RS, especially by determining them experimentally, e.g. before and after thermal treatments [17].

NBT contribute in general to the solution of important questions and problems related to the methodological restrictions of the analysis systems normally used: complementary to these investigation methods, they provide concrete and fundamental help to optimize the finished industrial product and increase its performance [18, 19].
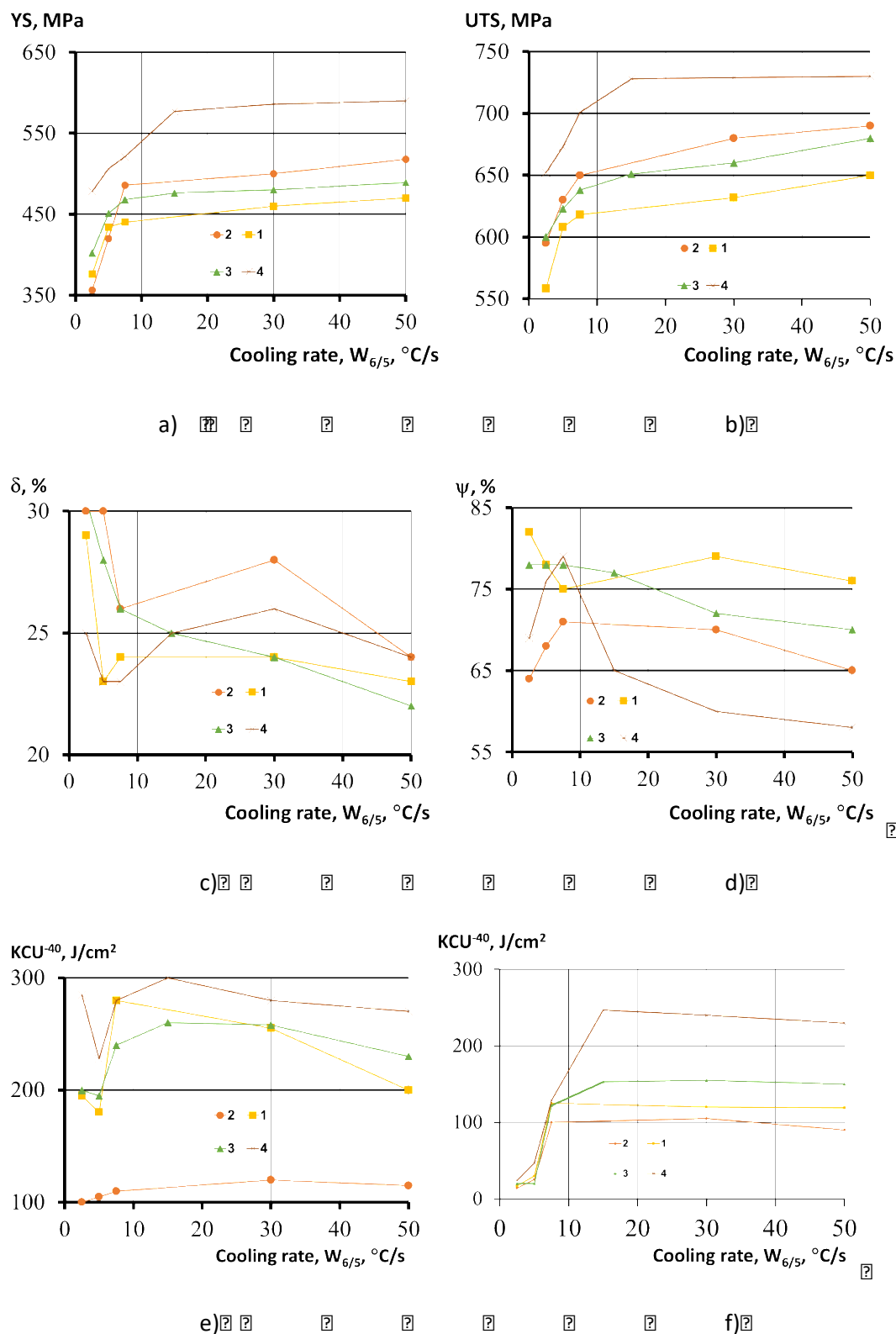
Figure 2. Influence of cooling rate W$_{6/5}$ on limit values yield strength (a); tensile strength (b); elongation (c); relative narrowing (d); toughness (e) of HAZ metal steels: (1) 06GBD; (2) 09G2SYuch; (3) 06G2B; (4)10G2FB
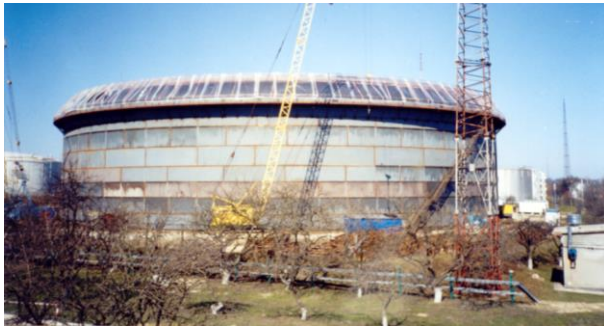
Figure 3. 75000 m³ oil storage tank made of steel hire 06G2B-440

Figure 5. The NSC "Olympic" in Kyiv

Figure 4. Construction of the Podilsky bridge crossing in Kyiv the arch of which is made of steel 06GBD strength class C390

4. Conclusions

In contrast to most structural low-alloy steels, the conversion of austenite in microalloyed vanadium and niobium steels of strength class from C350 to C 490 under continuous cooling over the thermal cycle of welding occurs mainly in the bainite region.

As a result of structural transformations that occur in steels under the influence of thermal welding cycles, the static strength of the metal of the zone of thermal influence of welded joints increases, and the plastic properties decrease.

A significant decrease of the impact strength in the metal of the zone of thermal impact of welded joints of microalloyed structural steels is observed at W6/5 ≤ 5.0 0C/s. As the cooling rate increases, the impact strength of the HAZ metal increases rapidly, and in some steels almost reaches the level of the base metal.

REFERENCES

[1] Zhdanov, S.L., Poznyakov, V.D., Maksimenko, A.A. Dovzhenko, V.A., Vasiliev, V.G., Vysokolyan, N.V., Korobka V.A., 2010. Structure and properties of arc-welded joints on steel 10G2FB. The Paton Welding J. 11, 8-12.

[2] Poznyakov, V.D., Zhdanov, S.L., Maksimenko, A.A., Sineok A.G., Gerasimenko A.M., 2013. Weldability of sparsely-alloyed steels 06GBD and 06G2B. The Paton Welding J, 4, 8-14.

[3] Poznyakov, V.D., Zhdanov, S.L., Maksimenko, A.A., 2012. Structure and properties of welded joints of steel S390 (S355 J2). The Paton Welding J. 8, 6-10.

[4] Poznyakov, V.D., Zhdanov, S.L., Zavdoveev, A.V., Maksimenko, A.A., Solomijchuk, T.G., 2016. Weldability of high-strength microalloyed steel S460M. The Paton Welding J. 12, 23-30.

[5] Mikhoduj, L.I., Kirian, V.I., Poznyakov, V.D., Strizhak, P., 2003. Sparsely-alloyed high-strength

steels for welded structures. The Paton Welding J. 5, 34-37.

[6] Ufuah, E., Ikhayere, J., 2013. *Elevated temperature mechanical properties of butt-welded connections made with high-strength steel grades S355 and S460M*, Int. Conf on Design, Fabrication and Economy of Metal Structures, Miskolc, Hungary

[7] Nazarov, A., Yakushev, E., Shabalov, I., Morozov, Y.D., Kireeva, T.S., 2014. Comparison of weldability of high-strength pipe steels microalloyed with niobium and vanadium. Metallurgist 7/9-10, 911-917.

[8] Ragu Nathan, S., Balasubramanian, V., Malarvizhi, S., Rao, A.G., 2015. Effect of welding processes on mechanical and microstructural characteristics of high strength low alloy naval grade steel joints. Defense Technology 11, 308-317.

[9] Show. B.K., Veerababu, R., Balamuralikrishnan, R., Malakondaiah, G., 2010. Effect of vanadium and titanium modification on the microstructure and mechanical properties of microalloyed HSLA steel. Mater. Sci. Eng. A 527, 1595-1604.

[10] Grigorenko, G.M., Kostin, V.A., Orlovsky, V.Yu., 2008. Modern possibilities for modeling of austenite transformations in low-alloyed steel welds. The Paton Welding J. 3, 31-34.

[11] Seyffarth, P., 1982. *Schweiss- Z.T.U.-Schaubilder*, VEB Verlag, Berlin

[12] Sarzhevsky V.A., Sazonov, V.Ya., 1981. Installation for simulation of welding thermal cycles based on machine MCR75. Avtomatich. Svarka 5, 69-70 [in Russian].

[13] Rogante, M., Mikula, P., Strunz, P., Zavdoveev, A., 2017. *Residual stress determination by neutron diffraction in low-carbon steel wires with accumulated shear deformation*, MTMS2017, Split

[14] Zavdoveev, A., Len, A., Pashinska, E., 2021. Small angle neutron scattering study of nanoscale structure of low-carbon steel after rolling with shear followed by cold drawing. Met. Mater. Int. 27, 481–487.

[15] Determinazione delle tensioni residue mediante diffrazione neutronica, Studio d'Ingegneria Rogante, Civitanova Marche, Italy, pagina web http://www.roganteengineering.it/pagine_servizi/servizi1.pdf (accessed 08 July 2022).

[16] Caratterizzazione di materiali e componenti a livello di micro- e nano-scala mediante Diffusione Neutronica a piccoli angoli, Studio d'Ingegneria Rogante, Civitanova Marche, Italy, pagina web http://www.roganteengineering.it/pagine_servizi/servizi2.pdf (accessed 08 July 2022).

[17] Rogante, M., 2020. Inside welds: advanced characterization of residual stresses by neutron diffraction - Метал швів: удосконалення методу оцінки остаточних напружень за допомогою нейтронної дифракції, Automatic Welding - Автоматическая сварка 11, 20-26; The Paton Welding J. 11, 18-24.

[18] Rogante, M., 2008. *Applicazioni Industriali delle Tecniche Neutroniche*, 1st. Italian Workshop for Industry "Industrial Applications of Neutron Techniques", Civitanova Marche, Italy

[19] Rogante M., Rosta, L., 2005. Nanoscale characterisation by SANS and residual stresses determination by neutron diffraction related to materials and components of technological interest. Proc. SPIE 5824, 294-305.

Neuroplastic structure of the connectome in relation to environmental quality

Claudio SANTELLI[1)]

1) Santelli Medical Office, Viale Europa n. 81,
   63831 Rapagnano (FM), **Italy**

claudiosantelli8@gmail.com

Keywords

Environment protection
Neuroplastic structural materials
Connectome
Reweighting
Reconnection
Rewiring
Regeneration

Original scientific paper

Abstract: This review article highlights the influence that natural and social environment, well cared for and redeveloped, can have on life quality of the people who live and work there.

The environment has always had a great deal of importance on health and well-being of the inhabitants, starting with the observations and practical applications of Hippocrates and the Romans.

Environmental requalification allows individuals who live there developing an experience capable of modulating the continuous reconfiguration of the neuronal electrical circuits forming the maps of the connectome.

From the studies initiated by Prof. Sebastian Seung at the Neuroscience Department of the Massachusetts Institute of Technology (MIT), it is highlighted how the epigenetic information received from the surrounding environment influences the neuroplastic structure of the connectome through continuous updates. These updates are defined with the 4 R occurring in neuronal cells, i.e. Reweighting, Reconnection, Rewiring, and Regeneration.

1. Introduction

The environment, understood as a natural, urban and social space, has always played a very important role in human well-being.

Hippocrates of Cos, father of the modern Western medicine, in the 4th century BC reported the results of observations on influence of the environment on human health in some volumes (such as "De Aer, aquis et locis") of his treatise "Corpus Hippocraticum" [1].

The Roman castrum also served as a model for subsequent cities based on a preventive study of the geological site and on the correct orientation according to the cardinal points: cardo maximus from north to south and decumano maximus from west to east (Figure 1).

Within the project of the Roman city, the presence of a theater, an amphitheater, architecture and marble sculptures and a spa center were foreseen, resulting from the fusion between the Greek gymnasium and the Egyptian Turkish bath.
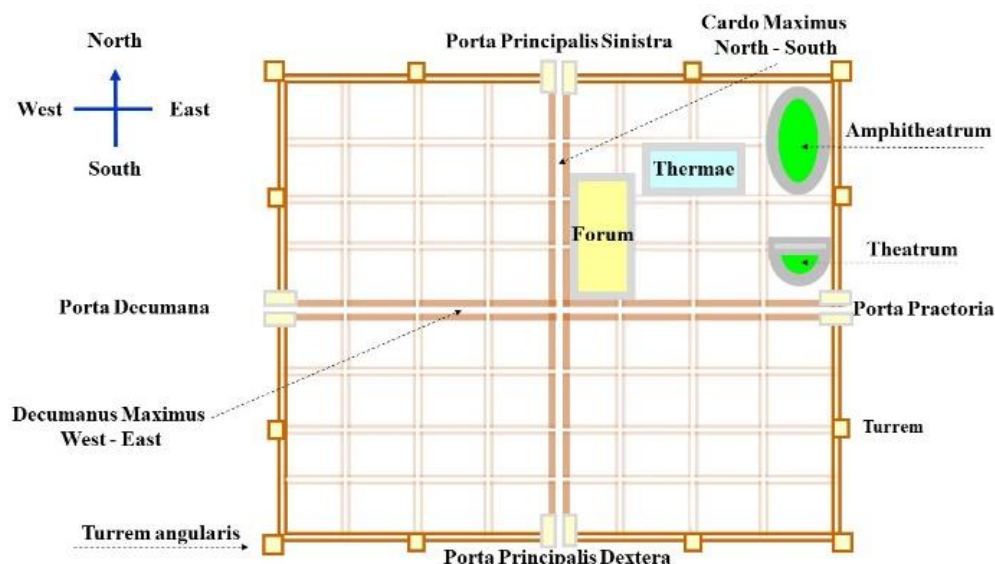
Figure 1. The Roman town

The SPA included the following zones: Gymnasium, Swimming pool, Tepidarium, Calidarium, Frigidarium, Laconicum, Library, Theater. They were the precursors of modern SPAs: some, in fact, attribute the meaning of the word SPA to the acronym of *Salus Per Aquam* while others refer to the name of the Belgian town famous for its thermal waters (Figure 2).

The same principles used for the design of the city, with the necessary internal adjustments, were also applied for the construction of the palaces, such as the Diocletian's Palace in Split (Figure 3).
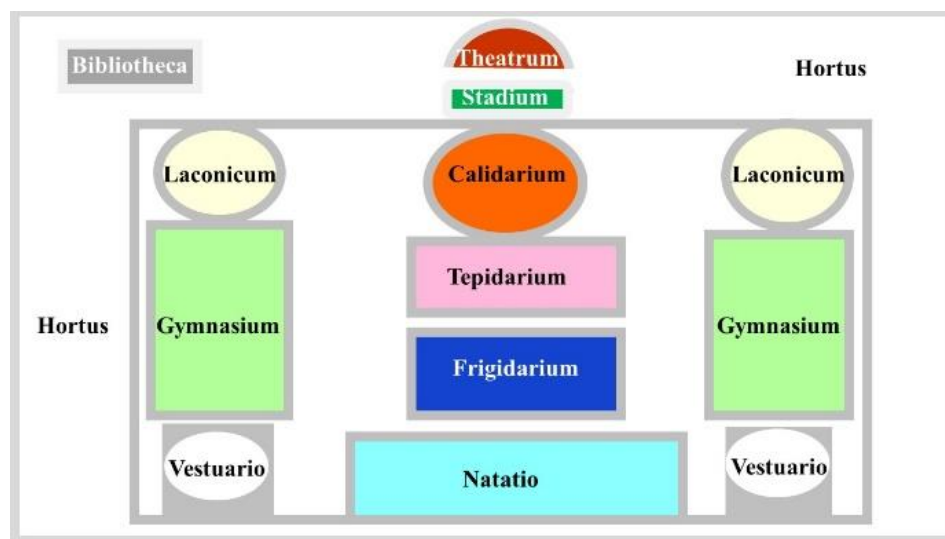
Figure 2. Thermae
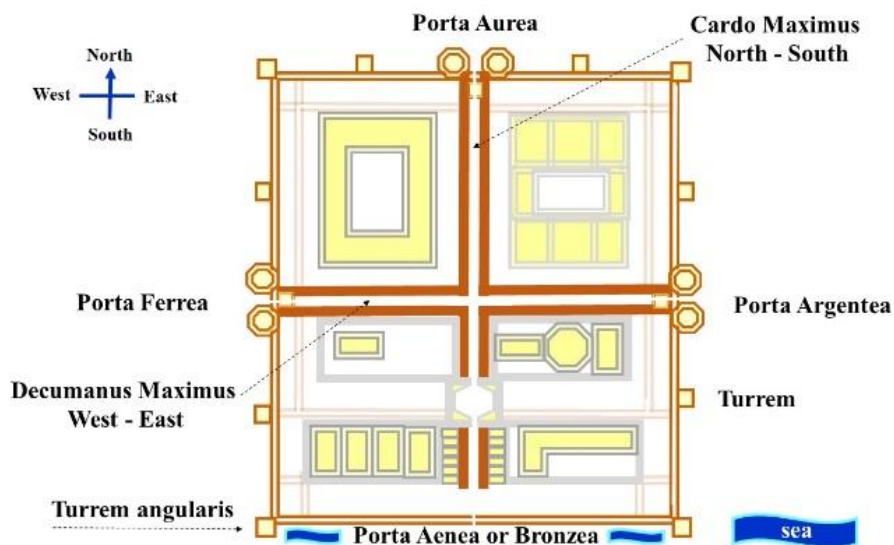
Figure 3. Diocletian's Palace, Split, Croatia

Currently, the value that the environment, well cared for and redeveloped, can have on life's quality of the people who live and work there is being rediscovered, with advantages also from an economic point of view for tourism and production activities in the enhancement and narration of the Local "terroir".

In recent years, a significant increase occurred of the number of companies, especially wineries, which protect the territory and combine their products with "site specific" works of art both in the landscape of the vineyard and within the cellar.

In these interventions the artist, after a careful observation and study of the place, designs a work that is in relationship with the surrounding landscape by changing its perception [2].

Claude Shannon (Petoskey, Michigan, USA 1916 - Medford, Massachusetts, USA, 2001) theorized the formula:

$$I = -E \qquad (1)$$

i.e., an increase in entropy corresponds to a loss of information on a given system and vice versa [3]. This equation is also valid at the environmental level.

The redevelopment of a territory, reducing entropy, will provide better information.

The environment in which people are born, grow up, live, work and age, affects the individual's ability to be healthy, the risk of getting sick and life expectancy.

In the face of an increase in life expectancy, preventive actions on society and environment will therefore become fundamental for healthy aging, including through a One Health approach to improve global health security that takes into account the relationship between humans, animals and environment. More and more countries have implemented this method in recent years, obtaining recognized benefits [4].

The stimuli that come from a certain environment are epigenetic signals that the brain processes by continuously reconfiguring the connectome that is a map formed by the network of connections between the neurons of the various brain areas.

Today it is possible to map these connections between neurons in the human brain through the development of Diffusion Magnetic Resonance Imaging (DW-MRI), which allows us visualizing them as a graph [5].

The connectome - describing the set of neuronal connections of the brain of a species with indications on the potential adaptations of the brain wiring network with the environment - has been used, on a macroscopic scale, also for comparative studies. In these analyses, the characteristics of the connectomes werw compared of different animal species, to acquire information on the evolution, at the network level, of connectivity and function of the human brain [6].

The environment in which we live affects the neural activity of the brain which stores and encodes memories, thoughts and lived experiences: in few words, everything that makes us the people we have become during the experience of life. Unlike the genome, an individual's connectome changes over the years.

Sebastian Seung started this project in 2009 at the Department of Brain and Cognitive Sciences and the Department of Physics at the MIT in collaboration also with European research centers, assuming to be able to complete the mapping of the human connectome within the end of this century.

The purpose of the study is to understand how the connectome of a healthy subject is made and how it varies during:
• learning,
• the disease and
• aging.

2. Discussion

Why to study connectomes if genomics are already so powerful? Because genes alone do not explain how the brain has become after the life experience and the interaction with the environment. Connectionism considers brain regions as complex networks whose organization is shaped by genes and can be modified by experience.

The effects of urban planning, landscape aesthetics of how exposure to nature is viewed and the role of individual preferences for the environment have been studied by researchers from different disciplines who have shown how they can impact on cognitive function, mental health and human well-being [7].

Inter-individual differences are more evident as people age; cultural and educational experiences contribute to this heterogeneity. Studies based on functional magnetic resonance imaging (fMRI) data, in a resting state, show how high levels of education and continuous cultural stimuli measured over the years increase the brain efficiency of elderly individuals by mitigating the effects of cerebral senescence, due to age, which is associated with decreased functional connectivity in most of the cerebral cortical network [8].

The neuroimaging methods used, i.e. fMRI to analyze the mechanisms of gray matter and DW-MRI to study white matter, allow representing the axon beams in different colors depending on the direction of the synaptic flow.

Unlike the genome, which is fixed at conception, an individual's connectome varies throughout life based on environmental experiences and learning by consolidating memory traces of learned skills [9]. There are continuous rearrangements of the synapses that remodel the neuronal electrical circuits by strengthening some synaptic connections and the selective elimination of others [10].

The synapses that form among the brain's 100 billion neurons constantly change over time through what Seung calls the 4R [11]:
• R1 = Reweighing: neurons adapt (or reweigh) their connections by strengthening or weakening them through variations in the number of neurotransmitter vesicles in the synaptic terminations
• R2 = Reconnection: neurons reconnect by creating or eliminating synapses
• R3 = Rewiring: neurons reform new circuits (rewire themselves) by making branches grow or retract
• Neuronal circuits form the physical structure of brain communication and the study of the

connectome allows us to understand how cognitive function and behavior originate from this structure Recent studies have shown that connections in neuronal circuits are not stable and, once formed, can modify the rewiring based on learning and experience, suggesting that the connectome is much more dynamic than previously believed [12]

- R4 = Regeneration: creation and elimination of neuronal cells (Figure 4).
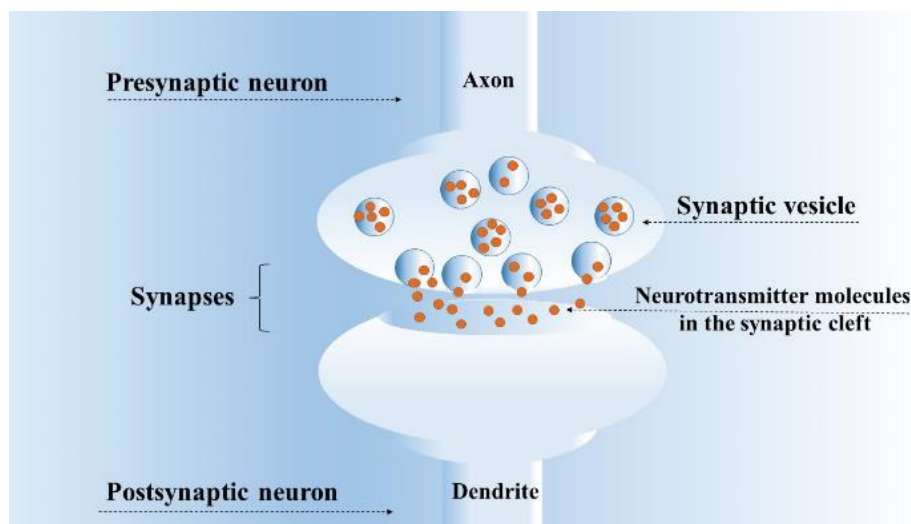

Figure 4. Synapses

3. Conclusions

"The external landscape is reflected on the internal landscape" one could say when talking about mirror neurons.

The environment that surrounds us (nature, people, objects, art, landscape, food, etc.) has epigenetic effects capable of influencing the plastic and dynamic formation of the brain maps of the connectome.

The environmental requalification, both structural and cultural, allows a better reconfiguration of the connectome maps and a consequent improvement of the lifestyle and well-being of the inhabitants.

REFERENCES

[1] Konstantinidou, M.K., Karaglani, M., Panagopoulou, M., Fiska, A., Chatzaki, E., 2017. Are the Origins of Precision Medicine Found in the Corpus Hippocraticum? Mol. Diagn. Ther. 21(6), 601-606.

[2] Santelli, C., 2018. *Scultura ambientale e connettoma*. Ph.D. Thesis, Academy of Fine Arts of Urbino, Italy

[3] Ricci, L., Perinelli, A., Castelluzzo, M., 2021. Estimating the variance of Shannon entropy. Phys. Rev. E. 104(2-1), 024220.

[4] Sinclair, J.R., 2019. Importance of a One Health approach in advancing global health security and the Sustainable Development Goals. Scient. Techni. Rev. 38(1), 145-154.

[5] Szalkai, B., Varga, B., Grolmusz, V., 2021. The Graph of Our Mind. Brain Sci. 11, 342.

[6] Ardesch, D.J., Scholtens, L.H., Van den Heuvel, M.P., 2019. The human connectome from an evolutionary perspective. Prog. Brain. Res. 250, 129-151.

[7] Bratman, G.N., Hamilton, J.P., Daily, G.C., 2012. The impacts of nature experience on human cognitive function and mental health. Ann N Y Acad Sci. 1249, 118-136.

[8] Marques, P., Soares, J., Magalhães, R. Santos N.C., Sousa N., 2015. The Bounds Of Education In The Human Brain Connectome. Sci. Rep. 5, 12812.

[9] Santelli, C., 2019. *Epigenetica e connettoma,* Exhibition/Conference Arte e Connettoma, 2019, Rasiglia, Italy

[10] Caroni, P., Chowdhury, A., Lahr, M., 2014. Synapse rearrangements upon learning: from divergent-sparse connectivity to dedicated sub-circuits. Trends Neurosci. 37(10), 604-614.

[11] Seung, S., 2013. Connettoma. La nuova geografia della mente. Le Scienze. https://www.lescienze.it/edicola/2013/08/01/news/connettoma_la_nuova_geografia_della_mente-1761453/ (accessed 01 August 2022).

[12] Bennett, S.H., Kirby, A.J., Finnerty, G.T., 2018. Rewiring the connectome: Evidence and effects. Neurosci. Biobehav Rev. 88, 51-62.

Manufacturing of replacement exhaust manifold for marine engine

Slaven ŠITIĆ[1], Mate BALIĆ[1]
1) University of Split, University Department of Professional Studies, Kopilica 5, 21000 Split, **Croatia**

sl.sitic@oss.unist.hr
mb47412@oss.unist.hr

Keywords

*production processes,
exhaust manifold,
aluminium alloy*

Professional paper

Abstract: Marine engine exhaust system is the most exposed part of the engine to various combinations of thermal and corrosive effects. Excessive corrosion often occurs due to insufficient system maintenance. The various materials used further enhance these processes. Older engines that have proven to be reliable in their operation, although regularly maintained, can result in the failure of certain parts due to operating conditions. Boat owners do not want to replace propulsion engines with new ones because of their simplicity and self-maintenance.

Some parts are not available and should be repaired if possible and sometimes completely replaced with newly made pieces. The exhaust manifold for older engine types is often not available and therefore the only option is making a replacement part.

The process of manufacturing a replacement marine engine exhaust manifold is the focus of this paper.

1. Introduction

Marine heat exchanger systems are engine parts exposed to various tribological processes. Every manufacturer strives to improve and create the highest quality exchanger, as different models appear on the market. The basic division of exchangers regard to function and mode of operation is direct and indirect systems. There is a greater number of divisions within different performance in ship systems, however there are two basic variants: plate or honeycomb and tubular exchangers. The first used for larger ship systems primarily due to their efficiency. In addition to boilers, tubular heat exchangers are also used for smaller power units. The exchanger has numerous roles of which the first is heat exchange. This takes place between the closed system inside the engine, driven by the water pump, and circulates through the water paths inside the engine.

At the exit from the engine water passes into the tubular exchanger, and the heat exchange takes place with the system, which enters the tubular exchanger via the sea intake. At the exit from the tubular heat exchanger, seawater is transported to the final part, where it mixes again in a special exhaust collector with the combustion gases, thus cooling them additionally. The cooled water from the tubular heat exchanger is returned through the engine and the compensating vessel tank and thus this cycle is completed. In addition to this function, the cooling water can also have the role of removing part of the heat from the exhaust gases. To insure this the radiator is also the exhaust collector and must be located on the engine block. The collector (cooler) installed in this way exchanges heat between water and combustion gases, and this process is indirect because it takes place through separate walls. In addition to this heat exchange, it is also possible to heat the intake gases via this collector. This last version of the exhaust manifold could be called "four in one". The quality maintenance process of both the engine and the exhaust system requires a periodic inspection with the appropriate replacement of consumable parts. In the case of such systems, the manufacturing technology and the materials used are based on aluminum casting alloys. However, older engines that have survived as old timers have exhaust manifolds made of gray cast iron. The advantages, both due to weight and thermal conductivity, are undoubtedly on the side of aluminum alloys, especially for smaller power units. The serial production of such exhaust manifolds can significantly affect the reduction of the price of the product, but also the unit production of the casting can significantly increase the price of the final product to the point of unprofitability for both the manufacturer and the user. However, the possibility of applying different production processes and using semi-finished products can significantly simplify the production of such an exhaust manifold, but there is still no possibility to completely replace the product which is an original casting. Such production would also require the production of a model and core.

2. The process of making a replacement part

The process of making a replacement part is defined in accordance with the possibilities of applying the appropriate available production procedures as well as the possibility of making a replacement piece. After

inspecting the worn part of an exhaust manifold for marine engine, significant damage to the exhaust manifold was observed in the form of a cavity created because of material peeling from the water side, visible in Figure 1.

Figure 1.   The picture shows damage to the exhaust duct due to the influence of temperature and erosion over a long period of time.

This indicates the impossibility of repair by the welding process. After concluding that it is impossible to carry out a high-quality and reliable repair, the preliminary design of the replacement piece is approached. This phase includes the definition of manufacturing possibilities using available production processes and standard available materials (sheets, profiles, pipes).

It is also important to note that a complete casting would be the highest quality product, but not from an economic point of view. Making all the necessary molds, models and cores would require a long process that would not be economically justified on one product. However, it should be emphasized that individual parts can be cast using simple molds and can be shaped appropriately by welding and subsequent machining. They were used to make the exhaust-intake manifold raw materials of known chemical composition to reduce the additional corrosive influences. In addition to standard products such as sheets, bars, which can be seen in Figure 2.

Figure 2.   Sheets and round bars cut, uncored and positioned in the corresponding holes on the sheet.

it is necessary to make the flanges of the tubular heat exchanger by casting in a mold. After machining the cast

flanges, the process of welding them to a seamless pipe of the appropriate diameter was carried out. Such an element is machined to approximate dimensions because it is necessary to leave an allowance for processing after the welding process, which can cause deformations. Figure 3. shows the machining of the tube exchanger in processing.

Figure 3.   Machining the inner diameter of the tube exchanger housing.

The production of exhaust gas ducts is specific due to its shape. In addition to the dimensions of the section, the design must allow the passage of channels between the bars to allow screws for tightening the exhaust manifold to the engine block. The exhaust gas channel will remain closed inside the housing. It is necessary to make the exhaust channel with high quality and precision because it will be inaccessible in the next phase. Figure 4 shows the exhaust gas channel in the intermediate space of the upper part of the exhaust manifold

Figure 4.   The picture shows the manufactured exhaust gas channel positioned between the aluminum rods.

Due to its curvature, the exhaust channel is made of previously prepared sheets and strips that are welded. All materials are AlMg4.5Mn alloy and additional material AlMg5. The TIG and MIG welding processes are combined to create slight transitions within the ducts that enable the normal flow of exhaust gases inlet channels are temporarily welded, and the outlet connected to the pressure side in order to test the tightness of the channel itself. After the leak test is completed, the final joining of all elements is started before the final welding process. Figure 5. shows the parts in the stage of preparation for welding with positioning via screw connections to the original block.

Figure 5. The picture shows the process of centering and preparation for welding previously made pieces.

It is important to note that the parts are tighten with prior fixing using screw connections to make the appropriate dimensions. It should be considered that the piece will undergo appropriate deformations during welding, which must be within the required limits after machining dimensions so that the piece could be placed on the engine block.

3.　Welding process and final machining

After the production of all the necessary parts and their joining, the welding process is started. As mentioned before, the welding processes used are MIG with additional material AlMg5 Ø 1.2, which is one of the most universal diameters and covers all thickness ranges from 1 to 20 mm, and TIG with additional material AlMg5 Ø 2 mm. Due to the impossibility of supplying

the appropriate sheet thicknesses for the overlap on the exhaust side, the process of welding and surfacing the surface was carried out in order to obtain the appropriate overlap and align the contact surfaces after machining. This phase of the straightening machining is only control because the finishing is done after the final welding process has been completed. Visual inspection revealed minor porosity in places, which will not significantly affect the quality and functionality of the welded surfaces. This phase allows for the repair of poorly executed weld as well as the replenishment of insufficiently overlap weld that appear in places. It should be taken that this is the first straightening followed by the final stage of welding and machining of the straightening and making the appropriate inner diameter of the tubular exchanger. The milling process will remove the excess weld and at the same time align the surfaces and shape them according to the corresponding ones on the side of the engine block to enable proper fitting and sealing. Figure 6 shows a piece ready for the final welding stage. Welding in this phase is performed on a workpiece that is not clamped to the engine block but is welded freely. The order of welding tries to influence the reduction of deformation of the workpiece due to heat input by the welding process. After welding, the piece is checked both visually and by pressure

b. For this testing process, it is necessary to seal and connect all elements. In addition to the flanges on the side of the tubular heat exchanger, it is necessary to make appropriate plugs that will enable this test. The pressures during the actual exploitation process within the exhaust system are negligible and the temperatures at the exhaust sensor location ranged from 55 to 60 °C.

Figure 6.　The picture shows a completely attached piece ready for the final welding stage

After machining, the replacement exchanger is subjected to testing again. In addition to the visual one, a pressure test is performed as well as for tanks of water. After the test phase, the piece is mechanically cleaned with appropriate tools that will not contaminate the surface. In this way, the protective aluminum oxide is removed to allow good adhesion of the base paint. The finishing paint is fire-resistant, which in this case, according to the manufacturer's instructions, can be used both as a base and finishing paint. It should be noted that special protectors based on magnesium (-2,37) are used for exchangers and, in general, marine aluminum alloys due to the corresponding electric potential.

It is wrong to use zinc (-0.76) protectors, which are often used for steel structures but are not suitable for aluminum alloys (-1.67) because they have a higher electrical potential. It is correct to use magnesium (-2.37) protectors because in this case the aluminum part will not corrode and lose mass.

Favorable corrosive conditions can occur in area of the tubular heat exchanger, so a magnesium protector must be additionally installed in that position. Figure 7. shows the final product ready for mounting on the engine block.

Figure 7. The picture shows a completely made and assembled heat exchanger with a suction branch.

In the next phase, the exhaust manifold is placed on the engine block with all seals and put

into test operation. Important parameters are certainly the condition in the compensation vessel, where there must be no increase in pressure due to the penetration of exhaust gases into the collector, i.e. the water part.

The second factor is the temperature at the exhaust, which is from 50 to 55 °C, which is several degrees lower than in the case of the original cast piece of gray cast iron, where the temperature remained in the range of 55 to 60 °C depending on the operating modes. Given that this is a unique piece, it is advisable to check and monitor the temperature of the exhaust gases as well as the coolant level more often.

4.   Conclusion

Due to the need for maintenance, it is customary to use reparation methods if they can be performed. If it is not possible to repair the damaged piece, it is replaced. In this case, due to the unavailability of a replacement exhaust manifold, a replacement piece was made. Production may require the use of different standard materials and elements, but also the possibility of applying appropriate available production processes. Today, aluminum alloys are used to produce exhaust manifolds in the serial factory production of smaller marine engines due to their low weight, good castability and high thermal conductivity. The economic aspect of making this piece should be viewed through the entire system, which includes a complete marine engine. Given that the engine was overhauled, the exhaust manifold in the total cost slightly affects the price that will enable the functionality of this system. The impossibility of repairing and supplying a new one leaves option of making a replacement exhaust collector, which is described in this paper. The motive behind the creation of this piece should be sought in the ability to maintain the ship's system without extensive professional knowledge. If the production of such a complex exhaust manifold is viewed from this aspect, then the economic profitability of the exhaust manifold itself is secondary. Making the exhaust manifold will enable the operation of the ship's system and extend the life of this product. As a conclusion, the fact that it is possible to make a suitable exhaust manifold by applying different production processes is imposed.

REFERENCES

[1] Deželić, R., 1987. *Metali 2*, Sveučilište u Splitu, FESB, Split

[2] Anzulović, B., 1990 *Zavarivanje i srodni postupci* FESB, Split

[3] ASM Handbook, (1993), *Vol 6- Welding,Brazing and Soldering* , ASM International, Metals Park, OH, USA,

[4] Engineering Failure Analysis
Volume 16, Issue 7, October 2009, Pages 2382-2387

[5] INTERNATIONAL RESEARCH JOURNAL OF MULTIDISCIPLINARY TECHNOVATION (IRJMT)
Published online 13 November 2020

[6] https://en.wikipedia.org/wiki/Heat_exchanger

[7] Engineering Toolbox - Resources, Tools and Basic Information for Engineering and Design of Technical Applications!

Experimental investigation on the mechanical properties of 3D printed structural polymer materials

Igor ŠULJIĆ[1]**, Igor GABRIĆ**[1]**, Ivan VRLJIČAK**[1]**, Marin BUTIR**[1]

1) University of Split, University Department of Professional Studies, Kopilica 5, 21000 Split, **Croatia**

isuljic@oss.unist.hr
igabric@oss.unist.hr
vrljicak@oss.unist.hr
mb48144@oss.unist.hr

Keywords

Polymers
Mechanical Properties
Tensile Strength
Creep
3D Printing

Original scientific article

Abstract: In recent years, additive manufacturing has become one of the most used methods of polymer parts manufacturing, especially Fused Deposition Modelling (FDM). Wide range of commercial polymer materials can be applied, with high print quality, using low cost open-source 3D Printers. However, due to lack of information on the mechanical properties of 3D printed materials, aim is to investigate the same. Tensile strength experimental tests were performed on specimens made of Tough PLA, ABS, and nylon PA 6/66, using in-house developed test rig. The specimens were designed and printed according to specimen standard ISO 527:2012. Also, due to polymer viscoelastic and viscoplastic properties, creep (cold flow) tests were performed, using in-house developed creep-testing machine, for better understanding of 3D printed polymer behavior at elevated temperatures. Finally, the characterization of 3D printed materials was performed by analyzing the results obtained by testing.

1. Introduction

The accelerating development and advancement of new technologies is a characteristic of today's economy, and it is also accompanied by the development of new materials. The main goal is faster and cheaper production with the lowest possible energy consumption and greater reliability and efficiency, while considering the protection and preservation of the environment. Materials that meet such requirements are polymers, specifically a group of synthetic polymers known as plastics. Throughout history, the era has often been named after the materials used, such as stone, bronze, or iron, and many agree that the steel age is slowly coming to an end and that the plastic age is coming. In 1950., world plastic production amounted to about one million tons, while in 2004. it amounted to 224 million tons [1]. Due to cheaper and simpler machinability of plastics, today there are many technologies to produce plastic. One of the technologies is additive manufacturing, also known as 3D printing, and Fused Deposition Modeling (FDM) stands out. Additive production begins with the creation of a three-dimensional model using software (CAD) that is transformed into a series of horizontal cross-sections or layers. FDM technology works on the principle of melting polymer filament in the form of wire. By passing through the nozzle, the material melts, and by moving the nozzle in the plane, the first layer is formed, on which the next layers are applied, and the process is repeated until the end-use product is made. Initially, FDM technology was used only for prototyping and conceptual models, but with the rapid development of

FDM devices of high accuracy and precision, its application has expanded to various fields such as electronics, automotive and aerospace, medicine, and many others. FDM technology applies a wide range of commercially available polymeric materials such as acrylic butadiene styrene (ABS), polycarbonate (PC), polypropylene (PP), polylactic acid (PLA) or nylon (PA) [2]. FDM devices are relatively cheap and easy to operate, but the main disadvantage of the technology is dimensional instability, sensitivity to temperature changes and the dependence of the mechanical properties of the end-use product on the orientation of layer printing. However, the short manufacturing time, low cost, quality of parts and flexibility of the process indicate the increasing use and representation of this technology and how it could become the future of producing polymer parts. Recently, there has been an effort to increase the precision of additive manufacturing devices to be able to produce items that require high dimensional accuracy, without additional finishing [3]. The mechanical properties of parts made with FDM technology depends on polymer material, print speed and orientation of printing, density, and pattern of infill, but also on the printing temperature and build plate temperature at which the molten material is laid. Dimić et al. [4] conducted an experimental test of the load capacity of polymer gears made of ABS and PLA. ABS is not suitable for making products that have sharp angles and demanding geometry, while PLA is. ABS is not biodegradable but can be recycled, while PLA is biodegradable. PLA printing temperature is lower

compared to ABS, and, in addition to the above advantages, is a better choice when it comes to elements that withstand higher loads and require high accuracy of geometry such as gears. Calignano et al. [5] studied the dependence of tensile strength, hardness, and impact strength of polyamide PA 612 reinforced with 20% carbon fiber on the infill density and layer orientation. The tensile strength of the tested samples depends on the direction of printing and increases with increasing infill density. Infill density has very little effect on hardness and impact strength while both properties depend on print orientation. Tensile strength testing was performed on standardized specimens according to ISO 527, but also ASTM D638, and differences in results between these standards were observed, mainly due to different shapes and rates of deformation of the tested samples [6, 7]. The addition of carbon or glass fibers to the base material has a positive effect on mechanical properties, tensile, compressive, and flexural strength, and impact strength [8]. As in [4], Zhang et al. [9] optimized the printing process on the example of polymer gears made of PA 618 polyamide. Optimization of four parameters of the FDM process was performed to save material and reduce the time of fabrication of polymer gears and used artificial neural network (ANN) and genetic algorithms (GA). The following print parameters were determined: print temperature 250 °C, build plate temperature 25 °C, print speed 70 mm / s and infill density 80%. Also, the influence of each of the parameters on the overall process of making gears was determined, with conclusion that greatest dependence of the process has infill density. The effect of build plate temperature is evident only on the first few layers during the printing process while the infill density directly affects the mass and mechanical properties of the gear. Kuznetsov et al. [10] investigated the effect of nozzle temperature and print speed on the strength of FDM printed parts. For PLA material, higher printing temperature causes 8% more mass of the part and up to 16% higher strength. By increasing the print speed, the resistances in the nozzle increase, due to greater friction and shear stresses in the molten material, and the mass and strength decrease. When a larger number of layers is applied, a higher print speed is desirable for better cohesion between layers. The quality of the bond between the layers determines the integrity and mechanical properties of the specimen, and as expected, in the zones of the bonding layers the properties of the part are worse than the properties of the filament. In paper [11, 12] ABS is investigated, and it has been experimentally confirmed that different cooling rates of layers have a significant impact on the structure of the bond, but also the overall quality and strength of the bond. Parts made by FDM technology consist of stacked layers and are always anisotropic [13, 14]. Among the mechanical properties being tested, tensile strength is the most common. Smaller values of individual layer thickness, raster width and air gap increase the tensile strength of the part made by FDM technology [15]. Onwubolu et al. [16] investigated the tensile strength of the specimens by analyzing and optimizing the layer thickness, part orientation, raster angle and width, and air gap. Tensile strength is highest when the orientation of the part in the direction of tensile stress, as well as when the air gap is negative or when the grid overlaps, while other parameters coincide with those described in [15]. Parameter optimization was performed using group method of data handling (GMDH) and differential evolution (DE) algorithm. Tanikella et al. [17] confirmed the dependence of tensile strength on the mass of the test sample for various materials. Among the tested materials, the highest tensile strength was achieved by PC (49 MPa), while slightly lower values were determined for HIPS (34 MPa), PA 618 (32 MPa) and ABS (29 MPa). Unlike ABS, HIPS and PC which are not flexible, PA 618 has proven to be the best material, which has an excellent ratio of strength, flexibility, and ductility. Yao et al. [18] experimentally investigated the dependence of tensile strength on the orientation of PLA samples. The test was performed for different orientations, and the difference in tensile strength was observed, up to 52.29% between 0 ° and 90 ° orientation, at a specimen layer thickness of 0.1 mm. As in [15, 16], higher tensile strength was achieved when specimens thickness of 0.1 mm compared to samples with a layer thickness of 0.2 mm or 0.3 mm. The thicker the layer, the greater the possibility of interlayer fractures. Bašić et al. [19] investigated the relationship between tensile strength and production costs of FDM technology on samples made of PLA polymer. The fuzzy logic approach was used for modeling, and it was proven that higher tensile strength leads to higher costs of FDM process. Long-term loaded polymers exposed to persistent tensile loads begin to stretch and this phenomenon is called creep. Creep in polymeric materials occurs at room temperature, and the increase in temperature accelerates the phenomenon itself. Like tensile strength, the creep of parts made by the FDM process depends on the orientation of the part, layer thickness, air gap and raster angle and width. For ABS and PC polymers by increasing the layer thickness, air gap and raster angle increase the tendency of the material to creep while the highest creep resistance was achieved by a specimen with an orientation of about 17 ° [20, 21]. In this paper, the tensile strength and creep test on ABS, Tough PLA, and nylon PA 6/66 samples, by Ultimaker manufacturer, was performed. The tensile strength test specimens were designed according to ISO 527:2012 and were made on an Ultimaker S5 FDM device. Experimental tests were performed on in-house tensile and creep test devices.

2. Experimental method

The tested specimens were made on an Ultimaker S5 FDM printer of easy use and high reliability, and the Ultimaker S5 was controlled using Ultimaker Cura software. The diameter of the filament used to make the samples is 2.85 mm and the diameter of the nozzle is 0.4 mm. The maximum printing temperature of the device is 280 °C, the positioning accuracy is about 7 μm, and the layer resolution is from 20 to 200 μm. Layers are built on a glass heated build plate that can be heated up to 140 °C. ABS, Tough PLA and PA 6/66 samples were made according to default parameters recommended by the manufacturer. For ABS the print temperature is 250 °C while the build plate temperature is 85 °C, for Tough PLA a print temperature of 215 °C is required with a build plate temperature of 60 °C, and for PA 6/66 the print temperature is 255 °C and the temperature build plate 70 °C. Layer thickness for all materials is 0.2 mm and a cubic infill pattern was used. Print speed for ABS is 60 mm / s, Tough PLA 50 mm / s, and for PA 6/66 70 mm / s. Specimens for different infill densities, from 70% to 100%, and different displacement rates were tested. Defining the test operating parameters that are changing during the experiment is made using the software Design-Expert (Version 6). After experimental testing on specimens and statistical analysis of the results are obtained, diagrams were generated for all response quantities.

2.1. Tensile strength

Experimental tensile testing of ABS, Tough PLA and PA 6/66 samples was performed on an in house developed device adapted to polymeric materials while standardized specimens, according to ISO 527: 2012 - Type 1A, with 4 mm thickness, were made on FDM device Ultimaker S5. The tensile strength testing machine and specimen with associated geometry are shown in Figure 1. The polymer tensile strength testing machine drives two stepper motors None 34 - M-3431-6.3 (double length), with a rated torque of 8.7 Nm and driven by a DMA860H driver. Jaw displacement is achieved via two 5 mm threaded spindles. The maximum tensile force that the device can achieve is 5000 N, displacement rates in the range of 1 - 30 mm / min can also be achieved. Displacement rates are calculated for the elastic region of the tested specimen by entering the modulus of elasticity and the desired displacement rate. The upper jaw is movable while the displacement of the lower jaw is linearly proportional to the tensile force (known stiffness of the measuring cell). Since the increase in force is achieved and the displacement of the lower jaw, the same is considered in the calculation of displacement rate.
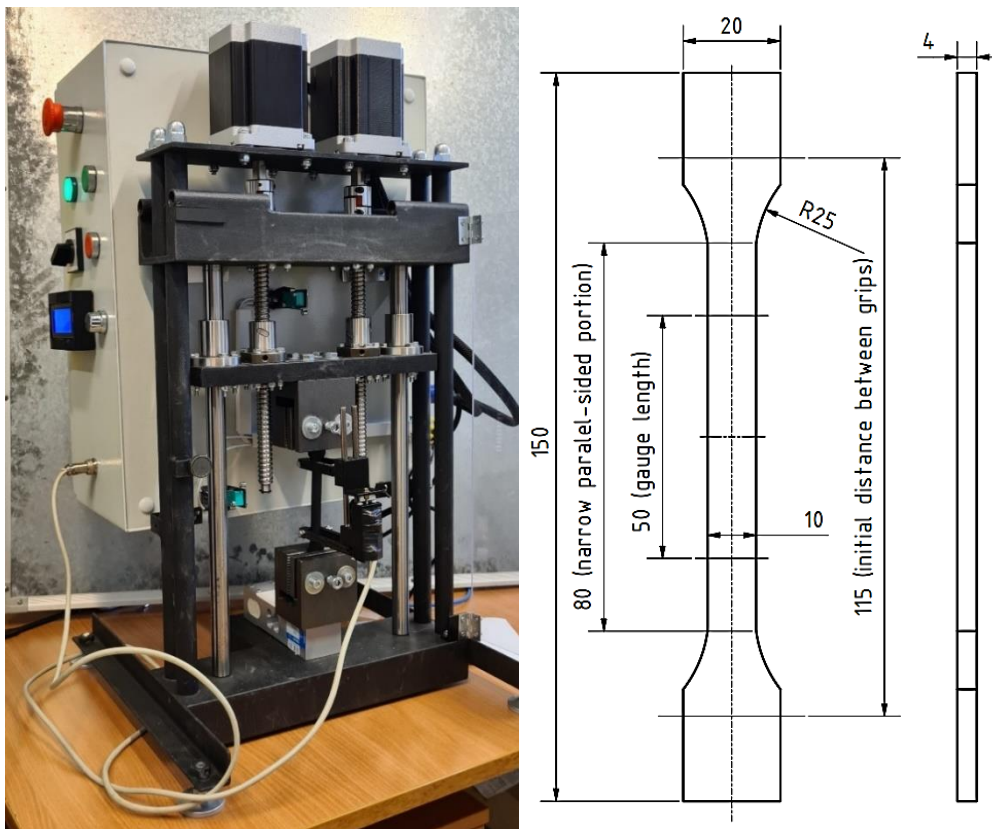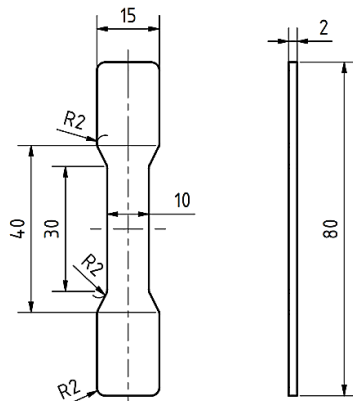

Figure 1. In house developed ultimate tensile strength device (left) and tensile strength testing specimen (right)

Displacement rate of the upper jaw is constant throughout the test so that from the moment the material loosens the actual rate of stretching of the specimen increases. The device is equipped with a force meter MAVIN NA4 (0 - 800 kg) and a signal amplifier HX711 which achieves 24bit resolution in the measuring range.

The resolution of the force measurement is 0.1 N, and the achievable measurement accuracy is ±1 N. The displacements were measured with the aid of a developed extensometer with a linear sensor Megatron MM30 measuring range 0 - 30 mm and amplifier ADC1115. The resolution of the displacement measurement is about 0.002 mm, and the achievable measurement accuracy is ±0.01 mm. The extensometer was made and adjusted for a measuring length of a large, standardized specimen of 80 mm.

Application of polymer materials exposed to persistent load at room temperature, especially at elevated temperatures, represents a challenge for engineers.

Under such conditions, the viscoelastic and viscoplastic properties of the polymer come to the fore, as well as creep. Although the stress in the material is below its elastic limit, the material deforms over time. In the case of metals, such deformations are smaller and high temperatures are required for creep to be pronounced, while in the case of polymers, creep can occur even at room temperature.

Creep testing was performed on ABS, Tough PLA and PA 6/66 samples made according to the ASTM D638 standard for tensile strength testing. In this paper small specimens, ASTM D638 – Type IV, were used to test the creep of polymers produced by FDM technology (Figure 2). The experimental test was carried out on an in-house developed creep testing rig. The experimental testing rig consists of a lower stationary and an upper movable jaw in which the specimen is attached, and they are in an insulated chamber with a heater of nominal power 50 W, where the temperature in the chamber is regulated by a thermocouple.

The maximum temperature that can be maintained in the chamber is 50 °C. Through the lever, at the end of which a load is suspended and to which the upper jaw is connected, stress is applied to the specimen, and the deformation of the specimen is measured based on the displacement of the upper jaw. During the creep test, the desired stress is usually expressed as a percentage of the tensile strength, and most often it is 50% - 70% of the tensile strength. Figure 3 shows in-house developed creep testing rig.

Figure 2. ASTM D638 – Type IV specimen
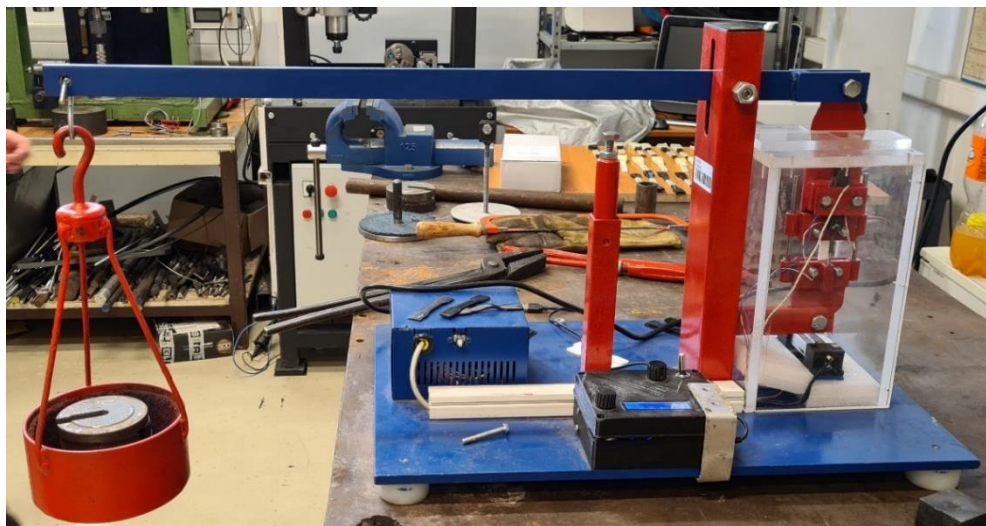
Figure 3. In house developed creep testing rig

3. Test results and discussion

3.1. Tensile strength

Experimental measurement of tensile strength was carried out on three different polymer materials, ABS, Tough PLA, and PA 6/66 for different deformation rates of 1, 2, 6, 10 mm/min and different infill densities of the examined specimens, 70%, 85% and 100 %. Test parameters, deformation rate and infill density, were determined using Design Expert, statistical software that is specifically dedicated to performing designs of experiments. Also, using Design Expert, 13 specimens of each material were tested in order to determine an analytical model that can describe the dependence of tensile strength on deformation rate and infill density of the sample. Figure 4 (a – c) shows samples made of ABS, Tough PLA, and PA 6/66 after tensile strength testing. Among the tested samples, the highest tensile strength (50.4 MPa) was achieved by the Tough PLA sample with an infill density of 100% at a deformation rate of 10 mm/min.

On all Tough PLA samples (Figure 4. b)), the fracture occurred at the place of the highest stress concentration, that is, at the transition from the waist of the specimen to its fillet. By increasing the deformation rate of Tough PLA specimens, the tensile strength increases because the time required for the rearrangement of the polymer chains is reduced, which results in greater stiffness and strength of the Tough PLA material. As expected, reducing the infill density at the same deformation rate reduces the strength of the sample, and in the case of Tough PLA, the reduction is as much as 42% at a deformation rate of 10 mm/min and its caused more by stress concentration than cross section reduction. Similar behavior was observed in ABS specimens (Figure 4. a)) where the specimen fracture occurred at the place of the highest stress concentration, like Tough PLA. The maximum measured tensile strength is 38.3 MPa at a deformation rate of 2 mm/min. It is interesting that with ABS specimens, deformation rate has almost no influence on the tensile strength, while reducing the infill density reduced the tensile strength (up to 32% at a deformation rate of 2 mm/min), but not nearly as much as with Tough PLA specimens. In only two out of thirteen PA 6/66 specimens (Figure 4. c)) specimen fracture occurred, while in the others there was stretching, but no fracture, due to the limitation of the stroke length of the tensile strength testing device. The highest measured tensile strength of PA 6/66 specimens is 28.4 MPa at a deformation rate of 10 mm/min and an infill density of 100%. The rate of deformation of the PA 6/66 material has an almost negligible influence, and it was noticed that the infill density has a much smaller influence on the tensile strength of the PA 6/66 polymer compared to ABS and Tough PLA. The tensile strength at a deformation rate of 2 mm/min and an infill density of 70% is 23.7 MPa, only about 16% less than the maximum strength.

By comparing the results of the tensile strength provided by Ultimaker Technical Data Sheet for ABS, Tough PLA, and PA 6/66 and the test results, it can be concluded that there are minor deviations, with the emphasis that the results of the manufacturer Ultimaker are shown exclusively for infill density 100% at a deformation rate of 5 mm/min for ABS and Tough PLA, while for PA 6/66 the deformation rate is 50 mm/min.


Figure 4. Specimens after tensile test: a) ABS, b) Tough PLA and c) PA 6/66

A comparison of the tensile strength results achieved by the experimental testing in this paper, at a deformation rate of 6 mm/min (ABS and Tough PLA) or 10 mm/min (PA 6/66) and for an infill density of 100%, and the results achieved by testing of the manufacturer Ultimaker, shown is in Table 1. All the results of the tensile strength test depending on the deformation rate and infill density are shown in diagrams in Figure 5 (a – c).

Table 1. Comparison of tensile strength results

Tensile strength, MPa			
Material	**ABS**	**Tough PLA**	**PA 6/66**
Experimental results	37,4	49,2	28,4
Ultimaker results	38,1	45,3	27,8
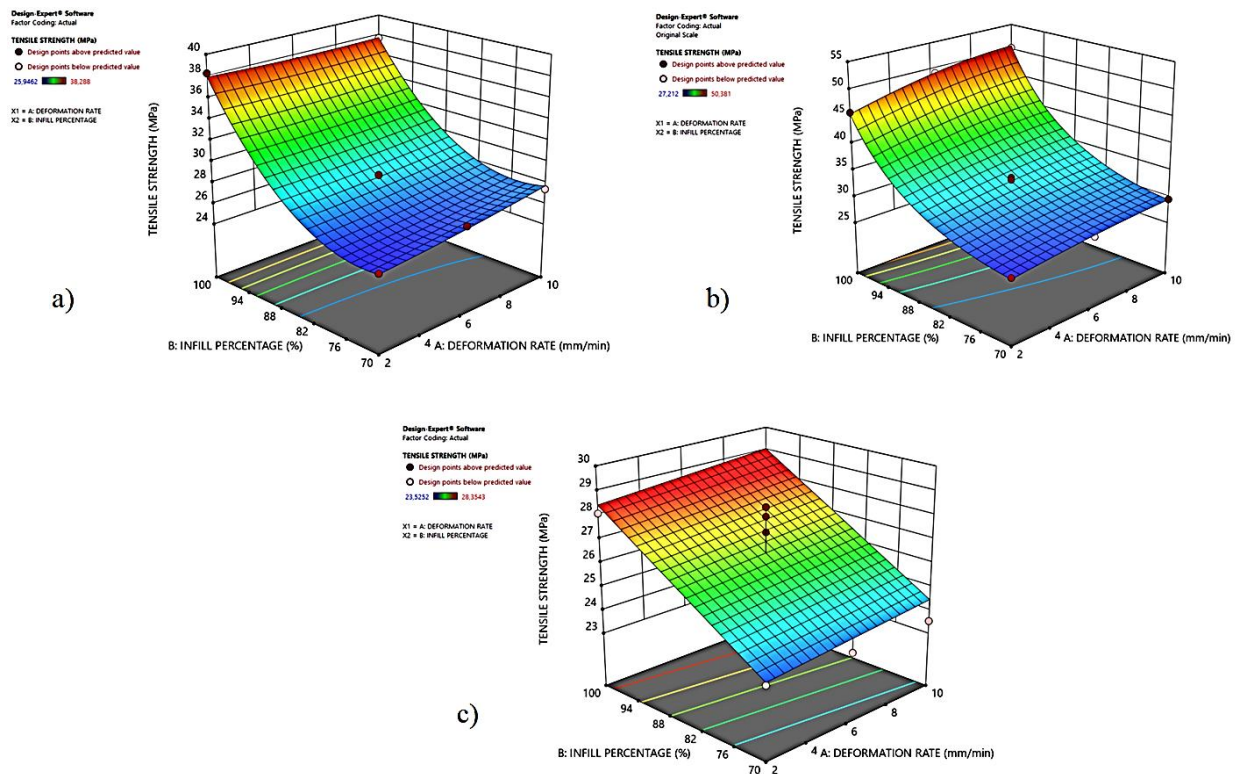
Figure 5. Tensile strength depending on deformation rate and infill density: a) ABS, b) Tough PLA and c) PA 6/66

3.2. Creep

Creep testing was performed on 2 specimens of each material on in house developed test rig at 20 MPa nominal stress and at two different temperatures, 32 °C and 40 °C and specimens are shown on Figure 6.

Diagram on Figure 7. a) shows creep test results at 32 °C. All specimens survived 1500 minutes when the testing is stopped. ABS and Tough PLA performed almost the same with around 1 mm elongation in total, while PA 6/66 suffered larger elongations of almost 10 mm without fracture. PA 6/66 showed great toughness but poor resistance to creep, compared to ABS and Tough PLA.

Experimental results performed at 40 °C are presented in Figure 7. b). Testing was performed for 300 minutes and as expected, larger elongations occurred at higher temperature. ABS specimens fractured after only around 210 seconds, unlike Tough PLA and PA 6/66 specimens which survived whole testing. Again, PA 6/66 elongated the most, up to 20 mm, while Tough PLA elongated for around 17 mm and its creep behavior can be divided into 3 phases: period of linear elongation followed by rapid elongation and narrowing, and at last, steeper almost linear elongation. It can be concluded that ABS is most sensitive to increase in temperature under permanent load.

Figure 6. Creep specimens at 32 °C (left) and 40 °C (right): PA 6/66 (top), ABS (middle) and Tough PLA (bottom)
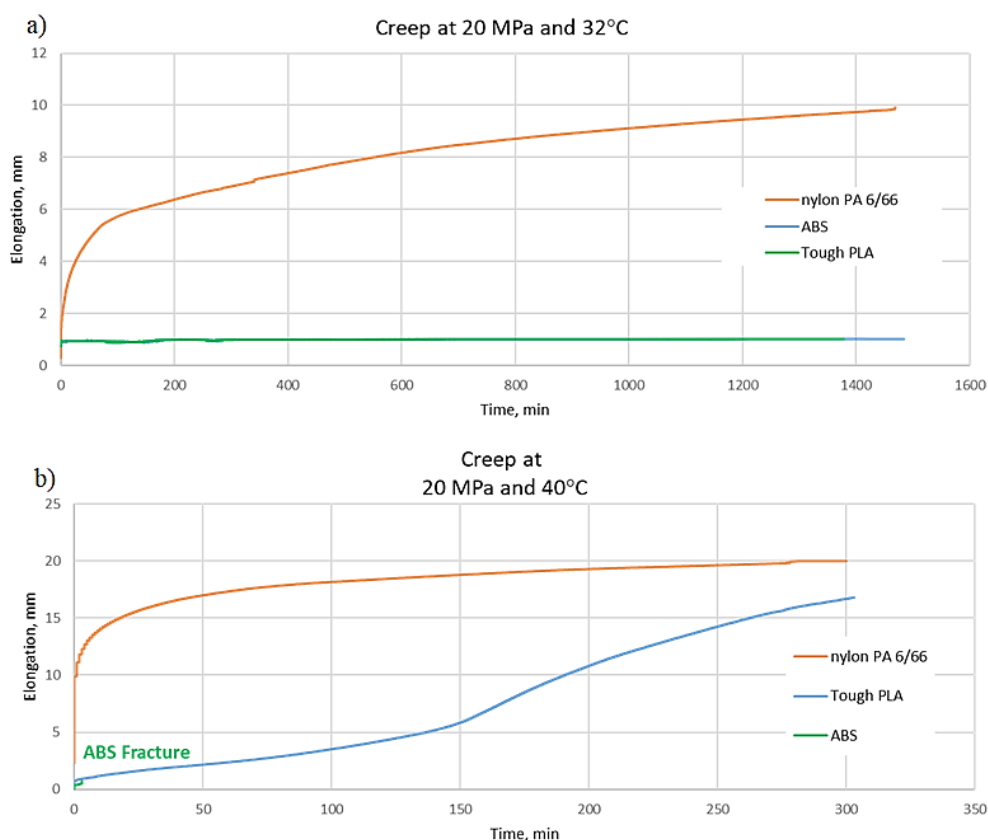
Figure 7. ABS, Tough PLA, and PA 6/66 creep test at nominal stress 20 MPa and temperature a) 32 °C and b) 40 °C

4. Conclusion

In this paper, influence of the deformation rate and infill density on the tensile strength of ABS, Tough PLA and PA 6/66 specimens produced by fused deposition modeling (FDM) was analyzed. Experimental investigation was carried out on in house developed testing rig, influence of deformation rate and infill density on the ultimate strength was presented and results are compared with the ones presented by manufacturer Ultimaker. Contribution of this research is significant due to the lack of information on the influence of deformation rate and infill density of FDM printing materials on its mechanical properties, in this case tensile strength. Also,

creep test was performed on mentioned materials, and influence of temperature on creep was investigated. These are preliminary results and this work will serve as a basis for future research on the influence of FDM printing parameters, such as printing speed, infill pattern, nozzle and build plate temperature, and layer thickness on tensile strength.

REFERENCES

[1] Barić, G., Pehnec-Pavlović, G., (2005), *Production and Processing of Polymers in the World, in Europe and in Croatia*, Polymeric materials and additives Conference, Zagreb, Croatia

[2] Novakova-Marcincinova L., Novak-Marcincin J., (2012), *Applications of rapid prototyping fused deposition modeling materials,* In Annals of DAAAM for 2012 & Proceedings of the 23rd International DAAAM Symposium 23, No. 1, p 57-60 Croatia

[3] Wong KV, Hernandez A., (2012), *A review of additive manufacturing*, ISRN Mechanical Engineering, vol. 2012, No. 4

[4] Dimić, A., Mišković, Ž., Mitrović, R., (2018), *The Influence of Material on the Operational Characteristics of Spur Gears Manufactured by the 3D Printing Technology*, Strojnicky časopis – Journal of Mechanical Engineering, Vol. 68, No. 3, p 261 – 270

[5] Calignano, F., Lorusso, M., Roppolo, I., (2020), *Investigation of the Mechanical Properties of a Carbon Fibre-reinforced Nylon Filament for 3D Printing*, Machines, Vol. 8, No. 3, 52

[6] García-Domínguez, A., Claver, J., Camacho, A.M., Sebastián, M.A., (2020), *Considerations on the applicability of test methods for mechanical characterization of materials manufactured by FDM*, Materials, vol. 13, No. 1, 28.

[7] Friday, M.J., (1999), *A comparison of tension test data using ASTM D 638 and ISO 527*, In ASTM Limitations of Test Methods for Plastics, ASTM International, West Conshohocken, PA, USA

[8] Karthi, V., Marimuthu, K., (2019), *Experimental Investigations of Nylon 6 Polymer Matrix Composites Material (70:30) for Wear Reduction in Gears*, Indian Journal of Engineering and Materials Sciences, Vol. 26, p 226 – 234

[9] Zhang, Y., Mao, K., Leigh, S., Shah, A., Chao, Z., Ma, G., (2020), *A Parametric Study of 3D Printed Polymer Gears*, The International Journal of Advanced Manufacturing Technology, vol. 107, No. 1-4, p 4481 – 4492

[10] Kuznetsov, V. E., Solonin, A. N., Tavitov, A., Urzhumtsev, O., & Vakulik, A. (2020), *Increasing strength of FFF three-dimensional printed parts by influencing on temperature-related parameters of the process*, Rapid Prototyping Journal, vol. 26, No. 1, p 107–121

[11] Bellehumeur, C., Li, L., Sun, Q., Gu, P. (2004), *Modeling of Bond Formation Between Polymer Filaments in the Fused Deposition Modeling Process*, Journal of Manufacturing Processes, vol. 6, No. 2, p 170–178

[12] Sun, Q., Rizvi, G. M., Bellehumeur, C. T., Gu, P. (2008), *Effect of processing conditions on the bonding quality of FDM polymer filaments*, Rapid Prototyping Journal, vol. 14, No. 2, p 72–80

[13] Dizon, J. R. C., Espera, A. H., Chen, O., Advincula, R. C., (2018), *Mechanical characterization of 3D-printed polymers*, Additive Manufacturing, vol. 20, pp. 44-67

[14] Ahn, S. H., Montero, M., Odell, D., Roundy, S., Wright, P.K., (2002), *Anisotropic material properties of fused deposition modeling ABS*, Rapid Prototying Journal, vol. 8, No. 4, p 248–257

[15] Popescu, D., Zapciu, A., Amza, C., Baciu, F., Marinescu, R., (2018), *FDM process parameters influence over the mechanical properties of polymer specimens: A review*, Polymer Testing, vol. 69, p 157–166

[16] Onwubolu, G. C., Rayegani, F., (2014), *Characterization and Optimization of Mechanical Properties of ABS Parts Manufactured by the Fused Deposition Modelling Process*, International Journal of Manufacturing Engineering, p 1–13

[17] Tanikella, N. G., Wittbrodt, B., Pearce, J. M., (2017), *Tensile strength of commercial polymer materials for fused filament fabrication 3D printing*, Additive Manufacturing, vol. 15, p 40–47

[18] Yao, T., Deng, Z., Zhang, K., Li, S., (2019), *A method to predict the ultimate tensile strength of 3D printing polylactic acid (PLA) materials with different printing orientations*, Composites Part B: Engineering, vol. 163, p 393-402

[19] Bašić, A., Peko, I., Krolo, J., Bagavac, P., (2021), *Fuzzy logic modeling of ultimate tensile strength and cost in fused deposition modeling process of additive manufacturing*, Proceedings of 10th International conference MTSM 2021, Split, Croatia, p 1-10

[20] Salazar-Martín, A. G., Pérez, M. A., García-Granada, A. A., Reyes, G., Puigoriol-Forcada, J. M., (2018), *A study of creep in polycarbonate fused deposition modelling parts*, Materials & Design, vol. 141, p 414–425

[21] Mohamed, O. A., Masood, S. H., Bhowmik, J. L., (2017), *Influence of processing parameters on creep and recovery behavior of FDM manufactured part using definitive screening design and ANN*, Rapid Prototyping Journal, vol. 23, No. 6, p 998–1010

Methodology for testing shaft slide bearings of the ship propulsion system

Vladimir VETMA[1], **Nenad VULIĆ**[2], **Nikola RAČIĆ**[2]

1) University Department of Professional Studies, University of Split, Split, **Croatia**
2) Faculty of Maritime Studies, University of Split, Split, **Croatia**

vvetma@oss.unist.hr
nvulic1@pfst.hr
nracic@pfst.hr

Keywords

Stern tube slide bearing
Water lubrication
Curvature of the elastic line
Testing of slide bearings

Original scientific paper

Abstract: From a technical and economic standpoint, the suitability of a ship's propulsion system depends significantly on the bearings of its shaft line. The paper compares oil-lubricated white metal stern tube slide bearings and water-lubricated polymer stern tube slide bearings. Practice has taught us that with water-lubricated polymer bearings, the minimum thickness of the lubricant film is significantly smaller compared to white metal bearings that are lubricated with oil. With insufficient lubricant film thickness in the bearings, liquid friction can easily change to mixed friction due to a certain disturbance. The disorder can result in an increase in load, temperature, a decrease in viscosity and speed, and a change in the geometry of the bearing sleeve. In particular, it is known that in the case of a realistically loaded water-lubricated stern tube slide bearing, the influence of the elastic line curvature of the sleeve is greater than the minimum thickness of the lubricant film. Due to the eccentric action, the thrust force of the ship also has an influence on the elastic line of the sleeve, comparable to the influence of radial loads. In the case of water-lubricated bearings, the influence of the change in the intensity of the thrust force and the size of the eccentricity also changes the curvature of the elastic line of the sleeve to the extent that there is no fluid friction along the entire length of the bearing. The wear of the polymer bush has an impact on the ecosystem. The paper points out the need to apply analytical and numerical models of the sleeve in the bearing and the need for testing that will faithfully simulate the condition of the stern tube slide bearing on the ship at sea.

1. Introduction

Slide bearings are a fundamental part of the ship's propulsion system. They enable the shaft line to transmit power from the driving machine to the ship's propeller and take radial and axial loads. Stern tube slide bearing are specific for the ship.

By sizing the shafts of the ship's propulsion system, the basic dimensions of the bearing sleeves were determined, that is, the diameters of the slide bearings D. The shaft diameter d of the shaft line (according to the harmonized requirement of IACS UR M68) is given by the expression [4]:

$$d \geq f \cdot k \cdot \sqrt{\frac{P}{n} \cdot \frac{1}{1-\varphi^4} \cdot \frac{560}{R_m + 160}} \quad \text{(mm)}, \qquad (1)$$

where: f is the factor of the driving machine in the propulsion system ($f = 100$ for propeller shafts), k is low-cycle fatigue factor ($k = 1.22$ for propeller shafts), φ is ratio of the outer and inner diameter of the shaft, R_m is tensile strength of the material of the shaft (MPa), P is nominal power transmitted by the shaft (kW), n is rotation speed of the shaft at the nominal power of the engine (r/min).

The length of the slide bearings L depends on the choice of bearing bush material and on the permissible pressure for that material. The stern tube slide bearing is longer compared to the radial support bearing of the same nominal diameter, because it is exposed to greater static and dynamic loads in operation, which come from the weight of the ship's propeller, the weight of the shaft and the thrust force.

Stern tube slide bearings could be divided according to the material of the bush and the associated lubricant. Bearings with bushes made of white metal are lubricated with oil, and those with bushes made of polymer materials are lubricated with water. Table 1 shows the basic properties of bushes made of white metal and polymer bushes. The material of the shaft, or bearing sleeves, is usually austenitic stainless steel AISI 304 (S30400), hardness 81 HRB (Rockwell B scale).

It is evident from Table 1 that the clearance required for polymer bearings is greater. The reason for this is higher temperature expansion of the bush material, swelling due to water absorption, and poorer heat dissipation, i.e. working clearance.

Symbols

d	- shaft diameter, mm	v	- ship speed, m s^{-1}
D	- slide bearing diameter, mm	z_1	- recommended clearance, mm
E	- modulus of elasticity, GPa	**Greek letters**	
e_T	- eccentricity of the thrust force, m	α	- coefficient of linear thermal expansion, K^{-1}
F	- load, N	β	- attitude angle, °
F_A	- resultant hydrodynamic pressure, N	Δh	- circular section height, mm
F_g	- ship's propeller weight, N	δ	- relative thickness
F_T	- friction force, N	ε	- relative eccentricity
f	- factor of the driving machine	λ	- thermal conductivity coefficient, W m^{-1} K^{-1}
h_o	- minimum lubricant thickness film, mm	η	- dynamic viscosity, Pa s
I_y	- moment of inertia, mm^4	η_{eff}	- effective dynamic viscosity, Pa s
k	- low-cycle fatigue factor	η_T	- total efficiency
L	- slide bearing length, mm	μ	- coefficient of friction
L/D	- constructive characteristic	ρ	- density, kgm^{-3}
n	- rotation speed, r min^{-1}	ρ	- elastic line curvature radius, m
P	- nominal power (engine), kW	φ	- shaft outer and inner diameter ratio
P_f	- friction power, kW	ψ	- relative clearance
$\bar{p}$	- mean specific pressure, Pa	ψ_{eff}	- effective relative clearance
q	- lubricant flow factor	ω_{eff}	- eff. hydrodynamic angular velocity, rad s^{-1}
R_m	- material tensile strength, MPa	Ω	- contact angle, °
So	- Sommerfeld's number	**Subscripts**	
T	- thrust force, N	o	- oil
t	- temperature, °C	w	- water

Table 1. Slide bearing bushes with basic characteristics [8], [12] and [14]

| $100 \leq d \leq 1000$ (mm)		E (GPa)	R_m (MPa)	L/D	z_1 (mm)	$\psi = z_1/d$	α (K^{-1})	λ (W/mK)
white metal	LM THERMIT	29.9	57	$L/D \leq 2$	$0.001d+0.3$	0.004-0.0013	$21 \cdot 10^{-6}$ $t \approx 50°C$	45
	W.M.80	55.7	89					
polymer	Visconate	T 3.726 C 2.3	63	$L/D \geq 2$	$0.0025d+1.9$	0.0215-0.0044	$60 \cdot 10^{-6}$	0.3
	Thordon COMPAC	T 0.605 C 0.440	37.5				$(109-151) \cdot 10^{-6}$ $0°C \leq t < 30°C$	0.25

In addition to the structural (diameter D and length L) and geometric characteristics of the bearing (roughness, clearance), the selected material of the bush affects the values of the elastic deformations of the contact surfaces due to the load F. The contact and relative movement of the slide surfaces of the shaft sleeve and the bush leads to friction and wear. Greater wear of the bush is expected because it is less hard (67-83 according to Shore-D for polymers, 13-27 HB for white metal) than the shaft sleeve. In order to reduce friction and wear, the slide surfaces are lubricated. Types of lubricants with basic mechanical and thermal characteristics are given in Table 2 [2] and [7]. Correct selection of a slide bearing is a tribological problem. The elements of a simple slide bearing tribosystem are shown in Figure 1. The tribosystem consists of shaft sleeve (1) and bush (2) materials (tribocouple), lubricant (3) and environmental influence (4).

Table 2. Liquid lubricants with basic mechanical and thermal characteristics

Lubricant	Types	ρ (kg/m³) at 20 °C	η (Pas) various temperatures (°C) at atmospheric pressure				λ (W/mK)
oil	Castrol CDX30 ISO VG 100	885	20 °C	40 °C	50 °C	60 °C	0.133-0.131 $t = 40$-60 °C
			$295 \cdot 10^{-3}$	$98 \cdot 10^{-3}$	$57 \cdot 10^{-3}$	$37 \cdot 10^{-3}$	
	Castrol A. SP150 ISO VG 150	893	20 °C	40 °C	50 °C	60 °C	
			$466 \cdot 10^{-3}$	$136 \cdot 10^{-3}$	$79 \cdot 10^{-3}$	$57 \cdot 10^{-3}$	
water	Fresh water	998.207	0 °C	0.5 °C	20 °C	32 °C	0.6 $t = 20$-22 °C
			freezing point	$1.79 \cdot 10^{-3}$	$1.003 \cdot 10^{-3}$	$0.78 \cdot 10^{-3}$	
	sea water salinity 35‰	1024.8	-1.91 °C	0.5 °C	20 °C	32 °C	0.596 $t = 20$-22 °C
			freezing point	$1.88 \cdot 10^{-3}$	$1.08 \cdot 10^{-3}$	$0.87 \cdot 10^{-3}$	
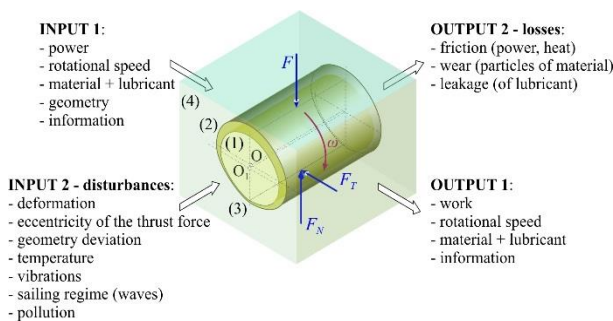
Figure 1. Elements of the slide bearing tribosystem

In order to achieve optimal results when solving tribological problems of friction, wear and lubrication of slide bearings, the load F, the friction force F_T, the direction of rotation of the shaft sleeve and the input-output parameters of the slide bearing tribosystem are taken into account. The goal is to minimize frictional losses and material wear, respectively, to maximize energy efficiency and environmental justification. A slide bearing chosen in this way should ensure optimal performance, long-term reliability and economic justification [3].

In case of leakage of lubricant from the bearing, lubricant with particles of material leave the boundaries of the tribosystem and directly affect the ecosystem of the sea and ocean as a functional unit. When choosing bearing materials and lubricants, in addition to energy efficiency, operating costs and maintenance costs, it is also necessary to know the extent of their impact on the ecosystem.

Information from the input-output side of the tribosystem represents a set of related data that defines the functionality and exploitability of the system. The slide bearing data set consists of parameters: pressure distribution in the bearing, temperature in the bearing, bearing load, friction force in the bearing, friction coefficient, lubricant flow through the bearing, Sommerfeld number, etc

2. Sommerfeld number

In the theory of hydrodynamic lubrication Sommerfeld's number So or bearing load characteristic is a basic calculation parameter in the design and construction of bearings, and is defined as the ratio of load and viscous friction force in the lubricating film. The expression that gives the amount of the Sommerfeld number So is [10]:

$$So = \frac{\bar{p} \cdot \psi_{eff}^2}{\eta_{eff} \cdot \omega_{eff}} \ , \tag{2}$$

where: $\bar{p}$ is mean specific pressure (Pa); $\bar{p} = F/(D \cdot L)$, ψ_{eff} is effective relative clearance; $\psi_{eff} = \bar{\psi} + \Delta\psi$, η_{eff} is effective dynamic lubricant viscosity (Pas) and ω_{eff} is effective hydrodynamic angular velocity (rad s⁻¹).

The effective hydrodynamic angular velocity for a slide bearing with a fixed bush is equal to the angular velocity of the shaft sleeve. The effective relative clearance also depends on the change in clearance due to the difference in the temperature of the material of the shaft sleeve and the bush (coefficients of linear thermal expansion). The effective dynamic viscosity of the lubricant is determined with regard to the mean temperature of the lubricant at the entrance and exit from the bearing.

The Sommerfeld number So is fundamental in solving lubrication problems. The diagram of the dependence of the relative eccentricity ε (relative thickness of the lubricating film δ) on the Sommerfeld number So and the constructive characteristic L/D for the contact angle of the bearing Ω is shown in Figure 2, indicates in which working area the slide bearing is located [11]. Knowing the Sommerfeld number allows determining the position of the shaft sleeve (angle β) in the bearing bush, the eccentricity and the minimum thickness of the lubricating film h_0. In the standard diagram shown in Figure 2, based on real values (Table 3), two working areas of marine slide bearings are drawn. It can be seen that water-lubricated polymer slide bearings work with large eccentricities, that is, with small lubricant film thickness δ.

Figure 2. Diagram $So = f(\varepsilon, L/D, \Omega)$
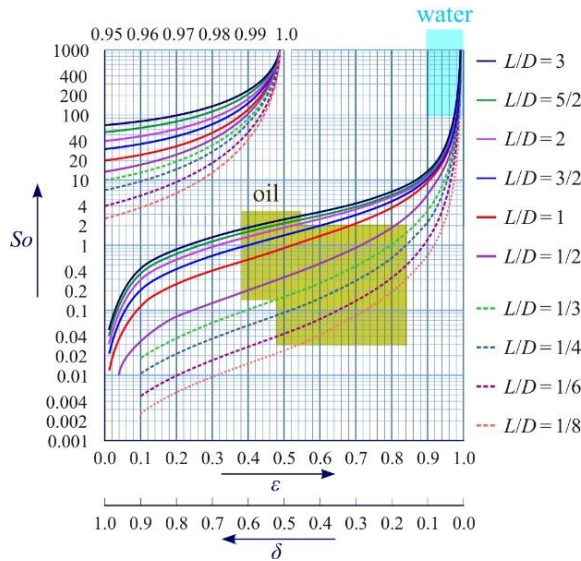
This is primarily a consequence of the significantly lower viscosity of water compared to the viscosity of oil. It can be assumed that, due to the small lubricant film thickness

δ, water-lubricated slide bearings are more sensitive to various disturbances than oil-lubricated bearings. Other parameters of the slide bearing tribosystem (power, rotation speed, load F, eccentricity of thrust force, sailing regime, etc.) have an influence on their correct operation, that is, hydrodynamic lubrication. It is of interest to analyze and quantify the impact of various disturbances on the tribosystem of the slide bearing, and due to the possibility that the type of friction may change due to the action of a disturbance or a change in an influential quantity, e.g., from liquid to mixed friction. In the case of mixed friction, there is direct contact between the shaft sleeve and the bush, which causes wear of the material of the bearing bush.

The minimum film thickness h_o expression we can draw from the equation $\varepsilon + \delta = 1$ [10]:

$$h_0 = 0.5 \cdot D \cdot \psi_{eff} \cdot (1 - \varepsilon). \tag{3}$$

Table 3 shows the comparative values of the output parameters (Figure 3) of stern tube bearings, classic oil-lubricated white metal bearings and newer water-lubricated polymer bearings.

Table 3. Output parameters of stern tube slide bearings with the contact angle $\Omega = 360°$

Output parameters	Oil-lubricated white metal slide bearings	Water-lubricated polymer slide bearings
Mean specific pressure (bearing load) $\bar{p}$ (MPa)	0.5 – 0.8 $L/D \leq 2$	0.2 – 0.6 $L/D \geq 2$
Operating temperature of the bearing (lubricant) t (°C)	40 °C – 60 °C	20 °C – 22 °C
Sommerfeld number So $So = f(\varepsilon, L/D, \Omega)$	≤ 20	100 – 500 (1000)
Relative eccentricity ε $\varepsilon = f(So, L/D, \Omega)$	0.5 – 0.8	0.998 - 0.99\.{9}
Minimal film thickness h_o (μm)	20 – 300	2 – 5
Attitude angle β $\beta = f(\varepsilon, L/D, \Omega)$	40° – 60°	0° – 5°
Friction coefficient μ according to the Stribeck curve $\mu - n$ [12] $\mu/\psi_{eff} = f(So, L/D, \Omega)$ e.g. for $d = 101.4$ (mm), $L/D = 2$, $\bar{p} = 0.6$ (MPa), $n = 0$ - 860 (r/min)		
Dry friction	0.1	0.3
Mixed friction	0.025 - 0.018	0.15 - 0.018
Liquid friction	0.02 - 0.01	0.01 - 0.002
Lubricant flow factor q $q = f(\varepsilon, L/D, \Omega)$	q_o	$q_w \approx 2 \cdot q_o$

The diagrams shown in Figure 2 refer to slide bearings that are normally in the hydrodynamic lubrication regime, which is reached by increasing the rotation speed of the shaft sleeve from the initial speed to the stationary speed. At the same time, the friction in the bearing changes from the area of semi-dry to mixed, finally to liquid friction. In this paper, the working areas of the slide bearing are defined in this way.
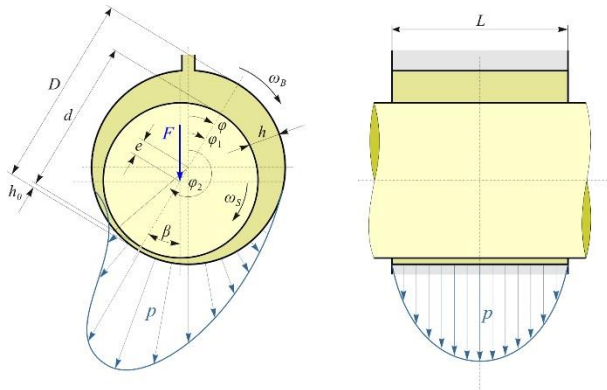
Figure 3. Schematic representation of radial slide bearing with hydrodynamic lubrication and relevant parameters

The energy efficiency of the shaft line depends on the efficiency of the bearings, that is, on the coefficient of friction μ, which depends on the working area of the slide bearing. Friction power loss P_f is defined according to the expression:

$$P_f = \mu \cdot F \cdot \frac{D}{2} \cdot \omega_{eff} \ \ (\text{kW}) \ . \tag{4}$$

If the amount of the friction coefficient, for example for mixed friction $\mu = 0.01$, is taken into consideration, it can be concluded that the power losses due to friction are relatively small and that the slide bearings are highly efficient with an energy efficiency of more than 99%. An equal or greater problem is the harmful impact on the environment, due to the wear of the bush material and the leakage of oil from the slide bearings. In addition to energy efficiency it would be of interest to analyze, evaluate and compare the impact of different tribosystems of bearings on the environment.

3. Effect of load on the working area of slide bearings

The direction of action of the thrust force T produced by the ship's propeller does not coincide with the axis of the shaft for several reasons. As a result, and in addition to the radial load that originates from the weight of the ship's propeller F_g and the weight of the shaft, the thrust force T also affects the load on the stern tube bearings. The thrust force T is in balance with the total resistance of the ship R when sailing at speed v, Figure 4. Direction of action, i.e., eccentricity in relation to the axis of the shaft, the direction (sailing astern) and the amount of the thrust force T have a direct influence on the working area of the slide bearing.

The magnitude of the thrust force T can be determined from the expression:

$$T = \frac{P}{v} \cdot \eta_T \ \ (\text{kN}) \tag{5}$$
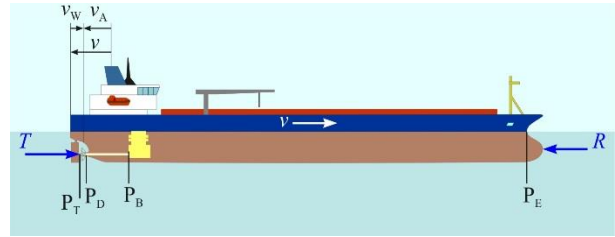
Figure 4. Thrust force

where: P is the power of the ship's engine (kW), v is the speed of the ship in relation to the environment (m/s), and η_T is the total efficiency that includes all bearings and the propeller efficiency.

In the ideal case shown in Figure 5, which represents a simplified theoretical model of the load of a stern tube slide bearing, the thrust force T acts in the direction that coincides with the axis of the shaft, and the resultant of the action of the hydrodynamic pressure in the bearing F_A passes through point A. The assumption takes into consideration stationary operating regime – sailing ($\omega =$ const., $F =$ const.) and liquid friction in the slide bearing.
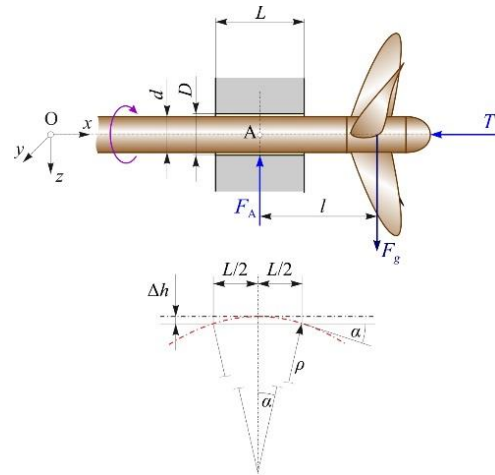
Figure 5. A simplified theoretical load model of the stern tube slide bearing

Even in this ideal case, due to elastic deformations, the bearing sleeve is not cylindrical. The elastic line curvature radius ρ at point A, Figure 5 can be determined by the expression:

$$\rho = \frac{E \cdot I_y}{M_y} \ \ (\text{m}), \tag{6}$$

where: $E \cdot I_y$ is bending stiffness of the shaft (Nm^2), M_y is bending moment of the shaft at point A (Nm); $M_y = F_g \cdot l$ (own weight of the shaft is not taken into consideration).

If the elastic line of the sleeve in a slide bearing of length L is approximated by a circular arc of the radius ρ, then the height of the circular section Δh is:

$$\Delta h = \rho \cdot (1 - \cos \alpha) \quad (\mu m), \tag{7}$$

where: $\alpha \approx L / (2 \cdot \rho)$.

The size Δh is a measure of the sleeve's deviation from cylindricity due to elastic deformations. If Δh is less than the lubricant film thickness $\Delta h < h_0$ which is achieved in operation, there may be hydrodynamic friction in the bearing, with the deviating of the hydrodynamic pressure distribution, more or less from the ideal. If $\Delta h \geq h_0$, the slide bearing is in the area of mixed friction and hydrodynamic lubrication in the entire length of the bearing L will be achieved by adjusting the surface of the bearing and sleeve by running-in – wear.

In order to evaluate whether and to what extent the elastic deformations of the sleeve have an impact on the type of friction in the bearing, two real-world examples will be provided. For example, a ship powered by a Wärtsilä slow-moving diesel engine UEC35LSE, RT-fl ex35 and RTA35 with a power of 3475 (kW), a rotation speed of 167 (r/min) [6] will be taken. According to expression (1), the diameter of the propeller shaft is assumed to be d = 300 (mm), the diameter of the bearing is D = 300 (mm), and the length of the bearing is L = 600 (mm). The diameter of the propeller is about 4 (m), its weight is F_g = 100 (kN), and it acts on the arm l = 0.5 (m) in relation to point A (Figure 5). The calculated thrust force T for a ship speed of 15 (knots) and a total efficiency η_T = 0.7 according to expression (5) is 315 (kN). According to expression (6), the radius of the circular arc is ρ = 1600 (m) and the height of the circular section, according to expression (7), is Δh = 28 (µm). Other output parameters are given in Table 4.

It can be seen from Table 4 that for equal loads, the minimum of the lubricant film thickness h_0 in oil-lubricated bearings are significantly larger than those lubricated with water.

Table 4. Output parameters of stern tube slide bearings with a contact angle Ω =360°

Output parameters	Oil-lubricated white metal slide bearings	Water-lubricated polymer slide bearings
Mean specific pressure (bearing load) $\bar{p}$ (MPa)	0.55	0.25
Relative clearance ψ	0.002	0.0088
Sommerfeld number So; $So = f(\varepsilon, L/D, \Omega)$ - Eq. (2)	1.935	1106.92
Relative eccentricity ε; $\varepsilon = f(So, L/D, \Omega)$	0.54	0.999
Minimal lubricant film thickness h_o (µm) - Eq. (3)	138	1.32

The minimum lubricant film thickness of oil-lubricated bearings is significantly greater than the influence of the elastic deformation of the shaft sleeve, $h_0 \gg \Delta h$. It can be concluded that in stationary operation, in slide bearings with ideal geometry and lubricated with oil, liquid friction is established (Figure 6). In the case of bearings lubricated with water, the expected minimum of the lubricant film thickness is smaller than the influence of the curvature of the elastic line of the sleeve, $h_0 < \Delta h$, so the bearing is expected to work in the area of mixed friction (Figure 7) [1].

Due to the elastic deformation of the sleeve in the area of mixed friction the slide bearing is run-in; that is, the bush is fitted to the geometry of the sleeve. By running-in the bush of the slide bearing, according to the elastic line of the shaft, the material of the bush wears out, which can represent an additional harmful impact on the environment. Using oil-lubricated bearings, on the other hand, may cause oil leakage. These environmental impacts may be the subject of future research.
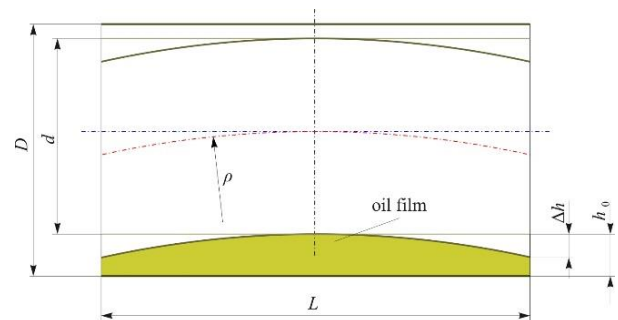
Figure 6. The working area of a classic slide bearing
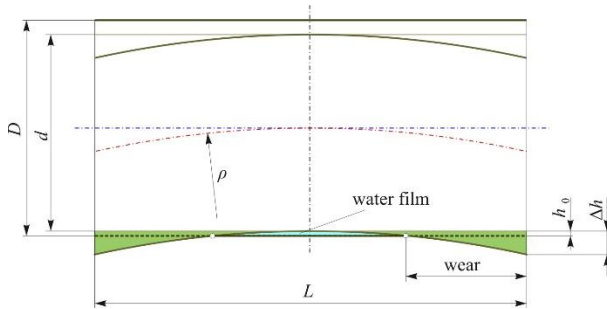
Figure 7. The working area of a polymer slide bearing

In real-world, the shape of the elastic line is also influenced by: the geometric and constructive characteristic of the bearing (length L of the bush), the configuration, the constructive solution and the centering of the shaft line, and the position of the supports (radial and stern tube bearing). In the paper, special emphasis is placed on different load levels that have a direct effect on the shape of the elastic line of the bearing sleeve. Because the direction of action of the thrust force T does not coincide with the axis of the shaft, the shape of the elastic line is also affected by the thrust force. The Croatian Register of Shipping suggests calculation in which the thrust force T acts in a direction parallel to the axis of the shaft, and shifted vertically upwards by the size e_T, which is 4% of the outer diameter of the ship's propeller. At this eccentricity, the moment of the thrust force with respect to point A in the middle of the sleeve, Figure 8, is comparable in size to the moment of the radial force F_g.

Figure 8. Thrust force eccentricity

The eccentricity of the thrust force is the result of the shape and form of the ship's line (stern), the design of the ship's propeller, rudder, and different sailing regimes (sailing with the bow, stern, turning, stopping, starting, positioning, sailing in shallow or deep seas, rough seas, sailing with cargo or without load, towing...). The position and amount of the thrust force eccentricity is determined by analyzing the velocity distribution at the propeller plane and the pressure field on its surface [5] and [13].

The effect of the moment of the eccentric thrust force on the bearing load results in a new radius of the circle ρ, which means a new curvature of the shaft inside the bush of the stern tube slide bearing which deviates from that

shown in Figure 5, so expression (6) for the curvature radius ρ takes the form:

$$\rho = \frac{E \cdot I_y}{M_y \pm T \cdot e_T} \quad \text{(m).} \tag{8}$$

The eccentricity e_T in expression (8) cannot be considered as a constant and as a characteristic of the ship propeller. The magnitude of the thrust force T is also not constant. The thrust force T is approximately proportional to the square of the ship's speed and therefore changes in the ship's speed v significantly affect to the magnitude of the thrust force. According to expression (8), the elastic line curvature radius ρ of the sleeve in the bearing will also change. Even the smallest oil film thickness h_0 is not constant and will change with load, rotation speed, sea temperature. If the influence of the change in the elastic line curvature of the sleeve is greater than the minimum of the lubricant film thickness h_0, it will not be possible to achieve fluid friction along the entire length of the bearing. This is positively influenced by the greater flexibility of the bush and construction. Anyway, certain wear of the bush material is to be expected, as well as changes in the output parameters of the slide bearing tribosystem.

The answers to the asked questions can be provided by analytical and numerical modeling of bearing sleeves in operation under different real loads. Due to the small lubricant film thickness, when lubricating with water, the inevitable deviation of the dimensions, shape and position of the real sleeve in the bearing, should be taken into account in relation to the ideal geometry.

The obtained results should be verified by a test which, apart from the bearing sleeve, would include all other parameters of the slide bearing tribosystem and simulate as faithfully as possible the real situation of the stern tube bearing on the ship at sea. This requires a special device and a suitable test program.

The test program must be formed according to the slide bearing tribosystem described in the introduction and the corresponding technical characteristics of the test device. By testing the bearing, the following benefits are expected: selection of the optimal tribosystem for the appropriate load, reduction of the harmful impact on the environment (leakage, wear, temperature), reduction of maintenance costs, extension of the bearing's service life, increase of the useful effect, increase of efficiency (availability), quantification of the impact of disturbances (geometry changes, deformations, foreign particles, vibrations), development of better means and lubrication systems, verification of new bearing materials, new standards, confirmation of the validity of the shaft line structural solution and the position of the supports, etc...

4. Conclusion

In addition to classic bearings with bushes made of white metal and lubricated with oil, bearings with bushes made

of various polymer materials that are lubricated with water are increasingly used. The disadvantage of oil-lubricated bearings is the potential danger of an oil leakage and thus a harmful effect on the ecosystem of the sea and ocean. Due to the significantly lower viscosity of water compared to oil, the minimum water lubricating film thickness is extremely small. The fluid friction in these bearings can turn into mixed friction even with small disturbances of the input parameters of the tribosystem. As an inevitable disturbance, the change in thrust force and the eccentricity of the direction of its action in relation to the axis of the shaft stands out. In real conditions, the influence of the elastic line curvature of the bearing sleeve is greater than the expected minimum water lubricating film thickness, so liquid friction along the entire length of the bearing can only be expected after running-in. The running-in – wear and tear of materials has a harmful effect on the ecosystem. A special problem is that by changing the sailing speed i.e. by changing the intensity of the thrust force, the elastic line curvature can be changed to the extent that the influence of the change in the elastic line is greater than the minimum of the lubricating film thickness. To quantify all the influencing parameters of the tribosystem of water-lubricated stern tube slide bearings, it is necessary to create analytical and numerical models and verify the results by testing on a device that can faithfully simulate the real situation of stern tube slide bearings on a ship at sea.

REFERENCES

[1] EXTERNAL | WP0254 Dodge Application Engineering, 2017, July 27, *Mounted Hydrodynamic Bearings: Comparison of Babbitt and PTFE-Based Polymers*, 1061 Holland Road, Simpsonville, SC 29681, U.S.A

[2] Komar I., 2012, *Contribution to the selection methodology of the most convenient marine propulsion stern tube bearings*, doctoral dissertation, University of Rijeka, Faculty of Maritime Studies, Rijeka

[3] Kovačević V., Vrsaljko D., 2011, *Tribology*, instructional material, University of Zagreb, Faculty of Chemical Engineering and Technology, Department of Surface Engineering of Polymer Materials, Zagreb

[4] Kulenović Z., Vulić N., 2020, *Elements of Marine Machinery and Maritime Structures*, University of Split, Faculty of Maritime Studies, Split

[5] Lee T., Song G., Kim J., Lee J., Park H., 2017, Samsung Heavy Industries Co. Ltd, *Effect of Propeller Eccentric Forces on the Bearing Loads of the Complicated Shafting System for Large Container Ships*, Fifth International Symposium on Marine Propulsors smp'17, Espoo, Finland, June 2017

[6] Maritime Reporter & Engineering News, 2008, *Wärtsilä and Mitsubishi - results of strategic alliance*, Brodogradnja 59(2008)4, Croatia

[7] Murray J. W., 2004, *Properties of Water and Seawater*, Chpt. 3, University Washington, U.S.A

[8] Nova TKL, *Properties of the white metal*, Donje Mrzlo polje, Duga Resa, Croatia

[9] Operating instruction, 1997, *Allowable clearances in the stern tube bearings*, QW20, Croatian Register of Shipping, Split, Croatia

[10] Standard DIN Deutsches Institut für Normung, 1983, *Plain bearings-Hydrodynamic plain journal bearings designed for operation under steady-state conditions* – Part 1: *Calculation of circular cylindrical bearings*, DIN 31652-1:1983, Berlin, Germany

[11] Standard DIN Deutsches Institut für Normung, 1983, *Plain bearings-Hydrodynamic plain journal bearings designed for operation under steady-state conditions* – Part 2: *Functions for the calculation of circular cylindrical bearings*, DIN 31652-1:1983, Berlin, Germany

[12] Thordon *Elastomeric Bearings*, Engineering manual, Version: 2022.1, TEBEM 02/22/NA, 3225 Mainway, Burlington, Ontario L7M 1A6, Canada

[13] Vartdal B. J., Gjestland T., Arvidsen T. I., 2009, Det Norske Veritas (DNV), *Lateral Propeller Forces and their Effects on Shaft Bearings*, First International Symposium on Marine Propulsors smp'09, Trondheim, Norway, June 2009

[14] Vesconite Bearings, *Typical Properties*, VB/09/2021/VS, 77 Mimetes Rd, Denver, Johannesburg, 2094, South Afric

Measuring setdown output parameter of cross-wire welded mesh with reconfigurable measuring system

Maja VLATKOVIĆ[1]**, Ivana ČABRIJAN**[1]**, Duško PAVLETIĆ**[1]**, Sandro DOBOVIČEK**[1]

1) University of Rijeka, Faculty of Engineering, Vukovarska 58, 51000 Rijeka, **Croatia**

mmarkovic2@riteh.hr

Professional paper

Abstract: This paper describes setdown output parameter dimension measuring procedure for the wire mesh obtained by the cross-wire welding process. The measurement is performed by non-contact reconfigurable measurement system enhanced with a machine vision. Advantage of this kind of a system are found in a fact that, apart from the necessary dimensions, also images of the welds are obtained, saved and used for further analysis of the parameters influence on the final weld appearance.

The analysis of the measuring system is shown in the paper in order to confirm that the measuring system is acceptable, also the measurement results are compared with ones obtained by conventional method. Analysis of the measurement system also shows that the change of measuring operator has no influence on the obtained measurements.

Measurements of the setdown dimensions are shown in the results section of the paper and it was determined that some measurements exceed the control limits.

1. Introduction

As the market demands ever higher quality from welded products, this paper presents a new approach to quality control of cross-wire welded samples. Cross-wire welding (CWW) is a form of projection welding and a subtype of electric resistance welding. It is used every day in the mass production of various steel products. Each welding process differs depending on the purpose and type of equipment used [1]. Resistance welding is one of the oldest types of welding. Heat is generated by the passage of an electric current through the contact point between two metal surfaces, where a resistance point is formed [2].

Cross-wire welding, used extensively in the production of wire mesh and other wire products, is a form of projection welding in which the weld is formed by the contact of two wires (Figure 1) placed between two electrodes.

When electrical current is applied, the wires continue to heat until they melt and join at the point of contact. Figure 2 shows a CWW machine in industrial production of welded wire mesh, where all the samples used for the research were produced. For this product, the machine was configured to produce 3 welds with an electrode press. The wire mesh is made of S235 steel and is inserted into a specially designed fixture mounted on the machine. There are a number of input parameters that must be set to achieve the target characteristics of the weld. One of these characteristic is the so-called setdown, which is the subject of this paper.

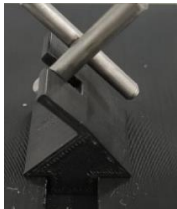**Figure 1.** Two welded wires that represents one sample

Figure 2 Cross-wire welding process

The objective of this paper is to perform quality control of the welded product by measuring the setdown. This is achieved with a designed reconfigurable measuring system (RMS) installed in the Laboratory of Technical Measurements on Faculty of Engineering University of Rijeka (Figure 3).
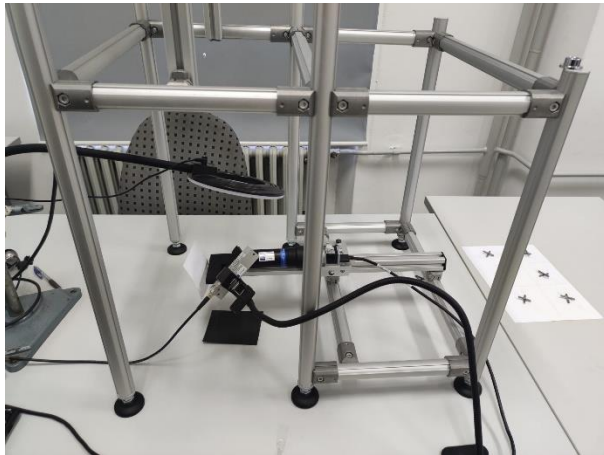
Figure 3   RMS installed in Laboratory of Technical measurements

Table 1   Modules of designed RMS

Specially designed fixture for holding group of product	Industrial Basler camera with telecentric lens	Compact LED light	Bosch standard modules for stand	Computer with software for taking images and performing analysis

A reconfigurable measuring system can be defined as one that is designed to be quickly adapted to control specific characteristics of a particular product group or within different product groups. The concept of reconfigurability is increasingly gaining practical importance and enables sufficiently rapid and complete control of product quality.

According to the concept of reconfigurability, certain requirements must be met in order for the system to be called reconfigurable. There are several types of reconfigurable machines used in production [3], and also different types of inspection machines [4-6].

The main advantage of this type of quality control for designed RMS is the non-contact measurement of certain characteristics using machine vision, which has become an indispensable part of industrial metrology today.

The architecture of RMS is modular, which means that the locations of the individual modules can be reconfigured to adapt RMS to a new product from the same product group. The main modules used in this study are listed in Table 1.
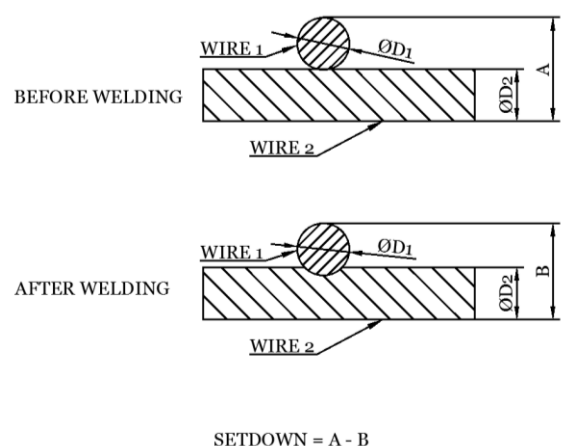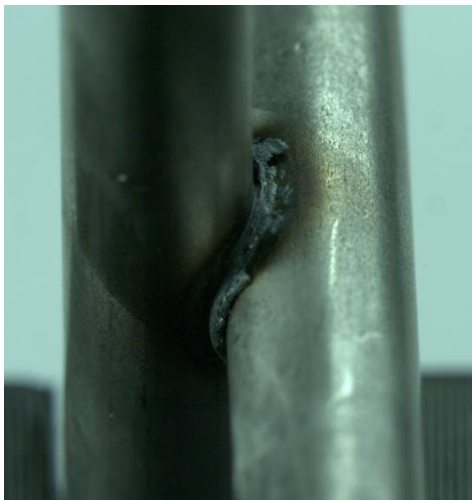
In this study, a product group consist of two perpendicular wires welded by the CWW process. The measured dimension is called setdown, which is the output parameter of this process, and it is shown on Figure 4. Setdown has a significant effect on the appearance, shape and quality of the welded product. If insufficient setdown is achieved, the welded joint will have low strength and interfacial failure will occure.

Setdown is also important for the next process step, which is related to corrosion protection testing. This means that each weld must be free of defects. A visual control is required to check whether defects are on the product. The image of the weld is saved for further analysis as there are a number of visual requirements that any weld should meet. Figure 5 shows an example of weld defects.
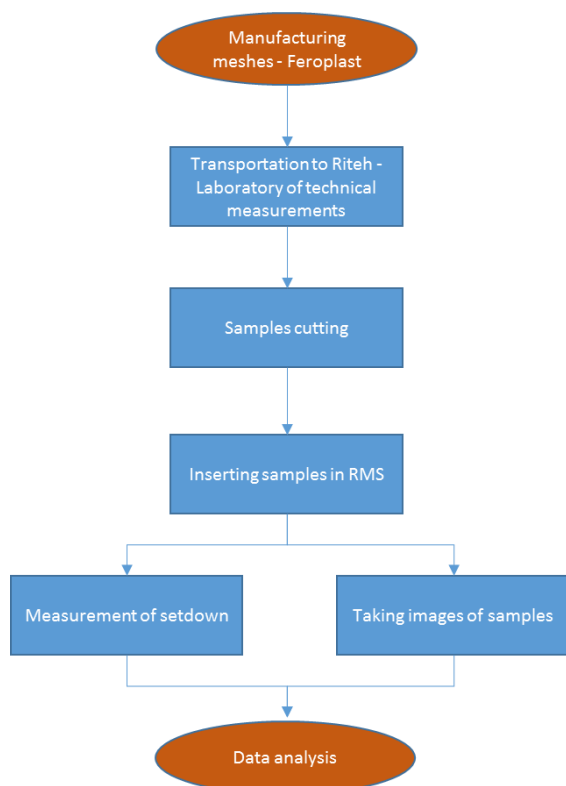

Figure 4 Setdown

Figure 5 Weld defects

2. Measurement procedure of setdown

This work shows an elaborated measuring procedure on CWW wire mesh samples. Measurement results are compared with results obtained by conventional method. Due to the specific shape of the welded sample, this section describes procedure (Figure 6) of welded product quality control.


Figure 6 Flow chart of measuring procedure on CWW wire mesh samples

First step was production of welded mesh from steel wire shown on Figure 7. Then, mesh is transported to Laboratory of Technical measurements where quality control is performed. To measure setdown, as first step in quality control, samples are cut and inserted in RMS (Figure 8). As it was described in previous section, during measuring of setdown, also images of samples are taken. With obtained results of measuring, further analyses are performed.
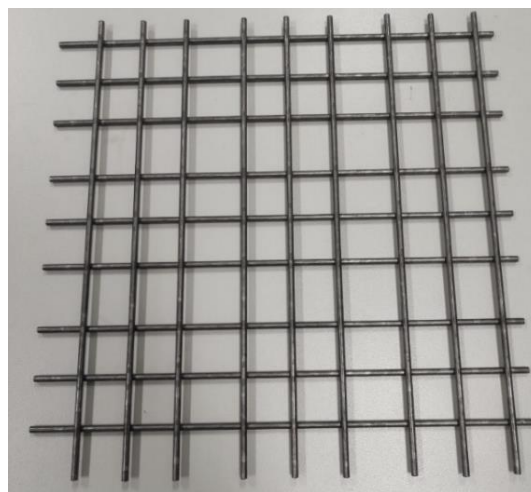
Figure 7 Welded wire mesh
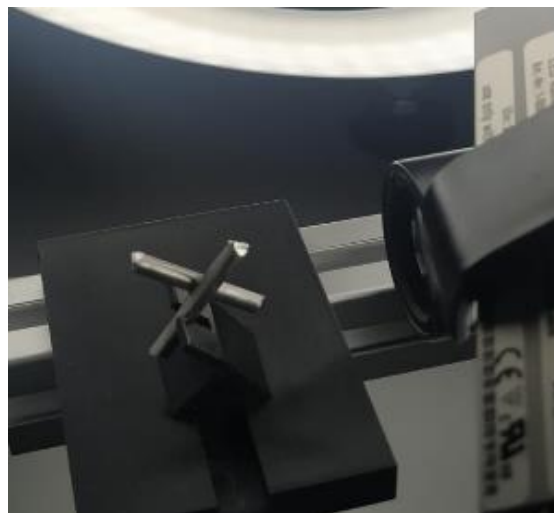
Figure 8 One sample inserted in RMS

3. Analyses of measuring system

Six samples are randomly selected, measured on RMS and on micrometre by two different measuring operators. Each sample is measured by one operator two times. Measure was performed randomly. Results are shown in Table 2.

Table 2 Results of measurements

Sample	Operator	Micrometre mm	RMS mm
1	1	7.306	7.31
1	1	7.306	7.31
2	1	6.881	6.87
2	1	6.882	6.88
3	1	6.972	6.95
3	1	6.971	6.94
4	1	6.918	6.89
4	1	6.917	6.91
5	1	7.248	7.24
5	1	7.255	7.23
6	1	6.855	6.85
6	1	6.854	6.85
1	2	7.306	7.32
1	2	7.305	7.32
2	2	6.881	6.89
2	2	6.881	6.88
3	2	6.971	6.98
3	2	6.972	6.98
4	2	6.918	6.92
4	2	6.918	6.93
5	2	7.255	7.25
5	2	7.257	7.25
6	2	6.855	6.86
6	2	6.855	6.86

Figure 9 and Figure 10 show measuring values of the first sample with two different methods. First method is performed with micrometre, and second one with RMS.

Figure 9 Measuring of the one sample on micrometre

The value of 7.306 mm shows on the micrometre display, but also this type of micrometre is connected to a computer in order to automatically save and process measuring values using dedicated software. Figure 10 shows value of 7.31mm in bottom left corner, and can

also be saved in dedicated software. Ni Vision Builder software is used for image processing as a part of RMS, while for the data analysis Minitab software is used.
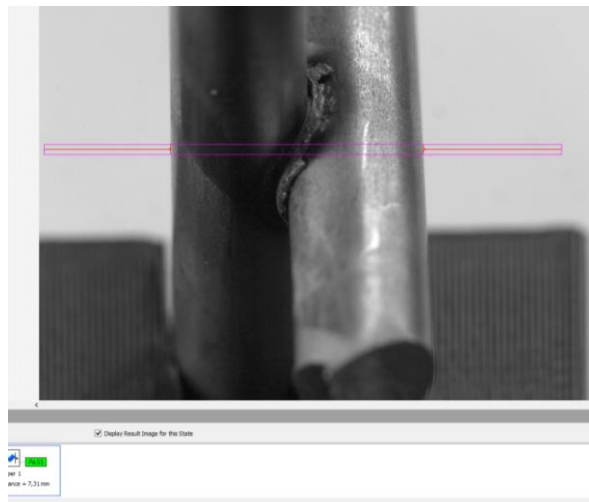
Figure 10 Measuring of the one sample on RMS in software

4. Results

The results of other samples are in Table 3, and analyses of data are shown on Figure 11 and Figure 12.

Gage R&R Study - Nested ANOVA

Gage R&R (Nested) for Micrometer

```
Source            DF        SS            MS         F        P
Operater           1  0,000003  0,0000034       0,0    0,995
Part (Operater)   10  0,779857  0,0779857   31723,0    0,000
Repeatability     12  0,000029  0,0000025
Total             23  0,779890
```

Gage R&R

```
                                  %Contribution
Source              VarComp      (of VarComp)
Total Gage R&R    0,0000025             0,01
  Repeatability   0,0000025             0,01
  Reproducibility 0,0000000             0,00
Part-To-Part      0,0389916            99,99
Total Variation   0,0389941           100,00
```

```
                             Study Var   %Study Var
Source            StdDev (SD)  (6 × SD)      (%SV)
Total Gage R&R      0,001568    0,00941       0,79
  Repeatability     0,001568    0,00941       0,79
  Reproducibility   0,000000    0,00000       0,00
Part-To-Part        0,197463    1,18478     100,00
Total Variation     0,197469    1,18482     100,00
```

Number of Distinct Categories = 177

Figure 11 ANOVA table - micrometre

In the ANOVA table of micrometre, the p-value for "Operator" is large (0.995), which means that the average setdown measurement does not depend on which operator takes the measurements.

For comparing the measurement system variation to the total variation, the %SV coefficient is used. The Total Gage R&R equals 0.79% of the study variation and the Part–to–Part variation equals 99.99%. The Total Gage R&R variation is acceptable.

Gage R&R Study - Nested ANOVA

Gage R&R (Nested) for RMS

```
Source           DF        SS        MS        F      P
Operater          1  0,001838  0,0018375     0,02  0,882
Part (Operater)  10  0,791908  0,0791908  2111,76  0,000
Repeatability    12  0,000450  0,0000375
Total            23  0,794196
```

Gage R&R

```
                                    %Contribution
Source              VarComp      (of VarComp)
Total Gage R&R    0,0000375             0,09
  Repeatability   0,0000375             0,09
  Reproducibility 0,0000000             0,00
Part-To-Part      0,0395767            99,91
Total Variation   0,0396142           100,00


                               Study Var   %Study Var
Source           StdDev (SD)   (6 × SD)      (%SV)
Total Gage R&R    0,006124      0,03674        3,08
  Repeatability   0,006124      0,03674        3,08
  Reproducibility 0,000000      0,00000        0,00
Part-To-Part      0,198939      1,19363       99,95
Total Variation   0,199033      1,19420      100,00


Number of Distinct Categories = 45
```

Figure 12 ANOVA table - RMS

In the ANOVA table of designed RMS, the p-value for "Operator" is large (0.882), which means that the average setdown measurement does not depend on which operator takes the measurements.

For comparing the measurement system variation to the total variation, the %SV coefficient is used. The Total Gage R&R equals 3.08% of the study variation and the Part–to–Part variation equals 99.91%. The Total Gage R&R variation is acceptable.

Micrometre measurement system can distinguish 177 distinct categories and RMS 45. According to the [7], at least 5 distinct categories have to be discovered to have an adequate measuring system.
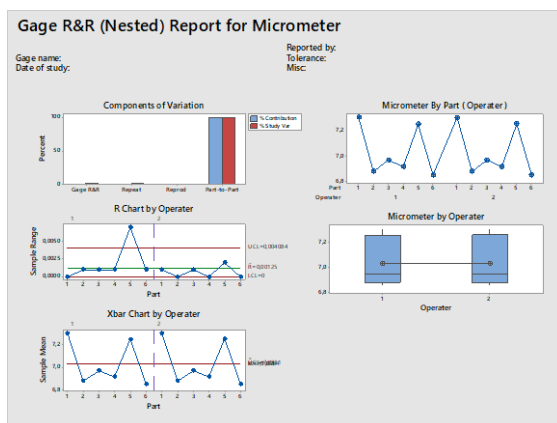

Figure 13 Graphical data analyses of samples measured on micrometre

This results of measurement system analyse can be also represent in graphs (Figure 13 and Figure 14) made in dedicated statistical software Minitab.
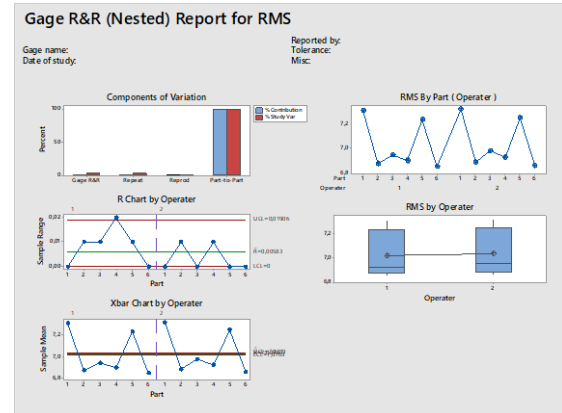

Figure 14 Graphical data analyses of samples measured on RMS

In the Components of Variation graph, most of the variability is explained by the Part–to–Part variation.

In the R Chart by Operator, most of the data are in control, which indicates that operators measure consistently. The By Part graph shows that the differences between parts are large. In the By Operator graph, the measurements for each operator vary by approximately the same amount. Also, the part averages vary by a small amount. While some variation is always present, the data indicate that the operators measure parts similarly.

5. Discussion

Once it has been determined that system is acceptable from a quality control standpoint, measurement of setdown can begin for all 81 samples. The result obtained are shown in Figure 15 and Figure 16.
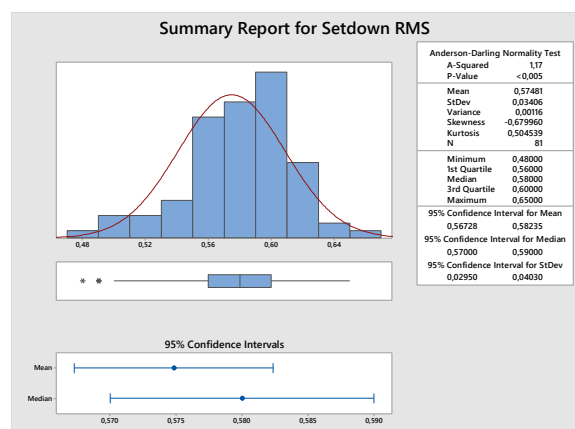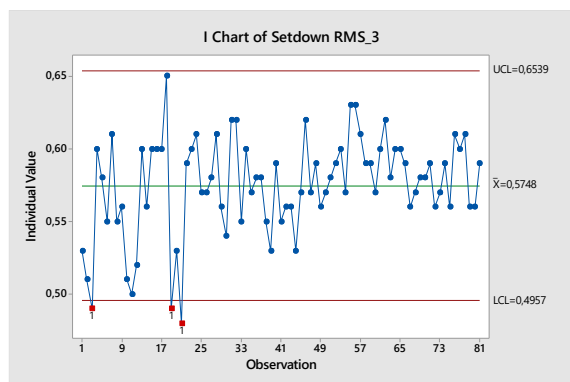

Figure 15 Histogram and summary report for 81 measured samples of one wire mesh

Figure 16 Control chart for 81 measured samples of one wire mesh

Analysis of the graphs suggests that there is an average setdown value of 0.575 mm, while 3 measured values exceed the control limits.

6. Conclusion

In this paper, an analysis of the conventional and the reconfigurable measuring system was performed and elaborated. In both methods, 2 different operators performed measurement operations. Each sample was numbered with the developed numbering system in order to track and compare the obtained values. The results were compared between two different operators and between two different measuring methods.

The analysed measuring systems are acceptable from the quality control point of view, and it was confirmed that the operator has no influence on measuring process. The added value of RMS is also the creation of images of each weld, which are later used for visual inspection and detection of various defects on the weld.

A wire mesh with 81 welding spots was processed and the results show that some of the measured values exceed the control limits, leading to the conclusion that further analysis must be performed to find cause of the deviation that occurred in the production process.

Acknowledgements

REFERENCES

[1] Naik, A.B., Reddy, A.C., 2018. Optimization of Tensile Strength in TIG Welding Using Taguchi Method and Analysis of Variance (ANOVA). Thermal Science and Engineering Progress. 8, 327-339.

[2] Weman, K., 2003. Welding processes handbook, Woodhead Publishing Ltd, Cambridge, England

[3] Koren, Y., 2010. The Global Manufacturing Revolution: Product-Process-Business Integration and Reconfigurable Systems; John Wiley and Sons: Hoboken, NJ, USA,

[4] Xing, B.; Eganza, J.; Bright, G.; Potgieter, J. 2006. Reconfigurable Manufacturing System for Agile Manufacturing. IFAC Proc. Vol., 12 Pt 1, 509–516.

[5] Bright, G.; Davrajh, S. 2007.Automated Apparatus for In-Line Inspection of Mass Produced Custom Parts. In Proceedings of the 2007 Australasian Conference on Robotics and Automation, Brisbane, Australia

[6] Davrajh, S.; Bright, G. 2010. An Automated Apparatus for Dynamic Inspection of Mass-Produced Custom Parts. Assem. Autom., 30, 47–55.

[7] https://support.minitab.com/en-us/minitab/21/ (accessed July 2022)

#nemado**plina**

Mi znamo kako doći od izazova do rješenja uz pravu energiju.

4u1

EVN Croatia Plin od 2009. godine radi na plinofikaciji Dalmacije. Dosad smo u Zadarskoj, Šibensko-kninskoj i Splitsko-dalmatinskoj županiji izgradili više od 139 kilometara nove plinske mreže u skladu s najvišim sigurnosnim standardima.

Svakodnevno plinom opskrbljujemo više od 1600 korisnika.

Zahvaljujući sjajnim rezultatima, EVN Croatia Plin prepoznat je kao pouzdan energetski partner, a Ličko-senjska županija nam je ove godine dodijelila koncesiju u trajanju 50 godina za plinofikaciju gradova Gospića i Otočca.

Veselimo se novim izazovima!

Priključite se na EVN zemni plin.
0800 820 820   www.evn.hr

Zemni plin. Komfor. Budućnost.

EVN

Split

Tourist Board of Split

TURISTIČKA ZAJEDNICA